Interfacial Degradation in Lithium Thiophosphate-Based Composite Cathodes for All-Solid-State Lithium-Ion Batteries

Dem Fachbereich Biologie und Chemie
der Justus-Liebig-Universität Gießen
vorgelegte Dissertation zur Erlangung
des akademischen Grades
Doktor der Naturwissenschaften
– Dr. rer. nat. –

Felix Walther

Juni 2021

Dekan / Dean	Prof. Dr. Thomas Wilke
1. Gutachter / 1st Reviewer	Prof. Dr. Jürgen Janek (Justus-Liebig-Universität Gießen)
2. Gutachter / 2nd Reviewer	PD Dr. Marcus Rohnke (Justus-Liebig-Universität Gießen)
3. Gutachter / 3rd Reviewer	Prof. Dr. Michael Dürr (Justus-Liebig-Universität Gießen)
Eingereicht / submitted	14.06.2021
Disputation / disputation	04.08.2021

Eidesstattliche Erklärung

Die vorliegende Arbeit wurde im Zeitraum vom 01.01.2017 bis 14.06.2021 am Physikalisch-Chemischen Institut der Justus-Liebig-Universität Gießen unter Betreuung von Prof. Dr. Jürgen Janek angefertigt.

Ich erkläre: Ich habe die vorgelegte Dissertation selbstständig und ohne unerlaubte fremde Hilfe und nur mit den Hilfen angefertigt, die ich in der Dissertation angegeben habe. Alle Textstellen, die wörtlich oder sinngemäß aus veröffentlichten Schriften entnommen sind, und alle Angaben, die auf mündlichen Auskünften beruhen, sind als solche kenntlich gemacht. Ich stimme einer evtl. Überprüfung meiner Dissertation durch eine Antiplagiat-Software zu. Bei den von mir durchgeführten und in der Dissertation erwähnten Untersuchungen habe ich die Grundsätze guter wissenschaftlicher Praxis, wie sie in der „Satzung der Justus-Liebig-Universität Gießen zur Sicherung guter wissenschaftlicher Praxis" niedergelegt sind, eingehalten.

Gießen, 14.06.2021

Felix Walther

Abstract

All-solid-state lithium-ion batteries are considered a promising alternative to conventional liquid electrolyte-based lithium-ion batteries. The use of solid electrolytes could enable lithium metal as the anode material, which would lead to higher energy densities compared to conventional energy storage systems. At the same time, safety aspects could be improved by replacing highly flammable organic liquid electrolytes, making such systems particularly attractive for the mobility sector. Thiophosphate solid electrolytes are considered particularly promising in this context, as this materials class usually exhibits a high ionic partial conductivity and is suitable for conventional industrial manufacturing processes due to their advantageous mechanical properties (i.e., their malleability). However, large-scale application of all-solid-state lithium-ion batteries is currently still hindered by numerous problems. On the positive electrode side, interfacial reactions of the cathode active material with the thiophosphate solid electrolyte are considered to be one of the main reasons for rapid capacity loss of the battery and poor long-term stability. Detailed knowledge on such interfacial phenomena is scarce and studies on this subject are rarely differentiated, currently hindering a fundamental understanding and thus preventing a targeted solution to the problem.

In this work, interfacial degradation phenomena in lithium thiophosphate- and $LiNi_{0.6}Co_{0.2}Mn_{0.2}O_2$-based composite cathodes were systematically investigated. It was shown that interfacial degradation occurs at all interfaces within the composite cathode. This includes interfacial reactions of the solid electrolyte against the (i) current collector, (ii) cathode active material, and, if used, (iii) carbon-containing conductive additive, which is often employed to enhance the electronic partial conductivity and to increase cathode active material utilization. By combining spectrometric and spectroscopic studies by means of time-of-flight secondary ion mass spectrometry and X-ray photoelectron spectroscopy, it was possible to separate the convoluted degradation processes and provide detailed insights into the reaction processes and the underlying chemistry. In addition, the reaction zones within the composite cathodes could be visualized based on local compositional information with high spatial resolution.

Based on the knowledge gained, interfacial protection concepts were developed and investigated in this doctoral thesis. This includes protection concepts for carbon-based conductive additives and for cathode active materials. Analyses of a Li_2CO_3/$LiNbO_3$-based coating on the cathode active material $LiNi_{0.6}Co_{0.2}Mn_{0.2}O_2$ showed that the protective effect can be attributed to the suppression of the interfacial reaction, in particular, of oxygenated phosphorus and sulfur compounds. Furthermore, it was possible to discuss the influence of the coating on the battery performance and the interfacial phenomena based on its microstructure (i.e., morphology and chemical composition).

The results of this work extend the knowledge and understanding of interfacial degradation and corresponding protection concepts in composite cathodes. Such knowledge is essential for developing targeted protection concepts, overcoming problems related to interfacial degradation, and paving the way to long-term stability in all-solid-state lithium-ion batteries. The analytical approaches and workflows established in this doctoral thesis provide the foundation for future investigations on interfacial processes. Corresponding concepts can be transferred to other systems and material combinations, thus enabling the analytical characterization of protection concepts.

Zusammenfassung

Feststoffbatterien gelten als vielversprechende Alternative zu konventionellen Lithium-Ionen-Batterien auf Flüssigelektrolytbasis. Die Verwendung von Festelektrolyten könnte den Einsatz von Lithiummetall als Anodenmaterial ermöglichen, was zu höheren Energiedichten gegenüber konventionellen Energiespeichern führen würde. Gleichzeitig könnten Sicherheitsaspekte durch das Ersetzen von leicht entzündlichen, organischen Flüssigelektrolyten verbessert werden, was derartige Systeme insbesondere für den Mobilitätssektor attraktiv macht. Sulfidische Festelektrolyte gelten in diesem Zusammenhang als besonders vielversprechend, da diese Materialklasse meist eine hohe ionische Teilleitfähigkeit besitzt und aufgrund ihrer vorteilhaften mechanischen Eigenschaften (u.a. Formbarkeit) für konventionelle industrielle Fertigungsprozesse geeignet ist. Der großtechnische Einsatz von Feststoffbatterien wird momentan jedoch noch durch zahlreiche Probleme verhindert. Auf der positiven Elektrodenseite gelten Grenzflächenreaktionen des Kathodenaktivmaterials mit dem sulfidischen Festelektrolyten als einer der Hauptgründe für einen schnellen Kapazitätsverlust der Batterie und eine daraus resultierende geringe Langzeitstabilität. Detailliertes Wissen zu derartigen Grenzflächenphänomenen ist rar und Untersuchungen hierzu sind selten differenziert, was ein grundlegendes Verständnis und somit eine gezielte Lösung des Problems derzeit oft erschwert.

Im Rahmen dieser Dissertation wurden Grenzflächendegradationsphänomene in Lithium-Thiophosphat- und $LiNi_{0.6}Co_{0.2}Mn_{0.2}O_2$-basierten Kompositkathoden systematisch untersucht. Es konnte gezeigt werden, dass Grenzflächendegradation an allen Grenzflächen innerhalb der Kompositkathoden stattfindet. Dies umfasst Grenzflächenreaktionen des Festelektrolyten zum (i) Stromabnehmer, (ii) Kathodenaktivmaterial und – falls verwendet – (iii) zum kohlenstoffhaltigen Leitadditiv, welches häufig zur Steigerung der elektronischen Teilleitfähigkeit und zur Erhöhung der Kathodenaktivmaterialausnutzung eingesetzt wird. Über die Kombination von spektrometrischen und spektroskopischen Untersuchungen basierend auf Flugzeit-Sekundärionen-Massenspektrometrie und Röntgen-Photoelektronenspektroskopie konnten die überlagerten Degradationsprozesse separiert und detaillierte Einblicke in die Reaktionsvorgänge und die zugrundeliegende Chemie gegeben werden. Zudem war es möglich, Reaktionszonen auf Basis von Informationen zur chemischen Zusammensetzung mit hoher räumlicher Auflösung zu visualisieren.

Auf Basis der gewonnen Erkenntnisse wurden im Rahmen dieser Dissertation Grenzflächenschutzkonzepte entwickelt und untersucht. Dies umfasst sowohl Schutzkonzepte für kohlenstoffhaltige Leitadditive als auch für Kathodenaktivmaterialien. Untersuchungen zu einer $Li_2CO_3/LiNbO_3$-basierten Beschichtung auf dem Kathodenaktivmaterial $LiNi_{0.6}Co_{0.2}Mn_{0.2}O_2$ zeigen, dass die Schutzwirkung auf die Unterdrückung der Grenzflächenreaktion – insbesondere von sauerstoffhaltigen Phosphor- und Schwefelverbindungen – zurückgeführt werden kann. Zudem war es möglich, den Einfluss der Beschichtung auf die Batterieperformance und die Grenzflächenphänomene auf Basis ihrer Mikrostruktur (Morphologie und chemische Zusammensetzung) zu diskutieren.

Die Ergebnisse dieser Arbeit erweitern die Erkenntnisse und das Wissen um Grenzflächendegradation und entsprechende Schutzkonzepte in Kompositkathoden. Derartiges Wissen ist essentiell, um gezielte Schutzkonzepte zu entwickeln, Grenzflächendegradationsprobleme zu überwinden und so den Weg zu langzeitstabilen Feststoffbatterien zu ebnen. Die in dieser Arbeit etablierten analytischen Ansätze und Arbeitsabläufe stellen das Fundament für zukünftige Grenzflächenuntersuchungen dar. Entsprechende Konzepte können auf andere Systeme und Materialkombinationen übertragen werden und ermöglichen so die analytische Charakterisierung von Schutzkonzepten.

List of Abbreviations

AFM	Atomic force microscopy
ALD	Atomic layer deposition
ASSB	All-solid-state lithium-ion battery
Atom Probe	Atom probe tomography
Auger	Auger electron spectroscopy
BSE	Back-scattered electron
CAM	Cathode active material
CEI	Cathode electrolyte interphase
CL	Cathodoluminescence
CV	Cyclic voltammetry
DEMS	Differential electrochemical mass spectrometry
DHEM	Differential hall effect metrology
DSC	Differential scanning calorimetry
DTA	Differential thermal analysis
EBIC	Electron beam induced current
EBSD	Electron backscatter diffraction
EDX/EDS	Energy dispersive X-ray spectroscopy
EELS	Electron energy loss spectroscopy
ETV	Electrothermal vaporization
FIB	Focused ion beam
FTIR	Fourier transform infrared spectroscopy
FWHM	Full width at half maximum
GC-MS	Gas chromatography mass spectrometry
GDMS	Glow discharge mass spectrometry
GPC	Gel permeation chromatography
hcp	Hexagonal close-packed
IC	Ion chromatography
ICP-MS	Inductively coupled plasma mass spectrometry
ICP-OES	Inductively coupled plasma optical emission spectroscopy
IGA	Instrumental gas analysis
LA	Laser ablation
LC-MS	Liquid chromatography mass spectrometry
LIB	Lithium-ion battery
LIBS	Laser induced breakdown spectroscopy
MWCNT	Multi-walled carbon nanotube
NCM	Lithium nickel cobalt manganese oxide ($LiNi_{1-x-y}Co_xMn_yO_2$)
NCM622	$LiNi_{0.6}Co_{0.2}Mn_{0.2}O_2$
NMR	Nuclear magnetic resonance spectroscopy
OP	Optical profilometry
PEDOT	Poly(3,4-ethylenedioxythiophene)
Raman	Raman spectroscopy
RBS	Rutherford backscattering spectrometry
ROI	Region-of-interest
RSF	Relative sensitivity factor
RTX	Real-time X-ray
sc	Simple cubic
SCL	Space-charge layer
SE	Solid electrolyte

SEI	Solid electrolyte interphase
SEM	Scanning electron microscopy
sMIM	Scanning microwave impedance microscopy
SOC	State-of-charge
STEM	Scanning transmission electron microscopy
TEM	Transmission electron microscopy
TGA	Thermogravimetric analysis
ToF-SIMS	Time-of-flight secondary ion mass spectrometry
TXRF	Total reflection X-ray fluorescence
VGCFs	Vapor-grown carbon fibers
XPS	X-ray photoelectron spectroscopy
XRD	X-ray diffraction
XRF	X-ray fluorescence
XRR	X-ray reflectometry

Table of Contents

1 Introduction

(Research Motivation and Outline)

Since its commercial introduction by Sony in 1991, the lithium-ion battery (LIB) has become the predominant energy storage technology in a wide field of applications and is part of our daily life.[1,2] The reason for this remarkable success is that today's LIBs can provide high energy densities, long-term cyclability and exhibit fast-charging capability. Nowadays, LIBs are used in portable devices such as smartphones, tablets, notebooks and more recently electric vehicles, to name a few. There is no doubt that the LIB has laid the foundation for today's wireless society, which is increasingly less dependent on fossil fuels. Against this background, it seems unsurprising that the 2019 Nobel Prize in Chemistry honors its development.[3]

However, conventional lithium-ion technology may soon reach its physical limit.[4,5] In contrast, the demand for energy storage devices with high energy density, long-term cyclability and fast-charging capability is continuously increasing. One of the most famous examples of such applications is in electric vehicles, which is seen as an important part of many measures to combat climate change and further reduce our society's dependence on fossil fuels.[6] The requirements for this type of battery are high, since driving range, fast-charging capability and safety are important marketing arguments.[7,8] In addition, the cost of such batteries must be low to enable large-scale application and commercialization.

In principle, the energy density of conventional LIBs could be increased, for example, by using lithium metal as anode material, since it is lightweight and has a low redox potential of -3.04 V vs. SHE.[4,9] However, problems mainly related to dendrite formation and thermodynamic stability of liquid electrolytes have not yet been solved, raising safety issues and limiting the energy density of today's conventional LIB technology.[4,7,9–13]

To overcome these issues, while meeting the aforementioned requirements, enormous research efforts have been made to find alternatives to the conventional LIB technology.[14] In this context, all-solid-state lithium-ion batteries (ASSBs) have turned out to be one of the most promising candidates.[5,15–17] In ASSBs, the liquid electrolyte and the separator of conventional LIBs are replaced by a lithium-ion conducting solid electrolyte (SE). It is believed that ASSBs may be superior to conventional LIB technology. The commonly used arguments can be summarized as follows:

First, ASSBs may enable the use of lithium metal as anode material, which could lead to higher specific energy densities compared to conventional LIBs.[2,5] At the same time, issues due to dendrite formation are considered to be prevented or at least reduced by introducing the SE. Second, the replacement of the highly flammable organic liquid electrolyte in LIBs can enhance safety. This makes ASSBs particularly attractive for the automotive sector, where safety plays a key role.[7,8] Third, the cell design can be simplified, opening up new possibilities for module and battery pack design.[2] At the same time, the cell production could be compatible with conventional roll-to-roll processes in the battery industry, which is an important driving factor for large-scale application of ASSBs.[18]

Several classes of SEs have been developed and tested for application in ASSBs.[19,20] Lithium sulfides/thiophosphates are considered to be one of the most promising material class, as they typically exhibit high ionic conductivities in the range of mS/cm and are of high practical relevance due to the low Young's moduli, which imparts good malleability and processability.[18,21–27] The latter is particularly important to enable continuous processes with

high throughput (e.g., roll-to-toll processes), which in turn is necessary to make ASSBs economically attractive.[18]

However, problems associated with the narrow thermodynamic stability window of this material class must be solved to enable large-scale application.[28–32] Furthermore, on the positive electrode side, which is the focus of this doctoral thesis, interfacial reactions can lead to passivating layers and undesirable products, resulting in increased cell resistance, overvoltage and ultimately to a strong capacity fading during cell cycling.[33–36]

To overcome these problems, it is necessary to characterize the underlying reactions in order to develop tailored solutions and characterize their protective effects. However, the analysis of such interfacial reactions (with and without protective layers) is highly challenging for several reasons: First, the solid/solid interfaces are mostly buried and therefore not easily accessible for analytical methods. Second, the reaction zones are small (nm range) and the degradation product volume fractions are low. Third, several reactions overlap within the composite cathode, making it very difficult to separate the individual contributions from the analytical data. Essentially, it is not possible to meet all upper requirements for a proper detection limit, a high spatial resolution and chemical information simultaneously with one analytical method. For this reason, it is necessary to combine several methods to compensate for their individual drawbacks.

In this doctoral thesis, degradation phenomena in the $LiNi_xCo_yMn_zO_2$- (NCM) and lithium thiophosphate-based composite cathodes are investigated using the method combination of time-of-flight secondary ion mass spectrometry (ToF-SIMS), X-ray photoelectron spectroscopy (XPS) and focused ion beam scanning electron microscopy (FIB-SEM). The aim was to gain detailed insights into interfacial degradation phenomena in composite cathodes, to develop protection concepts to overcome associated problems, and to characterize their protective effect. Since the measurement capabilities of ToF-SIMS were commonly not fully exploited in the field of battery materials research at the beginning of this work, a major challenge of this doctoral thesis was to extend the measurement capabilities and establish the method for the analysis of composite cathodes and their individual components.

In the first publication of this thesis, entitled: *"Visualization of the Interfacial Decomposition of Composite Cathodes in Argyrodite-Based All-Solid-State Batteries Using Time-of-Flight Secondary-Ion Mass Spectrometry",* the interfacial reaction between the cathode active material (CAM) and the lithium thiophosphate-based SE was comprehensively investigated using a combination of the analytical methods XPS and ToF-SIMS (see chapter 3.1).[37] In this study, the measuring capabilities of ToF-SIMS were fully exploited, providing valuable insights into interfacial degradation. In particular, the local structure and morphology of the degradation layer – the cathode electrolyte interphase (CEI) - was visualized for the first time on the basis of information on its chemical composition using ToF-SIMS.

In the second publication, entitled: *"Influence of Carbon Additives on the Decomposition Pathways in Cathodes of Lithium Thiophosphate-Based All-Solid-State Batteries",* the degradation picture of composite cathodes was extended by the effect of conductive carbon additives in lithium thiophosphate-based ASSBs, which are commonly used to enhance the electronic partial conductivity of the composite cathode and to increase the utilization of the CAM (see chapter 3.2).[38] In this study, the various reactions within the composite cathode could be deconvoluted and conclusions could be drawn on the individual reaction sites. It was shown that interfacial degradation reactions take place in three different areas of the composite cathode, namely at the interfaces of the SE towards (i) the current collector, (ii) the CAM and (iii)

the conductive carbon additive. Through this work, a comprehensive picture of degradation in lithium thiophosphate-based composite cathodes was obtained, which ultimately resulted in a detailed reaction scheme for the interfacial reaction between NCM and β-Li_3PS_4. Based on the knowledge gained, a protection concept (i.e., protective coating) for conductive carbon additives was developed as part of this thesis. The positive effect on the ASSB performance was demonstrated in a collaborative project with Randau *et al.* and led to a patent application together with BASF SE.[39]

In the third publication, entitled: *"Working Principle of a Li_2CO_3/$LiNbO_3$ Coating on NCM for Thiophosphate-based All-Solid-State Batteries"*, the effect of a protective CAM coating on the degradation processes within the composite cathode was investigated (see chapter 3.3).[40] Although CAM coatings are a common approach to address interfacial problems related to the CAM/SE interface, the protective nature remains widely elusive.[41] Even for $LiNbO_3$-based coatings, which are well established for application in ASSBs and whose beneficial effects have been demonstrated many times, the functional principle of the coating is not yet fully understood. The results of the third publication show that the protective coating suppresses the interfacial degradation between the CAM and the SE, namely the formation of oxygenated phosphorous and sulfur species. In addition, an analytical approach to comprehensively characterize the coating microstructure (in terms of its morphology and chemical composition) is provided. This publication further reveals the possibility to analytically benchmark the efficiency of protective coatings in suppressing interfacial degradation based on ToF-SIMS analyses.

Overall, the results of this doctoral thesis expand the understanding of degradation processes and protective concepts in lithium thiophosphate-based composite cathodes. The obtained picture of degradation phenomena within composite cathodes (with and without protective coatings) is important, on the one hand, to avoid any misleading interpretations of analytical data due to overlapping degradation processes and, on the other hand, to develop customized protection concepts on the way to long-term stable ASSBs. Additionally, this work highlights the key role that ToF-SIMS can play in such investigations and provides the foundation for future studies on interfacial processes.

2 Fundamentals

(Scientific Background, Analytical Hurdles and Degradation in Composite Cathodes)

In the following, the fundamentals necessary for understanding this doctoral thesis are briefly summarized. The aim of this chapter is to give the reader an impression of the samples investigated and the associated hurdles in the context of analytical investigations on interfacial degradation. In addition, analytical advances on interfacial degradation and protective coating analyses in composite cathodes are briefly summarized. This includes placing the results of this doctoral thesis and more recent findings on this topic in the scientific context.

2.1 All-Solid-State Batteries and the Structure of Composite Cathodes

In general, "ASSB" is a collective term for batteries that consist only of solid components. Currently, the term is mostly used to describe batteries that are similar to conventional LIBs in terms of the electrode active materials used and in which the liquid electrolyte and the separator have been replaced by a solid.[5] Accordingly, the ASSB basically consists of five components: the anode; the SE, which also serves as separator; the cathode; and two current collectors, one at each electrode side. For intercalation materials, the anode and cathode active materials accommodate lithium ions. The SE is a lithium ion conducting material that simultaneously isolates both electrodes from each other electronically. During discharging, the anode active material is oxidized and lithium ions are released from the anode, which move through the SE to the cathode. The electrons generated move through the external electric circuit over the device being powered to the cathode. On the cathode side, the CAM is reduced by the electrons and taking up the lithium ions formed at the anode. The charging process corresponds to the reverse process and can be described analogously. Charging is initiated by the application of an external electrical potential or current.

Although the basic operation principle is relatively simple, the detailed processes occurring during charging/discharging within the electrodes are complex. The following paragraph briefly outlines this to provide an idea on this topic and its consequences for analytical investigations.

The cell voltage is determined by the difference of the chemical potentials of the active species (here lithium) of both electrodes. The chemical potential in turn can be separated in an electronic and an ionic contribution.[42,43] For the cathode side, which is in the focus of this doctoral thesis, charging/discharging is accompanied by changes in the electronic and ionic states of the CAM and thus its chemical potential.[43–46] Considering the electronic contribution, changes in the electronic states can be described by the energetic position of the Fermi level E_F.[42,43] The CAM can electronically be described as a small-band gap semiconductor.[47] Therefore, charging/discharging results in changes in electronic states and thus the energetic position of E_F. Since its energetic position is highly dependent, for example, on defects such as intrinsic/extrinsic dopants, the mechanism during charging/discharging depends on the exact electronic band structure and thus on the composition and the microstructure of the CAM.[48] Consequently, effects such as *Fermi level pinning* can occur and need to be considered to avoid misinterpretation of analytical data. As highlighted in publication III, the energetic signal position in XPS data, for example, contains convoluted information on the chemical environment and changes in the electronic states due to battery cycling.[40] Since XPS data is often directly correlated to changes in the chemical environment, a shift in the relative binging energy position caused by charging/discharging-related changes in the electronic states can easily be misinterpreted as a chemical reaction and a change in oxidation states.

So far, only the electronic part to the chemical potential was described. Accordingly, the respective changes in the ionic states and the interactions between both contributions must additionally be taken into account in order to accurately describe the changes in the chemical potential during charging/discharging. While it is important to be aware of this interplay, it is not vital for understanding the results of this thesis. Of higher importance is the basic structure and microstructure of the samples investigated, which will be outlined in the following. Detailed information on the materials used, their supplier, material ratios and the cell assembly process can be found in the respective publication and are not further addressed here.

Within this doctoral thesis, pellet-type ASSBs were investigated. Figure 1 shows a scheme of the ASSB pellet structure studied. The ASSB pellet basically consists of three components: the anode, the separator, and the cathode. The anode is located at the bottom of the ASSB pellet schematic. In this work, anodes made of Li, In/InLi, or carbon-coated $Li_4Ti_5O_{12}$-based composites were used depending on the particular publication and the corresponding collaboration partner. The SE is placed in the middle between both electrodes. In particular, β-Li_3PS_4 and Li_6PS_5Cl were employed (described in the following as thiophosphate-based SEs), which are currently established as standard scientific materials for fundamental studies on thiophosphates. The cathode, which was studied in-depth, can be seen on the upper side of the ASSB pellet schematic in Figure 1. The cathode consists of a composite material containing CAM secondary particles, a thiophosphate-based SE and an optional conductive carbon additive (not shown). The CAM dominates the electronic partial conductivity, while the SE dominates the ionic partial conductivity of the composite cathode. Carbon additives can be used to increase the electronic partial conductivity and to simultaneously enhance the utilization of – otherwise electronically isolated – CAM. In contrast to common LIBs, no binder was used to reduce the complexity of the interfacial processes within the composite cathode for the subsequent analytical studies. The CAM used was $LiNi_{0.6}Co_{0.2}Mn_{0.2}O_2$ (NCM622), which is a common intercalation material in conventional LIBs. The CAM is spherical and exhibits a secondary structure consisting of small agglomerated primary particles (~100 nm range), resulting in a relatively high surface area and roughness. The diameter of the CAM secondary particles is typically in the range of ~ 5 µm. The SE material used in the composite cathode is the same that was used as the separator. The carbon additives used were either Super C65 (particulate) or vapor-grown carbon fibers (VGCFs, fibrous) depending on the particular publication. In addition, the composite cathodes exhibit a typical porosity in the range of ~8-17% for uniaxially cold-pressed ASSBs, which is dependent on the exact cell assembly process and the properties of materials used such as grain size and hardness.

Figure 1 (left) shows a typical cell setup in which the ASSB pellets were cycled.[49] The ASSB pellet (inner diameter: 10 mm) is located in the center of the setup and surrounded by a cell casing that is placed in an aluminum framework. Two stainless steel stamps serve as current collectors and apply pressure to the negative and positive electrode sides, respectively. The pressure on the ASSB pellet can be adjusted by the screw shown above and is typically in the range of ~50-70 MPa upon electrochemical testing. After cell cycling, the setup can be disassembled and the pellet can be extracted. Since the current collector can be simply removed, the surface of the electrodes is easily accessible for subsequent analytical investigations. Due to the relatively high pressures applied during cell cycling and the good malleability of the SE (low Young's modulus), the cathode composite surface is relatively smooth at the beginning of the follow-up studies.[23,25]

Overall, the microstructure of the composite cathodes and the material properties of its components must be considered while interpreting the results of this thesis. For example, as a

consequence of differences in hardness and thus sputtering rates of the composite components, differential sputtering can be expected in depth profiling experiments (see Figure 3). Furthermore, the results of this doctoral thesis show that the microstructure leads to different reaction zones within the composite cathode (see Figure 4).

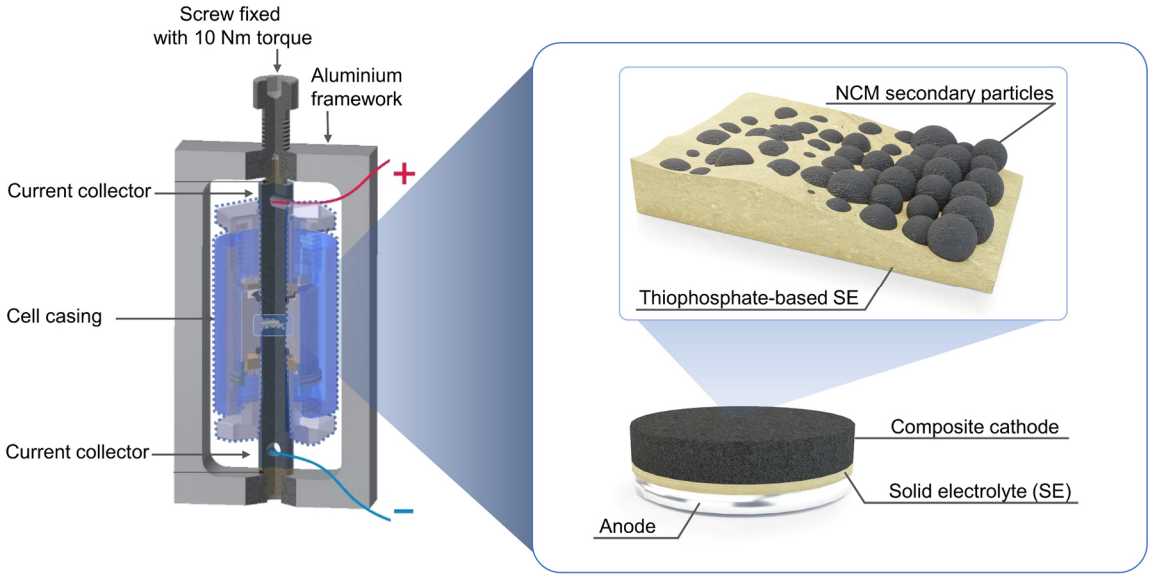

Figure 1 – Left: Typical cell setup for pelletized ASSB cells. The ASSB pellet is placed in the middle and surrounded by a cell casing. The cell casing is in turn placed in an aluminum framework. Two stainless steel stamps serve as current collector and apply pressure to the pellet. The screw on top of the setup is used to adjust the pressure. Adapted with permission from Zhang et al.[49] *Copyright © 2017 American Chemical Society. Right: Basic structure of a pellet-type ASSB analyzed in this doctoral thesis. The ASSB consists of anode, SE and cathode. The cathode corresponds to a composite containing NCM particles, thiophosphate-based SE and an optional conductive carbon additive (not shown).*

2.2 Analytical Challenges and Requirements on Analytical Investigations

This chapter summarizes the main analytical challenges associated with interfacial degradation studies in composite cathodes and the resulting requirements for analytical methods. Based on this, the suitability of analytical methods for such investigations is briefly discussed and the role of ToF-SIMS in the context of battery materials research is highlighted using the example of two collaborative projects related to this thesis where ToF-SIMS was used to characterize CAMs.[50,51]

In general, the analysis of interfacial degradation processes in composite cathodes is not straightforward for several reasons. In the following, three key challenges are introduced and briefly discussed:

i) Poor accessibility of solid/solid interfaces in composite cathodes.

Although the surface of the composite cathodes is easily accessible since the current collector can be simply removed (see chapter 2.1), most of the CAM/SE interface is buried within the composite. Basically, several strategies are conceivable to make such interfaces analytically accessible, including mechanical polishing, ion beam etching, or various sputtering techniques. However, it must be noted that each method can lead to material changes, for example by introducing impurities or by beam damage. Therefore, the choice of method to expose interfaces strongly depends on the respective sample properties and must be optimized in a way that adverse effects are minimized.

Mechanical polishing, for example, is not trivial, especially for NCM- and thiophosphate-based composite cathodes. The main reason for this is the composite cathode structure and the deviating mechanical properties of the individual components. Thiophosphates are relatively soft materials compared to oxides such as NCM.[23,25] Consequently, the requirements for mechanical polishing are different for both materials. The polishing process is further complicated by the fact that the materials used are generally sensitive to air and moisture.[27,52–55] Consequently, sample preparation must be performed under an inert atmosphere and typical water-based polishing procedures cannot be exploited.

In contrast, sputtering-based cleaning procedures and FIB crater-based analyses have proven to be suitable. However, an adjustment of the process parameters and cleaning procedure is mandatory. Surface cleaning experiments with Ar^+ ions for XPS analysis, for example, revealed a strong dependence on the acceleration voltage. At higher voltages such as 4 kV, significant material modifications could be observed in XP spectra, including decomposition of the SE (forming Li_2S and Li_xP) and damage of the CAM (reduction of Ni species due to differential sputtering). These effects could be significantly reduced by applying lower acceleration voltages such as 0.5 kV (0.5 µA, 2 x 2 mm^2 raster size), allowing for subsequent reliable analyses.

These exemplary results already underline the sensitivity of the materials used and highlight the general importance of optimizing sample preparation and cleaning routines. If such considerations are not carefully taken into account, material changes can easily be induced, which are subsequently wrongly attributed to interfacial degradation.

ii) Detection limit issues.

The structure of the composite cathode and the size and shape of its components already indicate low degradation product concentrations, mainly because the reaction zones are typically considered to be in the nm range. This can easily lead to detection limit issues and excludes the use of a number of analytical methods due to insufficient sensitivity. To further

highlight this point, a rough calculation was performed to estimate the theoretical fraction of the degradation layer (CEI) within a 2D analysis area (see Figure 2).

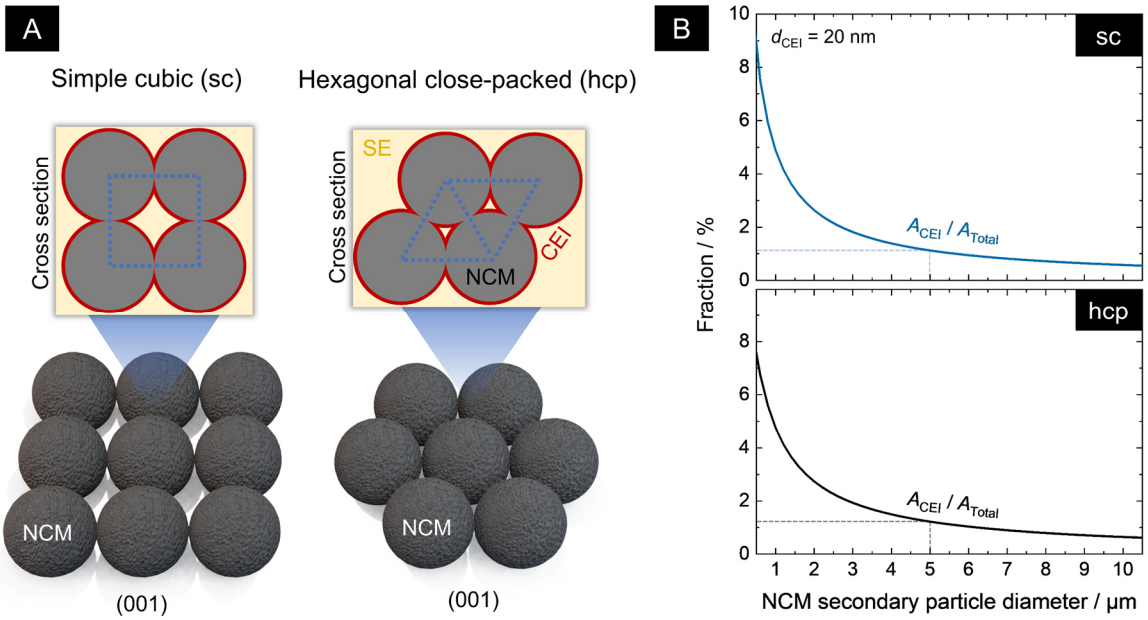

Figure 2 – Model to estimate the fraction of CEI within the analysis area. A) The (001) plane of the simple cubic (sc, left) and hexagonal close-packed (hcp, right) structure are shown at the bottom. The scheme above shows a cross-section assuming that the particles are bisected in half. B) Fraction of the CEI for the sc and the hcp structure as a function of the NCM particle size. A typical CAM secondary particle diameter of 5 µm is highlighted by dashed lines.

Two common packings of equal spheres were assumed (see Figure 2A), namely the hexagonal close-packed (hcp) and the simple cubic (sc) structure corresponding to packing fractions of 0.74 and 0.52 respectively. The latter packing fraction of 0.52 (sc structure) is close to practical CAM:SE volume ratios used (50:50), and is therefore more representative for practical application. In contrast, the hcp structure can be seen as the ideal case and thus the upper limit.

For both structures, analysis on the (001) plane was assumed, representing ideal measuring conditions since the fraction of CAM secondary particles and thus the degradation layer within the analysis area is maximized. Figure 2B shows the fraction of the CEI as a function of the NCM secondary particle size. A relatively thick degradation layer of 20 nm was assumed here. It can be seen, that the fraction of the CEI layer increases in both cases with decreasing NCM secondary particle size. This is not very surprising, since the fraction of NCM/SE interfaces is increased by reducing the CAM secondary particle diameter – in other words: the surface-to-volume ratio of CAM is increasing. Under the assumption of a typical NCM secondary particle diameter of 5 µm, the fraction of the CEI layer corresponds to ~1.2% of the total analysis area for the hcp structure. For the sc structure, this fraction is slightly reduced to ~1.1%.

Considering that the CEI contains a multitude of degradation products, the fractions of the individual products in the analysis area are even smaller. In addition, the idealized cutting planes assumed are practically impossible to achieve. Therefore, the fraction of the degradation layer can be expected to drop even further in practice.

At this point, the question arises why analytical methods with a relatively poor detection limit such as XPS can still measure relatively intense degradation product signals. Based on the results of publication I, the CEI layer appears to be more beam-stable/sputtering-resistive than the SE (see ToF-SIMS analyses on FIB crater sidewalls).[37] As a consequence, differential sputtering occurs in depth profiling experiments, and near-surface NCM particles (with CEI on the surface) are partially uncovered as the SE is removed more easily. This, in turn, increases the fraction of accessible CAM particles and CEI for XPS analysis and increases the intensity of associated XP signals. Another advantage for analytical studies is the rough NCM secondary particle surface, which leads to a larger contact area to the SE compared to the model assumed and shadowing effects during sputtering. These correlations are illustrated in Figure 3, showing the basic principle of differential sputtering. For simplification, the considerations are related to the CAM/SE interface and the influence of the current collector is neglected here.

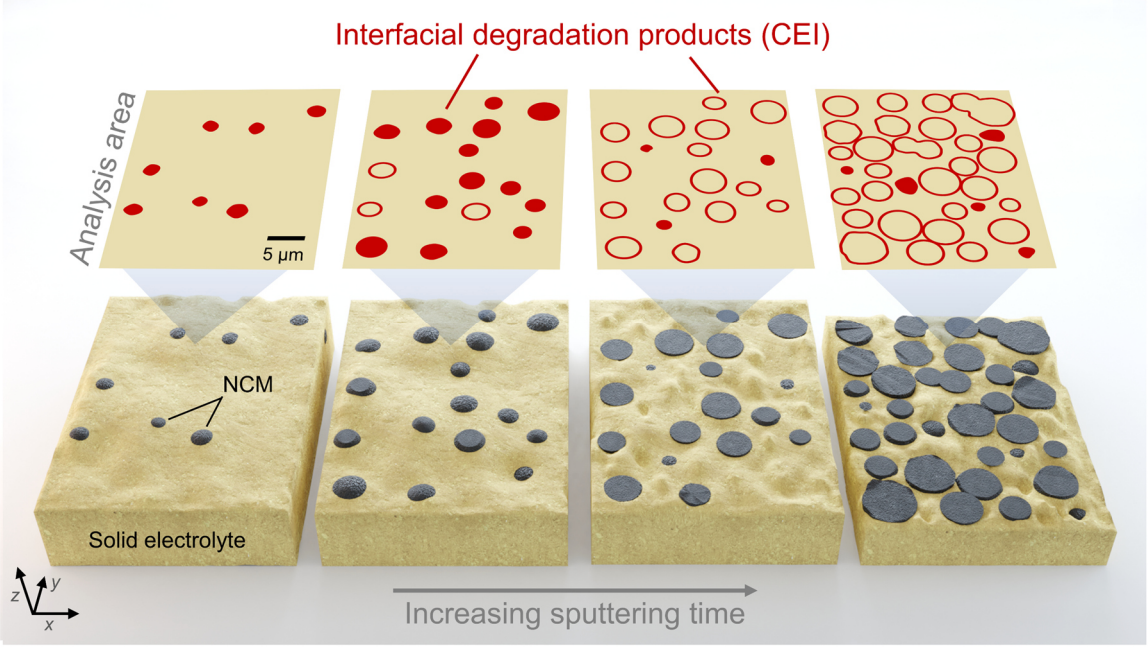

Figure 3 – Scheme of differential sputtering of composite cathodes. On the left, the sample is shown before sputtering. Towards the samples on the right, the sputtering time increases. Above, the fraction of CEI in the analysis area is shown schematically in red. The higher sputtering rate of the SE initially exposes CAM particles including CEI. With further sputtering, the CEI and CAM are also ablated. The roughness of the sputtered area typically increases with increasing sputtering time. The influence of the current collector has been neglected in this scheme.

At the beginning of depth profiling experiments, only a small fraction of CAM secondary particles and related degradation products are analytically accessible. Since the SE shows higher sputter rates compared to the CAM and the CEI, NCM secondary particles are partially uncovered upon sputtering, revealing a higher fraction of CEI in the analysis area. Further sputtering leads to a successive ablation of the CEI at the top of the CAM particles as well as to an ablation of the CAM itself. Under the assumption of a homogenous distribution of CAM within the composite and a sputter equilibrium, the fraction of CEI in the analysis area reaches constant value after a certain time. It can also be seen in Figure 3 that long-term sputtering typically results in

roughening effects due to local differences in sputtering rates stemming from compositional variations and different crystal orientations.

iii) Overlap of degradation processes within the composite cathodes.

Finally, it must be noted that several reaction zones overlap within the composite cathode, making it very difficult to separate the individual contributions in the analytical data. Figure 4 summarizes the findings on these reaction zones based on the results of publication II.[38]

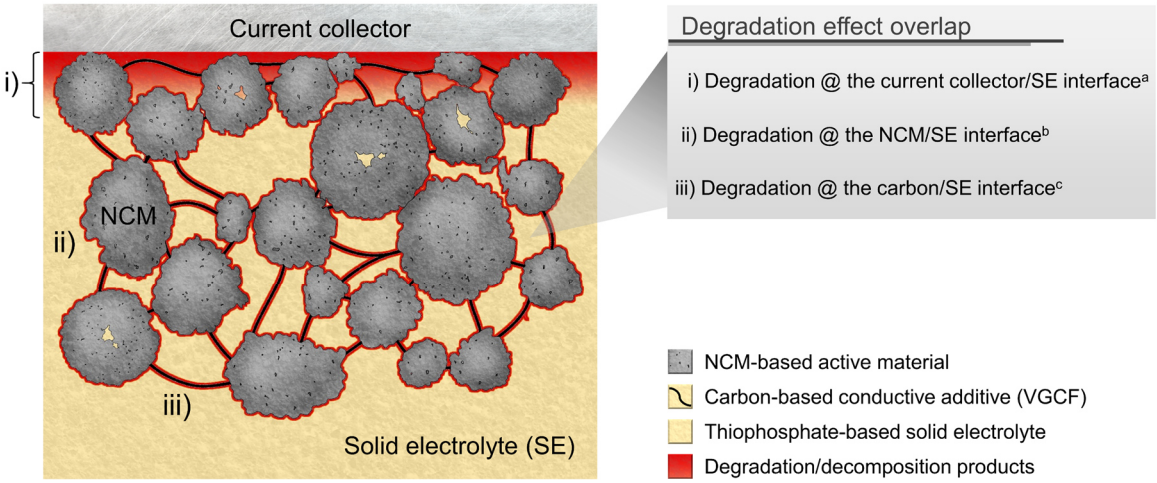

[a] Koerver *et al.*, *J. Mater. Chem. A* 2017, 5, 22750–22760.
[b] Walther *et al.*, *Chem. Mater.* 2019, 31, 3745−3755.
[c] Walther *et al.*, *Chem. Mater.* 2020, 32, 6123−6136.

Figure 4 – Scheme of reaction zones within thiophosphate-based composite cathode with conductive carbon additives. Degradation reactions occur at all interfaces, namely (i) the current collector/SE, (ii) the NCM/SE, and (iii) the carbon/SE interface. At the top of the composite cathode, where the analyses are performed, all degradation reactions overlap and must be considered to avoid misleading interpretation of analytical data. Adapted with permission from Walther et al.[38] *Copyright © 2020 American Chemical Society.*

Accordingly, decomposition and degradation reactions occur at all interfaces of the thiophosphate-based SE, namely towards (i) the current collector, (ii) the CAM, and, if used, (iii) the carbon-based conductive additive (VGCFs in this case). Therefore, a post-mortem analysis of the surface which was oriented towards the current collector contains information on all interfaces and is actually dominated by the degradation towards the current collector. Hence, surface cleaning prior to analysis is recommended and even mandatory for analytical methods with a poor detection limit in order to avoid misinterpretations. In contrast, a high detection sensitivity can enable the separation of the individual contributions. In fact, this could be observed in all three publications of this doctoral thesis. Accordingly, degradation signals could be well separated from each other in ToF-SIMS surface analysis due to the high sensitivity and the high mass resolution of the method. In contrast, this was not possible using XPS due to a much poorer detection limit and significant signal interferences of degradation products. More details on the analytical methods can be found in the next chapter. For a more detailed discussion on the overlapping reaction zones in composite cathodes, the reader is referred to publication II (see chapter 3.2).

Overall, the aforementioned considerations result in certain requirements for analytics. They can be summarized as follows:

- The entire characterization process (sample preparation, sample transfer, and analytical investigations) must be performed under inert atmosphere or vacuum conditions. Otherwise, reactions due to the air- and moisture-sensitivity of the materials cannot be excluded and the results cannot directly be related to specific interface reactions. In addition, most investigations, e.g., XPS analyses, require a surface cleaning step in order to increase the fraction of accessible interfaces and to reduce the detrimental influence by the current collector as mentioned previously. Ideally, the cleaning procedure and the subsequent analysis are both performed within the same instrument to avoid additional transferring steps and thus, potential contaminations.
- Ideally, analysis conditions do not change the sample composition. Consideration should therefore be given to the application of certain (more suitable) analytical methods, particularly for thiophosphates. These are known, for example, to be sensitive to high-energetic beams (e.g., in transmission electron microscopy (TEM) analyses) and thus can easily decompose during such analyses.
- The method chosen should provide information on the underlying chemistry. Basic information on the elemental concentration and distribution are not sufficient to comprehensively characterize degradation processes. Instead, compositional information is necessary.
- A proper detection limit/sensitivity is required to allow analyses even at low degradation product concentrations.
- A high spatial resolution is advantageous to distinguish between overlapping reactions. Accordingly, high spatial resolution allows direct assignment of degradation product signals to certain interfacial reactions within the composite cathode.
- Ideally, the analytical method can provide information on both surface and bulk processes to separate, for example, the influence of the current collector. In addition, locally resolved and bulk (i.e., integral) information is necessary to ensure the validity of the results for the entire composite cathode.

Essentially, it is not possible to meet all upper requirements on chemical information within a proper detection limit and a high spatial resolution simultaneously using only one analytical method. For this reason, it is necessary to combine several methods to compensate for their individual drawbacks. The next chapter addresses the question of which analytical methods are available and how they can be combined to elucidate interfacial phenomena.

2.3 *Analytical Methods and the Role of ToF-SIMS in Investigations of Interfacial Processes.*

For investigations in relation to interfacial processes in composite cathodes, a large variety of analytical methods is available. As mentioned before, no analytical method can meet all necessary requirements to characterize the interfacial processes. Therefore, combinations of different analytical methods are mandatory. This becomes clearer when Figure 5 is considered.

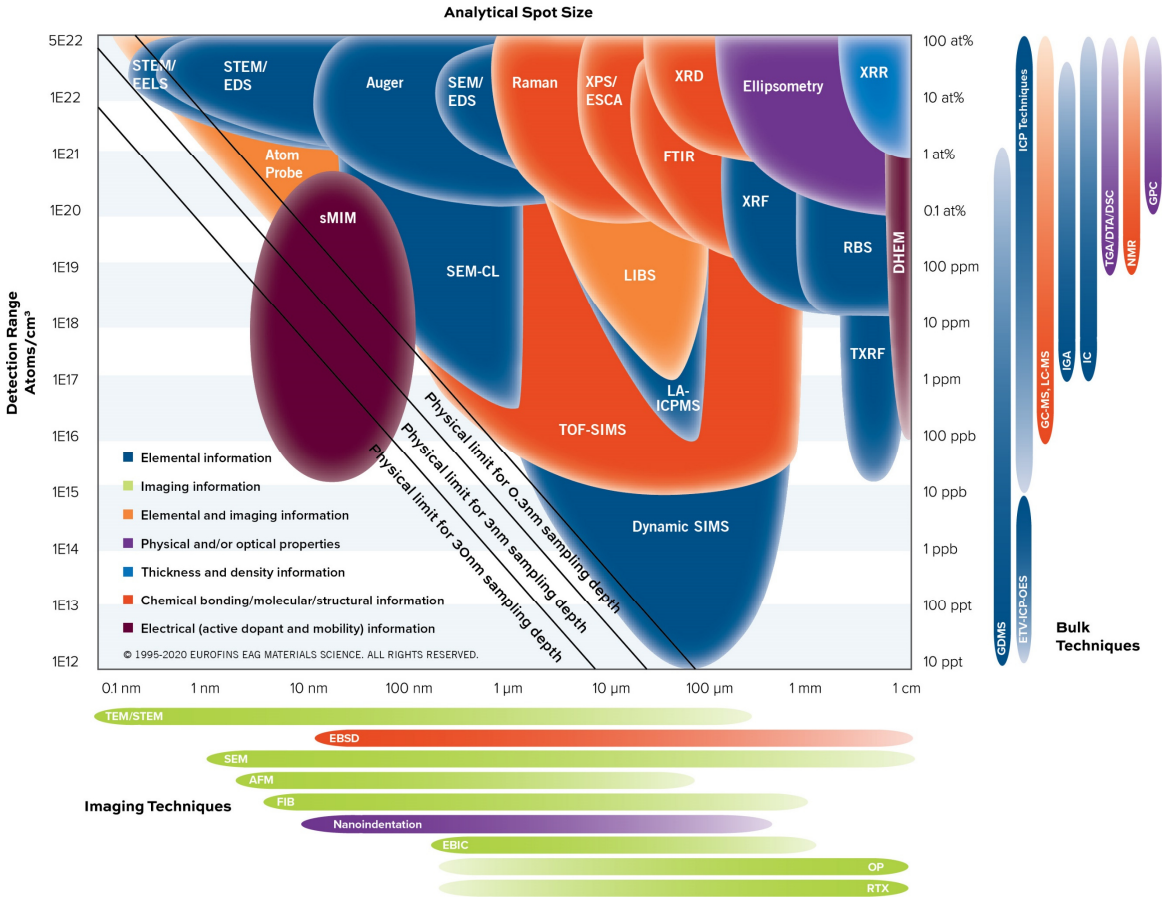

Figure 5 – Scheme for comparing analytical methods in terms of their typical method-specific properties such as detection limit, lateral resolution, and type of information obtained. It can be seen that no analytical method fulfills all criteria simultaneously to the same extent. Therefore, a combination of methods is usually the consequence for analytical investigations. Reprinted with permission. Copyright © Eurofins Scientific (www.eurofinsEAG.com).

The scheme in Figure 5 provides a good overview of the characteristics of different analytical methods and shows that they differ significantly in properties such as lateral resolution, detection range, and the nature of information obtained. Imaging techniques, for example, often lack chemical information, whereas spectrometric and spectroscopic methods tend to have poor lateral resolution. Accordingly, most analytical methods are specialized for certain tasks and must be combined in a way that they effectively compensate for their individual drawbacks and disadvantages to fully characterize interfacial processes in composite cathodes.

The role of several analytical tools in the context of interface analysis in ASSBs were recently reviewed by three research goups.[56–58] In addition, Strauss *et al.* specifically reviewed *operando*

techniques in the context of ASSBs very recently.[59] Accordingly, the reader is referred to these publications for detailed information on this topic. In the following, the choice of the combination of analytical methods relevant in this work is briefly outlined, which includes FIB-SEM, XPS, and ToF-SIMS.

FIB-SEM was used for imaging-related tasks since it can provide information on morphology/topography with high lateral resolution (nm range). In addition, very basic chemical information can be obtained by exploiting the sensitivity of back-scattered electrons (BSE) to the atomic number of elements. However, since the chemical information obtained with FIB-SEM is highly limited, a combination of XPS and ToF-SIMS was used in this thesis to gain detailed information on the chemical environment and the compounds involved in the interfacial reactions. XPS can provide information on the chemical environment, chemical bonding, and, more general, electronic states (e.g., oxidation states).[60,61] In addition, a major advantage is that quantitative statements can be derived. However, XPS suffers from poor lateral resolution (typical maximum lateral resolution of conventional XPS instruments: ~3-5 µm) and a relatively poor detection limit (~ 0.1 at%).[60,61] Considering the low degradation product concentrations in composite cathodes (see chapter 2.2), this can easily lead to detection limit-related problems. For this reason, ToF-SIMS is utilized to compensate for disadvantages of XPS and to gain further insights into the interfacial processes below the detection limit of XPS. ToF-SIMS exhibits high sensitivity and can achieve chemical information with much higher spatial resolution than XPS (see Figure 5 and 6).

Since ToF-SIMS is still not a standard method in the field of battery materials research and was only used in a few studies in the context of ASSBs at the beginning of this PhD project, the measuring capabilities and basic advantages of ToF-SIMS are exemplarily introduced in the following using two collaborative works related to this doctoral thesis.

The basic operating principle of ToF-SIMS is relatively simple and can be described as follows: A primary ion beam is exploited as a primary source and accelerated to the sample surface. There, bombardment of the surface with primary ions induces a collision cascade and leads to the ablation of secondary species such as electrons and material fragments from the surface into the vacuum. Whereas most of the fragments are neutral, charged fragments can be extracted by an electric field and subsequently analyzed in a ToF mass spectrometer system. It is important to note here that ToF-SIMS is a destructive method that uses fragmentation information to draw conclusions on the existing surface compounds. This means that the species are mostly not directly present in the detected form in the sample. Instead, they correspond to fragments of the existing compounds formed during the collision cascade and associated effects such as material recombination/mixing. However, if the specific fragmentation of compounds is known, it is possible to draw conclusions on the chemical environment.

Analogous to SEM, ToF-SIMS can be combined with various technical options such as sputter and FIB guns. An alternating sequence of analyzing and sputtering/milling allows, for example, depth profiling and 3D tomography. Therefore, ToF-SIMS can provide surface sensitive data as well as information on buried interfaces and the bulk. For more details on the operation principle, the underlying fundamental physical mechanisms and technical details related to ToF-SIMS, the reader is referred to literature.[60,62,63] Instead, the practicality of ToF-SIMS in the context of battery research is further addressed in the following sections.

Besides the analysis of interfacial processes in composite cathodes, ToF-SIMS can already be very helpful in the context of the pre-characterization of battery materials. This was demonstrated in two collaborative works related to this thesis, which are discussed in the following.

In a study by Neudeck *et al.*, ToF-SIMS was used to characterize an organophosphate-based CAM coating.[50] A major advantage here is that the signal intensity of secondary ions is not only directly proportional to the fractional concentration of a species *x*, but also to the ionization probability. Since the ionization probability of phosphorous-containing compounds (negatively charged fragments) is, based on experience, generally high, investigations at very low fractional concentrations are possible. This allows detailed insights into the coating microstructure (i.e., morphology and composition). In general, the intensity of secondary ion fragments is determined by the following equation:[60]

$$I_s^x = I_p \cdot y_x \cdot \alpha^{\pm} \cdot \theta_x \cdot \eta \quad (1)$$

with
I_s^x / A: secondary ion current
I_p / A: primary ion current
y_x / 1: sputter yield
$\alpha^{\pm}$ / 1: ionization probability
θ_x / 1: fractional concentration of species *x*
η / 1: transmission of the used SIMS system

The ionization probability is often directly connected to the so-called *matrix effect* which describes the dependency of the ionization probability on the chemical environment. Since the ionization probability is in most cases unknown, ToF-SIMS is generally described as a semi-quantitative method. Accordingly, under the assumption that all parameters on the right-hand side of Equation 1, with the exception of θ_x, are similar or can be compensated by normalization approaches, the secondary ion intensity is dominated by the fractional concentration θ_x. This in turn allows semi-quantitative conclusions on concentration changes to be drawn. In addition, model samples with known composition can be used to determine calibration curves (secondary ion intensity vs. fractional concentration) and thus the determination of so-called *relative sensitivity factors* (RSFs).[63] These RSFs allow a conversion of the secondary ion signal intensity I_s^x into the fractional concentration θ_x. Whereas this concept can be easily applied to, for example, well-defined semiconductor structures, it is not straight forward to utilize it for rather undefined composites (e.g., composite cathodes).[64] However, although the dependence of secondary ion intensity on ionization probability is often perceived rather negatively (due to the matrix effect), it enables a high sensitivity for many compounds. The example of the work of Neudeck *et al.* shows that this relationship can be exploited to visualize the coating material based on its chemical composition which was not possible with other methods (see Figure 6A).[50]

It is also advantageous that not only inorganic but also molecular information can be obtained by ToF-SIMS. Accordingly, it was possible to distinguish the two organic reactants used for the coating process on the basis of their molecular fragmentation. In principle, this allows for the monitoring of reactant residues on the CAM particle surface depending on the preparation parameters, which is advantageous for optimizing coating processes and later for quality control in large-scale applications.

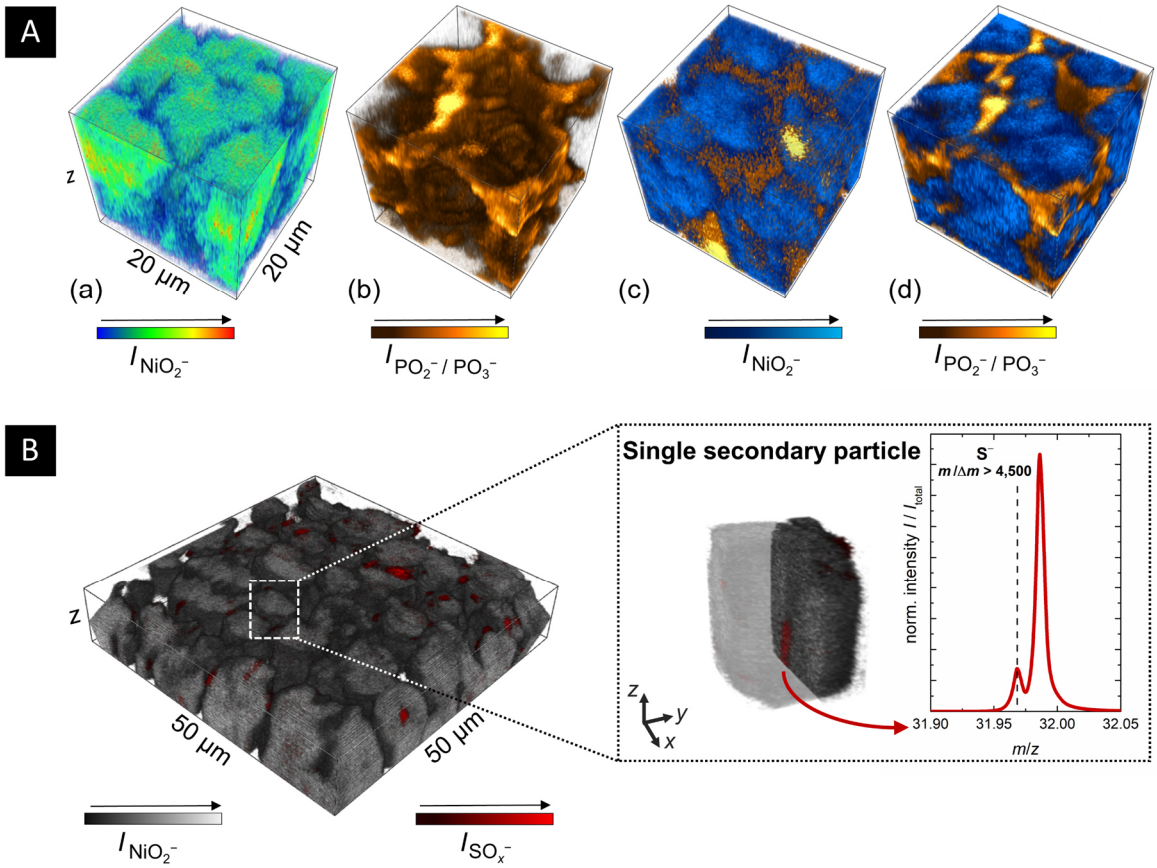

Figure 6 – Exemplarily ToF-SIMS analyses in battery material research. Both analyses were performed in fast imaging mode (high lateral resolution, low mass resolution) in combination with delayed extraction to provide high lateral resolution and simultaneously high mass resolution. A) 3D reconstructions of depth profiles of NCM particles covered with a phosphate-based coating. (a) NCM secondary particles represented by the NiO_2^- fragment. (b) Phosphate-based coating represented by the PO_2^- and PO_3^- fragments. (c), (d) Combined images of the NCM secondary particles and the coating for two different coating approaches. Adapted with permission from Neudeck et al.[50] Copyright © 2018 American Chemical Society. B) 3D reconstruction of depth profiles of an uncycled cathode for LIBs. The NCM secondary particles are shown in gray (represented by the NiO_2^- fragment), whereas sulfur-containing pores are depicted in red (represented by SO_x^- fragments). The cross-section on the right show that sulfur-containing pores/inclusions can be found within the CAM secondary particles. Adapted with permission from Ahmed et al.[51] Copyright © 2019 American Chemical Society.

Another example can be found in a collaborative work with Ahmed *et al.*[51] Previous to the ToF-SIMS analysis, intergranular nanopores were found in a NCM-based material using TEM-based techniques. Since these nanopores were found to be undesirable as they contribute to internal CAM degradation, the question of their origin emerged. While energy-dispersive X-ray spectroscopy (EDX) could only provide the very basic information that the pores contain sulfur, ToF-SIMS allowed to attribute corresponding fragments of the material in the nanopores to Li_2SO_4. Similar to the work by Neudeck *et al.*, ToF-SIMS analyses were beneficial here, since sulfur compounds usually have high ionization probabilities for negatively charged fragments.[50] This enabled their analysis despite extremely low concentrations. At the same time, the high special resolution of ToF-SIMS was also exploited. In this way, it was possible to determine sulfur-

rich areas in 3D reconstructions and analyze their origin with a region-of-interest (ROI) analysis. The high spatial resolution was necessary to unambiguously assign the sulfur species to regions within the CAM secondary particles and to exclude surface impurities as the cause of the signals.

Overall, these examples demonstrate the high value of ToF-SIMS in the field of battery materials research. Accordingly, ToF-SIMS is excellently suited to compensate for weaknesses of other methods. In particular, the combination of ToF-SIMS with XPS is extremely powerful to provide compositional information, since both methods are complementary and compensate for most of their respective drawbacks. Since both analysis techniques suffer from relatively poor lateral resolution compared to typical imaging techniques, they were complemented by SEM. All three methods (SEM, XPS, and ToF-SIMS) were combined with sputter and/or FIB profiling within this doctoral thesis to allow the separation of surface contributions and thus, the analysis of the bulk material.

2.4 Degradation Processes in Thiophosphate-Based Composite Cathodes

In general, degradation phenomena in composite cathodes can be divided into two main categories: morphological/structural degradation of the CAM and interfacial degradation due to (electro-)chemical reactions. In the following, both will be described in separate sections, with a focus on interfacial (electro-)chemical reactions, analogous to the entire doctoral thesis.

2.4.1 Morphological/Structural Degradation of the CAM

The morphological/structural degradation of CAM summarizes effects caused by structural changes during charging and discharging. A distinction can be made between structural changes due to (de)lithiation and phase transformations due to (electro-)chemical reactions. The latter already indicates that both degradation categories (chapter 2.4.1 and 2.4.2) can be mutually dependent and are often accompanied by each other, making a clear deviation of the individual processes highly challenging.

It is well known that NCM-based materials undergo anisotropic volume changes during (de)lithiation depending on the exact composition.[65–67] These effects can result in pressure-induced changes in the microstructure such as crack formation, contact loss between NCM and SE, voids and electronically isolated NCM particles within the composite cathode, to name a few.[66,67] This in turn has a massive influence on the resultant battery performance.[68] Strauss *et al.* have recently shown that it is possible to design quasi-zero strain NCM by intentionally modulating the composition.[65] However, commonly used NCM material compositions differ from the reported stoichiometries and are therefore affected by anisotropic volume changes. For this reason, pressure-dependent studies of battery performance are an ongoing research topic.[66,69]

Besides volume changes, phase transformations, e.g., the formation of spinel- and rock-salt-like phases cause additional stress/strain leading to cracking of the CAM. Analogous to LIBs, it was shown that rock-salt formation takes place at CAM/SE interfaces in ASSBs.[70,71] In addition, Ahmed *et al.* have recently shown that intragranular nanopores present within the CAM undergo morphological changes during cycling, which are based on the formation of spinel- and rock-salt-like phases.[51] This internal CAM degradation can in turn lead to strain-induced intragranular cracking and can be expected in LIBs and ASSBs.

2.4.2 Interfacial Degradation Due to (Electro-)Chemical Reactions

Interfacial degradation due to (electro-)chemical reactions is mainly attributed to the narrow thermodynamic stability of the thiophosphate-based SE and its reactivity with other materials.[28–32] Up to now, three interfacial degradation modes have been identified and need to be considered (see Figure 7).

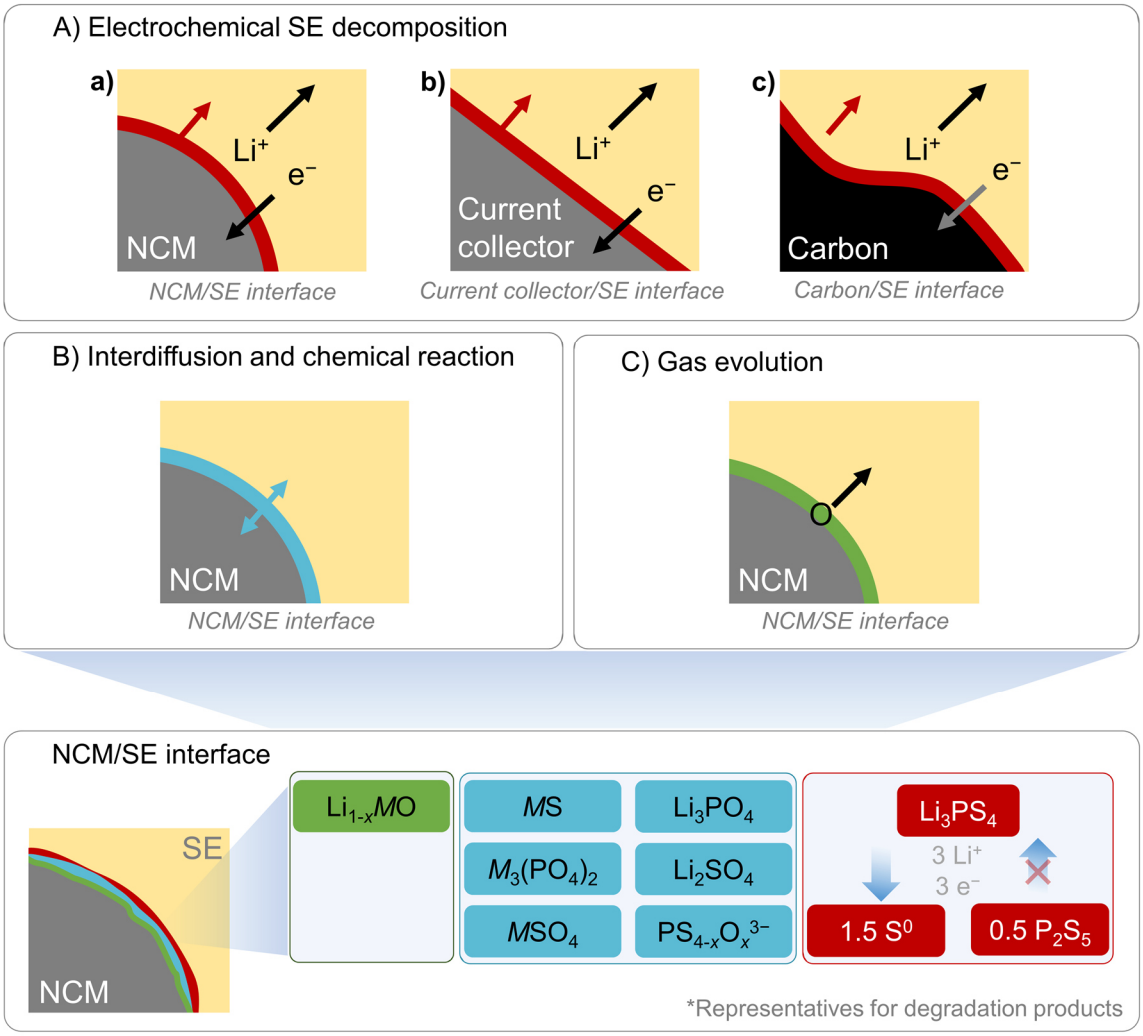

Figure 7 – Scheme for interfacial degradation due to (electro-)chemical reactions. Three interfacial degradation modes can be distinguished, namely A) electrochemical SE decomposition, B) interdiffusion and chemical reaction and C) gas evolution. Whereas mode A) dominates the degradation processes at the current collector/SE and carbon/SE interface, all three modes contribute to the CEI formation at the NCM/SE interface (bottom). Overall, the interfacial degradation due to (electro-)chemical reactions is detrimental for the ASSB performance and results in strong capacity fading upon cycling.

The processes shown in Figure 7 can be described as follows:

A) Electrochemical SE decomposition.

Electrochemical decomposition of the SE is due to the generally narrow thermodynamic stability of thiophosphates.[28–32] Accordingly, depending on the electric potential applied, an uptake and release of electrons is accompanied by decomposition reactions and phase transformations of the SE. First-principle calculations indicate that these oxidation reactions occur at about 2.1 – 2.3 V vs. Li^+/Li, whereas Dewald *et al.* have recently shown that the practical oxidative stability limit is in the range of 2.8 – 3.1 V vs. Li^+/Li and therefore noticeably higher than theoretically predicted.[28,72]

Taking the electronically conductive components on the positive electrode side into account, these reactions can be expected at all interfaces of the SE, namely towards: (a) the CAM, (b) the current collector, and (c) the conductive carbon additive. Indeed, in publication II, the three independent reaction zones were experimentally proven.[38] The products formed during oxidation were analyzed and described several times in literature.[34–38,73–77] The identified compounds mostly include various anionic frameworks that Li-P-S phases can pass through towards the formation of P_2S_5 and S^0-like species such as polysulfides. The latter was experimentally confirmed for NCM- and thiophosphate-based composite cathodes in publication II using XPS and ToF-SIMS.

In this context, it must be pointed out that these reactions are partially reversible. Accordingly, the redox behavior of thiophosphates was described several times in literature and allows, in principle, conversion-type composite cathodes based on thiophosphates.[36,72,77–79] Indeed, Wang *et al.* have very recently shown that the $Li_6PS_5Cl_{0.5}Br_{0.5}$ argyrodite can be used as precursor material in composite cathodes based on multi-walled carbon nanotubes (MWCNTs) and enables high capacities and long-term cyclability if the appropriate potential range is chosen.[80] In NCM-based ASSBs, however, the lower cut-off potential is too high to enable the reduction reactions postulated by Wang *et al.*[80] Therefore, most of the oxidation products formed during charging remain after discharging. Since the products formed such as polysulfides show poor ionic conductivities, the oxidative products result locally in an increased resistance in the interface region.[33,36] With prolonged SE decomposition, the overall effective ionic partial conductivity in the composite decreases and thus, the ASSB cell performance does as well. The SE decomposition mechanism must be considered as a dynamic process. Accordingly, the local CEI composition and the products present are dependent on the reactants, the state-of-charge (SOC) and the number of cycles, among others.

B) Interdiffusion and chemical reaction.

Chemical reactions can, in principle, occur at all interfaces (Figure 7A, a-c) and are dependent on various parameters such as the applied potential/SOC, temperature and time, to name a few.

At the interfaces of the SE towards the current collector and the carbon additives, the chemical reaction is mostly limited to reactions with functional groups on the surface. Indeed, Park *et al.* have shown that functional groups on carbon additives are directly involved in reactions with thiophosphate-based SEs.[81] The results of publication II indicate that despite material drying, oxygen-containing species on the carbon surface such as –OH groups, carbonates, and water residuals can react with the SE under the formation of compounds such as Li_3PO_4.[38] However, the fraction of functional groups on carbon additives and on the current collector are limited. Therefore, it can be assumed that degradation processes at these interfaces are rather dominated by the electrochemical SE decomposition.

In contrast, the chemical reaction plays a major role at the CAM/SE interface. Several computational studies were carried out to gain insights into the interfacial processes and the chemical reaction between CAM and SE.[29–32,82,83] It must be taken into account in this context that the reactions and related reaction products are strongly dependent on material combination (CAM/SE) and the SOC (degree of (de)lithiation). Nevertheless, some general conclusions and tendencies can be inferred:

Calculations indicate a strong tendency for the reaction of oxides and thiophosphates to form PO_x-containing compounds.[29–32,82] In addition, the formation of sulfates such as Li_2SO_4 and transition metal sulfides are often reported to be energetically preferable.[29–32] It should be noted here that these reactions can already occur due to the mere contact of NCM (lithiated) and thiophosphate-based SE and are not limited to cell operation.[32]

Experimental evidence for the predicted degradation reactions is highly challenging, not at least due to the poor accessibility of the CAM/SE interface and the convolution of degradation processes within the composite cathode as indicated in chapter 2.2. Accordingly, in many experimental studies, the electrochemical decomposition of the SE could not be well separated from the chemical reaction at the NCM/SE interface and therefore dominates degradation product signals, for example, in XP spectra. A clear correlation of degradation products to the CAM/SE interface is, therefore, often rare. However, some conclusions directly related to the CAM/SE interface can be drawn from literature and the results of this doctoral thesis.

Sakuda *et al.* have experimentally shown that interdiffusion occurs between $LiCoO_2$ and a lithium thiophosphate-based SE, which is in accordance with the calculations by Haruyama *et al.*[83,84] The interdiffusion process between CAM and the thiophosphate-based SE is accompanied by several reactions. Analogous to the computational studies mentioned, experimental evidence is often related to the formation of oxygenated phosphorous and sulfur species as well as to the formation of transition metal sulfides.[37,38,40,85–90]

Visbal *et al.*, for example, have shown that cell cycling can be correlated with an increase in SO_x^- and PO_x^- fragments in ToF-SIMS surface spectra ($LiNi_{0.8}Co_{0.15}Al_{0.05}O_2/Li_2S–P_2S_5$ glass ceramic).[85] Since this study was limited to surface analyses with low lateral resolution, clear evidence that these fragments can be unambiguously related to the CAM/SE interface was missing. In publication I, depth profiling with high spatial resolution and imaging of FIB crater sidewalls allowed for the direct correlation of the formation of the oxygenated phosphorous and sulfur compounds to the NCM622/Li_6PS_5Cl interface.[37] Accordingly, the CEI formed could be visualized for the first time based on chemical information with high spatial resolution using ToF-SIMS.[37] Combined with results from XPS, it was concluded that sulfates such as Li_2SO_4 and phosphates such as Li_3PO_4 and potentially transition metal phosphates such as $Ni_3(PO_4)_2$ and $Mn_3(PO_4)_2$ are reasonable interfacial degradation products. These results were further strengthened by the results of publication II.[38] Accordingly, similar interfacial processes were detected for NCM622 in contact to β-Li_3PS_4, indicating that these processes are somehow universal for NCM- and thiophosphate-based composite cathodes. In addition to the compounds discussed in both publications, anionic frameworks of thiophosphates such as $PS_{4-x}O_x^{3-}$ are also conceivable to be formed in the interfacial region. Such compounds could lead to similar fragments in mass spectra such as SO_x^- and PO_x^- and the energetic signal position in XPS spectra should be in the typical energy range of other phosphates and sulfates. Thus, a clear differentiation of the compounds mentioned is analytically quite challenging. However, overall, the aforementioned experimental results agree well with the reaction trends for the formation of oxygenated phosphorus and sulfur compounds derived from calculations.

The role of transition metal sulfides in the interfacial reaction is not entirely clear at the moment. In contrast to computational predictions and some experimental studies, there was no clear evidence gained for the formation of transition metal sulfides in XPS and ToF-SIMS data in this thesis.[29–32,86–91] Taking the small dimension of the CEI and the low fractions of degradation products into account, detection limit issues seem reasonable, as discussed in the respective publications. In fact, reliable studies suggesting the formation of transition metal sulfides are often based on highly resolving/highly sensitive analytical methods such as (scanning) transmission electron microscopy ((S)TEM), supporting the assumptions on low degradation product volume fractions.[86,87] In contrast, experimental studies using other methods with worse detection limits, such as XPS, are often rather questionable. Accordingly, some experimental studies show intense XP signals and postulate the formation of transition metal sulfides based on the assigned signal contributions.[88–90] However, the analytical data is often poorly documented and evaluation procedures (e.g., energy calibration in XP spectra and information on the fitting models used) remain rather elusive in these publications.

For example, Jung and Gwon *et al.* reported a significant change of SE-related XP signals and derived the formation of transition metal sulfides from these spectra.[88] Taking a closer look at the respective spectra revealed a systematic shift of about 0.25 eV in all SE-related signals (S 2p, P 2p and Cl 2p), indicating a misleading energy calibration. Since this shift was not detected after surface sputtering, detrimental surface effects such as differential charging and potential gradients seem reasonable, which can easily lead to a relative signal shift in XPS spectra and thus, an incorrect energy calibration.[92,93] Maibach *et al.* have already discussed effects related to detrimental surface layers and explicitly stated that LiF, among other polar compounds, can cause such phenomena.[92] Indeed, ToF-SIMS depth profiles shown in the study by Jung and Gwon *et al.* reveal an accumulation of Li_xCl_y fragments on the surface of the respective sample, indicating the presence of LiCl. Remarkably, despite ToF-SIMS analyses, no fragments associated with transition metal sulfides such as NiS^- or NiS_2^- were shown in this study which could further strengthen their conclusions. The proof of the formation of transition metal sulfides remains therefore highly doubtful here.

Another example can be found in a recent study by Lim and Park.[89] They investigated effects of a precursor-based CAM modification and performed XPS measurements to characterize interfacial degradation. Based on their XPS results, the modifications suppress interfacial reactions indicated by a decrease in S 2p signal contributions at lower binding energies, which are typically associated with transition metal sulfides. Taking a closer look at the XPS data and the information about the XPS measurements given in the work, several inconsistencies and questions arise. As already pointed out earlier, XPS alone is mostly not sufficient to deconvolute the individual degradation contributions, making it challenging to draw conclusions on the degradation at the NCM/SE interface. Since Lim and Park used conductive carbon additives in the thiophosphate-based composite cathode, electrochemical decomposition of SE can be expected, as previously mentioned. However, based on their results, the formation of species at higher binding energies, such as polysulfides, seem to play a minor role, which contradicts typical observations for thiophosphate-based composite cathodes. Consequently, the question of the energy calibration procedure arises, since a systematic energy shift could explain this observation. Unfortunately, the manuscript does not provide any information on the energy calibration procedure, nor on fitting parameters and respective fitting restrictions. In addition, when the envelope of S 2p of the cycled composite cathodes (unmodified and modified) are compared, it becomes clear that they match to a high extent. Taking the fits into account, it appears that the signal intensities of the degradation products for the unmodified case are only

higher due to a smaller full width at half maximum (FWHM) of the main contribution. Consequently, the postulated suppression in interfacial reactions seems mainly caused by a misleading signal fitting procedure.

Overall, the role of transition metal sulfides is not yet unequivocally clarified, largely due to the low quantities and related detection limit issues. Based on the results of this doctoral thesis, a reaction scheme for the interfacial reaction of NCM-based materials and β-Li_3PS_4 was proposed in publication II.[38] It was assumed that the thermodynamically preferred path involves the formation of transition metal sulfides as intermediate products, which can further react to oxygenated sulfur species such as sulfates upon charging, e.g., in a metathesis-type reaction. This could explain the low quantities of transition metal sulfides in the experimental data of this thesis and the aforementioned experimental observations. In addition, the proposed reaction scheme based on the interfacial reaction of both components could also explain the formation of a rock-salt-like phase on the surface of the CAM particles, which is a well-known degradation phenomenon in LIBs and was also very recently proven for thiophosphate-based ASSBs.[70]

Besides the identification of the compounds present in the interfacial region, the microstructure of the CEI is also important to understand the underlying interfacial mechanisms. However, information on the microstructure is highly limited due to the analytical requirements for high imaging resolution, high detection limit and sufficient stability of the CEI. While most analytical methods already suffer from the first two factors, the latter significantly prevents TEM-based investigations. Accordingly, the CEI is often partially destroyed by the sample preparation procedure and/or the high-energetic electron beam, making conclusions on the original CEI difficult to be drawn. Besides the more general statement that the CEI is homogeneously distributed on the CAM secondary particle surface according to publication I, Zhang *et al.* very recently observed a segregation of transition metals in Co/Ni-rich and Mn-rich domains within the CEI of NCM523/Li_3PS_4-based composite cathodes using STEM combined with EDX.[87] These observations suggest that the CEI microstructure is not necessarily a layered structure, but may be more mosaic-like and dependent on the elements involved. However, this needs to be further investigated in future experiments.

In general, it can be assumed that the CEI composition and microstructure changes during cell cycling. In follow-up studies to publication I and II, the dynamics of the interfacial degradation layer were investigated in more detail. Yamagishi *et al.* reported for a $LiNi_{0.8}Co_{0.15}Al_{0.05}O_2$ and $75Li_2S{\cdot}25P_2S_5$-based composite cathode that the fraction of oxygenated phosphorous species shows an increasing trend with cell cycling, whereas oxygenated sulfur species showed a partially reversible behavior indicating a redox-activity of such species.[94] This is consistent with the results of publication III, in which the successive formation of oxygen-containing phosphorus and sulfur species with increasing number of cycles was found for a composite cathode containing Li_2CO_3/$LiNbO_3$-coated NCM622 and Li_6PS_5Cl.[40] The increasing trend in oxygenated degradation products already suggests a diffusion-based model for the interfacial degradation processes. This was further strengthened by a very recent study of Zuo *et al.* which probed the kinetics of the interfacial degradation reactions in NCM622/$Li_{10}GeP_2S_{12}$-based composite cathodes.[95] Therein, the authors demonstrated that the interfacial reactions show a typical parabolic rate behavior and can be well described by the Wagner-type model for diffusion-controlled reactions. Since the chemical reactions between CAM and SE can be described by a diffusion-controlled model, it seems not very surprising that these reactions were reported to be dependent on SOC, temperature and time. Therefore, the CEI formation must be considered as a dynamic process. Overall, these results fit well to previous studies on the

chemical reaction between the CAM and thiophosphate-based SEs, including the results of publications I, II and III.

C) Gas evolution.

Analogous to conventional LIBs, gas evolution also needs to be considered in the context of ASSBs.[96–99] Accordingly, the evolution of gaseous O_2 and CO_2 was reported, which can be related to oxygen release from the NCM lattice at high SOCs and/or electrochemical decomposition of Li_2CO_3 which is a typical surface contaminant of Ni-rich NCM materials.[96–103] According to literature, the released oxygen could be partially present as highly reactive singlet $^1O_2$ which can lead to subsequent reactions with the SE in the interfacial region.[104,105] Indeed, SO_2 evolution was reported for thiophosphate-based ASSBs.[96–99] In addition, it seems conceivable that the formation of oxygenated phosphorous and sulfur species reported under reaction mode B) can be partially attributed to the reactions based on the released oxygen. The release of oxygen is probably accompanied by the formation of spinel-like and rock-salt-like phases on the particle surface, as already mentioned in the context of morphological/structural degradation.

At this point it becomes clear again that the degradation processes within the composite cathodes are somehow interconnected and accompanied by each other. It must also be noted here that the processes mentioned in A) - C) are to some extent in competition with each other. Depending on the reaction conditions, a dynamic change of reactions and the associated products can be expected. In fact, such behavior could be observed in publication II.[38] In this work, the influence of conductive carbon additives in NCM622/β-Li_3PS_4-based composite cathodes was investigated. ToF-SIMS studies indicated the formation of oxygenated sulfur species and polysulfides due to cell cycling for the sample without conductive additives. In contrast, with conductive additives, polysulfide formation was dominant and signal intensities for oxygenated sulfur fragments (SO_x^-) even fell below the signal intensities for the uncycled reference. Accordingly, the polysulfide formation appeared to be preferred in this case and sulfates/sulfites acted rather as intermediate products. Similar processes could explain the findings of Yamagishi *et al.* who observed a partially reversible SOC dependence of oxygenated sulfur fragments (SO_x^-) in $LiNi_{0.8}Co_{0.15}Al_{0.05}O_2$/$75Li_2S{\cdot}25P_2S_5$-based composite cathodes.[94]

Overall, the processes in Figure 7 A) – C) result in undesirable products and highly resistive interfacial layers that impede lithium-ion transport and ultimately lead to a decrease in ASSB performance. For this reason, several strategies to overcome these interfacial issues were developed. These include modifications of the CAM and the SE, e.g., by doping approaches, but also protective coatings for modifying interfacial regions.[41,106,107] The latter strategy will be discussed in more detail in the next section.

2.5 Protective Coatings in Composite Cathodes

Coating approaches are a common strategy to address degradation phenomena in composite cathodes (see chapter 2.4). In this context, it must be noted that protective coatings are not limited to the CAM. Accordingly, coatings were also successfully applied to conductive additives and were reported to enhance the ASSB performance.[39,108] The desired function of the coatings and the material properties required for this purpose therefore depend strongly on the component and the associated degradation phenomena.

2.5.1 Coatings on the CAM

In general, CAM coatings can address both categories of degradation phenomena, namely morphological/structural degradation of the CAM (see chapter 2.4.1) and interfacial degradation due to (electro-)chemical reactions (see chapter 2.4.2).

The aim of CAM coatings is often directly related to the narrow thermodynamic stability of the thiophosphate-based SE and its reactivity with the CAM.[28–32,83] Therefore, the coating material should prevent the thiophosphate-based SE from electrochemical decomposition and the chemical reaction between the CAM and the SE. Additionally, protective coatings could stabilize the CAM surface preventing gas evolution at high potentials and accompanied phase-transitions to spinel-like and rock-salt-like phases on the particle surface. It is also not completely clear whether a protective layer can mechanically stabilize the CAM surface to inhibit volume changes and particle cracking. Such an effect could be caused, for example, by mutual diffusion between the coating and the CAM corresponding to a surface-like doping. Another parameter discussed in the context of CAM coatings is the influence on so-called space-charge layers (SCLs).[109–113] SLCs can be formed in the interfacial region between the CAM and the SE due to differences in the electrochemical potential and are reported to potentially impede the Li-ion transport and thus, cause high interfacial resistance. Calculations indicate that the detrimental effects of SCLs can be reduced by coatings.[110] However, the extent of SLC-related effects on the interfacial transport of Li-ions is controversially discussed in the literature and seems to be strongly dependent on the material combination used.[111,113]

Guidelines and design criteria derived from these considerations such as *electron-blocking* and *ion-conducting* and calculations in the context of the reactivity of CAM coatings can be found in literature and are not further addressed here.[28,30,32,41,114–116]

The suitability of CAM coatings to enhance the performance of thiophosphate-based ASSBs was widely demonstrated experimentally in the literature, as described in a recent progress report by Culver *et al.*[41] Accordingly, it has been clearly proven that CAM coatings can reduce the rise of interfacial resistance between the CAM and the SE during battery cycling, suppress related interfacial degradation, improve the rate performance and enhance the long-term cycling stability of CAMs.

However, since many studies focus mainly on electrochemical investigations related to ASSB performance, detailed knowledge on the underlying mechanistic working principle of CAM coatings is lacking.[117–119] Therefore, it is often not clear as to which specific degradation mechanism the coating has an influence on and which mechanistic effects correlate with the improvement of ASSB performance. Analytical investigations often suffer from an insufficient pre-characterization of the coating which makes it almost impossible to interpret its influence on the processes within the composite cathode. Accordingly, information on the composition and the microstructure of the coating is often rather vague. In addition to the insufficient

coating pre-characterization, the individual degradation processes in the composite cathode (see chapter 2.4) are often not sufficiently separated from each other in analytical data. In many cases this results in unspecific statements such as a *general suppression of interfacial degradation* or, much worse, in misleading conclusions. However, a small number of studies give detailed experimental insights into the working principle of protective coatings. At this point it should be considered that the functioning of the CAM coating is, among others, highly dependent on the coating composition and its microstructure. Therefore, the protective effect and reactions may differ depending on the material combination.

Sakuda *et al.* demonstrated that a Li_2SiO_3 coating on $LiCoO_2$ suppresses the mutual diffusion of Co, P and S and thus, the formation of the interphase between the CAM and the thiophosphate-based SE using (S)TEM and EDX.[84] This is in accordance to a report by Zhang *et al.* who additionally stated that segregation effects of transition metals in Co/Ni-rich and Mn-rich domains were inhibited by the protective coating.[87]

Analogous to reports on the reaction of the uncoated CAM with thiophosphate-based SE, the protective effect of CAM coatings can be mainly correlated with three different types of interfacial reactions: (i) suppressed electrochemical decomposition of the SE (ii) suppressed formation of oxygenated phosphorous and sulfur species and (iii) suppressed formation of sulfides such as transition metal sulfides.[40,85,87–91] From an analytical point of view, reports on the latter must be considered with caution.[88–90] As pointed out in chapter 2.4.2, the postulation of transition metal sulfides is frequently based on poorly documented XPS analysis. Thus, the evaluation procedure is often not comprehensible since information on energy calibration and fitting procedure is lacking and deficiencies in energy calibration and fitting models are present (e.g., systematic signal shifts, poor signal matching, lack of signal fitting contains).[88–90] However, since the calculated, thermodynamically preferred path should involve the formation of transition metal sulfides, a suppression of the transition metal sulfide formation due to the CAM coating is generally reasonable and should therefore be considered.

Conclusions on the influence of the protective layer on the electrochemical decomposition of the SE are difficult to draw from the literature. The reason for this is that these processes also occur at the current collector/SE and the carbon/SE interface and can therefore often not be directly attributed to the CAM/SE interface. In principle, a coating compromising an insulating material (e.g., a wide-band gap semiconductor) should suppress the electrochemical decomposition of the SE due to an inhibited electron transfer between the CAM and the SE. Since common coating materials, such as $LiNbO_3$, are at least semiconducting materials, the suppression of such decomposition processes seems plausible.[120] However, unequivocal experimental proof of this has yet to be provided for the CAM/SE interface.

Publication III supports the conclusions drawn on a suppressed formation of oxygenated phosphorous and sulfur species due to the CAM coating, similar to a study by Visbal *et al.*[40,85] Accordingly, a reduced formation of species, such as phosphates and sulfates/sulfites, seems reasonable and could be correlated with significantly enhanced ASSB performance. In addition, a suppressed formation of anionic frameworks such as $PS_{4-x}O_x^{3-}$ is also conceivable, as indicated in chapter 2.4. In contrast, no clear evidence of transition metals could be found in XPS and ToF-SIMS data, analogous to publication I and II.

Indirect evidence for a suppressed interfacial reaction due to CAM coatings was recently provided by differential electrochemical mass spectrometry (DEMS).[98,99] Accordingly, it was reported that CAM coatings can suppress the SO_2 evolution during cell cycling, which is associated with degradation reactions involving the SE. Since the oxygen source in this reaction

can be, in principle, due to oxygen release from the NCM lattice at high SOCs and/or electrochemical decomposition of surface contaminants such as Li_2CO_3, the protective effect is not completely clarified here.[96–100] Therefore, it remains unclear whether the coating stabilizes the CAM particle surface, and inhibits an accompanied phase transformation, or interacts with the surface contaminant (e.g., Li_2CO_3) and prevents its typical electrochemical decomposition behavior.[101–103]

In this context it must also be considered that the coating material microstructure can change upon cycling. Zhang *et al.* have experimentally shown that a Li_2ZrO_3 coating is not stable at high voltages and undergoes a phase transition to ZrO_2 nanocrystallites.[87] Therefore, it must also be taken into account that CAM coatings can change dynamically in terms of their microstructure (composition and morphology) and thus, their material properties during cell cycling.

All experimental studies mentioned up to this point prove, more or less, that the working principle of CAM coatings can be related to the suppression of the interfacial degradation due to (electro-)chemical reactions. Details on the exact compounds differ depending on the materials and conditions used. In contrast, effects of the coating on morphological/structural degradation in ASSBs are unclear, since studies on this topic are rather rare at the moment. As previously mentioned, the influence of the gas evolution could be an indirect indication for stabilizing effects of the CAM particle surface that inhibits oxygen release from the CAM lattice.[98,99] More detailed insights on morphological/structural degradation were recently provided by Zhang *et al.*[87] In this study, the formation of a rock-salt-like structure underneath a $Li_3B_{11}O_{18}$-based protective coating after cell cycling was observed, indicating that this particular coating could not generally prevent phase transformations of the CAM particle surface.[87] This study indicates that not only the electron and lithium-ion transport through the CAM coating is of interest, but also the transport of other species present, such as oxygen-ions, to better interpret the interfacial processes. However, studies on morphological/structural degradation need to be further addressed in future experiments to gain a deeper understanding of the functioning of CAM coatings.

More generally, it is necessary to clarify whether other approaches such as doping of the CAM or the transition from the secondary particle structure to CAM single crystals are more effective strategies to solve degradation-related problems, analogous to LIBs.[121–126] Especially in relation to structural degradation, such approaches are highly interesting and promising.[123]

2.5.2 Coatings on Conductive Carbon Additives

Coatings on conductive carbon additives should mainly address degradation related to electrochemical SE decomposition, since such processes are dominating at the carbon/SE interface (see chapter 2.4.2). Because these processes are highly dependent on electron transfer at the carbon/SE interface, coatings should preferably be electronic insulators to prevent SE decomposition. However, an insulating coating also prevents the electrically conductive contact of the carbon with the CAM, the current collector, and between the carbon additives themselves. Thus, the function of the coating is dependent on inherently uncoated areas or the mechanical abrasion of coating material in the contact areas, which contradicts the general requirement for a closed coating.

Based on the results of publication II, a protective coating was developed in the context of this doctoral thesis. In a collaborative work with Randau *et al.*, the positive effect of this approach was demonstrated.[39] Accordingly, an insulating Al_xO_y coating was deposited on the surface of VGCFs by atomic layer deposition (ALD) to suppress electron transfer at the carbon/SE interface.

Since the coating exhibited island growth, the coating reduced the fraction of interfacial reaction zones, thus suppressing the electrochemical decomposition of the SE. At the same time, the coating allowed electrical contact in less coated areas between the islands. In fact, the coating resulted in a reduced capacity fading during cell cycling and significantly enhanced the overall ASSB performance compared to the uncoated case. In addition, Deng *et al.* recently demonstrated the positive effect of a surface coating on conductive carbon additives.[108] In contrast to Randau *et al.*, the semiconductive polymer poly(3,4-ethylenedioxythiophene) (PEDOT) was used as coating material.[39,108] Based on their results comprising cyclic voltammetry (CV) and XPS analysis, the beneficial effect of the coating is comparable to the results of Randau *et al.*[39] Accordingly, the electrochemical decomposition of the SE at the carbon/SE interface is suppressed and thus the ASSB performance can be enhanced. However, the underlying processes leading to the suppressed electron transfer appear to be different in detail, since PEDOT is semiconducting whereas Al_xO_y is electronically insulating. Overall, both studies demonstrate that protective coatings can effectively address interfacial issues related to the carbon/SE interface.

3 Results

(Scientific Publications)

At the beginning of this doctoral thesis, insights on individual interfacial degradation phenomena within NCM- and thiophosphate-based positive electrodes were highly limited. Due to significantly overlapping reaction processes and reaction zones, the separation of individual contributions is highly challenging and was therefore not often performed in literature. The aim of this thesis was hence to gain detailed insights into individual interfacial degradation phenomena in composite cathodes and to characterize the protective effect of CAM coatings in terms of the interfacial degradation at the NCM/SE interface.

In this chapter, the three publications related to this doctoral thesis are introduced. Publication I and II contribute to a better understanding on the individual degradation phenomena in NCM- and thiophosphate-based composite cathodes. Accordingly, both publications deal with interfacial degradation due to (electro-)chemical reactions within the composite cathode and separate the overall interfacial degradation into the influence of the current collector, the CAM and the conductive carbon additive. Publication III deals with the functionality of a Li_2CO_3/$LiNbO_3$ coating, which was introduced to overcome interfacial reaction related to the CAM/SE interface. Accordingly, the effect of the protective coating on the interfacial degradation was analytically investigated and characterized in this publication.

3.1 Publication I: "Visualization of the Interfacial Decomposition of Composite Cathodes in Argyrodite-Based All-Solid-State Batteries Using Time-of-Flight Secondary-Ion Mass Spectrometry"

In the first publication of this doctoral thesis, an analytical approach to characterize the interfacial degradation in composite cathodes was developed. For this purpose, a degraded composite cathode of an In/InLi|Li_6PS_5Cl|NCM622/Li_6PS_5Cl ASSB was investigated.

By combining results from integral XPS measurements with local compositional information derived by ToF-SIMS, the CEI formation was visualized for the first time with information about their morphology and chemical composition. In contrast to previous studies, the measuring capabilities of ToF-SIMS were fully exploited and routines for investigations related to composite cathodes were developed and established. The results of this publication show that the capacity fading and thus the degradation of the ASSB is accompanied by a formation of oxygenated phosphorous and sulfur species in the NCM/SE interfacial region, which form a uniform shell around the NCM secondary particles. In addition, XPS data indicate the formation of polysulfides (S^0-like species) within the composite cathode. In contrast, no evidence for the formation of transition metal sulfides and transition metal phosphides was observed.

Overall, the results of publication I improve the understanding of degradation processes in thiophosphate-based composite cathodes and provide an analytical approach to characterize and compare the local structure and composition of interfacial reactions. This approach can be used, for example, to study the influence of protection concepts such as CAM coatings - as done in publication III - which will help to develop and characterize advanced protection concepts to enable stable, or at least slowly degrading, interfaces/interphases analogous to conventional LIBs.

The experiments were designed and planned by the first author under the supervision of W. G. Zeier and J. Janek. S. Ohno synthesized and characterized the SE used. R. Koerver and T. Fuchs prepared the ASSB cells and performed the electrochemical characterization. The first

author performed the analytical measurements (XPS and ToF-SIMS) and the subsequent analysis and evaluation. All authors contributed to the scientific discussion. In particular, J. Sann and M. Rohnke assisted with scientific discussions on the XPS and ToF-SIMS data, respectively. The manuscript was written by the first author and edited by seven co-authors.

This study was part of the International Network for Batteries and Electrochemistry by BASF SE.

Reprinted with permission from Walther, F.; Koerver, R.; Fuchs, T.; Ohno, S.; Sann, J.; Rohnke, M.; Zeier, W. G.; Janek, J. Visualization of the Interfacial Decomposition of Composite Cathodes in Argyrodite-Based All-Solid-State Batteries Using Time-of-Flight Secondary-Ion Mass Spectrometry. *Chem. Mater.* **2019**, *31* (10), 3745–3755. https://doi.org/10.1021/acs.chemmater.9b00770.

CHEMISTRY OF MATERIALS
Cite This: Chem. Mater. 2019, 31, 3745−3755
Article
pubs.acs.org/cm

Visualization of the Interfacial Decomposition of Composite Cathodes in Argyrodite-Based All-Solid-State Batteries Using Time-of-Flight Secondary-Ion Mass Spectrometry

Felix Walther,[†,‡] Raimund Koerver,[†,‡] Till Fuchs,[†,‡] Saneyuki Ohno,[†,‡] Joachim Sann,[†,‡] Marcus Rohnke,[†,‡] Wolfgang G. Zeier,[†,‡] and Jürgen Janek*[,†,‡]

[†]Institute of Physical Chemistry, Justus Liebig University Giessen, Heinrich-Buff-Ring 17, D-35392 Giessen, Germany
[‡]Center for Materials Research (LaMa), Justus Liebig University Giessen, Heinrich-Buff-Ring 16, D-35392 Giessen, Germany

Supporting Information

ABSTRACT: All-solid-state lithium-ion batteries (ASSBs) are expected to represent a future alternative compared to conventional lithium-ion batteries with liquid electrolytes (LIBs). The excellent performance of today's LIBs relies to a large extent on the development of liquid electrolytes that form stable, or at least slowly degrading, interfaces (interphases) with both anodes and cathodes. This has not yet been achieved in ASSBs, and degradation of anode and cathode interfaces of solid electrolytes (SE) is one of the key issues to be solved. Unlike investigations of liquid/solid interfaces, the degradation of interfaces between the solid electrodes and the SE is challenging since (i) solid/solid interfaces are less easily accessed analytically, (ii) interface compounds may contribute only in very low concentrations to spectroscopic or spectrometric data, and (iii) a high spatial resolution is required to determine the local component distribution. Typically, solid/solid interface investigations are primarily based on electrochemical experiments, diffraction studies, electron microscopy, or on theoretical calculations to obtain sufficient information. Interestingly, the prospects of recent advanced analytical tools such as time-of-flight secondary-ion mass spectrometry (ToF-SIMS) are not fully exploited yet; therefore, we demonstrate in this paper that ToF-SIMS can provide valuable insights into the interphase composition and microstructure of ASSBs. For this purpose, we combine local compositional information from ToF-SIMS and complementary X-ray photoelectron spectroscopy measurements to characterize and visualize the degradation mechanism in the $LiNi_{0.6}Co_{0.2}Mn_{0.2}O_2/Li_6PS_5Cl$-composite cathode of an ASSB. Our results indicate that sulfates and phosphates play an important role in the formation of a solid electrolyte interface (SEI), whereas transition-metal chlorides, phosphides, and sulfides can be neglected. Furthermore, to the best of our knowledge, we show for the first time the local structure and morphology of the SEI layer on the basis of information about the chemical composition using ToF-SIMS analysis.

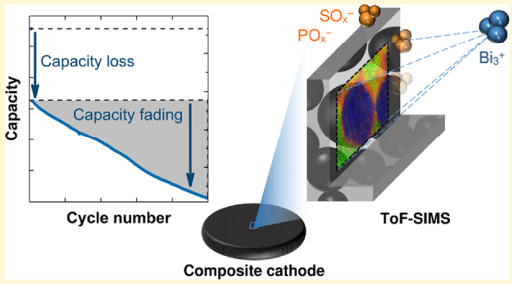

INTRODUCTION

All-solid-state batteries (ASSBs) are expected to serve a future generation of various energy storage applications. Recent developments of highly conductive solid electrolytes (SE) have created a large momentum in the research of ASSBs.[1−5] Employing SE can, in principle, help in achieving high cell voltages, high specific capacities, and high cycle stability, and it can even improve safety aspects compared with conventional Li-ion batteries by avoiding flammable organic substances.[2,6−9] However, there are still some remaining serious challenges to be overcome before transitioning this new technology to practical application. One of the major issues is the high charge-transfer resistance between the solid electrolyte and the electrode materials due to the interfacial degradation, which results in a strong capacity fading.[10,11] The reasons for interface degradation are manifold and can be interdependent, making their study and interpretation particularly challenging. The degradation depends mostly on the materials and operating conditions during charge and discharge, such as temperature, applied pressure, applied current, and cutoff potentials and also on cell design, which complicates the knowledge transfer to other cell systems.

In general, there are two major degradation processes at interfaces in composite cathodes: morphological/structural degradation and degradation due to (electro-)chemical reactions. The morphological/structural degradation results from volume effects during charging and discharging, which can lead to a contact loss between the solid electrolyte and the active material.[11,12] Furthermore, it has been shown that structural transformations take place within the active material,

Received: February 22, 2019
Revised: April 28, 2019
Published: April 29, 2019

DOI: 10.1021/acs.chemmater.9b00770
Chem. Mater. 2019, 31, 3745−3755

which can cause an additional stress/strain leading to the cracking, in particular, in high-Ni materials at high upper cutoff potential.[13−15] The degradation due to chemical reactions is usually attributed to the SE/electrode interface and the electrochemical instability of the solid electrolyte at high electrode potential.[16−18] Side reactions at the interface can lead to the formation of passivating layers and undesirable products that cause an increase in cell resistance, unwanted additional overvoltage, and ultimately capacity loss.[19−21]

To elucidate the degradation processes, different experimental approaches can be specifically adapted to the task. In view of the reaction at the SE/electrode interface, this usually includes X-ray photoelectron spectroscopy (XPS), energy-dispersive X-ray spectroscopy, and transmission electron microscopy (TEM), which have been widely used in the investigation of interfaces in all-solid-state batteries.[19−24] In addition, a small number of studies employing time-of-flight secondary-ion (SI) mass spectrometry (ToF-SIMS) has been reported in the field of battery research but only a few studies focus on ASSBs.[25−33] However, ToF-SIMS is still rarely used in this field of research and often not to the full extent of its measurement capabilities. With regard to analytical methods, detailed information about the chemical composition together with a high spatial resolution is often required, although usually only one of both is provided. Another challenge is that often low concentrations of chemical components need to be detected, which for many methods are close to or below the detection limit. With XPS studies, for example, changes in the chemical environment can be addressed very well but due to a relatively low maximum spatial resolution in the typical range of approx. 5 μm for conventional instruments,[34] the information of local elemental distributions is usually not accessible. Furthermore, the suitability of XPS depends on the specific element and the compound of interest. At low concentrations, low relative sensitivity factors, or low binding energy differences between the compounds, signal changes are difficult to identify and may remain undetected. These correlations are later important for the interpretation of the XPS results. Although TEM theoretically meets all of the above requirements, the analysis is usually impossible due to the instability of thiophosphate SE against the analysis beam. Furthermore, due to the small spatial analysis range, only a local single particle analysis is possible. As a consequence, a comprehensive analysis is only possible using multiple complementary methods.

In this work, the degradation of the composite cathode in a pellet-type In/InLilLi_6PS_5Cl|$LiNi_{0.6}Co_{0.2}Mn_{0.2}O_2$/$Li_6PS_5Cl$ ASSB is investigated ($LiNi_{0.6}Co_{0.2}Mn_{0.2}$ is abbreviated as NCM622 in the following). Following the corroboration of cell degradation based on electrochemical measurements, we perform systematic XPS and ToF-SIMS investigations to elucidate the degradation mechanism. With XPS, we draw quantitative conclusions about the chemical composition of the samples. We use ToF-SIMS to compensate the relatively low maximum lateral resolution (in our case, 9 μm) and the comparatively low detection limit of XPS. The combination of both methods allows us to obtain detailed information about the degradation processes in Li_6PS_5Cl-based NCM composite cathodes. In this context, it should be noted that ToF-SIMS has a very high sensitivity for compounds with high ionization probabilities (several orders of magnitude compared with XPS) but is only a semiquantitative method. Accordingly, with ToF-SIMS, it is possible to visualize reactions below the detection limit of XPS with a relatively high lateral resolution (up to 150 nm in our case) and to detect relative concentration changes in decomposition products. In contrast, it is usually not possible to determine absolute concentrations. Overall, this work shows that the combination of both methods is well suited to characterize and interpret the degradation processes. On the basis of the results obtained from the method combination, we finally use ToF-SIMS to visualize the formation of the solid electrolyte interface (SEI) at the NCM622/SE interface. To the best of our knowledge, this work visualizes for the first time the SEI formation between an argyrodite-type SE and an NCM cathode material with information about its morphology and chemical composition. Knowing the morphology and the chemical composition of the SEI will help designing the microstructure at the cathode−electrolyte interface to further optimize long-term cycling stabilities and is hence a stepping stone toward a successful integration of all-solid-state batteries.

EXPERIMENTAL SECTION

Preparation of the Solid-State Battery Cell. The argyrodite solid electrolyte, Li_6PS_5Cl, was synthesized through solid-state synthesis, analogous to a recent publication.[35] All preparations were carried out under an argon atmosphere. Stoichiometric ratios of lithium sulfide (Li_2S, Sigma-Aldrich, 99.98%), phosphorus pentasulfide (P_2S_5, Sigma-Aldrich, 99%), and anhydrous LiCl (Alfa Aesar, 99%) were hand ground in an agate mortar, pressed into pellets, and loaded into quartz ampoules, which were sealed under vacuum (~10^{-3} mbar). In advance, all ampoules were carbon-coated and preheated at 800 °C under a dynamic vacuum to avoid undesired reaction with residual moisture. The reaction was performed at 550 °C for a week. The obtained mixture was subsequently manually ground for 15 min to a powder for characterization and battery testing.

X-ray diffraction was carried out with a PANalytical Empyrean powder diffractometer in a Bragg−Brentano geometry with Cu Kα radiation. Measurements were performed in the 2θ range between 10 and 85° with a step size of 0.026°. All powders were placed on silicon zero background holders with a polyimide (Kapton) film to avoid air and moisture decomposing samples during measurements. Rietveld refinements were carried out using TOPAS-Academic V6 software package (Bruker Corporation), using the Thompson−Cox−Hastings pseudo-Voigt function for the profiles. The XRD pattern and the Rietveld refinements are shown in Figure S1 (Supporting Information) and reveal a highly pure material. Only 2 wt % Li_3PO_4 was detected.

All-solid-state batteries of the composition In/InLilLi_6PS_5Cl|NCM622/Li_6PS_5Cl were assembled. NCM622 (provided by BASF SE) was dried at 200 °C in a Büchi vacuum furnace prior to use. The morphology and the microstructure of the pristine NCM622 particles are shown in scanning electron micrographs in the Supporting Information Figure S2. An indium foil (Alfa Aesar, 0.125 mm thickness, 6 mm diameter, capacity ~7.7 mAh cm^{-2}) was used as anode material. For the In/InLi anode, a constant potential of 0.6 V versus Li^+/Li was assumed.[36] Furthermore, the mechanical support of the indium foil allows easy extraction of the battery for the following analysis.

The cell casing was manufactured in-house and is described in a previous publication in detail.[10] The pellet-type ASSB cells (inner diameter: 10 mm) were assembled inside an argon-filled glovebox according to the previously described procedure.[11] A mass of 60 mg of Li_6PS_5Cl was used as a separator. The cathode composite, consisting of 70 wt % NCM622 and 30 wt % Li_6PS_5Cl, was prepared in an agate mortar. Twelve milligrams of the cathode composite (2.14 mAh cm^{-2}) were added on top of the separator and distributed homogenously. The powders were compressed uniaxially at 35 kN (approximately 445 MPa). Thereafter, the indium foil was added and

DOI: 10.1021/acs.chemmater.9b00770
Chem. Mater. 2019, 31, 3745−3755

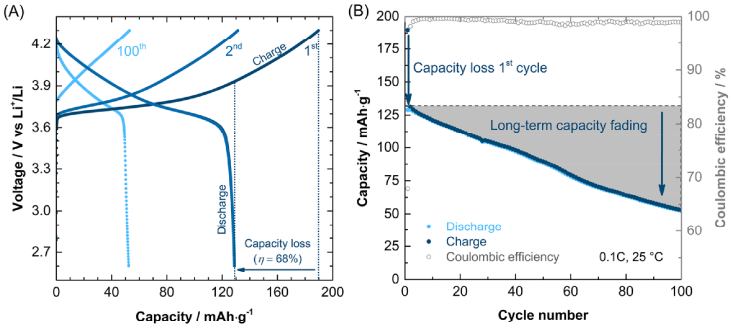

Figure 1. (A) Charge and discharge profiles for the first, second, and 100th cycle of an In/InLilLi_6PS_5ClllLi$Ni_{0.6}Co_{0.2}Mn_{0.2}$/Li_6PS_5Cl cell cycled at 214 μA cm^{-2}. (B) Charge/discharge capacities and Coulombic efficiency as a function of the cycle number. The dark blue circles indicate the charge and the light blue circles the discharge capacities, respectively. The capacity loss in the first cycle, as well as the gradual long-term capacity fading, is attributed to the NCM622/SE-interphase formation (SEI). The blue squares show the Coulombic efficiency as a function of the cycle number.

a reduced pressure of roughly 70 MPa was applied to the cell and maintained during the electrochemical experiments.

Electrochemical Characterization. Temperature-dependent electrochemical impedance spectroscopy was performed using the EC-Lab Electrochemistry SP-300 (Bio-Logic Science Instruments SAS) between −10 and 60 °C to evaluate the Li-ion conductivity (1.8 mS cm^{-1}@25 °C) and activation energy (0.38 eV) of the synthesized solid electrolyte. Measurements were conducted in a frequency range of 7 MHz to 1 Hz applying a 10 mV signal amplitude. The spectra were fitted using the RelaxIS software package (Version 3, rhd instruments GmbH & Co. KG, Germany).

Battery cycling was performed on a MACCOR battery cycler. The cells were galvanostatically charged to 3.70 V (vs In/InLi) and discharged to 2.00 V. The current density was 214 μA cm^{-2} (corresponding to 0.1C), calculated on the basis of the theoretical capacity of 200 mAh g^{-1} of the cathode material.

Scanning Electron Microscopy. Microstructure images of the cathodes extracted from disassembled cells were obtained on a Merlin high-resolution scanning electron microscope (Carl Zeiss AG). The samples were transferred from a glovebox into the analysis chamber under an argon atmosphere using a transfer vessel (Leica EM VC500). Measurements were carried out by application of an acceleration voltage of 5 kV and a probing current of 100 pA.

Time-of-Flight Secondary-Ion Mass Spectrometry. Time-of-flight secondary-ion mass spectrometry was performed with a TOF.SIMS 5 instrument (IONTOF GmbH) equipped with a 25 keV Bi cluster primary-ion gun for analysis and a dual-source column with 2 keV O_2^+ and Cs^+ low-energy guns for depth profiling. In addition, the instrument has a 30 keV focused ion beam (FIB) gun, which allows to mill craters with monoatomic gallium. All samples were transferred under an argon atmosphere with a transfer vessel (IONTOF GmbH) from the glovebox into the analysis chamber. All ToF-SIMS experiments were performed in negative ion mode to draw conclusions about the chemical environment. In positive ion mode, fragments were mainly limited to the monoatomic metal ions since sulfur, phosphate, chlorine, and oxygen species tend to form negatively charged fragments.

The spectrometry mode (bunched mode) was used to determine changes in the mass spectra caused by cycling. This operation mode enables simultaneously high signal intensities and a high mass resolution (FWHM $m/\Delta m$ > 4500 @ m/z = 34.97 (Cl^-)), which reduces signal interference. Bi_3^+ ions with an energy of 25 keV were used as primary-ion species and the (150 × 150) μm^2 analysis area was rasterized with (128 × 128) pixels. The measurements were stopped after reaching a primary-ion dose of 1.00×10^{12} ions per cm^2 to achieve comparable measuring conditions. To check the reproducibility of the results depending on the measuring position, we measured three mass spectra per sample in different areas of the surface. The data evaluation was carried out with the software SurfaceLab 6.7 (IONTOF GmbH).

Depth profiling in fast imaging mode was combined with delayed extraction[37,38] to allow surface near three-dimensional (3D) tomography studies for investigations regarding the local fragment distribution. This operation mode enables investigations with high lateral resolution in the range of ∼150 nm with a high mass resolution, as previously reported for battery materials.[32] For example, using delayed extraction enabled mass resolution in the range of ∼6000 for the mass 34.97 (Cl^-). The measurements were performed in a non-interlaced mode with Bi_3^+ (25 keV) as primary-ion species and Cs^+ (2 keV) for sputtering. The surface was flooded with low-energy electrons for 1s for charge compensation. The analysis area was (50 × 50) μm^2 and placed in the center of the (400 × 400) μm^2 sputter crater. Every single plane within the analyzed volume was rasterized with (512 × 512) pixels at 1 shot per pixel and 40 frames. Afterward, the surface was sputtered for 100 s.

To verify the results and to exclude distorting sputter effects perpendicular to the surface, ToF-SIMS analysis was combined with FIB. A crater was milled into the composite cathodes, and the crater sidewall was imaged in fast imaging mode after a cleaning step with the primary-ion gun in direct current (DC) mode.

X-ray Photoelectron Spectroscopy. X-ray photoelectron spectroscopy was carried out using a PHI5000 Versa Probe II instrument (Physical Electronics GmbH, Germany). Monochromatic Al Kα radiation was used for analysis (1486.6 eV). The power of the X-ray source was 50 W, and the beam voltage was 15 kV. The beam diameter was 200 μm. Depth profiling was performed using Ar^+ ions (soft sputtering with 0.5 kV) to clean the surface and to avoid misinterpretations due to reactions that occur only on the surface. The rasterized area was (6 × 6) mm^2. The data evaluation was carried out with the software CasaXPS (version 2.3.17, Casa Software Ltd). All X-ray photoelectron (XP) spectra were calibrated in relation to the signal of adventitious carbon at 284.8 eV. A Shirley background and GL(30) line shapes were used for evaluation and signal fitting.

■ RESULTS

Cell Cycling. The In/InLilLi_6PS_5ClllLi$Ni_{0.6}Co_{0.2}Mn_{0.2}O_2$/$Li_6PS_5Cl$ cell was cycled between 2.00 and 3.70 V at 214 μA cm^{-2} (0.1C) over 100 cycles (corresponds to 2.60 and 4.30 V against Li^+/Li). Figure 1 shows charge−discharge profiles (Figure 1A) as well as the battery capacity as a function of the cycle number (Figure 1B). The initial charge and discharge capacities are 189.8 and 128.9 mAh g^{-1}, which equals an initial Coulombic efficiency of η = 67.9%. Over the 100 cycles, a continuous capacity loss is observed. It can be seen that the first cycle causes a capacity loss of 58.4 mAh g^{-1}, which

DOI: 10.1021/acs.chemmater.9b00770
Chem. Mater. 2019, 31, 3745−3755

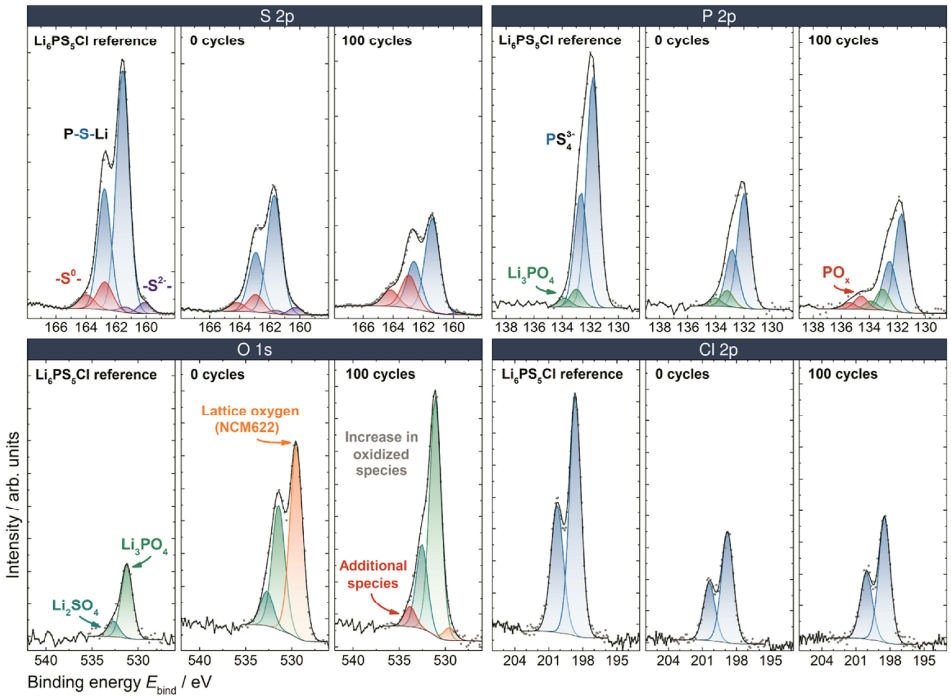

Figure 2. XP spectra of the S 2p, P 2p, Cl 2p, and O 1s signals of a Li_6PS_5Cl reference and the uncycled and cycled composite cathode. The pass energy was 23.50 eV in all measurements. All detail spectra were calibrated in relation to the signal of adventitious carbon at 284.8 eV, and a Shirley background was used for signal fitting.

significantly diminishes the overall capacity retention. Between the first and the second charging cycle, this corresponds to a relative capacity loss of 30.7%. The average capacity loss in subsequent cycles is 0.9%, resulting in charge and discharge capacities of 52.9 and 52.4 mAh g^{-1}, respectively, in the 100 cycles. The overall Coulombic efficiency of the ASSB is 98.7% (99.1% without the first cycle).

Overall, the electrochemical data show that battery performance is decreasing, indicating degradation processes. To characterize and visualize decomposition products, the ASSB was recharged before disassembly. Afterward, SEM images of the cycled composite cathode were taken. The images reveal that some particles show not only signs of chemomechanical degradation, such as particle cracks and fragmentation, but also changes in the stacking sequence of NCM (see Supporting Information Figure S3). These interrelationships can lead to contact loss between the NCM622 particles and the SE and have already been investigated by several research groups.[11,13,14,39]

X-Ray Photoelectron Spectroscopy. To confirm the degradation in relation to chemical side reactions, X-ray photoelectron spectroscopy was performed. In Figure 2, the cycled composite cathode is compared to a Li_6PS_5Cl reference and an uncycled cathode that was prepared in the same way as the cycled cathode. Shown are detail spectra of the S 2p, P 2p, Cl 2p, and O 1s signals after surface cleaning by soft sputtering with Ar^+ ions (0.5 kV). Overall, the XPS data show that the signals of S 2p, P 2p, and O 1s change due to battery cycling. In contrast, no change could be detected in the Cl 2p signal. Further, the detail spectra of Ni 2p and Li 1s do not show an unambiguous change upon cycling, as shown in the Supporting Information (Figure S4). In this context, the detection limitation of XPS has to be considered. With XPS, it is not possible to detect reactions that only lead to low concentration changes (~<0.5 atom %) and/or do not cause a shift in binding energy. Therefore, it cannot be concluded at this point that Li, Cl, and Ni do not react; rather, such reactions cannot be detected in the corresponding detail spectra with XPS.

The resulting S 2p signal can be described with three doublet peaks: The signal around 159.9 eV likely stems from the S^{2-} ions within the crystal structure of Li_6PS_5Cl. The intensity decreases significantly after 100 cycles, indicating oxidation of the solid electrolyte. The highest signal contribution for all three samples at 161.6 eV can be assigned to the PS_4^{3-} tetrahedra of the argyrodite structure (P−S−Li bonds).[20,24] At higher binding energies, an additional signal shoulder is visible for all three samples. A single doublet is sufficient to take the signal shoulder in the signal fit into account. The formation of this shoulder upon cycling has been discussed for various sulfide solid electrolytes.[11,20,24,40] The origin of the signal feature can be related to the formation of polysulfides or oxidized species such as $Li_2P_2S_6$.[21,41] Polymerization or oligomerization of the anions of the SE can lead to the formation of P−[S]$_n$−P-type anions. With increasing number n, the relative amount of bridging sulfur atoms increases, resulting in an increasing number of anions in which sulfur is uncharged (−S_0− groups). Therefore, we assume that the doublet at higher binding energies contains several contributions that depend on the chain length and the exact chemical composition of the polysulfides. Overall, the detail spectra of the S 2p signal show that the fraction of oxidized sulfur species increases due to cell cycling (roughly by a factor

DOI: 10.1021/acs.chemmater.9b00770
Chem. Mater. 2019, 31, 3745−3755

of 2). In addition, the background in the binding energy range of sulfites and sulfates (E_{bind} > 165.5 eV) is increased. However, it is not possible to detect individual signals, which makes quantification with a Shirley background impossible. The increased background could indicate the formation of SO_x-containing compounds with different oxygen contents x. The assumption of sulfates is supported by the spectra measured before soft sputtering (see Supporting Information Figure S5). Accordingly, SO_x species can be seen on the surface, whose quantity is further enhanced upon cycling. The concentrations appear to be in the range of the detection limit of the XPS. However, ToF-SIMS measurements, which are described later in more detail, confirm the assumption of SO_x formation due to cell cycling even in the bulk material. This is possible due to the higher sensitivity of ToF-SIMS compared with XPS.

The P 2p signal can be divided into three contributions. The main contributions at 131.8 eV can be assigned to the PS_4^{3-} tetrahedra of the argyrodite structure.[20,24] The oxidized phosphorus species at 133.0 eV was already observed for Li_6PS_5Cl and was attributed to P_2S_5 or P_2S_x,[20,24] which is not visible in our diffraction pattern. Since the Rietveld refinement reveals 2 wt % Li_3PO_4, we assume that this compound causes the signal contribution. Published binding energies of Li_3PO_4 match quite well with the herein determined value.[42,43] The average concentration of this species corresponds to 0.72 atom % of the total composition, which is close to the expected value due to Li_3PO_4 (2 wt % corresponds to 0.56 atom % phosphorus). This is further supported by the detailed spectrum of the O 1s spectrum. In the case of the pristine argyrodite, an oxygen species is visible at a binding energy of 531.2 eV and thus also corresponds well with published values of Li_3PO_4 (531.1 eV).[42] Even if the experimentally proven quantity is only slightly higher than the quantity expected from XRD data (0.72 vs 0.56 atom %), the question arises that where this difference can come from. Since Li_6PS_5Cl is highly reactive, surface impurities seem reasonable. Accordingly, Li_6PS_5Cl reacts immediately with oxygen and water, even for amounts in the ppm range. These small amounts of water and oxygen cannot be completely excluded either in the glovebox (long-term values are typically $x(H_2O)$ < 0.1 ppm and $x(O_2)$ < 0.1 ppm) or in the transfer system and in the analysis chamber (no cryo system). This allows phosphates such as Li_3PO_4 and sulfates such as Li_2SO_4 to form even in relatively clean atmospheres. The binding energy of the O 1s signal of the latter compound corresponds very well to the second signal at 532.8 eV[44] so that both products seem reasonable. The concentration of Li_2SO_4 is probably in a range not detectable in the S 2p detail spectra. Interestingly, the amount of Li_3PO_4 seems to increase due to the mere contact of the argyrodite with the NCM622 particles indicated by an increase of the corresponding signals in the O 1s and P 2p detail spectra. It seems reasonable that the argyrodite reacts analogously to the sample surface with small amounts of water and oxygen, even if the NCM was dried before (see the Experimental Section). However, since compounds such as carbonates may also be present on the NCM surface and the surface composition may change due to aging, it is difficult to draw conclusions about the actual origin.[45] The surface species can react with the argyrodite and can lead to the formation of decomposition products such as Li_2SO_4 and Li_3PO_4. Accordingly, we assume that the first reactions at the interface take place already upon mere contact of both materials. However, since the measurement conditions and the materials were identical for all samples, these effects are the same for both cathodes.

The third P 2p signal at 134.6 eV is sufficient to take the oxidized shoulder into account, which is only clearly visible in the cycled composite cathode and is, therefore, directly correlated with the formation of decomposition products due to cell cycling. There are probably several doublet signals in this energy range, depending on the exact phosphate compound. From the combination of XPS and ToF-SIMS results (described later) it seems plausible that transition-metal (TM) phosphates are formed, since the binding energy of compounds such as $Mn_3(PO_4)_2$ and $Ni_3(PO_4)_2$ can be found in this binding energy range.[46] This is supported by the fact that no signals can be detected in the energy range of transition-metal phosphides (<130 eV).[47−49]

In contrast to other publications,[20,22,24,50] we took a closer look at the O 1s detail spectrum. As already mentioned, we assume that Li_2SO_4 and Li_3PO_4 cause the small fraction of oxygen in the case of the pure argyrodite (6.8 atom %). Oxygen-containing surface adsorbates (e.g., C═O-type adsorbates) can also contribute to the main component. However, since we worked under an argon atmosphere and vacuum conditions, we assume a minor influence. Considering the O 1s spectra of the cathodes, two further contributions are recognizable. The signal at 529.5 eV can be assigned to the lattice oxygen of NCM and is not observed in the case of the pure electrolyte.[51] Interestingly, the signal contribution is drastically decreased after cycling. This indicates the formation of a passivation layer around the NCM622 particles as XPS is a surface sensitive process with a typical maximum analysis depth in the range of 10 nm for Al Kα radiation. Thus, a layer thickness in the range of 10 nm can already cause the lattice oxygen signal to disappear. At the same time, the signal intensities in the higher binding energy range increase, which are in the typical energy range of sulfates and phosphates,[52] confirming the observations on the S 2p and the P 2p signal.

ToF-SIMS Analysis. In addition to the usually employed XPS analyses, we performed ToF-SIMS measurements to obtain further information on the composition and morphology of the SEI. The cycled composite cathode was compared to a Li_6PS_5Cl reference and an uncycled cathode, which was prepared in the same way as the cycled cathode. In the following discussion, it must be noted that during the ToF-SIMS measurements charged fragments formed as a result of the collision cascade initiated by the highly energetic analysis beam detected. Hence, the detected secondary ions do not necessarily exist in this form in the material. Nevertheless, there is a strong correlation with the chemical bonding situation of the sample so conclusions can be drawn about the chemical environment from local fragment distributions.[34] In addition, it should be noted for the interpretation of these results that ToF-SIMS has a very high sensitivity for fragments with high ionization probabilities (several orders of magnitude higher than XPS). Therefore, concentrations of decomposition products are detectable that cannot be resolved with XPS.

Secondary-ion mass spectra of the surface were recorded to determine the differences in the fragmentation due to battery cycling. To ensure the reproducibility of the results, the recordings were performed on three different surface areas per sample. The relatively large analysis area of (150 × 150) μm^2 includes several NCM622 particles and minimizes effects due to fluctuations in the particle number. A direct comparison of the mass spectra, exemplarily shown in Figure 3, allowed

DOI: 10.1021/acs.chemmater.9b00770
Chem. Mater. 2019, 31, 3745−3755

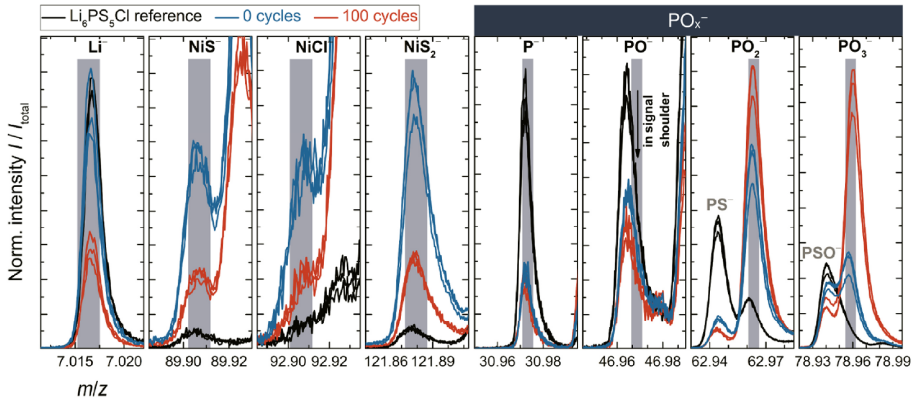

Figure 3. Negatively charged fragments from surface spectra measured with ToF-SIMS operated in spectrometry mode using 25 keV Bi_3^+ primary ions. For each sample, mass spectra were measured in three different surface positions to ensure reproducibility of the results. The intensities are normalized to the total ion signal. On the left side, the Li^- fragment and exemplary fragments for MS_x^- and MCl_x^- fragments (M = Ni, Mn, Co) are shown. The signal intensity of these fragments decreases after battery cycling. On the right side, PO_x^- fragments (with $0 \leq x \leq 3$) are shown. Battery cycling leads to an increase in signal intensity of PO_x^- fragments with higher oxygen content x. Analogous results to PO_x^- fragments could be observed for SO_x^- fragments (see the Supporting Information).

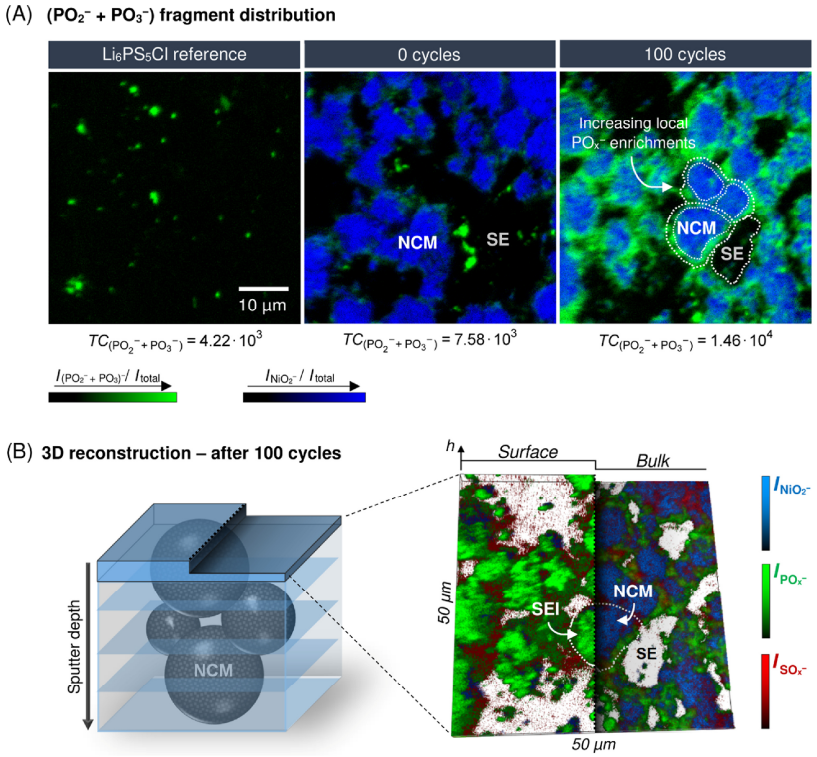

Figure 4. (A) Local fragment distribution of NiO_2^- (blue) and PO_x^- (green) fragments for the reference SE and the uncycled and cycled composite cathode. The sum of the first four scans of the depth profile is shown. The solid electrolyte shows local PO_x^- fragment enrichments, which can also be identified in the composite cathodes (middle picture, most intensive signals). Signals from PO_x^- fragments at the NCM622/SE interface significantly increase after the battery cycling (total counts (TC) of PO_x^- fragments become double). (B) Three-dimensional reconstruction of the depth profile of the cycled composite cathode. Shown are local fragment distributions of NiO_2^- (blue), PO_x^- (green), and SO_x^- (red) on the surface and in the bulk. This shows that a SEI layer is formed directly at the NCM622/SE interface due to battery cycling.

several conclusions. For instance, the delithiated (charged) state of the cycled cathode becomes obvious as the Li^- signal decreases in comparison with the reference, which confirms a successful cycling process. With respect to the NCM622/SE

DOI: 10.1021/acs.chemmater.9b00770
Chem. Mater. 2019, 31, 3745−3755

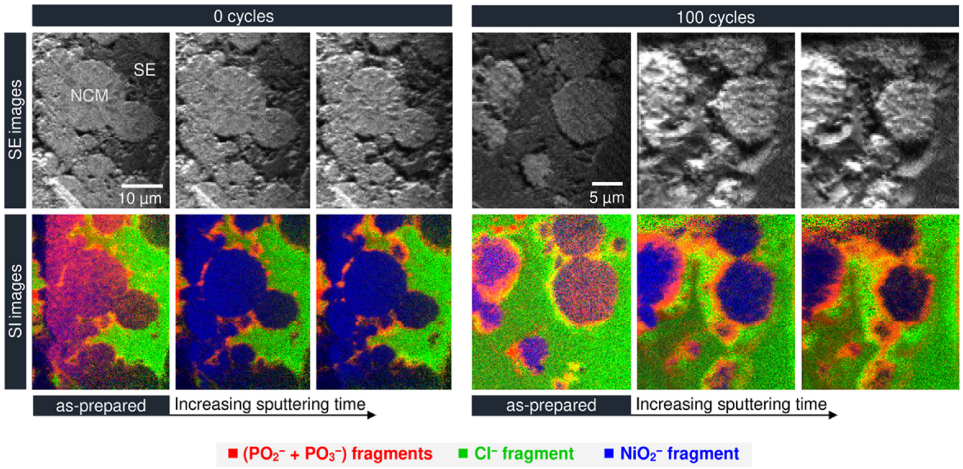

Figure 5. ToF-SIMS measurements on crater sidewalls for cathodes before and after cycling. Shown are secondary electron (SE) and corresponding secondary-ion (SI) images of the crater sidewall depending on the sputtering time (surface cleaning). The cleaning step is necessary to remove the surface defect layer formed during the sample preparation by the FIB and to restore the original signals. It was achieved by rasterizing the analysis beam over the analysis area in DC mode, which causes gentle sputtering. The SI images show a significant increase of PO_x^- and SO_x^- fragments (see the Supporting Information) at the NCM622/SE interface due to battery cycling. Accordingly, the SEI can be imaged with these fragments. In addition, different sputter rates of the NCM622 and the SE allow the particles to be dug out.

interface, the formation of fragments such as MS_x^- and MCl_x^- (M = Ni, Mn, Co) is expected since the analysis beam introduces a collision cascade at the NCM622/SE interface that causes local ion mixing effects. In fact, some of these fragments were detected (see Figure 3 and Supporting Information Figure S6). Interestingly, the signal intensities of these fragments decrease after battery cycling. The lower formation probability of these fragments after battery cycling indicates that the metal ions of the NCM622 particles and the sulfur and chlorine ions of the solid electrolyte are no longer located directly next to each other. This indicates a change in the interface composition and points to the formation of a solid electrolyte interphase. In this context, it should be emphasized that the ToF-SIMS results show that the SEI formation is not associated with an increase of transition-metal sulfides and chlorides. In contrast, battery cycling leads to an increase in the signal intensity of PO_x^- and SO_x^- fragments (with $2 \leq x \leq 3$). Figure 3 shows a dependence of the signal intensity of PO_x^- fragments on the oxygen content x. Combining NCM622 with the argyrodite without battery cycling increases already the amount of PO_2^- and PO_3^- fragments. Analogous results could be observed for SO_x^- fragments (see Supporting Information Figure S7). The reason for this can be attributed to two main reasons. On one hand, the collision cascade induced by the analysis beam mixes P and S species (from the SE) with O species (from the NCM622) at the NCM622/SE interface, which can already lead to PO_x^- and SO_x^- fragments. On the other hand, it is reasonable from the XPS results that the argyrodite reacts with small amounts of water and oxygen on the rough NCM622 surface, resulting in the formation of sulfates and phosphates such as Li_2SO_4 and Li_3PO_4. However, the battery cycling causes a further increase in the signal intensities of these fragments. This is in good agreement with the XPS results and suggests that the SEI formation is associated with a further increase of phosphate and sulfate species, which, in turn, blocks the detection of the Ni-containing, fragments such as NiS^-, $NiCl^-$, and NiS_2^- (see Figure 3).

ToF-SIMS depth profiling experiments were performed in the near-surface region to investigate the local distributions of PO_x^- and SO_x^- fragments (see Figure 4). The depth profiling into the bulk has shown disturbing effects due to the differences in the sputter rates of the different materials, which can lead to material mixing effects due to the increasing roughness (complex structure) of the analysis surface. Nevertheless, the near-surface depth profiles show the formation of PO_x^- and SO_x^- fragments and their increase in signal intensities (see Supporting Information Figure S8). This is the same trend as shown in Figure 3 for PO_x^- and SO_x^- fragments and confirm our hypothesis about the composition of the SEI.

To investigate the spatial fragment distribution, the depth profiles were reconstructed in 3D (see Figure 4). As expected, the pristine argyrodite shows already local enrichments of the PO_2^- and PO_3^- fragments, which are caused by Li_3PO_4 (2 wt %). A quantitation of these impurities is not possible with ToF-SIMS since it is a semiquantitative method (signal intensity is not only proportional to the concentration but among other factors also to the ionization probability).[34] A detection of these local enrichments is possible due to the high ionization probability of PO_x^- fragments. As the XRD and XPS data show, the concentration of these impurities is low (see above). Figure 4 shows that, for both cathodes before and after cycling, the PO_x^- signals are mainly located at the NCM622/SE interface. In the case of the uncycled cathode, the local enrichments in the solid electrolyte (away from the NCM622/SE interface) are partly recognizable. However, the fragment intensities are dominated by the interface region (see total counts (TC)). Region-of-interest analyses in the interface region support this assumption. Three-dimensional (3D) reconstructions (Figure 4B) confirm that the increase in the intensity of phosphate and sulfate fragments takes place at the interface, indicating the SEI formation. In contrast, the PO_x^-

DOI: 10.1021/acs.chemmater.9b00770
Chem. Mater. 2019, 31, 3745−3755

and SO_x^- signals from regions within the solid electrolyte do not seem to be influenced by battery cycling.

To minimize the disturbing effects due to the different sputter rates of cathode components and material mixing effects, ToF-SIMS imaging was also performed on FIB crater sidewalls. This way, the formation of the complex structure can be reduced during the analysis and the distribution of the fragments in the bulk can be assessed with higher reliability. In the following, we illustrate the SEI formation using phosphate fragments. Analogous observations could be made for sulfate fragments (see Supporting Information Figure S10). Figure 5 shows secondary-ion (SI) images of the cycled and the uncycled cathode and the corresponding secondary electron (SE) images. The NCM622 particles are represented in blue by the NiO_2^- fragment and the argyrodite in green by Cl^- ions. The linear combination of PO_2^- and PO_3^-, which have the highest signal intensity of the phosphate fragments, is shown in red. Although a defect layer was initially observed on the surface of as-prepared FIB crater sidewalls due to the material mixing of the NCM622 and the SE (see the first picture in each case), this could be easily removed by rasterizing the analysis beam over the analysis area in DC mode. Afterward, a clear distinction between the NCM622 particles (blue) and the SE (green) is possible. The phosphate fragments are located at the NCM622/SE interface, even for the uncycled composite cathode. As already discussed, we assume that reactions of the Li_6PS_5Cl with surface species on the rough NCM622 particle surfaces, such as water, oxygen residuals, and/or carbonates, can already lead to sulfate and phosphate species, such as Li_2SO_4 and Li_3PO_4, which is supported by the XPS and ToF-SIMS results mentioned above. However, the phosphate and sulfate signals are drastically increased at the interface by battery cycling, further indicating the SEI formation. This follows from a single-pixel normalization approach, which takes disturbing effects into account, such as fluctuations in the particle number in the analysis area and different particle cut planes, and enables a semiquantitative comparison of the fragment intensities (see the Supporting Information). Overall, the data show that the SEI layer consists of phosphate- and sulfatelike species and forms a uniform shell around the NCM622 particles.

It should be noted that the different sputter rates of the components can be further exploited to dig out the NCM particles. The argyrodite (soft material) has a higher sputter rate compared with the NCM622 particles (hard material). On the basis of our observations, the SEI layer shows lower sputter rates compared to that of the electrolyte. Accordingly, the particles with the SEI layer can be separated from the surrounding solid electrolyte. This could be a great advantage in experiments where the separation of the electrolyte from the particles is necessary since the separation of both components is very difficult or almost impossible.

■ DISCUSSION

It has already been shown that (electro-)chemical reactions on the cathode side in ASSB cells with LCO/NCM and thiophosphate SE are associated with the formation of oxidized sulfur and phosphorus species.[11,20,21,25,50,53,54] Investigations are mostly based on XPS investigations and show an increase of oxidized species in the S 2p and P 2p signals. Our investigations extend these observations to the $LiNi_{0.6}Co_{0.2}Mn_{0.2}O_2/Li_6PS_5Cl$ composite cathode. Our results show that battery cycling leads to the local formation of oxidized species (most probably phosphates and sulfates) in the composite cathode, which can be observed in the detail spectra of S 2p, P 2p, and O 1s. In contrast, the role of chlorine could not be unambiguously clarified in this work. Auvergniot et al. described for $Li_4Ti_5O_{12}/Li_6PS_5Cl/LiCoO_2$ full cells the formation of LiCl in the composite cathode by the detail spectrum of Li 1s,[20] which could not be observed as clearly here (see the Supporting Information). Accordingly, neither XPS nor ToF-SIMS could provide evidence for the formation of LiCl in the composite cathode. Also, no evidence of transition-metal chlorides could be found either. As already mentioned, it cannot be concluded at this point that Cl does not react (note detection limits etc.) but our data do not show any indications of ongoing reactions.

However, it seems that in general, the combination of layered lithium transition-metal oxides with sulfur-/phosphorus-containing SE leads to similar reactions at the active material/SE interface with respect to sulfur and phosphorus species. With regard to the degradation of Li_6PS_5Cl, various conclusions can be drawn:

We assume that phosphates and sulfates such as Li_3PO_4 and Li_2SO_4, respectively, can already be formed by reactions with water and oxygen residues in the ppm range due to the high reactivity of the argyrodite. These could be detected on the surface of the argyrodite with XPS. We attribute the increase of this species in the XP spectra of the uncycled cathode to reactions at the NCM622/SE interface due to NCM622 surface species, such as water, oxygen residues, and carbonates. It seems reasonable that the reaction is similar to the surface reaction and caused by the mere contact of the SE with the NCM622 particles (see Figures 4 and 5). The reason that Li_2SO_4 cannot be detected in the S 2p spectrum is probably due to the low concentration, which is below the detection limit of XPS. However, due to the high ionization probability of SO_x^- fragments, the detection is still possible using ToF-SIMS.

Investigations on the influence of cell cycling show a significant increase in decomposition products. Visbal et al. have already shown with ToF-SIMS surface analysis that the species forming SO_x^- and PO_x^- fragments play an important role in cycled composite cathodes based on $LiNi_{0.8}Co_{0.15}Al_{0.05}O_2$ and $Li_2S-P_2S_5$ glass ceramics.[25] Our investigations extend these observations to degradation processes in $LiNi_{0.6}Co_{0.2}Mn_{0.2}O_2/Li_6PS_5Cl$ composite cathodes with more detailed information on the composition of the SEI and its morphology. Our results show that PO_x^- (intense) and SO_x^- fragments (weaker) are significantly enriched in the NCM622/SE interfacial region. Accordingly, 3D reconstructions of depth profiles and ToF-SIMS surface imaging on FIB crater sidewalls show that species forming these SO_x^- and PO_x^- fragments form a uniform shell around the NCM622 particles. This means that the formation of the SEI can be visualized and monitored by detecting SO_x^- and PO_x^- fragments. The herein performed XPS studies confirm an increase of signals in the binding energy range of phosphates such as $Mn_3(PO_4)_2$ and $Ni_3(PO_4)_2$,[46] indicating that transition-metal phosphates are conceivable. At the same time, no signals in the binding energy range of transition-metal phosphides (<130 eV) are recognizable.[47−49] The evaluation of the ToF-SIMS mass spectra in mass ranges of transition-metal sulfides, phosphides, and chlorides also suggests that these species play a minor role. In the S 2p spectrum, an intensity increase can be seen for the signal, which we attribute

DOI: 10.1021/acs.chemmater.9b00770
Chem. Mater. 2019, 31, 3745−3755

to polysulfides. Again, SO_x species in the higher binding energy range are not unambiguously detectable because we assume that their concentration is below the detection limit of XPS. Nevertheless, we can detect an increase of SO_x^- species with ToF-SIMS due to the high sensitivity of the method. In contrast, polysulfides cannot be detected with ToF-SIMS because long chains break during depth profiling or focused ion beam milling, even if the formation of polysulfides appears plausible according to XPS measurements.

Overall, our results indicate that the SEI layer is formed by an interface reaction between the NCM particles (oxygen source) and the electrolyte (phosphorus and sulfur source), whereas no influence could be observed within the electrolyte bulk. The layer thickness of the SEI can only be approximated here. The lateral resolution of the ToF-SIMS investigations is typically in a range of 150 nm. This can only be seen as an upper limit due to the information broadening by the analysis beam, since a spatial subdivision of the signal origin is not possible. Sputter effects or the influence of the FIB additionally blur this information. Therefore, the ToF-SIMS images indicate a broader SEI than it actually is. The XPS investigations showed that the signal of the NCM lattice oxygen almost disappeared due to cell cycling. Assuming a homogeneous, closed layer on the NCM622 secondary particles, the SEI layer thickness should be below the maximum XPS analysis depth (typically in the range of 10 nm), since the lattice oxygen signal and the Ni 2p signal are still detectable. At this point, however, it cannot be ruled out that damaged or broken particles are on the surface. Nevertheless, the layer thickness estimation about the XPS results seems reasonable. Knowing the interphase composition and thickness will help the development and characterization of protection concepts to influence the SEI formation to better understand the underlying mechanisms.

■ CONCLUSIONS

The degradation of a composite cathode in an In/InLil Li_6PS_5Cl|$LiNi_{0.6}Co_{0.2}Mn_{0.2}O_2$/$Li_6PS_5Cl$ ASSB was investigated. Electrochemical investigations showed a decrease in battery performance as a function of the cycle number, which corroborates the presence of degradation processes. The degradation of the cycled NCM622/Li_6PS_5Cl composite cathode is characterized by combining findings from XPS analysis with local compositional information from ToF-SIMS. The combination of both methods allows us to visualize the formation of the SEI layer and to draw conclusions about their chemical composition. Our results indicate that the SEI layer consists of phosphate- and sulfatelike species whereas transition-metal (TM) compounds, such as TMS^-, TMP^-, $TMCl^-$, etc. can be neglected. In addition, XPS measurements suggest the formation of polysulfides. Therefore, an SEI layer of max. 10 nm thickness is formed by an interfacial reaction between the NCM622 particles (oxygen source) and the solid electrolyte (phosphorus and sulfur source), resulting in a uniform shell around the NCM622 particles.

In summary, we show that combining XPS with ToF-SIMS is well suited to characterize degradation in ASSBs and to visualize the formation of the SEI layer. To the best of our knowledge, we show for the first time, the local structure and morphology of the SEI layer on the basis of information about their chemical composition using ToF-SIMS analysis. This approach can be used, for example, to better understand protection concepts for cathode materials (coatings, additives, etc.) and their influence on the formation of SEI, e.g., on layer thickness or chemical composition.

■ ASSOCIATED CONTENT

Supporting Information

The Supporting Information is available free of charge on the ACS Publications website at DOI: 10.1021/acs.chemmater.9b00770.

SEM images of NCM622 primary particles, XP spectra of the Li 1s and Ni 2p signal and the influence of surface cleaning on the S 2p signal, ToF-SIMS measurements in relation to SO_x^- fragments, including surface analysis, depth profiling, and imaging on FIB crater sidewalls, normalization approach to determine the influence of cell cycling on the signal intensity of the combined (PO_2^- + PO_3^-) signal (PDF)

■ AUTHOR INFORMATION

Corresponding Author

*E-mail: Juergen.Janek@phys.Chemie.uni-giessen.de.

ORCID

Saneyuki Ohno: 0000-0001-8192-996X
Marcus Rohnke: 0000-0002-8867-950X
Wolfgang G. Zeier: 0000-0001-7749-5089
Jürgen Janek: 0000-0002-9221-4756

Notes

The authors declare no competing financial interest.

■ ACKNOWLEDGMENTS

The authors acknowledge the financial support by BASF SE within the International Network for Batteries and Electrochemistry.

■ REFERENCES

(1) Kato, Y.; Hori, S.; Saito, T.; Suzuki, K.; Hirayama, M.; Mitsui, A.; Yonemura, M.; Iba, H.; Kanno, R. High-Power All-Solid-State Batteries Using Sulfide Superionic Conductors. *Nat. Energy* **2016**, *1*, 16030.

(2) Seino, Y.; Ota, T.; Takada, K.; Hayashi, A.; Tatsumisago, M. A Sulphide Lithium Super Ion Conductor Is Superior to Liquid Ion Conductors for Use in Rechargeable Batteries. *Energy Environ. Sci.* **2014**, *7*, 627−631.

(3) Xu, R.; Xia, X.; Li, S.; Zhang, S.; Wang, X.; Tu, J. All-Solid-State Lithium−sulfur Batteries Based on a Newly Designed $Li_7P_{2.9}Mn_{0.1}S_{10.7}I_{0.3}$ Superionic Conductor. *J. Mater. Chem. A* **2017**, *5*, 6310−6317.

(4) Kuhn, A.; Gerbig, O.; Zhu, C.; Falkenberg, F.; Maier, J.; Lotsch, B. V. A New Ultrafast Superionic Li-Conductor: Ion Dynamics in $Li_{11}Si_2PS_{12}$ and Comparison with Other Tetragonal LGPS-Type Electrolytes. *Phys. Chem. Chem. Phys.* **2014**, *16*, 14669−14674.

(5) Kamaya, N.; Homma, K.; Yamakawa, Y.; Hirayama, M.; Kanno, R.; Yonemura, M.; Kamiyama, T.; Kato, Y.; Hama, S.; Kawamoto, K.; et al. A Lithium Superionic Conductor. *Nat. Mater.* **2011**, *10*, 682−686.

(6) Goodenough, J. B.; Kim, Y. Challenges for Rechargeable Li Batteries. *Chem. Mater.* **2010**, *22*, 587−603.

(7) Ulvestad, A. A Brief Review of Current Lithium Ion Battery Technology and Potential Solid State Battery Technologies. 2018, arXiv:1803.04317. arXiv.org e-Print archive. https://arxiv.org/abs/1803.04317.

(8) Xu, W.; Wang, J.; Ding, F.; Chen, X.; Nasybulin, E.; Zhang, Y.; Zhang, J.-G. Lithium Metal Anodes for Rechargeable Batteries. *Energy Environ. Sci.* **2014**, *7*, 513−537.

DOI: 10.1021/acs.chemmater.9b00770
Chem. Mater. 2019, 31, 3745−3755

(9) Wang, Y.; Richards, W. D.; Ong, S. P.; Miara, L. J.; Kim, J. C.; Mo, Y.; Ceder, G. Design Principles for Solid-State Lithium Superionic Conductors. *Nat. Mater.* **2015**, *14*, 1026−1031.
(10) Zhang, W.; Weber, D. A.; Weigand, H.; Arlt, T.; Manke, I.; Schröder, D.; Koerver, R.; Leichtweiss, T.; Hartmann, P.; Zeier, W. G.; et al. Interfacial Processes and Influence of Composite Cathode Microstructure Controlling the Performance of All-Solid-State Lithium Batteries. *ACS Appl. Mater. Interfaces* **2017**, *9*, 17835−17845.
(11) Koerver, R.; Aygün, I.; Leichtweiß, T.; Dietrich, C.; Zhang, W.; Binder, J. O.; Hartmann, P.; Zeier, W. G.; Janek, J. Capacity Fade in Solid-State Batteries: Interphase Formation and Chemomechanical Processes in Nickel-Rich Layered Oxide Cathodes and Lithium Thiophosphate Solid Electrolytes. *Chem. Mater.* **2017**, *29*, 5574−5582.
(12) Koerver, R.; Zhang, W.; de Biasi, L.; Schweidler, S.; Kondrakov, A. O.; Kolling, S.; Brezesinski, T.; Hartmann, P.; Zeier, W. G.; Janek, J. Chemo-Mechanical Expansion of Lithium Electrode Materials − on the Route to Mechanically Optimized All-Solid-State Batteries. *Energy Environ. Sci.* **2018**, *11*, 2142−2158.
(13) Ishidzu, K.; Oka, Y.; Nakamura, T. Lattice Volume Change during Charge/Discharge Reaction and Cycle Performance of Li[$Ni_xCo_yMn_z$]O2. *Solid State Ionics* **2016**, *288*, 176−179.
(14) Kondrakov, A. O.; Schmidt, A.; Xu, J.; Geßwein, H.; Mönig, R.; Hartmann, P.; Sommer, H.; Brezesinski, T.; Janek, J. Anisotropic Lattice Strain and Mechanical Degradation of High- and Low-Nickel NCM Cathode Materials for Li-Ion Batteries. *J. Phys. Chem. C* **2017**, *121*, 3286−3294.
(15) Ghanty, C.; Markovsky, B.; Erickson, E. M.; Talianker, M.; Haik, O.; Tal-Yossef, Y.; Mor, A.; Aurbach, D.; Lampert, J.; Volkov, A.; et al. Li^+-Ion Extraction/Insertion of Ni-Rich $Li_{1+x}(Ni_yCo_zMn_z)_wO_2$ (0.005<x<0.03; y:Z = 8:1, W≈1) Electrodes: In Situ XRD and Raman Spectroscopy Study. *ChemElectroChem* **2015**, *2*, 1479−1486.
(16) Zhu, Y.; He, X.; Mo, Y. Origin of Outstanding Stability in the Lithium Solid Electrolyte Materials: Insights from Thermodynamic Analyses Based on First Principles Calculations. *ACS Appl. Mater. Interfaces* **2015**, *7*, 23685−23693.
(17) Richards, W. D.; Miara, L. J.; Wang, Y.; Kim, J. C.; Ceder, G. Interface Stability in Solid-State Batteries. *Chem. Mater.* **2016**, *28*, 266−273.
(18) Zhu, Y.; He, X.; Mo, Y. First Principles Study on Electrochemical and Chemical Stability of Solid Electrolyte−electrode Interfaces in All-Solid-State Li-Ion Batteries. *J. Mater. Chem. A* **2016**, *4*, 3253−3266.
(19) Hakari, T.; Deguchi, M.; Mitsuhara, K.; Ohta, T.; Saito, K.; Orikasa, Y.; Uchimoto, Y.; Kowada, Y.; Hayashi, A.; Tatsumisago, M. Structural and Electronic-State Changes of a Sulfide Solid Electrolyte during the Li Deinsertion-Insertion Processes. *Chem. Mater.* **2017**, *29*, 4768−4774.
(20) Auvergniot, J.; Cassel, A.; Foix, D.; Viallet, V.; Seznec, V.; Dedryvère, R. Redox Activity of Argyrodite Li_6PS_5Cl Electrolyte in All-Solid-State Li-Ion Battery: An XPS Study. *Solid State Ionics* **2017**, *300*, 78−85.
(21) Koerver, R.; Walther, F.; Aygün, I.; Sann, J.; Dietrich, C.; Zeier, W. G.; Janek, J. Redox-Active Cathode Interphases in Solid-State Batteries. *J. Mater. Chem. A* **2017**, *5*, 22750−22760.
(22) Wu, X.; Villevieille, C.; Novák, P.; El Kazzi, M. Monitoring the Chemical and Electronic Properties of Electrolyte−electrode Interfaces in All-Solid-State Batteries Using Operando X-Ray Photoelectron Spectroscopy. *Phys. Chem. Chem. Phys.* **2018**, *20*, 11123−11129.
(23) Kato, A.; Kowada, H.; Deguchi, M.; Hotehama, C.; Hayashi, A.; Tatsumisago, M. XPS and SEM Analysis between Li/Li_3PS_4 Interface with Au Thin Film for All-Solid-State Lithium Batteries. *Solid State Ionics* **2018**, *322*, 1−4.
(24) Auvergniot, J.; Cassel, A.; Ledeuil, J. B.; Viallet, V.; Seznec, V.; Dedryvère, R. Interface Stability of Argyrodite Li_6PS_5Cl toward $LiCoO_2$, $LiNi_{1/3}Co_{1/3}Mn_{1/3}O_2$, and $LiMn_2O_4$ in Bulk All-Solid-State Batteries. *Chem. Mater.* **2017**, *29*, 3883−3890.
(25) Visbal, H.; Aihara, Y.; Ito, S.; Watanabe, T.; Park, Y.; Doo, S. The Effect of Diamond-like Carbon Coating on $LiNi_{0.8}Co_{0.15}Al_{0.05}O_2$ Particles for All Solid-State Lithium-Ion Batteries Based on $Li_2SeP_2S_5$ Glass-Ceramics. *J. Power Sources* **2016**, *314*, 85−92.
(26) Börner, M.; Horsthemke, F.; Kollmer, F.; Haseloff, S.; Friesen, A.; Niehoff, P.; Nowak, S.; Winter, M.; Schappacher, F. M. Degradation Effects on the Surface of Commercial Li-$Ni_{0.5}Co_{0.2}Mn_{0.3}O_2$ Electrodes. *J. Power Sources* **2016**, *335*, 45−55.
(27) Gilbert, J. A.; Bareño, J.; Spila, T.; Trask, S. E.; Miller, D. J.; Polzin, B. J.; Jansen, A. N.; Abraham, D. P. Cycling Behavior of NCM523/Graphite Lithium-Ion Cells in the 3−4.4 V Range: Diagnostic Studies of Full Cells and Harvested Electrodes. *J. Electrochem. Soc.* **2017**, *164*, A6054−A6065.
(28) Hwang, J. Y.; Myung, S. T.; Choi, J. U.; Yoon, C. S.; Yashiro, H.; Sun, Y. K. Resolving the Degradation Pathways of the O3-Type Layered Oxide Cathode Surface through the Nano- Scale Aluminum Oxide Coating for High-Energy Density Sodium-Ion Batteries. *J. Mater. Chem. A* **2017**, *5*, 23671−23680.
(29) Jo, C.-H.; Cho, D.-H.; Noh, H.-J.; Yashiro, H.; Sun, Y.-K.; Myung, S. T. An Effective Method to Reduce Residual Lithium Com-Pounds on Ni-Rich Li[$Ni_{0.6}Co_{0.2}Mn_{0.2}$]O_2 Active Material Using a Phosphoric Acid Derived Li_3PO_4 Nanolayer. *Nano Res.* **2015**, *8*, 1464−1479.
(30) Lee, S. W.; Kim, M. S.; Jeong, J. H.; Kim, D. H.; Chung, K. Y.; Roh, K. C.; Kim, K. B. Li_3PO_4 Surface Coating on Ni-Rich $LiNi_{0.6}Co_{0.2}Mn_{0.2}O_2$ by a Citric Acid Assisted Sol-Gel Method: Improved Thermal Stability and High-Voltage Performance. *J. Power Sources* **2017**, *360*, 206−214.
(31) Li, W.; Dolocan, A.; Oh, P.; Celio, H.; Park, S.; Cho, J.; Manthiram, A. Dynamic Behaviour of Interphases and Its Implication on High-Energy-Density Cathode Materials in Lithium-Ion Batteries. *Nat. Commun.* **2017**, *8*, No. 14589.
(32) Neudeck, S.; Walther, F.; Bergfeldt, T.; Suchomski, C.; Rohnke, M.; Hartmann, P.; Janek, J.; Brezesinski, T. Molecular Surface Modification of NCM622 Cathode Material Using Organophosphates for Improved Li-Ion Battery Full-Cells. *ACS Appl. Mater. Interfaces* **2018**, *10*, 20487−20498.
(33) Wang, S.; Xu, H.; Li, W.; Dolocan, A.; Manthiram, A. Interfacial Chemistry in Solid-State Batteries: Formation of Interphase and Its Consequences. *J. Am. Chem. Soc.* **2018**, *140*, 250−257.
(34) Vickerman, J. C.; Gilmore, I. S. *Surface Analysis: The Principal Techniques*, 2nd ed.; John Wiley & Sons Ltd: Chichester, U.K., 2009.
(35) Ohno, S.; Koerver, R.; Dewald, G.; Rosenbach, C.; Titscher, P.; Steckermeier, D.; Kwade, A.; Janek, J.; Zeier, W. G. Observation of Chemomechanical Failure and the Influence of Cutoff Potentials in All-Solid-State Li−S Batteries. *Chem. Mater.* **2019**, *31*, 2930−2940.
(36) Takada, K.; Aotani, N.; Iwamoto, K.; Kondo, S. Solid State Lithium Battery with Oxysulfide Glass. *Solid State Ionics* **1996**, *86*−*88*, 877−882.
(37) Vanbellingen, Q. P.; Elie, N.; Eller, M. J.; Della-Negra, S.; Touboul, D.; Brunelle, A. Time-of-Flight Secondary Ion Mass Spectrometry Imaging of Biological Samples with Delayed Extraction for High Mass and High Spatial Resolutions. *Rapid Commun. Mass Spectrom.* **2015**, *29*, 1187−1195.
(38) Henss, A.; Otto, S.-K.; Schaepe, K.; Pauksch, L.; Lips, K. S.; Rohnke, M. High Resolution Imaging and 3D Analysis of Ag Nanoparticles in Cells with ToF-SIMS and Delayed Extraction. *Biointerphases* **2018**, *13*, No. 03B410.
(39) Zhang, W.; Richter, F. H.; Culver, S. P.; Leichtweiss, T.; Lozano, J. G.; Dietrich, C.; Bruce, P. G.; Zeier, W. G.; Janek, J. Degradation Mechanisms at the $Li_{10}GeP_2S_{12}$/$LiCoO_2$ Cathode Interface in an All-Solid-State Lithium-Ion Battery. *ACS Appl. Mater. Interfaces* **2018**, *10*, 22226−22236.
(40) Wang, Y.; Matsuyama, T.; Deguchi, M.; Hayashi, A.; Nakao, A.; Tatsumisago, M. X-Ray Photoelectron Spectroscopy for Sulfide Glass Electrolytes in the Systems Li_2S−P_2S_5 and Li_2S−P_2S_5−LiBr. *J. Ceram. Soc. Japan* **2016**, *124*, 597−601.
(41) Dietrich, C.; Weber, D. A.; Culver, S.; Senyshyn, A.; Sedlmaier, S. J.; Indris, S.; Janek, J.; Zeier, W. G. Synthesis, Structural

DOI: 10.1021/acs.chemmater.9b00770
Chem. Mater. 2019, 31, 3745−3755

Characterization, and Lithium Ion Conductivity of the Lithium Thiophosphate $Li_2P_2S_6$. *Inorg. Chem.* **2017**, *56*, 6681−6687.
(42) Appapillai, A. T.; Mansour, A. N.; Cho, J.; Shao-Horn, Y. Microstructure of $LiCoO_2$ with and without "$AlPO_4$" Nanoparticle Coating: Combined STEM and XPS Studies. *Chem. Mater.* **2007**, *19*, 5748−5757.
(43) Wang, B.; Liu, J.; Sun, Q.; Li, R.; Sham, T.-K.; Sun, X. Atomic Layer Deposition of Lithium Phosphates as Solid-State Electrolytes for All-Solid-State Microbatteries. *Nanotechnology* **2014**, *25*, No. 504007.
(44) Nagao, K.; Hayashi, A.; Deguchi, M.; Tsukasaki, H.; Mori, S.; Tatsumisago, M. Amorphous $LiCoO_2$-Li_2SO_4 Active Materials: Potential Positive Electrodes for Bulk-Type All-Oxide Solid-State Lithium Batteries with High Energy Density. *J. Power Sources* **2017**, *348*, 1−8.
(45) Jung, R.; Morasch, R.; Karayaylali, P.; Phillips, K.; Maglia, F.; Stinner, C.; Shao-Horn, Y.; Gasteiger, H. A. Effect of Ambient Storage on the Degradation of Ni-Rich Positive Electrode Materials (NMC811) for Li-Ion Batteries. *J. Electrochem. Soc.* **2018**, *165*, A132−A141.
(46) Franke, R.; Chassé, T.; Streubel, P.; Meisel, A. Data Bank - Auger Parameters and Relaxation Energies of Phosphorus in Solid Compounds. *J. Electron Spectrosc. Relat. Phenom.* **1991**, *56*, 381−388.
(47) López, M. C.; Ortiz, G. F.; Tirado, J. L. A Functionalized Co_2P Negative Electrode for Batteries Demanding High Li-Potential Reaction. *J. Electrochem. Soc.* **2012**, *159*, A1253−A1261.
(48) Henderson, L. B.; Ekerdt, J. G. Chemical Vapor Deposition of Amorphous Cobalt−Phosphorus Alloy Films. *Electrochem. Solid-State Lett.* **2009**, *12*, D36−D38.
(49) Nemoshkalenko, V. V.; Didyk, V. V.; Krivitskii, V. P.; Senkevich, A. I. Study of the Charge State of Atoms in Iron, Cobalt and Nickel Phosphides. *Zh. Neorg. Khim.* **1983**, *28*, 2182−2186.
(50) Wu, X.; El Kazzi, M.; Villevieille, C. Surface and Morphological Investigation of the Electrode/Electrolyte Properties in an All-Solid-State Battery Using a Li_2S-P_2S_5 Solid Electrolyte. *J. Electroceram.* **2017**, *38*, 207−214.
(51) Bodenes, L.; Dedryvère, R.; Martinez, H.; Fischer, F.; Tessier, C.; Pérès, J.-P. Lithium-Ion Batteries Working at 85 °C: Aging Phenomena and Electrode/Electrolyte Interfaces Studied by XPS. *J. Electrochem. Soc.* **2012**, *159*, A1739−A1746.
(52) Moulder, J. F.; Stickle, W. F.; Sobol, P. E.; Bomben, K. D. In *Handbook of X-Ray Photoelectron Spectroscopy; A Reference Book of Standard Spectra for Identification and Interpretation of XPS Data*; Chastain, J., King, R. C., Jr., Eds.; Physical Electronics: Eden Prairie, US-MN, 1995.
(53) Wu, X.; Villevieille, C.; Novák, P.; El Kazzi, M. Monitoring the Chemical and Electronic Properties of Electrolyte−electrode Interfaces in All-Solid-State Batteries Using Operando X-Ray Photoelectron Spectroscopy. *Phys. Chem. Chem. Phys.* **2018**, *20*, 11123−11129.
(54) Swamy, T.; Chen, X.; Chiang, Y.-M. Electrochemical Redox Behavior of Li Ion Conducting Sulfide Solid Electrolytes. *Chem. Mater.* **2019**, *31*, 707−713.

DOI: 10.1021/acs.chemmater.9b00770
Chem. Mater. 2019, 31, 3745−3755

3.2 Publication II: "Influence of Carbon Additives on the Decomposition Pathways in Cathodes of Lithium Thiophosphate-Based All-Solid-State Batteries"

In the second publication of this doctoral thesis, the degradation scheme of NCM- and thiophosphate-based composite cathodes was extended by the effect of conductive carbon additives. For this purpose, the influence of VGCFs on the degradation processes in composite cathodes based on NCM622/β-Li_3PS_4 was investigated.

Carbon additives are used in conventional LIBs to improve the electronic partial conductivity and to maximize the utilization of the CAM within the composite cathode. The introduction of carbon additives in ASSBs, however, typically suffers from increased capacity fading during cell cycling. The underlying chemical degradation processes were widely unknown due to the complexity of the composite cathode with convoluted degradation processes, making it difficult to draw conclusions on individual degradation processes and to develop targeted solutions to overcome related problems.

In publication II, the various degradation processes within the composite cathode could be deconvoluted. By means of comprehensive surface and bulk analyses with XPS and ToF-SIMS, it was shown that three independent degradation zones can be distinguished, namely degradation reactions at the interfaces of current collector/SE, CAM/SE and carbon/SE. In addition, information on the respective degradation reactions was provided. This work reveals, for example, that the application of conductive carbon additives is accompanied by a massive increase in polysulfide formation, which is directly detected in such composite cathodes for the first time by ToF-SIMS. Through this work, a comprehensive picture of degradation in thiophosphate-based composite cathodes has been provided and a detailed reaction scheme for the interfacial reaction between NCM-based CAM and β-Li_3PS_4 has been proposed.

The second publication extends the knowledge about degradation phenomena in composite cathodes with conductive carbon additives significantly. Furthermore, the results clearly show that all interfaces within the composite cathode must be independently addressed to prevent thiophosphate-based SE from decomposition/degradation reactions. Indeed, based on this knowledge, a protection concept for conductive carbon additives was developed and its suitability was demonstrated in a recent collaborative work with Randau *et al.*[39] These studies in turn resulted in a patent application together with BASF SE.

The first author designed the experiments under the supervision of F. H. Richter, W. G. Zeier and J. Janek. S. Randau and Y. Schneider prepared the ASSB and CV cells and performed the electrochemical characterization. The analytical measurements (XPS and ToF-SIMS) and the subsequent analysis and evaluation were performed by the first author. All authors contributed to the scientific discussion. In particular, the analytical data was discussed with J. Sann and M. Rohnke. The manuscript was written by the first author and edited by seven co-authors.

This study was part of the International Network for Batteries and Electrochemistry by BASF SE. The project was accompanied by J. Kulisch and X. Wu through scientific exchange.

CHEMISTRY OF MATERIALS

pubs.acs.org/cm Article

Influence of Carbon Additives on the Decomposition Pathways in Cathodes of Lithium Thiophosphate-Based All-Solid-State Batteries

Felix Walther, Simon Randau, Yannik Schneider, Joachim Sann, Marcus Rohnke,* Felix H. Richter,* Wolfgang G. Zeier,* and Jürgen Janek*

Cite This: *Chem. Mater.* 2020, 32, 6123–6136 Read Online

ACCESS | Metrics & More | Article Recommendations | Supporting Information

ABSTRACT: On the way to a large-scale industrial application of all-solid-state batteries (ASSBs) it is necessary to overcome a number of challenges. An important task is to maximize the utilization of active material in the cathode composite to achieve high capacities. Carbon-based conductive additives are common in cathode composites for conventional lithium-ion batteries based on liquid electrolytes. In all-solid-state batteries, the beneficial effect of carbon additives is often not maintained over a sufficient number of charge/discharge cycles. Thus, ASSB cells often suffer from an increased long-term capacity loss with an enhanced formation of decomposition products. So far, these effects have not been analyzed in depth and are not fully understood because of the complexity of the composite cathode structure. Together with overlap of the occurring degradation paths, this makes a separation of the individual decomposition processes challenging. In this work, we investigate the influence of vapor-grown carbon fibers as carbon-based conductive additives on the degradation of a $LiNi_{0.6}Co_{0.2}Mn_{0.2}O_2$/$\beta$-$Li_3PS_4$ composite cathode. We use a combination of X-ray photoelectron spectroscopy and time-of-flight secondary ion mass spectrometry (ToF-SIMS) and combine surface and bulk analyses to separate the overlapping decomposition processes from each other. The results show an initially higher capacity by using vapor-grown carbon fibers due to higher utilization of the active material and an additional capacity contribution caused by redox-active decomposition reactions. The observed capacity fading is associated with the formation of sulfates/sulfites, phosphates, and polysulfides, which are detected directly in $LiNi_{0.6}Co_{0.2}Mn_{0.2}O_2$/$\beta$-$Li_3PS_4$ composite cathodes with ToF-SIMS for the first time. Overall, the results extend the knowledge and understanding of degradation phenomena in thiophosphate-based composite cathodes considerably, which is an essential step to develop protection concepts more efficiently on the way to long-term stable ASSBs.

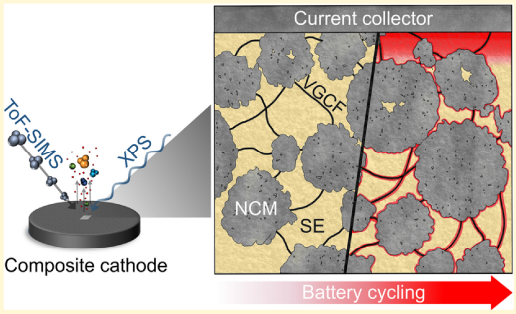

INTRODUCTION

All-solid-state batteries (ASSBs) are considered as promising candidates for future energy storage devices as they may enable the use of lithium metal as anode material and lead to higher specific energies compared to conventional lithium-ion batteries (LIBs) that are based on organic liquid electrolytes.[1−5] At the same time, device safety may be improved if the flammable organic liquid electrolyte is replaced with a solid electrolyte (SE), and the cell design can be simplified.[6] The use of thiophosphate-based SEs seems to be particularly attractive since this material class typically shows high ionic conductivities and can be easily processed due to their malleability.[7]

A number of challenges still need to be addressed on the way to large-scale industrial application, and it is important to optimize electrode interfaces and cell design to make ASSBs economically attractive.[8] Cathode design includes parameters such as the active material/SE ratio and the optimization of the active material particle size, whose influence has already been investigated by several groups.[9−12] Another approach to maximize the utilization of the active material is the use of conductive additives analogous to conventional LIBs. However, Zhang et al. showed that the use of various commercial conductive carbons in the composite cathode leads to a stronger long-term capacity fading of thiophosphate-based ASSBs.[13] Yoon et al. also observed a deteriorated kinetic performance with a large interfacial impedance buildup for $Li_{10}GeP_2S_{12}$-based composite cathodes by using conductive carbons.[14] In a recent study, Strauss et al. investigated the influence of various conductive additives on the ASSB performance, observing a beneficial effect only when using

Received: April 29, 2020
Revised: July 1, 2020
Published: July 1, 2020

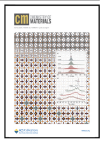

https://dx.doi.org/10.1021/acs.chemmater.0c01825
Chem. Mater. 2020, 32, 6123–6136

the particulate conductive carbon additive Super C65.[15] It seems that a simple and direct transfer of conductive additives from LIBs to ASSBs is not straightforward. Therefore, Deng et al. introduced a poly(3,4-ethylenedioxythiophene) modification to eliminate the detrimental effects of the conductive additive, leading to an improved ASSB performance.[16]

The underlying decomposition mechanisms are still widely unknown, making it difficult to address these problems and to develop targeted solutions. The reason for this is that degradation processes occurring in different locations of the composite cathode are often convoluted within the analysis area. From an analytical perspective, the separation of the different, partly significantly overlapping degradation mechanisms in composite cathodes and the identification of the decomposition products are extremely challenging. Koerver et al. have shown by X-ray photoelectron spectroscopy (XPS) depth profiling experiments that a potential-dependent decomposition reaction toward the current collector can be observed for thiophosphate-based composite cathodes.[17] Based on this work and a more recent study by Dewald et al., decomposition reactions of the SE at the current collector/SE interface itself can be expected.[18] Taking into account the current collector/SE interphase, Walther et al. additionally revealed the local decomposition in the interfacial area between NCM secondary particles and the thiophosphate-based SE by time-of-flight secondary ion mass spectrometry (ToF-SIMS) measurements.[19]

However, spectroscopic and spectrometric investigations on the identification of decomposition products in composite cathodes after long-term cycling are mostly based on "global" investigations on the uncleaned composite cathode surface, which was in contact with the current collector. Thus, the analyzed volume contains several convoluted degradation processes, which often cannot be separated from each other. Conclusions based on such measurements easily lead to misinterpretations. Accordingly, an analysis to identify decomposition products in thiophosphate-based composite cathodes inevitably requires an initial surface cleaning step to minimize the influence of the current collector.

Taking these considerations into account, we investigate the influence of vapor-grown carbon fibers (VGCF) as carbon-based conductive additives in a pellet-type composite cathode in a Li|β-Li_3PS_4|$LiNi_{0.6}Co_{0.2}Mn_{0.2}O_2$/$\beta$-$Li_3PS_4$ ASSB cell. We chose VGCF since it has advantageous morphological properties for the application as conductive additive and is of high practical relevance: The fiberlike structure (diameter: 100 nm; length: 20−200 μm) makes it possible to bridge large distances and thus contact particles electronically over a wider space. In addition, the specific surface area of 24 $m^2\ g^{-1}$ is relatively small in comparison to other carbon additives, which is advantageous with regard to possible interfacial reactions.[13,14]

The aim of this work is to unfold the significantly overlapping degradation mechanisms by means of surface and bulk analysis and to provide detailed insight into the degradation mechanisms in such composite cathodes. Therefore, we use a combination of the analytical methods XPS and ToF-SIMS. Especially the high spatial resolution of ToF-SIMS can help to characterize the degradation phenomena more precisely. In addition, the secondary ion fragments provide direct information about the composition of the degradation products present. We show that besides the formation of phosphates and sulfates/sulfites, polysulfide formation plays an important role in the degradation of composite cathodes. Also, we reveal similarities to degradation phenomena reported for Li−S solid-state batteries. The polysulfide formation is detected here for the first time by using ToF-SIMS. Finally, we propose a reaction scheme for the $LiNi_{0.6}Co_{0.2}Mn_{0.2}O_2$/$\beta$-$Li_3PS_4$ interfacial reaction during battery charging. With this work, we extend the knowledge about degradation phenomena in composite cathodes based on thiophosphate SEs and NCM considerably, which will help to develop interface protection concepts more efficiently.

■ EXPERIMENTAL SECTION

Preparation of ASSB Cells and Electrochemical Characterization. *Materials.* The active material $Li(Ni_{0.6}Co_{0.2}Mn_{0.2})O_2$ (NCM622) and the solid electrolyte β-Li_3PS_4 (σ_{bulk} = 1.2 × 10^{-4} S cm^{-1}) for this study were provided by BASF SE. The NCM622 particle morphology and microstructure of the β-Li_3PS_4 are shown in scanning electron micrographs in the Supporting Information (Figure S1). The used VGCF (Sigma-Aldrich, iron-free) has an average specific surface area of 24 $m^2\ g^{-1}$ with a diameter of 100 nm and a fiber length of 20−200 μm. The NCM622 active material and the VGCF were dried in a Büchi furnace at 200 °C overnight to minimize the influence of moisture. A 120 μm thick lithium foil disc (Albemarle, Rockwood Lithium GmbH) with 9 mm diameter was used as anode. The surface of the lithium foil was mechanically polished before use. All chemicals were stored in an argon-filled glovebox (<0.1 ppm of O_2, <0.1 ppm of H_2O).

Composite Cathode. The reference composite cathode contained only dried NCM622 and β-Li_3PS_4. The mass ratio was 70:30 (volume ratio 47:53) of NCM622 and β-Li_3PS_4, respectively. For the composite cathode with VGCF, 100 mg of the NCM622/β-Li_3PS_4 composite (mass ratio 70:30) was mixed first, and afterward 3.0 mg of VGCF (corresponding to a mass ratio of 2.9 wt %) was added. In the following this sample is abbreviated as "3 wt % VGCF". The different composites were then ground in an agate mortar by hand for 15 min. For cell assembly, the composite mixture was prepared fresh daily.

Cell Assembly. All cell tests were performed using a (pellet-type) cell casing manufactured in house.[12,20] For assembly, a stainless steel stamp was placed at the bottom of the inner poly(ether ether ketone) (PEEK) cylinder (inner diameter: 10 mm). All materials were added via the remaining opening on the top. 60 mg of the β-Li_3PS_4 solid electrolyte was added first. This powder was uniformly compressed manually by hand. Afterward, 10 mg of cathode composite mixture were added and distributed evenly. This powder stack was then compressed uniaxially at 30 kN (~380 MPa) for 3 min. After compacting the pellet, we added the lithium metal anode. The lithium foil was placed on the β-Li_3PS_4 solid electrolyte, and a copper foil was added on the lithium toward the stainless-steel current collector. The copper foil was added to mechanically stabilize the pellet for an easier extraction of the cell from the casing for the following analysis. An external frame is used around the cell casing during all electrochemical tests, applying a constant pressure of ~50 MPa.

Cell Test. Charge and discharge tests were performed using VMP-300 Biologic and MACCOR potentiostats/galvanostats. The VMP-300 Biologic potentiostat was used to be able to perform impedance measurements during the first cycles. Afterward, the MACCOR potentiostat was used for long-term battery cycling. Cells with lithium metal anode are charged to 4.3 V and discharged to 2.6 V versus Li^+/Li at 25 °C. The C-rate for charge and discharge experiments was 0.1C, corresponding to 1.78 mA cm^{-2} for cells with an active material loading of 8.9 mg cm^{-2}. Electrochemical impedance spectroscopy (EIS) was performed with a VMP-300 potentiostat. Before the EIS step, a 10 min open circuit voltage (OCV) measurement was performed to enable relaxation of the test cells. The EIS measurement was conducted in a frequency range of 7 MHz−1 Hz, applying a 10 mV sinus amplitude.

Time-of-Flight Secondary Ion Mass Spectrometry (ToF-SIMS). All samples were transferred under an argon atmosphere from the glovebox into the ToF-SIMS instrument by using the transfer

https://dx.doi.org/10.1021/acs.chemmater.0c01825
Chem. Mater. 2020, 32, 6123−6136

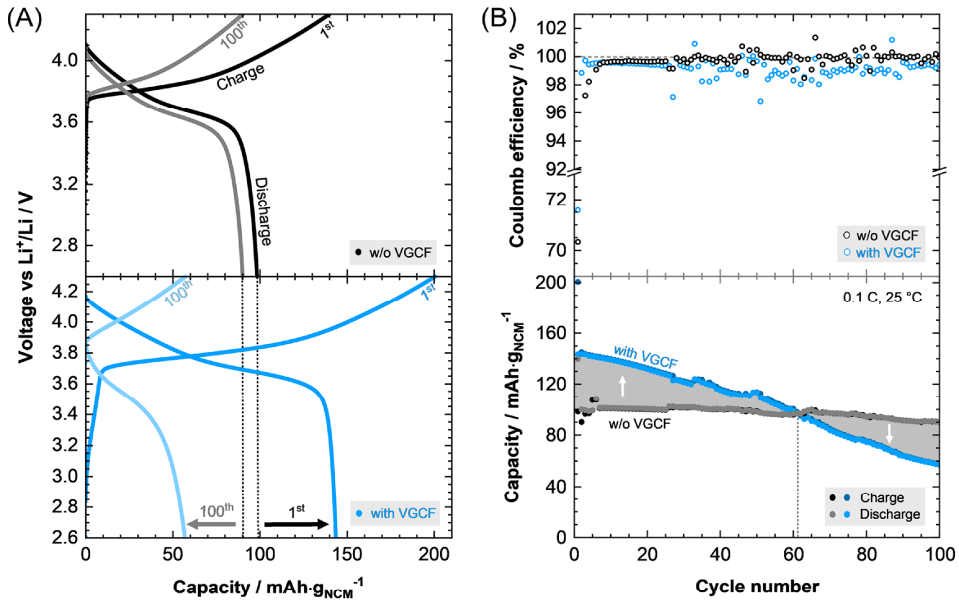

Figure 1. (A) Charge and discharge curves for the first and the hundredth cycle of a Li|β-Li_3PS_4|$LiNi_{0.6}Co_{0.2}Mn_{0.2}$/$\beta$-$Li_3PS_4$ ASSB with 3 wt % and without (w/o) VGCF in the composite cathode. (B) Charge and discharge capacity and Coulomb efficiency as a function of the cycle number. Adding VGCF results in higher initial capacities, but at the same time in a significantly increased capacity fading.

system Leica EM VCT500 (Leica Microsystems GmbH). ToF-SIMS was performed by using a TOF.SIMS 5 system (IONTOF GmbH). The instrument is equipped with a 25 keV Bi cluster primary ion gun for analysis. Depth profiling can be realized by using an additional dual-source column, which can be operated with 2 keV O_2^+ or Cs^+. An additional focused ion beam (FIB) option allows to create craters with monatomic gallium (30 keV). Afterward, the crater sidewalls can be analyzed in the same system without an additional transferring step.

Measurements on the composite cathode surfaces, depth profiling, and analyses on FIB crater sidewalls were performed to ensure reliable results. All ToF-SIMS measurements were performed in negative ion mode using Bi_3^+ ions with an energy of 25 keV as primary ion species.

For surface analysis, we operated the instrument in spectrometry mode (bunched mode) to determine changes in the mass spectra caused by battery cycling. This operation mode enables simultaneously a high mass resolution (FWHM $m/\Delta m$ > 5000 at m/z 31.97 (S^-)) and high signal intensities. The analysis area was 150 × 150 μm^2 and was rasterized with 256 × 256 pixels. The cycle time was set to 60 μs. To enable static and comparable measuring conditions, the measurements were stopped after a primary ion dose of 1.00×10^{12} ions/cm^2. We measured five mass spectra per sample in different areas on the surface of the composite cathodes to ensure reproducibility of the results and to discuss their reliability.

To investigate the bulk material, depth profiling experiments were performed in a noninterlaced mode. For analysis, the primary ion gun was operated in the spectrometry mode (bunched mode). The primary ion current was about 0.4−0.5 pA and the cycle time was set to 60 μs. An analysis area of 150 × 150 μm^2 was chosen and rasterized with 256 × 256 pixels at 2 shots per pixel and 5 frames. The mass resolution was in the range of FWHM $m/\Delta m$ > 6600 for the mass m/z 31.97 (S^-) for all measurements. For sputtering, Cs^+ species were used with an acceleration voltage of 2 keV. The sputter current was ∼150 nA. The crater size was 400 × 400 μm^2 and created with 450 frames per sputter step. The surface was flooded with low-energy electrons for 1 s for charge compensation.

ToF-SIMS analysis was performed on 45 °FIB crater sidewalls. The 100 × 80 μm^2 crater was milled with 512 × 512 pixels (FoV: 150 × 150 μm^2) into the composite cathode by using monatomic gallium (30 keV). A 700 μm aperture was used, and the dwell time was set to 180 ms per pixel. The analysis of the crater sidewall was performed in fast imaging mode. The primary ion current was about 0.2 pA and the cycle time was set to 60 μs. A region-of-interest (ROI) was defined within a 125 × 125 μm^2 analysis area. The damage layer on the crater sidewall caused by the FIB was removed by a cleaning step using the primary ion gun in DC mode analogous to our previous work.[19] The crater sidewall analysis was performed with a raster size of 1024 × 1024 pixels at 1 shot per pixel and 50 frames leading theoretically to a maximum lateral resolution of 122 nm. However, because of the topographic effects and height differences, this value should be considered as the maximum resolution under ideal conditions.

The evaluation of the ToF-SIMS data was performed in all cases with the software SurfaceLab 7.0 (IONTOF GmbH).

X-ray Photoelectron Spectroscopy (XPS). All samples were transferred under an argon atmosphere from the glovebox into the XPS instrument by using a transfer vessel. XPS was performed with a PHI5000 Versa Probe II system (Physical Electronics GmbH). For analysis, we used monochromatic Al Kα radiation (1486.6 eV). The power of the X-ray source was 50 W with a voltage of 15 kV. The analysis beam diameter was 200 μm. Depth profiling was performed by using a sputter gun with Ar^+ ions (0.5 μA setting). An acceleration voltage of 0.5 kV was used to clean the surface and to enable a relatively soft material abrasion in depth profiling experiments afterward. The sputtered area was 2 × 2 mm^2. A dual beam charge neutralization (ion beam combined with a low-energy electron beam) was applied. The pass energies ranged between 23.50 and 29.35 eV. The exact values can be found in the captions of the respective XP spectra. Data evaluation was performed with the software CasaXPS (version 2.3.22, Casa Software Ltd.). First, the XP spectra of the β-Li_3PS_4 reference were calibrated in relation to the signal of adventitious carbon at 284.8 eV. Afterward, the signal position of the main component of the S 2p signal was determined (PS_4^{3-} units), and the XP spectra of the composite cathodes were calibrated in relation to the main component of the β-Li_3PS_4 reference. In this way, detrimental effects due to surface effects were minimized.[21,22] Signal fitting was performed by using a Shirley background and GL(30) line

https://dx.doi.org/10.1021/acs.chemmater.0c01825
Chem. Mater. 2020, 32, 6123−6136

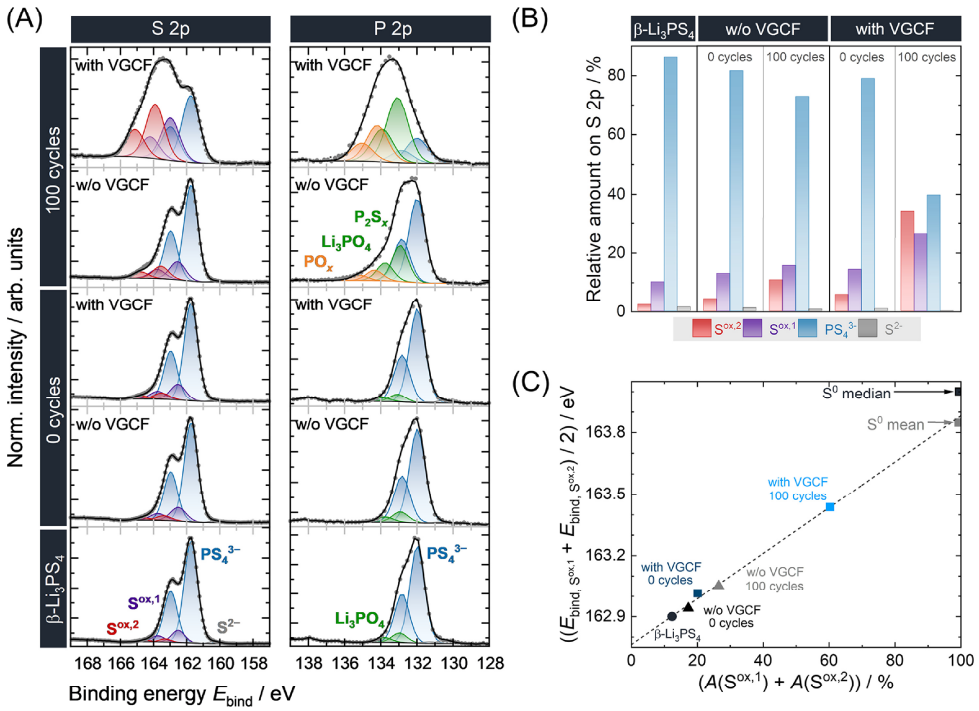

Figure 2. (A) XP spectra of the S 2p and P 2p signals for cycled and uncycled composite cathodes with and without VGCF after surface cleaning. Reference spectra for β-Li_3PS_4 are shown at the bottom. The pass energy was 23.50 eV in all cases. A Shirley background and GL(30) line shapes were used for signal fitting. The XP spectra were normalized in relation to the respective signal maximum to be able to compare the contributions of the signal components more easily. (B) Comparison of the relative amounts of the S 2p components for the five samples. (C) Mean signal position of the oxidized species ($S^{ox,1}$ and $S^{ox,2}$) as a function of the S 2p signal fraction. The mean and median values for the S^0 signal were calculated from values in the NIST database for elemental S.[29] With increasing fraction of oxidized species (corresponding to an increasing degree of decomposition), the mean signal position approaches the value for elemental sulfur.

shapes. Common fitting restrictions were used including theoretical signal area ratios dependent on the orbital (e.g., p orbitals 1:2), FWHM constraints, and published values for spin−orbit splitting.[23]

RESULTS

The results of this work are divided into three parts in the following. First, we show the influence of 3 wt % VGCF in the composite cathode on the initial capacity and the long-term ASSB performance and compare it with a corresponding ASSB without conductive additive. We have chosen a VGCF mass fraction of 3 wt % to enable a strong influence of the conductive additive and to provide sufficient product concentrations for reliable analytical investigations (concerning the detection limits of the analytical methods). After the electrochemical data, we show a comprehensive *post-mortem* analysis of ASSBs after 100 cycles with XPS (second part) and ToF-SIMS (third part) to characterize the degradation mechanisms in the composite cathodes. Taking into account the overlapping degradation processes (see above), surface measurements, depth profiles, and investigations on FIB crater sidewalls are combined to unfold the decomposition processes and to draw more precise conclusions on the individual degradation contributions. XPS is used for quantitative statements and to identify decomposition products. The postulation of decomposition products based on XPS measurements is often rather speculative due to small energetic XP signal position differences of published decomposition products.[16,17,24,25] For this reason, ToF-SIMS investigations on the surface and into the depth are used to verify statements made by XPS analysis and to provide further insights into the degradation phenomena. On the basis of the comparatively high sensitivity of ToF-SIMS for fragments with high ionization probabilities (several orders of magnitude compared to conventional XPS), reactions in the concentration range below the XPS detection limit can be investigated semi-quantitatively with ToF-SIMS. This allows the investigation of reactions that would remain undetected with XPS (e.g., formation of sulfates/sulfites; see below). Afterward, we show ToF-SIMS analysis on FIB crater sidewalls to verify the statements for the bulk and to characterize the local fragment distribution with high lateral resolution (~150 nm).

Electrochemical Cell Performance. To investigate the effects of VGCF on the charge and discharge capacities and the cycling performance, we constructed pellet-type Li|β-Li_3PS_4|$LiNi_{0.6}Co_{0.2}Mn_{0.2}O_2$/$\beta$-$Li_3PS_4$ ASSBs with 3 wt % VGCF in the composite cathode and a corresponding ASSB without any conductive additives. On reproducing the cells without VGCF, the specific capacity of discharge varied between 98 and 128 mAh g^{-1}, while the variation was less for the cells with VGCF (between 144 and 155 mAh g^{-1}). For the detailed instrumental analysis, we used cells that had achieved 98 mAh g^{-1} initial discharge capacity without VGCF and 144 mAh g^{-1} with VGCF. Figure 1A shows the corresponding potential profiles

https://dx.doi.org/10.1021/acs.chemmater.0c01825
Chem. Mater. 2020, 32, 6123−6136

of the first and hundredth cycles. We assume that the increase of the charge and discharge capacities can mainly be attributed to two (overlapping) effects: On the one hand, more NCM secondary particles are electronically addressed by using VGCF, which leads to a higher active material utilization and thus to higher initial capacities. On the other hand, decomposition reactions can take place at the additionally introduced VGCF/SE interface since the decomposition products of thiophosphates are reported to be redox-active, which may lead to further capacity contributions.[17,18,25−27]

This is supported by the shape of the first charge curve of the ASSB with VGCF. The smaller slope compared to the reference indicates an increase in side reactions. To further support this assumption, we assembled another ASSB with a slightly higher VGCF fraction (3.8 wt %) and investigated the effect on the initial charge and discharge capacity (see Figure S2). Both capacities are further increased compared to the sample with 3 wt % VGCF. For example, the initial charge capacity is enhanced from 201 mAh g^{-1} (3 wt %) to 227 mAh g^{-1} (3.8 wt %), which corresponds to 114% of the capacity, that is usually offered by NCM cathode active materials (assumption: Q_{theo} = 200 mAh g^{-1}).[28] Overall, these observations support the hypothesis of further capacity contributions due to decomposition reactions.

Figure 1B shows a comparison of the cycling performance. Both cells were cycled between 2.6 and 4.3 V (vs Li^+/Li) at 1.78 mA cm^{-2} (corresponds to 0.1C). As indicated by Figure 1B, the initial advantage of higher capacities by using VGCF cannot be maintained over a high number of cycles due to an increased long-term capacity fading. After 62 cycles, the specific capacity of the ASSB with VGCF falls below the value of the reference. The increased capacity fading can also be seen in the Coulomb efficiencies. The mean Coulomb efficiency for the reference is 99.5%, while the sample with VGCF achieves a mean Coulomb efficiency of only 98.9%, indicating a larger irreversibility by using VGCF. To study the mechanisms behind the capacity fading, comprehensive XPS and ToF-SIMS investigations were performed on such composite cathodes after 100 cycles. For analysis, the ASSBs were disassembled in the charged state of the cell.

Post-Mortem Analysis by X-ray Photoelectron Spectroscopy (XPS). XPS measurements were performed on cycled composite cathodes to identify decomposition products and to draw quantitative conclusions. Depth profiling was performed to clean the surface and to minimize the influence of the degradation processes that were recently found at the current collector/SE interface.[17] The change of the signals was monitored as a function of the sputtering time for all samples. The XP spectra shown in this work correspond to spectra for which no further signal change was observed with additional sputtering time (~240 s in this case). We assume that at this point the influence of the current collector is minimized, and the signals represent the bulk of the cathode composite. To exclude any modification by sputtering, depth profiles were also measured for the references (uncycled composite cathodes and the β-Li_3PS_4 reference) to allow a direct comparison.

Figure 2 shows the detail spectra of the S 2p and the P 2p signals after surface cleaning for cycled cathodes with and without VGCF and the corresponding uncycled references. In addition, a comparison with a β-Li_3PS_4 reference is shown. The Supporting Information also contains the O 1s, Li 1s, and C 1s signals (see Figure S3). For the latter two, however, no systematic dependence could be determined.

Comparing the S 2p detail spectra of the uncycled cathodes and the β-Li_3PS_4 reference, only minor differences, which are all within the range of the XPS detection limit, were detected. Basically, the reference signal can be described with four components: The main component is detected at a binding energy of 161.7 eV and corresponds to the PS_4^{3-} units of the β-Li_3PS_4 structure.[20] A small contribution in the low-binding energy shoulder can be attributed to Li_2S residues.[25,26] In the higher binding energy range a signal shoulder is visible, which can be represented by using two doublets. This signal shoulder has often been reported for thiophosphates in the literature and is mostly assigned to polysulfides or oxidized species such as P_2S_5, P_2S_7, or $Li_2P_2S_6$.[17,24,25,27] However, because of the small differences in the binding energy of such compounds, an assignment without additional proof is rather speculative. For this reason, we describe the two doublets necessary to represent the signal shoulder at higher binding energies in the following with $S^{ox,1}$ and $S^{ox,2}$. The origin of these signals will be discussed later in more detail. In the case of uncycled cathodes, the signal shoulder at higher binding energies ($S^{ox,1}$ and $S^{ox,2}$) is slightly increased compared to the β-Li_3PS_4 reference (see Figure 2B). This indicates the formation of oxidized sulfur species already due to the mere NCM/SE contact. Adding VGCF seems to lead to an additional slight signal increase. However, these observations are close to the detection limit, making reliable statements on the origin of these signals difficult.

In contrast, the influence of battery cycling on the S 2p signal can easily be seen. For both composite cathodes, battery cycling leads to a significant increase in signals in the higher binding energy range, while the signal attributed to Li_2S is reduced. By use of VGCF, the amount of oxidized species increases enormously—almost 60% of the total signal area can be related to decomposition products. As already mentioned, polysulfides have already been discussed as decomposition products in this binding energy range, which include species such as P-$[S]_n$-P-type anions (P_2S_n), Li_2S_n, and $Li_3PS_4(\mu$-$S_n)S_4PLi_3$ ($(Li_3PS_4)_2S_n$).[17,19,24−26] Accordingly, the XP signal position of polysulfides should depend on the chain length n. With increasing n, the relative amount of uncharged sulfur ($-S^0-$ groups) signals should increase. Therefore, a signal shift toward the theoretical signal position of uncharged sulfur (~164 eV) is expected to occur with increasing n. We assume that the signal shoulder at higher binding energies contains numerous -$[S]_n$- containing species with different chain lengths. The exact binding energy depends on their stoichiometry leading to a distribution function of oxidized species, which causes the signal shoulder. The signals $S^{ox,1}$ and $S^{ox,2}$ we used for signal fitting must therefore be considered as a simplified model to describe this distribution function. The average signal position of both ($S^{ox,1}$ and $S^{ox,2}$) is determined in the first approximation by the mean -$[S]_n$- chain length of all polysulfides. Figure 2C shows the mean energetic signal position of the oxidized species $S^{ox,1}$ and $S^{ox,2}$ as a function of the fraction of these species on the total S 2p signal for all samples shown in Figure 2A. It can be seen that a higher amount of degradation products is associated with an increase in the energetic signal position. Therefore, a stronger degradation is correlated to an enhanced polysulfide formation with longer mean chain lengths. This is a strong indication of the formation of polysulfides, which is further supported by ToF-SIMS measurements (see below).

https://dx.doi.org/10.1021/acs.chemmater.0c01825
Chem. Mater. 2020, 32, 6123−6136

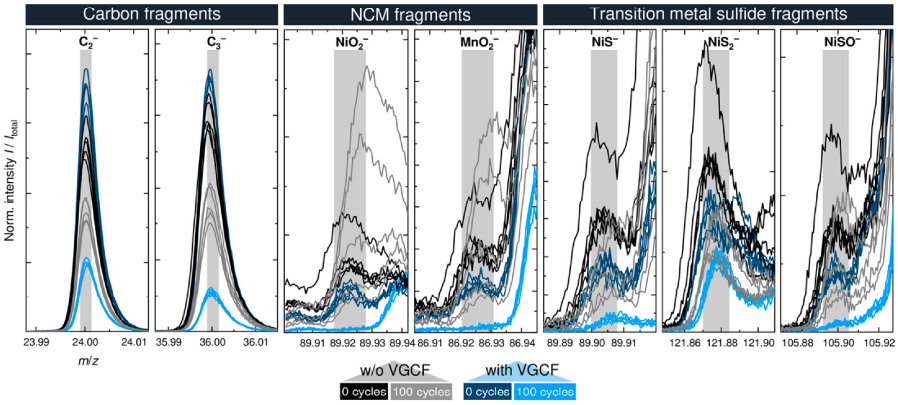

Figure 3. ToF-SIMS mass spectra for negatively charged fragments, which can be assigned to carbon, NCM, and transition metal sulfides. Shown are measurements on the composite cathode surface. The primary ion gun was operated in spectrometry mode (bunched mode) by using Bi_3^+ (25 keV) as primary ion species. Five mass spectra were measured for each sample to ensure reproducibility of the results and to discuss the dependence of the mass spectra on the position of the measurement spot. Accordingly, the cycled composite cathode without VGCF shows the strongest dependence on the spot position for all samples. Carbon and NCM signals tend to decrease due to battery cycling, indicating a degradation layer formation on NCM and VGCF. Accordingly, the degradation layer shields the analysis beam from the NCM and VGCF under static measurement conditions. At the same time, we do not see evidence for the formation of transition metal sulfides, since such fragments tend to decrease due to battery cycling.

The P 2p detail spectra of the three reference samples show no significant differences. The detail spectra of the uncycled cathodes and the β-Li_3PS_4 reference can be described using two doublets. The main component at 132.0 eV can be assigned to the PS_4^{3-} units of the β-Li_3PS_4 structure.[20] A further contribution can be seen at 133.0 eV in the signal shoulder at higher binding energies. Analogous to observations with other thiophosphates, this contribution can be attributed to P_2S_5, P_2S_n and Li_3PO_4.[19,24,27] In the case of both uncycled cathodes, this contribution increases slightly compared to the β-Li_3PS_4 reference indicating a reaction due to the mere NCM622/SE contact. Analogous to our previous work, we think that this is mainly due to the formation of phosphates such as Li_3PO_4 in the NCM622/SE interfacial region, which is supported by the O 1s signal (see the Supporting Information) and our ToF-SIMS data (see below).[19] This is in good agreement with a report by Xiao et al., who have suggested, based on calculations, that the mere contact between NCM (fully lithiated)/Li_3PS_4 can already lead to the formation of Li_3PO_4.[30] In addition, it is known from the literature that NCM materials generally tend to take up moisture rapidly and the surface composition of Ni-rich NCM materials strongly depends on aging effects, which can lead to the formation of carbonates.[31−33] Therefore, it is also conceivable that despite material drying, oxygen-containing surface species remain on the NCM surface and react with the SE forming Li_3PO_4. ToF-SIMS imaging on FIB crater sidewalls confirms small local enrichments of phosphate fragments (PO_x^-) in the NCM622/SE interfacial region before battery cycling (see Figure 5). However, the increase in signal intensity due to the mere NCM/SE contact is relatively weak (near the XPS detection limit), indicating that only small amounts are formed.

In contrast, battery cycling leads to a strong rise in signals at higher binding energies. The binding energy range indicates the formation of P_2S_n species, Li_3PO_4 (both are in the same binding energy range, green signal) and transition metal phosphates (red signal) such as $Ni_3(PO_4)_2$, $Mn_3(PO_4)_2$.[19,24,34−36] Using VGCF significantly increases the fraction of such species. The O 1s detail spectra (see Figure S3) also show an increase in signals in the range of phosphates due to battery cycling, thus supporting the assumption of phosphate formation. At the same time, the O 1s signal at 529.4 eV, which can be assigned to the lattice oxygen of the NCM, disappears.[37] This is due to the formation of a degradation layer at the NCM622/SE interface.[19] The degradation layer formation takes place at the NCM622 secondary particle surface. Because of the surface sensitivity of XPS, the lattice oxygen signal can hardly be detected above a certain layer thickness (roughly ∼10 nm), which explains the weakening of the signal.

At this point we conclude that using VGCF increases the amount of degradation products drastically, and it seems that VGCF promotes the formation of long-chain polysulfides during battery cycling. However, it is not yet clear whether the increase in the amount of degradation products can be due to their formation at the VGCF/SE interface or simply due to the fact that more NCM secondary particles are addressed within the composite cathode. Indeed, a higher utilization of active material corresponds to more reaction sites (more reactive NCM/SE interfaces), resulting in more reaction products.

To check the reactivity of the VGCF/SE interface, CV experiments with a VGCF/SE composite were performed similar to a study by Dewald et al. (see the Supporting Information).[18] The VGCF/SE ratio of the composite is analogous to the composite cathode with VGCF. The aim of this experiment was to test whether an applied potential leads to decomposition reactions at the VGCF/SE interface. Therefore, the VGCF/SE composite was investigated before and after the CV experiment by XPS analogously to the previous samples. The detail spectra of the S 2p, the P 2p, and the O 1s signal are shown in Figure S5. The detail spectra show a similar decomposition behavior compared to the composite cathodes (Figure 2A), indicating polysulfide formation in the VGCF/SE composite. These observations are consistent with studies by Dewald et al. and a recent report by Nagai et al. in the context of Li−S SSBs.[18,26] In addition, the P 2p signal

https://dx.doi.org/10.1021/acs.chemmater.0c01825
Chem. Mater. 2020, 32, 6123−6136

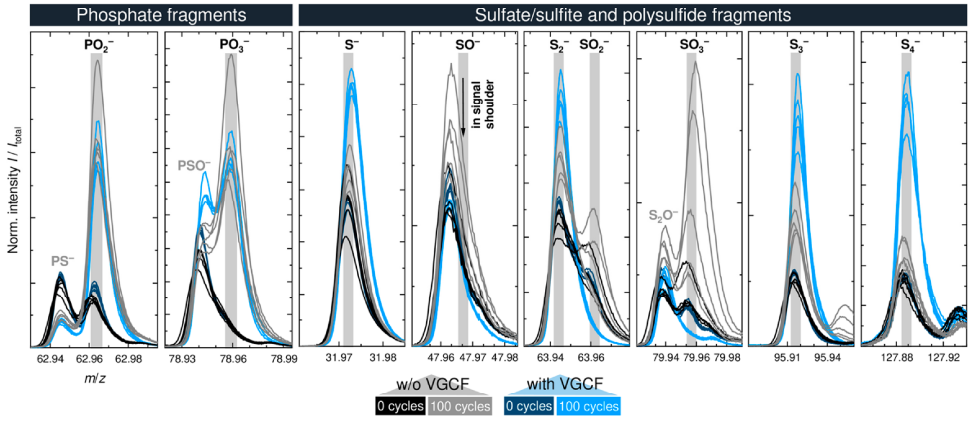

Figure 4. ToF-SIMS mass spectra for fragments that can be assigned to phosphates, sulfates/sulfites, and polysulfides. Shown are measurements of the composite cathode surface. Battery cycling leads in both cases (with and without VGCF, light blue and gray) to an increase in fragments that can be assigned to phosphates. At the same time, the PS^- fragment decreases, indicating damage in the anion lattice of the SE in both cases. Interestingly, sulfate/sulfite fragments (SO_2^- and SO_3^-) increase after battery cycling without VGCF, whereas they nearly vanish with VGCF. Signals for fragments which indicate polysulfides (S_2^-, S_3^-, S_4^- are shown in Figure 4; S_6^-, and S_8^- are shown in the Supporting Information) increase in both cases but are more pronounced in the case with VGCF.

shows a slight increase of species in the higher binding energy range. Next to the possibility of formation of P_2S_n species according to previous studies for other thiophosphates, we assume that oxygen-containing species on the VGCF surface (−OH groups, carbonates, and water residuals) lead to the formation of small amounts of phosphates such as Li_3PO_4.[19,24,35] Park et al. have already pointed out that functional groups on carbon additives are directly involved in side reactions with thiophosphate-based SEs, which further supports this assumption.[38] The formation of Li_3PO_4 formation is also indicated by an increase of the corresponding signal in the O 1s detail spectrum after the CV experiment (see Figure S5). Overall, we conclude that strong decomposition reactions (mainly polysulfide formation) occur at the VGCF/SE interface. Therefore, the increase in decomposition products in XP spectra by using VGCF can be in part attributed to decomposition reactions in the VGCF/SE interfacial region.

Post-Mortem Analysis by Time-of-Flight Secondary Ion Mass Spectrometry (ToF-SIMS). ToF-SIMS measurements were performed to verify the XPS results and to obtain complementary insight into the decomposition reactions. Measurements on the sample surface as well as depth profiling and analysis on FIB crater sidewalls were performed to obtain a reliable overall picture of the degradation processes.

First, measurements were performed on the sample surface. We measured five mass spectra per sample in different areas on the surface to ensure reproducibility of the results and to discuss the dependence of the results on the position of the measurement spot. We note that in this area the degradation processes at the three interfaces (current collector/SE, NCM/SE, and VGCF/SE) overlap. Figure 3 shows mass spectra of negatively charged fragments that can be assigned to carbon, NCM, and transition metal sulfides. Concerning NCM fragments, these tend to disappear due to battery cycling. Analogous to the XPS results, this indicates a degradation layer formation on the NCM secondary particle surface. Accordingly, the degradation layer shields the NCM surface from the analysis beam, which decreases the amount of detected NCM fragments.[19] It is noticeable that with VGCF the NCM signals disappear for all measurements reproducibly, while without VGCF the dependence on the position of the measurement spot is larger. This can be explained by a higher utilization of active material with the use of VGCF. We assume that almost all NCM particles are electronically connected using VGCF. Accordingly, the degradation layer forms at almost all NCM/SE interfaces. Without VGCF, however, statistically not all NCM particles are electronically connected, so that interfacial reactions do not occur at all secondary particle surfaces. For this reason, the measurements for the cycled sample without VGCF show a greater analysis area dependence for NCM fragments. Interestingly, carbon fragment signals such as C^- and C_2^- also decrease due to battery cycling. Again, this indicates a decomposition reaction at the VGCF/SE interface that shields the VGCF from the analysis beam. In the case of samples without VGCF, the carbon fragments are mainly caused by impurities such as adsorbed hydrocarbons. In this context it must be noted that SIMS is a semiquantitative method that does not allow direct conclusions on the absolute concentration from the signal intensity. However, assuming a comparable average matrix, semiquantitative conclusions are possible.

Our XPS and ToF-SIMS data do not provide clear evidence for the formation of transition metal sulfides and phosphides. In the case of XPS measurements, it is conceivable that the relatively high detection limit is problematic due to low product quantities. In the ToF-SIMS mass spectra, transition metal sulfide fragments such as NiS^- or NiS_2^- could be detected due to the higher detection sensitivity of ToF-SIMS (see Figure 3). However, it cannot be clearly distinguished here whether these species are already formed by a reaction of the mere NCM/SE contact or whether they are formed during the analysis by the collision cascade of the analysis beam in the interfacial region. Nevertheless, battery cycling seems to lead by trend to a decrease in the signal intensity of these species. Because such species were not detectable in XP spectra, we assume small quantities.

https://dx.doi.org/10.1021/acs.chemmater.0c01825
Chem. Mater. 2020, 32, 6123−6136

Phosphate indicating fragments (PO_x^- with $2 \leq x \leq 3$) increase significantly due to battery cycling, independent of VGCF (Figure 4). For the uncycled references, the weak PO_x^- signals are probably due to Li_3PO_4, which can be formed at the NCM/SE interface (see Figure 5). Furthermore, it can be seen

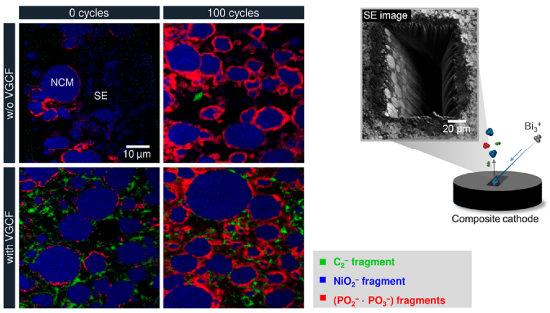

Figure 5. ToF-SIMS measurements on 45° crater sidewalls for cycled and uncycled composite cathodes with and without VGCF. On the right side, a scheme of the crater analysis is shown with a secondary electron (SE) image of a FIB crater. On the left side, secondary ion images of the crater sidewalls are shown. In the secondary ion images, the individual components (NCM, VGCF, and the degradation layer) can be clearly distinguished from each other by their specific fragments. Weak phosphate fragments intensities (red) are already detected in the uncycled composite cathodes. A significant increase in phosphate fragments can be seen as a result of cell cycling in both cases (with and without VGCF). ROI analyses support the conclusion of an increase in phosphate and polysulfide fragments also for the bulk material (see the Supporting Information).

that the signal intensity of the PS^- fragment decreases due to cell cycling. The lower formation probability of the PS^- fragment indicates that fewer P−S units are present in the anion lattice after battery cycling, which suggests a change in the anion lattice and further indicates the SE decomposition.

In addition to phosphate fragments, the detection of sulfate/sulfite fragments (SO_x^-) in relation to cell degradation in thiophosphate-based ASSBs has already been shown in previous studies.[19,39] Figure 4 shows the mass ranges of SO_x^- fragments for the composite cathodes. Already for the uncycled references weak SO_x^- signals were detected. Small amounts of Li_2SO_4 seem reasonable for this, since Li_2SO_4 can be formed by decomposition reactions of the SE but has also been detected in nanopores of NCM primary particles.[40] However, these species can only be detected due to the high sensitivity of ToF-SIMS, while they remain undetected in the S 2p spectra due to the higher detection limit of XPS. Therefore, small quantities (~ppm range) can be assumed. For the composite cathode without VGCF, an increase in SO_x^- fragments was detected after cell cycling. Interestingly, with VGCF in the composite cathode, the intensity of SO_x^- fragment signals decreases significantly and even falls below the values for the uncycled references. The formation of sulfates/sulfites does not seem to be preferred in this case, and sulfates/sulfites appear to be rather intermediate products. Analogous observations for SO_x^-, PO_x^-, and PS^- fragments were made in the depth profiles, which confirm these results also for the bulk material (see Figure S6).

To verify the polysulfide formation indicated by XPS measurements, S_x^- fragments were checked as a function of the chain length x. Two major observations can be derived from this: First, in both cases (with and without VGCF) signal intensities for S_x^- fragments with longer chains increase due to battery cycling. Second, by using VGCF, the signal intensity for such signals increases significantly. This is a strong indication that battery cycling leads to the formation of long-chain sulfur compounds and that carbon additives further increase the amount of polysulfides formed. This is the first direct evidence for polysulfide formation using ToF-SIMS, which is possible because the analysis beam (Bi_3^+ cluster) allows a relatively gentle removal of the $-[S]_n-$ species with low fragmentation. In contrast, the fragmentation of polysulfides is enhanced in depth profiling experiments due to the high impact of the Cs^+ sputter species. Nevertheless, these trends could also be observed in depth profiles (see Figure S6).

In the next step, analyses on FIB crater sidewalls were performed to obtain information about the local fragment distribution with high lateral resolution. The local distribution of fragments allows more precise statements on the degradation compounds and their origins. Figure 5 shows RGB overlays of secondary ion images of the crater sidewalls. In blue the local distribution of the NiO_2^- signal is shown representing the NCM material. Green color shows fragments that are mainly attributed to the conductive additive VGCF. In red, PO_x^- fragments are shown, which represent degradation products.

The structure of the composite cathode is analyzed very well by high lateral resolution mass spectrometric imaging. Accordingly, the SE, the NCM secondary particles, the conductive additive, and the degradation layer (represented by PO_x^- fragments) are distinguished easily. First, it can be seen that the mere contact of NCM and SE already leads to the formation of phosphates in the interfacial region. To a certain extent, the formation of the phosphate fragments could be due to the impact of the FIB during the cater milling process and/or the induced collision cascade in the interfacial region during the analysis with the primary ion beam. Both can lead to material mixing effects at the interface, resulting in the detection of these fragments. However, the size of the local enrichments is large and their distribution is random, so we can assume that these effects have only a minor influence. The formation of small amounts of phosphates such as Li_3PO_4 in the interfacial region seems much more likely. This is supported by the XPS measurements shown in Figure 2, in which a slight signal increase in binding energy range for phosphates is detected by the mere NCM/SE contact. Reactive surface species, dangling bonds, or water residuals (despite drying before cell assembly) could lead to the formation of such species in the interfacial region. In addition, Xiao et al. have shown by calculations that the mere NCM (fully lithiated)/Li_3PS_4 contact can already lead to a reaction with formation of Li_3PO_4.[30] However, a significant increase in PO_x^- fragments in the NCM/SE interfacial region can be observed after cell cycling, independent of the conductive additive. This clearly indicates a potential-induced interfacial reaction due to battery cycling. The local distribution of sulfate/sulfite fragments (SO_x^-) was investigated analogously to our previous work by multiplication of secondary ion images to eliminate mass interferences.[19] However, SO_x^- fragments show only weak signals at the NCM/SE interface and almost none within the SE. Accordingly, SO_x^- formation seems to be less pronounced compared to our results for the Li_6PS_5Cl argyrodite.[19]

https://dx.doi.org/10.1021/acs.chemmater.0c01825
Chem. Mater. 2020, 32, 6123−6136

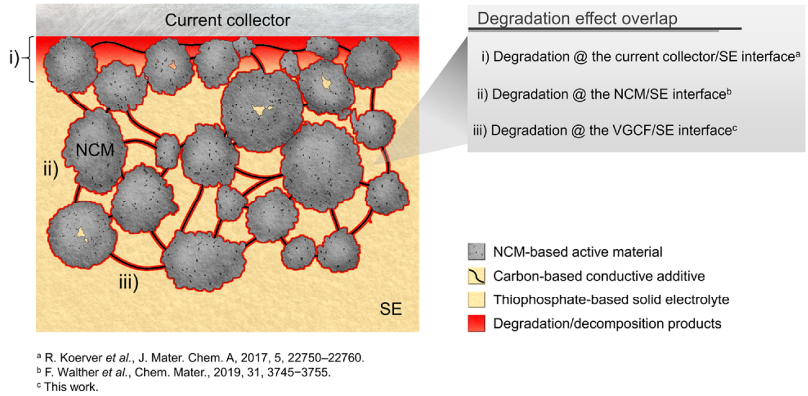

Figure 6. Scheme showing the overlapping degradation effects within the composite cathode based on NCM, thiophosphate SE, and carbon additives due to battery cycling. These include decomposition reactions at the interfaces of the SE toward (i) the current collector, (ii) the active material, and (iii) the carbon-based conductive additive. All interfaces must be addressed to prevent thiophosphate-based solid electrolytes from decomposition reactions.

A ROI analysis was applied to verify polysulfide formation during battery cycling (see the Supporting Information). For this purpose, the S_3^- and S_4^- fragments were used, which showed relatively small mass interferences with neighboring signals compared to other S_x^- fragments. In this context, it should be noted that the high-energy FIB generates a defect layer on the crater sidewall that needs to be removed before analysis. The FIB and the following cleaning step with the analysis beam in DC mode cause a relatively high fragmentation of the existing compounds similar to the depth profiling experiments. Consequently, polysulfides break into smaller fragments, which makes the analysis of such fragments in the bulk material more difficult. Analogous to previous publications, a signal threshold (for S_3^- and S_4^- fragments) was used to define a ROI.[19,40] The total intensity of the respective fragment was determined for this ROI and normalized to the number of corresponding pixels. In this way, deviations due to different FIB cut planes within the composite cathode such as different NCM/SE ratios are minimized. Although fragmentation is highly critical for the analysis of polysulfides in the bulk material, the ROI analysis shows that the amount of long-chain S_x^- fragments tends to increase after battery cycling and thus confirms the XPS results and the ToF-SIMS surface analysis.

■ DISCUSSION

In the following, the main findings from the Results section are summarized and discussed in relation to the literature. First, we discuss the electrochemical studies. Afterward, we address the results of the XPS and ToF-SIMS analyses and consider the influence of the mere contact of the composite components followed by the influence of battery cycling and the role of VGCF. Finally, an overall degradation scheme of the composite cathode is presented, and we hypothesize a reaction scheme for the NCM/SE interfacial reaction during charging (NCM delithiation) based on our experimental work.

Influence of VGCF on the ASSB Performance. Our electrochemical measurements show that using VGCF in the composite cathode leads to higher initial capacities compared to a corresponding ASSB without additives. However, because the capacity fade during cycling is increased, this initial advantage is not maintained over a higher number of cycles. We assume that the initial capacity increase by using VGCF can be attributed to two overlapping effects: On the one hand, more NCM secondary particles are electronically addressed by using VGCF, which leads to a higher utilization of the active material and thus to higher initial capacities. On the other hand, degradation reactions can take place on more NCM/SE interfaces and at the additionally introduced VGCF/SE interface, which can lead to further capacity contributions. The increase in side reactions is evident from the electrochemical studies as well as from the spectroscopic and spectrometric analyses and seems reasonable for the increased capacity fading. Accordingly, the promoted SE decomposition in the composite cathode ultimately leads to an increased negative influence on the Li-ion transport. In the literature, the redox activity of thiophosphate-based SEs has often been observed and described.[17,18,25−27] However, so far it is not completely clear whether the SEs themselves are redox-active and/or their decomposition products. In a recent study, Dewald et al. proposed that the often observed redox-active behavior of thiophosphate-based SE is rather dominated by the redox activity of the decomposition products.[18] The VGCF seems to further facilitate these decomposition reactions.

Influence of the Mere Contact between the Composite Materials. The mere contact between the composite materials does not seem to cause significant degradation (in terms of decomposition product concentrations). XPS measurements reveal a slight increase in species in the signal shoulders of the S 2p and P 2p signals at higher binding energies with and without the conductive additive. The origin of sulfur signals in this binding energy range is critically discussed and controversially interpreted for thiophosphate-based SE in the literature.[17,24,25,27] Based on the comprehensive analysis results of this work, polysulfide formation seems reasonable. This is indicated by the results for both uncycled composite cathodes which follow the trend shown in Figure 2C. However, because of the low concentrations and thus small signal changes, we cannot uniquely prove the origin of these sulfur signals here. Concerning phosphorus-containing compounds, Li_3PO_4 formation in the NCM/SE interfacial region seems reasonable, analogous to our previous study with Li_6PS_5Cl.[19] Corresponding signal contributions were detected in the P 2p and O 1s

https://dx.doi.org/10.1021/acs.chemmater.0c01825
Chem. Mater. 2020, 32, 6123−6136

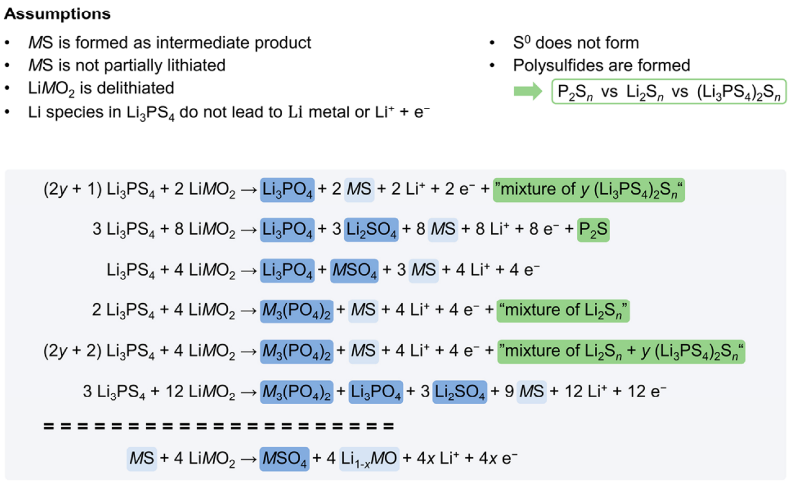

Figure 7. Reaction scheme for the electrochemically driven NCM/SE interfacial reaction during battery charging under the formation of transition metal sulfides (*MS*) as intermediate products. Basic assumptions for the reaction equations are given on the top. Reactions of the SE with the NCM material can lead to the formation of different phosphates, sulfates, and polysulfides. For the polysulfides (marked in green), various combinations with different sulfur chain length S_n are often possible to meet the stoichiometry. If this is the case, these species are labeled with the term "mixture of". Combinations of the equations can lead to an increase in polysulfide chain length.

spectra. Additionally, ToF-SIMS imaging analyses on FIB crater sidewalls reveal local PO_x^- fragments enrichments in the NCM/SE interfacial region. We assume that Li_3PO_4 can already be formed by a reaction of the SE with the pristine NCM material, which was also suggested by previous calculations.[30] In addition, a reaction of the SE with reactive surface species such as residual water (despite material drying) is conceivable, since NCM materials generally tend to take up moisture rapidly and the surface composition of NCM materials can be highly complex and depends strongly on the synthesis and aging effects.[31−33]

In contrast to computational studies and previous experimental work, we find no clear evidence of the formation of transition metal sulfides by the mere contact between NCM and the thiophosphate-based SE.[30,41−43] Jung and Gwon et al. reported a massive change in XP spectra for uncoated NCM materials, which we cannot confirm.[41] We were able to detect transition metal sulfide fragments such as NiS^- or NiS_2^- in the ToF-SIMS mass spectra due to the high detection sensitivity of the method, but we cannot clearly distinguish here whether these species are already formed by a reaction of the mere NCM/SE contact, whether they occur as reaction intermediates, or whether they are due to the collision cascade in the interfacial region induced by the analysis beam. Because such species are not visible in our XP spectra, we assume only small quantities below the XPS detection limit. The conclusions of Jung and Gwon et al. are based on XP spectra taken from the composite cathode surface. Because these species were not detected after surface sputtering, surface effects cannot be excluded, which may result in an incorrect energy calibration and thus to a misleading interpretation of the XPS data, as Maibach et al. have already shown.[21] However, the influence of aging effects was not the main focus of this work and cannot be adequately discussed here.

Influence of Battery Cycling. The results of this work extend the existing knowledge about degradation processes in thiophosphate-based composite cathodes by the influence of carbon additives. To provide a thorough understanding and stimulate further discussion, we condense the results into the degradation schemes shown in Figures 6 and 7. According to Figure 6, degradation reactions of the SE take place independently at its interface with the current collector, the active material, and the conductive additive. With regard to the individual reaction mechanisms, it must be noted that, analogous to LIBs, decomposition reactions do not take place along a single reaction path. Rather, the composition of the respective degradation layer can change dynamically—the redox activity of the decomposition products is only one example in this context. The buildup of concentration gradients, electric fields, and resistance-induced generation of heat, to name a few, can have a massive influence on the direction and the equilibrium of reactions and can lead to local composition differences in the composite. Accordingly, the reaction in areas where decomposition paths clearly overlap (e.g., toward the current collector) can differ significantly from the other areas, since the reaction conditions are different.

Taking these considerations into account, several conclusions about the degradation mechanisms are possible. With regard to sulfur-containing decomposition products, our results show two dominant degradation paths: (i) sulfate/sulfite formation and (ii) formation of polysulfide species.

The sulfate/sulfite formation inevitably requires an oxygen source. The detection of these species is therefore mainly related to their locally restricted formation in the NCM/SE interface region. For the ASSB without VGCF, ToF-SIMS measurements confirm an increase in SO_x^- fragments at the NCM/SE interface region due to battery cycling analogous to previous results.[19,39] Interestingly, by using VGCF this is not the case, and sulfur-containing decomposition products are mainly related to polysulfide formation. In general, based on quantitative analysis, polysulfide formation appears to be dominant/preferred in both cases, with and without carbon additives. Our results show that a stronger degradation is associated with an increased amount of polysulfides and longer

https://dx.doi.org/10.1021/acs.chemmater.0c01825
Chem. Mater. 2020, 32, 6123−6136

-[S]$_n$- units. They also indicate that the polysulfide formation takes place in all interfacial regions within the composite cathode. Therefore, we assume that the increased formation of polysulfides by using VGCF is, on the one hand, due to the higher active material utilization leading to more reacted NCM622/SE interfaces and, on the other hand, due to the additionally introduced degradation reactions at the VGCF/SE interface. The latter agrees very well with recent reports on reactions at carbon/thiophosphate interfaces, which show the importance of considering these interfaces.[18,26,38] Similar to a study by Nagai et al. for solid-state Li−S batteries, our results indicate that the formation and cleavage of S−S bonds play an important role in NCM-based composite cathodes.[26] Because the amount of polysulfides and the mean -[S]$_n$- chain length rise with stronger degradation, formation and cleavage seem to be partially irreversible within the used potential range, which increasingly leads to greater damage of the SE. The exact structure of the polysulfides cannot be clarified here since the detection is based on long-chain -[S]$_n$- units. As already mentioned, polymerization and oligomerization of P_2S_n, Li_2S_n, and $(Li_3PS_4)_2S_n$ has already been discussed.[17,19,24−26]

In contrast to computational studies and experimental work, we do not have a clear experimental evidence of the formation of transition metal sulfides after battery cycling.[30,42−44] ToF-SIMS mass spectra of surface analyses showed a decrease in signal intensity of transition metal sulfide fragments, whereas no signals were detectable in XP spectra due to the comparatively high detection limit. We think that the thermodynamically preferred path should involve the formation of transition metal sulfides in a metathesis type reaction, as suggested by calculations.[30,42,43] However, on the basis of our results, we assume that the transition metal sulfides are formed as intermediate products that then further react into sulfates upon oxidation, which could explain their low quantities in our experimental data.

With regard to phosphorus-containing decomposition products, our results indicate that phosphate formation is dominant, regardless of whether a conductive additive is used or not. Our XPS results show a rise in signals which can be attributed to phosphates such as Li_3PO_4, $Ni_3(PO_4)_2$, and $Mn_3(PO_4)_2$.[34−36] Comprehensive ToF-SIMS analyses confirm the formation of phosphates due to battery cycling and show that the formation occurs mainly locally in the NCM/SE interfacial region (see Figure 5), thus further supporting the XP signal assignments. This fits well with previous experimental results and computational studies that show a strong tendency of the interfacial reaction of oxides and thiophosphates to form PO_4^--containing compounds.[19,30,39,42,43,45] Concerning Li_3PO_4, our data also indicate a small contribution from the VGCF/SE interface (see the Supporting Information). We assume that despite material drying, this is caused by oxygen-containing species on the VGCF surface (−OH groups, carbonates, and water residuals). These can react with the SE under the formation of Li_3PO_4. This is supported by a study by Park et al., which shows that functional groups on carbon additives are directly involved in side reactions with thiophosphate-based SEs.[38] However, since the oxygen source on the VGCF surface is limited, the phosphate signals are dominated by the NCM/SE interfacial reaction. Therefore, the increase of these phosphate species in XP spectra and ToF-SIMS depth profiles (see the Supporting Information) by using VGCF can mainly be related to a higher utilization of NCM622 secondary particles, resulting in more reacted NCM622/SE interfaces.

Taking all results into account, we hypothesize the reactions in Figure 7 for the NCM/SE interfacial reaction during charging. These equations are the attempt to obtain a simplified degradation scheme, which can describe our experimental results in consideration of computational studies.[30,42,43] We want to emphasize here that we do not aim to postulate specific stoichiometries but rather give an indication for the complex interfacial reactions. We assume that the thermodynamically preferred path of the NCM/SE interfacial reaction involves the formation of transition metal sulfides as intermediate products, as suggested by calculations, which ultimately would lead to the observed phosphates due to a metathesis-type reaction.[30,42,43] For simplification, here we choose MS for transition metal sulfides, $M_3(PO_4)_2$ for transition metal phosphates, and MSO_4 for transition metal sulfates. As already mentioned, other stoichiometries and oxidation states are also conceivable. Additionally, we consider the formation of Li_3PO_4 and Li_2SO_4 in our reaction scheme, which are energetically preferred reaction products according to calculations.[30,42,43] Because we cannot distinguish experimentally between the polysulfides P_2S_n, Li_2S_n, and $(Li_3PS_4)_2S_n$, we hypothesize equations with different polysulfide species. Further assumptions can be seen in Figure 7.

Figure 7 indicates many possibilities for the formation of phosphates, which fits well with calculations showing a strong tendency of forming PO_4^--containing compounds.[30,42,43,45] With regard to sulfur-containing decomposition products, sulfates and polysulfides can be seen next to the formation of transition metal sulfides as intermediate products. By combining several equations, polysulfides with longer sulfur chains are possible, which corresponds to our experimental observation.

We assume that the intermediate phases of transition metal sulfides can react further with $LiMO_2$ to form transition metal sulfates and a rock-salt-like NiO phase upon oxidation. The formation of a rock-salt-like phase seems plausible because this is a well-known degradation phenomenon for NCM materials.[40,46] In addition, Jung and Kim et al. demonstrated very recently the formation of a rock-salt-like phase for Ni-rich cathode active materials in thiophosphate-based ASSBs by using ex-situ transmission electron microscopy.[47]

An analogous reaction scheme can be set up, which leads directly to the formation of the rock-salt-like NiO phase (see Figure S9). However, as mentioned above, it is likely that the thermodynamically preferred path should involve the formation of transition metal sulfides as intermediate products.

Finally, we want to emphasize that the degradation picture given in Figure 6 must necessarily be considered when analyzing degradation mechanisms in composite cathodes to avoid misinterpretations due to the convoluted degradation processes. For example, an XPS analysis to identify decomposition products in the NCM/SE interfacial region inevitably requires an initial surface cleaning step to minimize the influence of the current collector. Otherwise, the decomposition reaction toward the current collector would dominate the decomposition product signals.

■ CONCLUSIONS

We investigated the influence of the conductive additive VGCF in the composite cathode on the cell performance and the degradation phenomena in Li|β-Li_3PS_4|$LiNi_{0.6}Co_{0.2}$-

https://dx.doi.org/10.1021/acs.chemmater.0c01825
Chem. Mater. 2020, 32, 6123−6136

$Mn_{0.2}O_2$/β-Li_3PS_4 ASSB cells. Electrochemical studies revealed a higher initial capacity by using VGCF, which we attribute not only to a higher utilization of active material but also to a contribution from redox-active decomposition products of the SE. At the same time, however, the capacity fading during cycling was significantly increased, making the conductive additive detrimental for higher charge/discharge cycles. XPS and ToF-SIMS investigations showed that three independent degradation paths can be distinguished in the composite cathode. These include decomposition reactions at the interfaces of the SE toward (i) the current collector, (ii) the active material, and (iii) the carbon-based conductive additive. The decomposition reactions show a high degree of similarity. With regard to sulfur-containing decomposition products, sulfate/sulfite formation (e.g., Li_2SO_4 seems plausible) and polysulfide formation were observed. The latter seems to be dominant and could be directly verified for the first time by long-chain S_x^- fragments with ToF-SIMS. In the case of phosphorus-containing decomposition products, phosphate formation was dominant—Li_3PO_4 and transition metal phosphates seem reasonable. Finally, we proposed a reaction scheme for the $LiNi_{0.6}Co_{0.2}Mn_{0.2}O_2$/$\beta$-$Li_3PS_4$ interfacial reaction during battery charging. Overall, this work shows that all interfaces in the composite cathode must be independently addressed to prevent thiophosphate-based solid electrolytes from decomposition reactions. Accordingly, not only the modification of the active material by doping or coating strategies is necessary but also the optimization of the conductive additive to ensure a high utilization of the active material and a good cycling performance. This knowledge will help to design interfaces more specifically to further optimize composite cathodes on the way to high-capacity and long-term performance stable ASSBs. Furthermore, we demonstrate in this study the high suitability of the combination of the complementary methods XPS and ToF-SIMS for the investigation of degradation phenomena. We show that the respective method-related disadvantages can be compensated very well, making this method combination very powerful.

■ ASSOCIATED CONTENT

Supporting Information

The Supporting Information is available free of charge at https://pubs.acs.org/doi/10.1021/acs.chemmater.0c01825.

SEM images of the used NCM622 secondary particles and the β-Li_3PS_4 SE (both provided by BASF SE), charge and discharge curve for the first cycle of an ASSB with 3.8 wt % VGCF in the composite cathode, XP spectra of the O 1s, Li 1s, and C 1s signals for the (un)cycled composite cathodes and the β-Li_3PS_4 reference, cyclic voltammogram for a VGCF/SE composite, XP spectra of the S 2p, P 2p, and O 1s signals before and after the CV experiment of a VGCF/SE composite, negatively charged fragments from ToF-SIMS depth profiles and from surface analysis of (un)cycled composite cathodes, ROI analysis of secondary ion images of FIB crater sidewalls, reaction scheme for the NCM/SE interfacial reaction during charging with formation of a rock-salt-like NiO phase (PDF)

■ AUTHOR INFORMATION

Corresponding Authors

Marcus Rohnke − *Institute of Physical Chemistry and Center for Materials Research (LaMa), Justus Liebig University Giessen, D-35392 Giessen, Germany*; orcid.org/0000-0002-8867-950X; Email: Marcus.Rohnke@phys.Chemie.uni-giessen.de

Felix H. Richter − *Institute of Physical Chemistry and Center for Materials Research (LaMa), Justus Liebig University Giessen, D-35392 Giessen, Germany*; Email: Felix.H.Richter@phys.Chemie.uni-giessen.de

Wolfgang G. Zeier − *Institute of Physical Chemistry and Center for Materials Research (LaMa), Justus Liebig University Giessen, D-35392 Giessen, Germany*; orcid.org/0000-0001-7749-5089; Email: Wolfgang.G.Zeier@phys.Chemie.uni-giessen.de

Jürgen Janek − *Institute of Physical Chemistry and Center for Materials Research (LaMa), Justus Liebig University Giessen, D-35392 Giessen, Germany*; orcid.org/0000-0002-9221-4756; Email: Juergen.Janek@phys.Chemie.uni-giessen.de

Authors

Felix Walther − *Institute of Physical Chemistry and Center for Materials Research (LaMa), Justus Liebig University Giessen, D-35392 Giessen, Germany*

Simon Randau − *Institute of Physical Chemistry and Center for Materials Research (LaMa), Justus Liebig University Giessen, D-35392 Giessen, Germany*

Yannik Schneider − *Institute of Physical Chemistry and Center for Materials Research (LaMa), Justus Liebig University Giessen, D-35392 Giessen, Germany*

Joachim Sann − *Institute of Physical Chemistry and Center for Materials Research (LaMa), Justus Liebig University Giessen, D-35392 Giessen, Germany*

Complete contact information is available at: https://pubs.acs.org/10.1021/acs.chemmater.0c01825

Notes

The authors declare no competing financial interest.

■ ACKNOWLEDGMENTS

The authors acknowledge the financial support by BASF SE within the International Network for Batteries and Electrochemistry. We thank J. Kulisch and X. Wu for the valuable scientific exchange. Furthermore, the authors thank S.-K. Jung and H. Gwon for the fruitful discussion about their analytical results on decomposition processes due to the mere NCM/SE contact.[41]

■ REFERENCES

(1) Seino, Y.; Ota, T.; Takada, K.; Hayashi, A.; Tatsumisago, M. A Sulphide Lithium Super Ion Conductor Is Superior to Liquid Ion Conductors for Use in Rechargeable Batteries. *Energy Environ. Sci.* **2014**, 7 (2), 627−631.

(2) Janek, J.; Zeier, W. G. A Solid Future for Battery Development. *Nat. Energy* **2016**, *1* (9), 16141.

(3) Xu, W.; Wang, J.; Ding, F.; Chen, X.; Nasybulin, E.; Zhang, Y.; Zhang, J.-G. Lithium Metal Anodes for Rechargeable Batteries. *Energy Environ. Sci.* **2014**, 7 (2), 513−537.

(4) Ulvestad, A. A Brief Review of Current Lithium Ion Battery Technology and Potential Solid State Battery Technologies. 2018, arXiv:1803.04317. arXiv.org e-Print archive. https://arxiv.org/abs/1803.04317 (accessed May 2, 2020).

(5) Lee, Y.; Fujiki, S.; Jung, C.; Suzuki, N.; Yashiro, N.; Omoda, R.; Ko, D.; Shiratsuchi, T.; Sugimoto, T.; Ryu, S.; et al. High-Energy

Long-Cycling All-Solid-State Lithium Metal Batteries Enabled by Silver−Carbon Composite Anodes. *Nat. Energy* **2020**, *5* (4), 299−308.
(6) Goodenough, J. B.; Kim, Y. Challenges for Rechargeable Li Batteries. *Chem. Mater.* **2010**, *22* (3), 587−603.
(7) Lee, H.; Oh, P.; Kim, J.; Cha, H.; Chae, S.; Lee, S.; Cho, J. Advances and Prospects of Sulfide All-Solid-State Lithium Batteries via One-to-One Comparison with Conventional Liquid Lithium Ion Batteries. *Adv. Mater.* **2019**, *31* (29), 1−26.
(8) Randau, S.; Weber, D. A.; Kötz, O.; Koerver, R.; Braun, P.; Weber, A.; Ivers-Tiffée, E.; Adermann, T.; Kulisch, J.; Zeier, W. G.; et al. Benchmarking the Performance of All-Solid-State Lithium Batteries. *Nat. Energy* **2020**, *5* (3), 259−270.
(9) Bielefeld, A.; Weber, D. A.; Janek, J. Microstructural Modeling of Composite Cathodes for All-Solid-State Batteries. *J. Phys. Chem. C* **2019**, *123* (3), 1626−1634.
(10) Shi, T.; Tu, Q.; Tian, Y.; Xiao, Y.; Miara, L. J.; Kononova, O.; Ceder, G. High Active Material Loading in All-Solid-State Battery Electrode via Particle Size Optimization. *Adv. Energy Mater.* **2020**, *10* (1), 1902881.
(11) Strauss, F.; Bartsch, T.; De Biasi, L.; Kim, A. Y.; Janek, J.; Hartmann, P.; Brezesinski, T. Impact of Cathode Material Particle Size on the Capacity of Bulk-Type All-Solid-State Batteries. *ACS Energy Lett.* **2018**, *3* (4), 992−996.
(12) Zhang, W.; Weber, D. A.; Weigand, H.; Arlt, T.; Manke, I.; Schröder, D.; Koerver, R.; Leichtweiss, T.; Hartmann, P.; Zeier, W. G.; et al. Interfacial Processes and Influence of Composite Cathode Microstructure Controlling the Performance of All-Solid-State Lithium Batteries. *ACS Appl. Mater. Interfaces* **2017**, *9* (21), 17835−17845.
(13) Zhang, W.; Leichtweiß, T.; Culver, S. P.; Koerver, R.; Das, D.; Weber, D. A.; Zeier, W. G.; Janek, J. The Detrimental Effects of Carbon Additives in $Li_{10}GeP_2S_{12}$-Based Solid-State Batteries. *ACS Appl. Mater. Interfaces* **2017**, *9* (41), 35888−35896.
(14) Yoon, K.; Kim, J.-J.; Seong, W. M.; Lee, M. H.; Kang, K. Investigation on the Interface between $Li_{10}GeP_2S_{12}$ Electrolyte and Carbon Conductive Agents in All-Solid-State Lithium Battery. *Sci. Rep.* **2018**, *8* (1), 1−7.
(15) Strauss, F.; Stepien, D.; Maibach, J.; Pfaffmann, L.; Indris, S.; Hartmann, P.; Brezesinski, T. Influence of Electronically Conductive Additives on the Cycling Performance of Argyrodite-Based All-Solid-State Batteries. *RSC Adv.* **2020**, *10* (2), 1114−1119.
(16) Deng, S.; Sun, Y.; Li, X.; Ren, Z.; Liang, J.; Doyle-Davis, K.; Liang, J.; Li, W.; Norouzi Banis, M.; Sun, Q.; et al. Eliminating the Detrimental Effects of Conductive Agents in Sulfide-Based Solid-State Batteries. *ACS Energy Lett.* **2020**, *5*, 1243−1251.
(17) Koerver, R.; Walther, F.; Aygün, I.; Sann, J.; Dietrich, C.; Zeier, W. G.; Janek, J. Redox-Active Cathode Interphases in Solid-State Batteries. *J. Mater. Chem. A* **2017**, *5* (43), 22750−22760.
(18) Dewald, G. F.; Ohno, S.; Kraft, M. A.; Koerver, R.; Till, P.; Vargas-Barbosa, N. M.; Janek, J.; Zeier, W. G. Experimental Assessment of the Practical Oxidative Stability of Lithium Thiophosphate Solid Electrolytes. *Chem. Mater.* **2019**, *31* (20), 8328−8337.
(19) Walther, F.; Koerver, R.; Fuchs, T.; Ohno, S.; Sann, J.; Rohnke, M.; Zeier, W. G.; Janek, J. Visualization of the Interfacial Decomposition of Composite Cathodes in Argyrodite-Based All-Solid-State Batteries Using Time-of-Flight Secondary-Ion Mass Spectrometry. *Chem. Mater.* **2019**, *31* (10), 3745−3755.
(20) Koerver, R.; Aygün, I.; Leichtweiß, T.; Dietrich, C.; Zhang, W.; Binder, J. O.; Hartmann, P.; Zeier, W. G.; Janek, J. Capacity Fade in Solid-State Batteries: Interphase Formation and Chemomechanical Processes in Nickel-Rich Layered Oxide Cathodes and Lithium Thiophosphate Solid Electrolytes. *Chem. Mater.* **2017**, *29* (13), 5574−5582.
(21) Maibach, J.; Lindgren, F.; Eriksson, H.; Edström, K.; Hahlin, M. Electric Potential Gradient at the Buried Interface between Lithium-Ion Battery Electrodes and the SEI Observed Using Photoelectron Spectroscopy. *J. Phys. Chem. Lett.* **2016**, *7* (10), 1775−1780.
(22) Lindgren, F.; Rehnlund, D.; Källquist, I.; Nyholm, L.; Edström, K.; Hahlin, M.; Maibach, J. Breaking Down a Complex System: Interpreting PES Peak Positions for Cycled Li-Ion Battery Electrodes. *J. Phys. Chem. C* **2017**, *121* (49), 27303−27312.
(23) Moulder, J. F.; Stickle, W. F.; Sobol, P. E.; Bomben, K. D. *Handbook of X-Ray Photoelectron Spectroscopy; A Reference Book of Standard Spectra for Identification and Interpretation of XPS Data*; Chastain, J., King, Jr., R. C., Eds.; Physical Electronics: Eden Prairie, MN, 1995.
(24) Auvergniot, J.; Cassel, A.; Ledeuil, J. B.; Viallet, V.; Seznec, V.; Dedryvère, R. Interface Stability of Argyrodite Li_6PS_5Cl toward $LiCoO_2$, $LiNi_{1/3}Co_{1/3}Mn_{1/3}O_2$, and $LiMn_2O_4$ in Bulk All-Solid-State Batteries. *Chem. Mater.* **2017**, *29* (9), 3883−3890.
(25) Auvergniot, J.; Cassel, A.; Foix, D.; Viallet, V.; Seznec, V.; Dedryvère, R. Redox Activity of Argyrodite Li_6PS_5Cl Electrolyte in All-Solid-State Li-Ion Battery: An XPS Study. *Solid State Ionics* **2017**, *300*, 78−85.
(26) Nagai, E.; Arthur, T. S.; Bonnick, P.; Suto, K.; Muldoon, J. The Discharge Mechanism for Solid-State Lithium-Sulfur Batteries. *MRS Adv.* **2019**, *4* (49), 2627−2634.
(27) Tan, D. H. S.; Wu, E. A.; Nguyen, H.; Chen, Z.; Marple, M. A. T.; Doux, J.; Wang, X.; Yang, H.; Banerjee, A.; Meng, Y. S. Elucidating Reversible Electrochemical Redox of Li_6PS_5Cl Solid Electrolyte. *ACS Energy Lett.* **2019**, *4* (10), 2418−2427.
(28) de Biasi, L.; Schwarz, B.; Brezesinski, T.; Hartmann, P.; Janek, J.; Ehrenberg, H. Chemical, Structural, and Electronic Aspects of Formation and Degradation Behavior on Different Length Scales of Ni-Rich NCM and Li-Rich HE-NCM Cathode Materials in Li-Ion Batteries. *Adv. Mater.* **2019**, *31* (26), 1900985.
(29) *NIST X-Ray Photoelectron Spectroscopy Database*; National Institute of Standards and Technology: Gaithersburg, MD, 2000.
(30) Xiao, Y.; Miara, L. J.; Wang, Y.; Ceder, G. Computational Screening of Cathode Coatings for Solid-State Batteries. *Joule* **2019**, *3* (5), 1252−1275.
(31) Xiong, X.; Wang, Z.; Yue, P.; Guo, H.; Wu, F.; Wang, J.; Li, X. Washing Effects on Electrochemical Performance and Storage Characteristics of $LiNi_{0.8}Co_{0.1}Mn_{0.1}O_2$ as Cathode Material for Lithium-Ion Batteries. *J. Power Sources* **2013**, *222*, 318−325.
(32) Liu, W.; Oh, P.; Liu, X.; Lee, M. J.; Cho, W.; Chae, S.; Kim, Y.; Cho, J. Nickel-Rich Layered Lithium Transition-Metal Oxide for High-Energy Lithium-Ion Batteries. *Angew. Chem., Int. Ed.* **2015**, *54* (15), 4440−4457.
(33) Jung, R.; Morasch, R.; Karayaylali, P.; Phillips, K.; Maglia, F.; Stinner, C.; Shao-Horn, Y.; Gasteiger, H. A. Effect of Ambient Storage on the Degradation of Ni-Rich Positive Electrode Materials (NMC811) for Li-Ion Batteries. *J. Electrochem. Soc.* **2018**, *165* (2), A132−A141.
(34) Franke, R.; Chassé, T.; Streubel, P.; Meisel, A. Data Bank - Auger Parameters and Relaxation Energies of Phosphorus in Solid Compounds. *J. Electron Spectrosc. Relat. Phenom.* **1991**, *56* (4), 381−388.
(35) Wang, B.; Liu, J.; Sun, Q.; Li, R.; Sham, T.-K.; Sun, X. Atomic Layer Deposition of Lithium Phosphates as Solid-State Electrolytes for All-Solid-State Microbatteries. *Nanotechnology* **2014**, *25* (50), 504007.
(36) Appapillai, A. T.; Mansour, A. N.; Cho, J.; Shao-Horn, Y. Microstructure of $LiCoO_2$ with and without "$AlPO_4$" Nanoparticle Coating: Combined STEM and XPS Studies. *Chem. Mater.* **2007**, *19* (23), 5748−5757.
(37) Bodenes, L.; Dedryvère, R.; Martinez, H.; Fischer, F.; Tessier, C.; Pérès, J.-P. Lithium-Ion Batteries Working at 85°C: Aging Phenomena and Electrode/Electrolyte Interfaces Studied by XPS. *J. Electrochem. Soc.* **2012**, *159* (10), A1739−A1746.
(38) Park, S. W.; Oh, G.; Park, J.; Ha, Y.; Lee, S.; Yoon, S. Y.; Kim, B. G. Graphitic Hollow Nanocarbon as a Promising Conducting Agent for Solid-State Lithium Batteries. *Small* **2019**, *15* (18), 1900235.
(39) Visbal, H.; Aihara, Y.; Ito, S.; Watanabe, T.; Park, Y.; Doo, S. The Effect of Diamond-like Carbon Coating on $LiNi_{0.8}Co_{0.15}Al_{0.05}O_2$

https://dx.doi.org/10.1021/acs.chemmater.0c01825
Chem. Mater. 2020, 32, 6123−6136

Particles for All Solid-State Lithium-Ion Batteries Based on $Li_2SeP_2S_5$ Glass-Ceramics. *J. Power Sources* **2016**, *314*, 85−92.
(40) Ahmed, S.; Pokle, A.; Schweidler, S.; Beyer, A.; Bianchini, M.; Walther, F.; Mazilkin, A.; Hartmann, P.; Brezesinski, T.; Janek, J.; et al. The Role of Intragranular Nanopores in Capacity Fade of Nickel-Rich Layered $Li(Ni_{1-x-y}Co_xMn_y)O_2$ Cathode Materials. *ACS Nano* **2019**, *13* (9), 10694−10704.
(41) Jung, S.-K.; Gwon, H.; Lee, S.-S.; Kim, H.; Lee, J. C.; Chung, J. G.; Park, S. Y.; Aihara, Y.; Im, D. Understanding the Effects of Chemical Reactions at the Cathode−Electrolyte Interface in Sulfide Based All-Solid-State Batteries. *J. Mater. Chem. A* **2019**, *7* (40), 22967−22976.
(42) Richards, W. D.; Miara, L. J.; Wang, Y.; Kim, J. C.; Ceder, G. Interface Stability in Solid-State Batteries. *Chem. Mater.* **2016**, *28* (1), 266−273.
(43) Nolan, A. M.; Zhu, Y.; He, X.; Bai, Q.; Mo, Y. Computation-Accelerated Design of Materials and Interfaces for All-Solid-State Lithium-Ion Batteries. *Joule* **2018**, *2* (10), 2016−2046.
(44) Jung, S. H.; Oh, K.; Nam, Y. J.; Oh, D. Y.; Brüner, P.; Kang, K.; Jung, Y. S. $Li_3BO_3 - Li_2CO_3$: Rationally Designed Buffering Phase for Sulfide All-Solid-State Li-Ion Batteries. *Chem. Mater.* **2018**, *30* (22), 8190−8200.
(45) Tang, H.; Deng, Z.; Lin, Z.; Wang, Z.; Chu, I.-H.; Chen, C.; Zhu, Z.; Zheng, C.; Ong, S. P. Probing Solid−Solid Interfacial Reactions in All-Solid-State Sodium-Ion Batteries with First-Principles Calculations. *Chem. Mater.* **2018**, *30* (1), 163−173.
(46) Jung, S.-K.; Gwon, H.; Hong, J.; Park, K.-Y.; Seo, D.-H.; Kim, H.; Hyun, J.; Yang, W.; Kang, K. Understanding the Degradation Mechanisms of $LiNi_{0.5}Co_{0.2}Mn_{0.3}O_2$ Cathode Material in Lithium Ion Batteries. *Adv. Energy Mater.* **2014**, *4* (1), 1300787.
(47) Jung, S. H.; Kim, U.; Kim, J.; Jun, S.; Yoon, C. S.; Jung, Y. S.; Sun, Y. Ni-Rich Layered Cathode Materials with Electrochemo-Mechanically Compliant Microstructures for All-Solid-State Li Batteries. *Adv. Energy Mater.* **2020**, *10* (6), 1903360.

https://dx.doi.org/10.1021/acs.chemmater.0c01825
Chem. Mater. 2020, 32, 6123−6136

3.3 Publication III: "The Working Principle of a Li_2CO_3/$LiNbO_3$ Coating on NCM for Thiophosphate-Based All-Solid-State Batteries"

In the third publication of this doctoral thesis, the effect of a Li_2CO_3/$LiNbO_3$-based protective CAM coating on the battery performance and the degradation processes within a thiophosphate-based composite cathode was investigated. For this purpose, composite cathodes based on NCM622/Li_6PS_5Cl/Super C65 were analyzed.

Although CAM coatings are a common strategy to address issues related to interfacial degradation and seem promising to increase the battery performance, the working principle often remains elusive, which makes it difficult to draw fundamental conclusions necessary to develop tailored protection concepts on the way to long-term stability in ASSBs. From an analytical point of view, this is mostly due to an insufficient pre-characterization of the coating and an insufficient separation of degradation processes within the composite cathode.

To meet these requirements, the coating microstructure was comprehensively characterized using a combination of FIB-SEM, XPS and ToF-SIMS and revealed a particulate coating (thickness ~15 nm) consisting of an amorphous $LiNbO_3$ core, a Li_2CO_3 shell and a low fraction of carbon-containing residues from the coating process. By means of in-depth post-mortem analyses using XPS and ToF-SIMS, it was shown that the CAM coating suppresses the interfacial chemical reaction at the CAM/SE interface. In particular, it was revealed that the improved ASSB performance is accompanied by a suppressed formation of oxygenated phosphorous and sulfur species.

Overall, publication III extends the knowledge on the working principle of protective CAM coatings considerably and contributes to a deeper understanding of the protective nature of coating materials in general.

The analytical approach developed in this work can easily be applied to other protective coatings and allows for the semi-quantitative benchmarking of the influence of protective coatings on the degradation processes in thiophosphate-based composite cathodes.

The experiments were designed and planned by the first author under the supervision of T. Brezesinski and J. Janek. F. Strauss prepared the ASSB cells and performed the electrochemical characterization. B. Mogwitz conducted the FIB-SEM analysis. J. Hertle prepared and provided the Li_2CO_3/$LiNbO_3$-coated reference sample. The first author performed the analytical measurements (XPS and ToF-SIMS) and the subsequent analysis and evaluation. The scientific discussion was stimulated by all authors. In particular, J. Sann and M. Rohnke assisted with scientific discussions on the XPS and ToF-SIMS data, respectively. The manuscript was written by the first author and edited by eight co-authors.

This study was part of the International Network for Batteries and Electrochemistry by BASF SE. The project was accompanied by J. Kulisch and X. Wu through scientific exchange. In particular, X. Wu contributed to the scientific discussions.

Reprinted with permission from Walther, F.; Strauss, F.; Wu, X.; Mogwitz, B.; Hertle, J.; Sann, J.; Rohnke, M.; Brezesinski, T.; Janek, J. The Working Principle of a Li_2CO_3/$LiNbO_3$ Coating on NCM for Thiophosphate-Based All-Solid-State Batteries. *Chem. Mater.* **2021**, *33* (6), 2110–2125. https://doi.org/10.1021/acs.chemmater.0c04660.

CHEMISTRY OF MATERIALS

pubs.acs.org/cm Article

The Working Principle of a $Li_2CO_3/LiNbO_3$ Coating on NCM for Thiophosphate-Based All-Solid-State Batteries

Felix Walther, Florian Strauss, Xiaohan Wu, Boris Mogwitz, Jonas Hertle, Joachim Sann, Marcus Rohnke, Torsten Brezesinski, and Jürgen Janek*

Cite This: *Chem. Mater.* 2021, 33, 2110–2125 Read Online

ACCESS | Metrics & More | Article Recommendations | Supporting Information

ABSTRACT: Large-scale industrial application of all-solid-state-batteries (ASSBs) is currently hindered by numerous problems. Regarding thiophosphate-based ASSBs, interfacial reactions with the solid electrolyte are considered a major reason for capacity fading. On the positive electrode side, cathode active material coating addresses these issues and improves the ASSB performance. Yet, the working principle of the coating often remains unclear, and protection concepts on the way to long-term stable ASSBs remain empirical. In this work, we characterize the influence of a $Li_2CO_3/LiNbO_3$ cathode active material coating on the battery performance and cathode degradation reactions of a $Li_4Ti_5O_{12}/Li_6PS_5Cl$/Super C65|$Li_6PS_5Cl$|$LiNi_{0.6}Co_{0.2}Mn_{0.2}O_2/Li_6PS_5Cl$/Super C65 cell. The coating microstructure is characterized comprehensively using a combination of focused ion beam scanning electron microscopy (FIB-SEM), X-ray photoelectron spectroscopy (XPS), and time-of-flight secondary ion mass spectrometry (ToF-SIMS). Based on this knowledge, we demonstrate and discuss the positive effect of the coating on the ASSB performance. Finally, we present an in-depth post-mortem analysis of composite cathodes by combining XPS depth profiling with ToF-SIMS. The $Li_2CO_3/LiNbO_3$ coating suppresses the interfacial reaction at the cathode active material/solid electrolyte interface, in particular, the formation of oxygenated phosphorous and sulfur compounds such as phosphates and sulfates/sulfites, leading to a significantly enhanced ASSB performance.

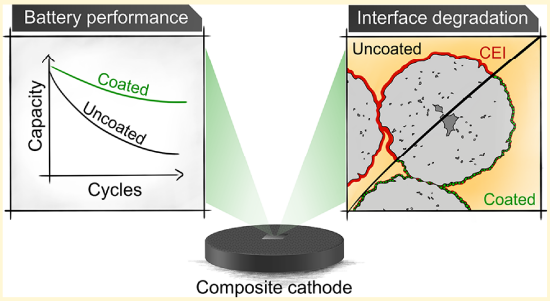

INTRODUCTION

All-solid-state batteries (ASSBs) are one of the most promising candidates for future energy storage devices.[1−5] They are considered to have many advantages over conventional energy storage systems. First, ASSBs may enable the use of lithium metal as an anode material, which could lead to energy storage devices with higher specific energies compared to conventional lithium-ion batteries (LIBs) based on liquid electrolytes.[6] Second, the cell design can be simplified, which enables the possibility of roll-to-roll cell production.[7] The latter is often considered to be mandatory for large-scale applications to make ASSBs economically more attractive. Third, the replacement of the flammable organic liquid electrolyte in LIBs can enhance safety, which makes ASSBs particularly attractive for the automotive sector, since safety is one of the most important arguments for marketing.[8,9]

Several classes of solid electrolytes can be distinguished and have already been tested for use in ASSBs.[10] Thiophosphates are considered as one the most promising candidates since they provide high ionic conductivities and can be processed readily due to their malleability.[11] However, problems, which are often associated with the stability of these materials, must be addressed and solved to enable the transfer from research status to large-scale application.[12,13]

Research efforts are currently ongoing in various fields to overcome problems related to ASSBs. Simulations deal with the detection of critical parameters for cell performance and the optimization of cell designs.[14−18] In the field of materials synthesis, novel anode/cathode materials and new solid electrolytes are being developed.[19,20] In addition, much research is done to clarify degradation phenomena and develop strategies to prevent them. With regard to thiophosphate-based composite cathodes, this mainly includes doping approaches of the solid electrolyte and the development of protective coatings for cathode active materials (CAM).[21−23] According to literature, the latter strategy seems promising to address interfacial issues and enhance the ASSB performance. However, the functionality of the CAM

Received: December 15, 2020
Revised: February 17, 2021
Published: March 3, 2021

https://dx.doi.org/10.1021/acs.chemmater.0c04660
Chem. Mater. 2021, 33, 2110−2125

modification often remains unclear.[21] From an analytical point of view, two main reasons can be derived as follows:

(i) Insufficient Characterization of the Coating

Knowledge about coating morphology and composition is needed to obtain a comprehensive picture of the microstructure. This in turn is mandatory to discuss the coating influence on the ASSB performance and the corresponding decomposition processes. However, the characterization of the coating microstructure is highly challenging due to the small dimensions of thin coatings (in the nanometer (nm) range) and the low material concentrations. Basically, a wide variety of analytical methods can be used to solve this task, but there is no analytical tool that can provide all the necessary information at once. Microscopic methods such as scanning electron microscopy (SEM) and transmission electron microscopy (TEM), for example, offer a very high spatial resolution, but they cannot intrinsically provide detailed information on the chemical composition. In contrast, spectroscopic methods such as X-ray photoelectron spectroscopy (XPS) and energy-dispersive X-ray spectroscopy (EDX) can provide detailed information on the chemical composition, but they suffer from relatively poor spatial resolution. Therefore, a combination of several methods is required. When selecting the methods, it is important to know the respective method-specific limits to compensate for them. Accordingly, a coating characterization by global investigations such as top-view SEM for morphological information and EDX for chemical information, for example, is not sufficient to comprehensively characterize the coating since only rough conclusions on morphological changes and the element distribution on the CAM particles are possible. In contrast, information on the spatially resolved coating microstructure (morphology and chemical composition) cannot be obtained in this way. Consequently, the effect of the coating on the battery performance is difficult to interpret and the reasons for the often-remaining capacity fade during battery cycling remain elusive.

(ii) Insufficient Separation of the Individual Degradation Processes in the Composite Cathode

The post-mortem analysis of composite cathodes is often insufficient to separate the individual decomposition contributions. Accordingly, it is often not clear on which part of the degradation in the composite cathode the coating has an influence. Walther *et al.* have very recently shown that global (i.e., integral) measurements on the (uncleaned) cathode surface make an interpretation of the results extremely difficult due to spatially convoluted decomposition processes, which in turn does not allow any conclusions to be drawn on the individual decomposition contributions.[24] As a result, the protective effect of a coating is generally related to the suppression of battery degradation processes (unspecific statements) or, what is basically worse, wrong conclusions are drawn due to the overlap of one or more degradation processes that occur in different areas of the cathode composite.

In this work, we investigate a $Li_2CO_3/LiNbO_3$ coating on $LiNi_{0.6}Co_{0.2}Mn_{0.2}O_2$ (NCM622). A $LiNbO_3$-based coating has been chosen since it is a well-established material for protective coatings in ASSBs and its positive effect on the battery performance has been widely demonstrated in literature.[21,25−27] We have combined $LiNbO_3$ with Li_2CO_3, as Li_2CO_3 is reported to be potentially beneficial for ternary lithium metal oxide coatings.[26,28] In addition, Ni-rich NCM materials are known to form carbonates on the surface depending on storage conditions and aging effects.[29,30] Therefore, we assume that the presence of Li_2CO_3 is inherently relevant when it comes to the interface reaction between the CAM and solid electrolyte. For these reasons, we have intentionally introduced Li_2CO_3 to the coating.

Although $LiNbO_3$-based coatings are well-established for ASSBs, the protective mechanism is still not yet fully understood. Thus, the aim of this work is to gain detailed insights into the working principle of such a protective coating. The focus of the study is on its influence on the interfacial decomposition processes between the CAM and thiophosphate-based solid electrolyte.

First, we characterize the microstructure of the coating, which includes the morphology and chemical composition. In general, TEM is a highly suitable technique for this task, especially in combination with EDX and/or electron energy loss spectroscopy (EELS). However, the sample preparation requires a relatively high effort and TEM investigations involve the risk of decomposition of radiation-sensitive compounds, like Li_2CO_3, which can only be partially compensated by measuring under cryogenic conditions. In addition, the results obtained are locally restricted to a relatively small analysis area, making it difficult to draw more general conclusions, e.g., on the overall coating coverage. Kim *et al.* already used the combination of TEM, EDX, and EELS to characterize the coating microstructure of a $Li_2CO_3/LiNbO_3$ hybrid coating.[26] Since the information obtained was limited to basic statements such as the local coating thickness and the element distribution, the authors had to apply additional techniques to gain further insights into the coating composition. Therefore, we develop here a different approach to gain a comprehensive picture of the coating microstructure. The characterization is mainly achieved by using a combination of focused ion beam scanning electron microscopy (FIB-SEM), X-ray photoelectron spectroscopy (XPS), and time-of-flight secondary ion mass spectrometry (ToF-SIMS). With this approach, we show that the coating is particulate and homogeneously distributed over the NCM622 secondary particle structure. In addition, we reveal its chemical composition and finally clarify the coating microstructure. Second, we demonstrate the positive influence of the $Li_2CO_3/LiNbO_3$ coating on the cycling performance of a $Li_4Ti_5O_{12}/Li_6PS_5Cl$/Super C65|$Li_6PS_5Cl$|NCM622/$Li_6PS_5Cl$/Super C65 cell. Third, a comprehensive post-mortem analysis is performed to characterize the influence of the CAM coating on the decomposition processes in the composite cathode using XPS and ToF-SIMS. We show that the CAM coating suppresses the interfacial reaction at the NCM622/solid electrolyte interface mainly in terms of phosphate and sulfate/sulfite formation. However, because it cannot be completely prevented, we still expect capacity fading due to reactions occurring at the CAM/solid electrolyte interface.

Overall, we demonstrate that ToF-SIMS in particular is very powerful to determine the influence of coatings on the interfacial decomposition processes and seems suited for benchmarking the effectiveness of protective CAM coatings in such composite cathodes on a semiquantitative basis.

EXPERIMENTAL SECTION

Preparation of ASSB Cells. *Materials.* NCM622 (d_{50} = 2.9 μm and d_{90} = 6.0 μm) powder (BASF SE) and Super C65 carbon black

https://dx.doi.org/10.1021/acs.chemmater.0c04660
Chem. Mater. 2021, 33, 2110−2125

(Timcal) were dried for 12 h in vacuum at 300 °C and then stored in an argon-filled glovebox (<0.1 ppm O_2, <0.1 ppm H_2O).[31] Li_6PS_5Cl solid electrolyte was prepared by milling 5 g of a stoichiometric mixture of a Li_2S (10 mol % deficiency), P_2S_5, and LiCl (Alfa Aesar; 99 + %) under an argon atmosphere for 1 h at 250 rpm first and then for 20 h at 450 rpm using a 250 mL zirconia jar containing 10 mm zirconia balls with a 30:1 ball-to-powder ratio. LiCl was dried in vacuum (~10^{-3} mbar) for ~12 h at 300 °C prior to usage. After milling, the powder was annealed in vacuum (~10^{-3} mbar) for 5 h at 300 °C. The room-temperature ionic conductivity of the resulting Li_6PS_5Cl solid electrolyte was ~2.0 mS/cm. Further details such as X-ray diffraction patterns can be found in a previous work.[32]

Coating Approach. The $Li_2CO_3/LiNbO_3$ coating was applied to the NCM622 according to a procedure published in literature.[25,26] Lithium ethoxide solution (1 M) was prepared by reacting absolute ethanol (Sigma-Aldrich; 99.8%) and Li metal (Albemarle Germany GmbH). For 0.5 M niobium ethoxide solution, $Nb(OCH_2CH_3)_5$ (Sigma-Aldrich; 99.95%) was dissolved in absolute ethanol. Note that the Li-to-Nb molar ratio was 2 to 1. The obtained powder was subsequently heated in air at 300 °C for 2 h (5 °C/min heating rate) and stored under an argon atmosphere for further use.

A coating reference was prepared analogously on a silicon wafer. The Li metal supplier for this sample was abcr GmbH. In this case, the Li-to-Nb molar ratio was 1 to 1 (for the stoichiometry $LiNbO_3$).

Material Characterization. Scanning electron microscopy (SEM) was performed using a LEO-1530 microscope (Carl Zeiss AG) to characterize the CAM in terms of particle size distribution and basic morphology (see the Supporting Information, Figure S1).

Attenuated total reflection-infrared spectroscopy (ATR-IR) was performed using an ALPHA FT-IR spectrometer (Bruker Corporation) equipped with a Ge crystal in an argon filled glovebox to confirm the presence of Li_2CO_3 in the coating material (see the Supporting Information, Figure S2). The spectra were collected using the OPUS software.

Preparation of Electrode Composites. The cathode composite powder was prepared by milling NCM622, Li_6PS_5Cl, and Super C65 carbon black (1 g, 7/3/0.1 weight ratio) using 10 (10 mm) zirconia balls in a planetary mill at 140 rpm for 30 min under an argon atmosphere. The anode composite powder was a 3/6/1 weight ratio mixture of carbon-coated $Li_4Ti_5O_{12}$ (NEI Corporation; LTO), Li_6PS_5Cl, and Super C65 carbon black and was prepared in the same way as the cathode composite.

Cell Assembly and Electrochemical Characterization. For pelletized ASSB test cells (Ø 10 mm), a custom setup comprising two stainless steel dies and 10 mm diameter PEEK sleeve was used. In the assembling procedure, Li_6PS_5Cl (100 mg) was compressed at 125 MPa. Afterward, the anode composite (65 mg) was pressed to the solid electrolyte pellet at 125 MPa (~120 μm thickness), and finally, the cathode composite (10−12 mg) was pressed onto the other side at 375 MPa. A pressure of 55 MPa was maintained upon electrochemical testing. Galvanostatic measurements were performed at a C/5 rate (1C = 180 mA·g^{-1}) and 45 °C in the voltage range between 1.35 and 2.85 V vs $Li_4Ti_5O_{12}/Li_7Ti_5O_{12}$ using a MACCOR battery test system.

Sample Handling and Sample Transfer. All samples were prepared at the Battery and Electrochemistry Laboratory, Karlsruhe Institute of Technology (KIT) (Eggenstein-Leopoldshafen, Germany). The chemicals were stored and handled in an argon-filled glovebox (<0.1 ppm O_2, <0.1 ppm H_2O). For analysis, the samples were sealed in pouches under an argon atmosphere and shipped to the Institute of Physical Chemistry, Justus Liebig University Giessen (Giessen, Germany). The samples were stored and prepared for analyses in an argon-filled glovebox again (<0.1 ppm O_2, <0.1 ppm H_2O). The sample transfer into the instruments was realized using two different transfer systems. For FIB-SEM and ToF-SIMS analyses, the transfer system Leica EM VCT500 (Leica Microsystems GmbH) was used. For XPS analyses, all samples were transferred under an argon atmosphere from the glovebox into the instrument by using a transport box for PTS sample holders by PREVAC.

Focused Ion Beam Scanning Electron Microscopy. The cross-sections in this work were created and analyzed using a TESCAN XEIA3 system (TESCAN GmbH) equipped with a Xe plasma FIB column. The CAM particles were attached to conductive double-sided adhesive carbon-tabs. For charge compensation, the samples were previously (nonconformally) coated with Pt using a Leica EM ACE600 high vacuum sputter coater (Leica Microsystems GmbH). Typically, a layer thickness of 4 nm was used. Cross-sections were carried out on clusters of secondary particles. Then, the inner secondary particles were analyzed to exclude detrimental effects of the Pt layer. Accordingly, geometrical shadowing effects due to the directional sputtering flux were exploited and all measurements were double-checked to ensure the reliability of the results. In all experiments, the Xe ion beam energy was 30 kV. The beam current was 130 nA for milling and 8 nA for polishing.

Time-of-Flight Secondary Ion Mass Spectrometry. ToF-SIMS analysis was performed by using a TOF.SIMS 5-100 system (IONTOF GmbH). The system is equipped with a 25 keV Bi cluster primary ion gun for analysis and a dual-source column, which enables depth profiling by using either O_2^+ or Cs^+ (up to 2 keV). In addition, a focused ion beam (FIB) option can be used to mill craters with monatomic gallium (30 keV).

The samples were attached to the sample holder using non-conductive adhesive tape. The surface of the samples was flooded with low-energy electrons for charge compensation. All measurements in this work were performed in negative ion mode using Bi_3^+ species (25 keV) for analysis and a cycle time of 60 μs.

Surface analysis was performed by operating the instrument in spectrometry mode (bunched mode). This mode enables high signal intensities and a high mass resolution (FWHM $m/\Delta m$ > 4500 @ m/z = 31.97 (S^-)), which minimizes the effects of signal interferences in the mass spectra. The analysis area was set to 150 × 150 μm^2 and rasterized with 256 × 256 pixels. Every patch was analyzed with 1 frame and 1 shot per pixel and frame. For comparable measuring conditions, the analyses were stopped after a primary ion dose of 1.00·10^{12} ions/cm^2 (static conditions). The primary ion current was about 0.5 pA. We measured 10 mass spectra per sample in different areas on the sample surface to minimize area-dependent effects and ensure the reproducibility of results.

To investigate the bulk material, ToF-SIMS analysis was carried out on 45° FIB crater sidewalls. The 120 × 80 μm^2 craters were milled (FoV: 150 × 150 μm^2, 512 × 512 pixels) into the composite cathodes by using the FIB option of the instrument, allowing subsequent analysis of the crater sidewalls without additional transfer steps. A 700 μm aperture was used, and the dwell time was 200 ms per pixel. The FIB current was about 16−17 nA (100% duty cycle). The analysis of the crater sidewall was performed by operating the instrument in fast imaging mode. The primary ion current was about 0.2 pA. A region-of-interest (ROI) was defined within a 125 × 125 μm^2 analysis area to analyze only the crater sidewall. Before analysis, the damage layer on top of the crater sidewall caused by the FIB was removed by a cleaning procedure analogous to our previous work.[33] The subsequent analysis of the crater sidewall was performed with a raster size of 1024 × 1024 pixels at 1 shot per pixel and 50 frames. This corresponds theoretically to a maximum lateral resolution of 122 nm. However, this value should be seen as the maximum resolution under ideal conditions since topographic effects and the inclined position of the crater have a nonnegligible negative influence.

The analysis of the $LiNbO_3$ reference on a silicon wafer was performed by operating the instrument in fast imaging mode. The analysis current was ~0.2 pA. The analysis area was 200 × 200 μm^2 and rasterized with 512 × 512 pixels. Every patch was analyzed with 10 frames, whereas 1 shot per pixel and frame was used. Depth profiling was performed in non-interlaced mode with Cs^+ (2 keV) as sputter species. The sputter current was ~136 nA. The crater size was set to 500 × 500 μm^2 and sputtered with 600 frames followed by a pause of 1.0 s.

The evaluation of ToF-SIMS data was done with the software SurfaceLab 7.0 (IONTOF GmbH). All secondary ion images in this work were normalized in relation to the total ion signal to minimize

https://dx.doi.org/10.1021/acs.chemmater.0c04660
Chem. Mater. 2021, 33, 2110−2125

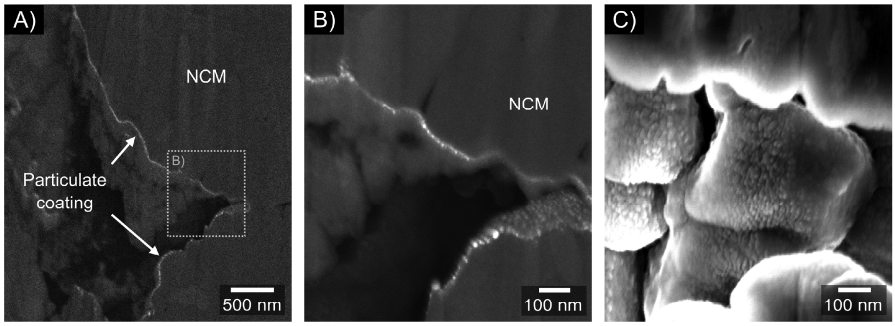

Figure 1. FIB-SEM micrographs of the $Li_2CO_3/LiNbO_3$-coated NCM622 particles. (A) Cross-sections of coated NCM622 particles. (B) Magnified SEM image. (C) Top-view on the secondary particle surface. The images were obtained using a BSE detector, allowing for sufficient material contrast to distinguish the coating from the NCM. The images reveal a particulate coating (mean thickness ~15 nm) with a high particle density. The coating particles are homogeneously distributed on the NCM622 particle surface; however, some uncoated areas are visible.

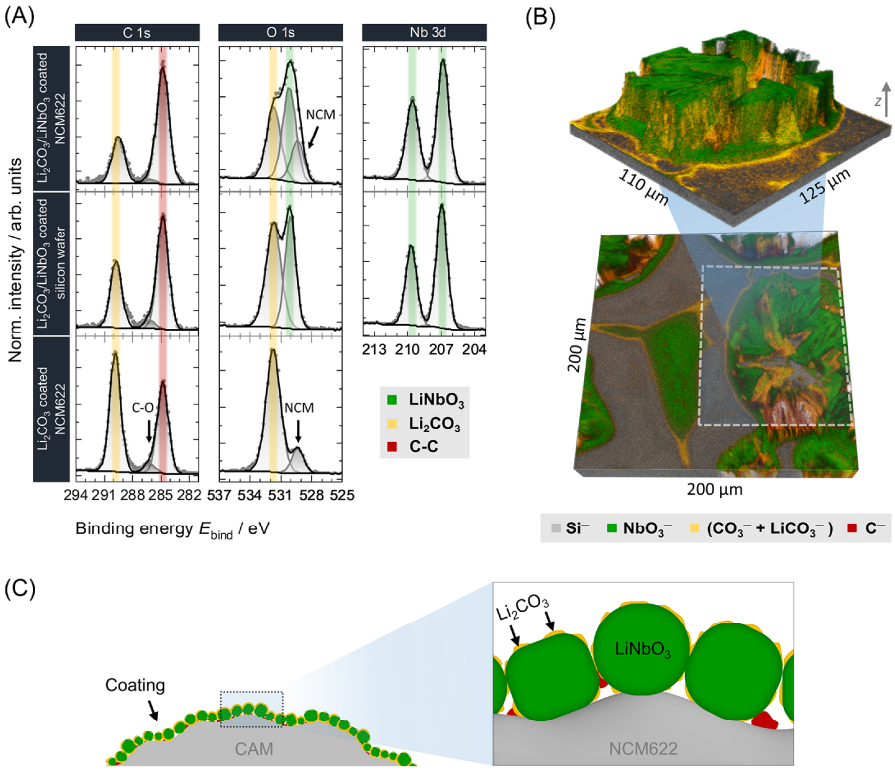

Figure 2. (A) XP detail spectra of the $Li_2CO_3/LiNbO_3$-coated NCM622 particles. Reference spectra of a $Li_2CO_3/LiNbO_3$-coated silicon wafer (model sample) and Li_2CO_3-coated NCM622 particles are shown for comparison. All spectra were measured using a pass energy of 23.50 eV. The energetic signal positions agree with literature values for $LiNbO_3$, Li_2CO_3, and NCM.[37−41] In addition, contributions in the C 1s spectrum caused by ethoxide residues and related side products seem reasonable. (B) ToF-SIMS 3D reconstruction of a $Li_2CO_3/LiNbO_3$-coated silicon wafer (model sample) to clarify the microstructure of the coating particles. The upper image was obtained by using a 3D correction. (C) Proposed microstructure for the $Li_2CO_3/LiNbO_3$ coating. Accordingly, the coating is particulate with a mean particle size in the range of ~15 nm. The inner part of the particles consists of $LiNbO_3$, surrounded by a Li_2CO_3 containing shell. In between, ethoxide residues from the synthesis process may be expected.

topographic effects. The signal intensities were extracted from the respective normalized secondary ion images.

X-ray Photoelectron Spectroscopy. XPS analyses were carried out by using a PHI5000 Versa Probe II system (Physical Electronics GmbH). The samples were attached to the sample holder using nonconductive adhesive tape. A dual-beam charge neutralization (ion beam combined with a low-energy electron beam) was applied during the measurements. Depth profiling was performed analogous to our previous work to clean the surface of the composite cathode to minimize the detrimental influence of the degradation processes at the current collector/solid electrolyte interface.[24,33] The change of signals was monitored as a function of the sputtering time for all samples to

https://dx.doi.org/10.1021/acs.chemmater.0c04660
Chem. Mater. 2021, 33, 2110−2125

minimize the influence of the current collector/solid electrolyte interface on the one hand and exclude further sample modification by sputtering on the other hand. For comparison of XP spectra, a Li_6PS_5Cl reference (NEI Corporation) was used.

For analysis, monochromatic Al Kα radiation (1486.6 eV) was used. The X-ray source was operated with a power of 50 W and a voltage between 15−17 kV. The analysis beam diameter was 200 μm. The pass energies of the analyzer ranged from 23.50 to 46.95 eV. The exact values are given in the respective captions of the XP spectra.

The depth profiling experiments were performed in alternating sputter mode. For material abrasion, a sputter gun with Ar^+ ions was used. The acceleration voltage was set to 0.5 kV with a sputter current of ∼0.5 μA. The raster size was 2 × 2 mm^2.

The experimental data was evaluated with the software CasaXPS (version 2.3.22, Casa Software Ltd). The energy calibration was performed analogous to previous work to minimize detrimental surface effects.[34,35] Accordingly, the XP spectra of the Li_6PS_5Cl reference were calibrated in relation to the signal of adventitious carbon at 284.8 eV first. Afterward, the energetic signal position of the main component of the S 2p signal (PS_4^{3-} units) was determined and the XP spectra of the composite cathodes were calibrated in relation to this signal at 161.6 eV. The suitability of the energy calibration was double-checked with other main components of the solid electrolyte. For signal fitting, Shirley background, GL(30) line shapes, and common fitting restrictions were used. The latter include theoretical signal area ratios dependent on the analyzed orbital (e.g., 1:2 for p orbitals), FWHM constraints, and published values for spin orbit splitting.[36]

■ RESULTS

The results section of this work is divided into three parts. First, we characterize the microstructure of the Li_2CO_3/$LiNbO_3$ coating, namely, the morphology and composition. In the second part, we address the influence of the CAM coating on the ASSB performance and demonstrate its beneficial effect. In the third part, we present a comprehensive post-mortem analysis of composite cathodes by XPS and ToF-SIMS measurements to clarify the working principle of the Li_2CO_3/$LiNbO_3$ coating.

Characterization of the Coating Microstructure. For thorough characterization of the coating microstructure, it is necessary to address the coating morphology and coating composition. In this work, we used FIB-SEM to characterize the coating morphology, followed by the characterization of the coating composition using XPS and ToF-SIMS.

The difference in the atomic mass of Nb compared to the elements of NCM allows for sufficient material contrast in SEM micrographs measured using a back-scattered electron (BSE) detector to distinguish the CAM coating from the NCM material. Figure 1 shows representative SEM images, revealing the morphology of the Li_2CO_3/$LiNbO_3$ coating and its distribution on the CAM surface.

The SEM micrographs reveal a particulate coating with a mean thickness of about 15 nm. The coating particles are homogenously distributed on the NCM622 particle surface, leading to a high degree of coverage. However, the particular character still allows open (uncoated) areas between the particles, which will be particularly important later on in the context of decomposition phenomena in the composite cathodes. Accordingly, we still expect decomposition reactions to occur in the uncoated/less-coated areas. However, the SEM analyses reveal a high quality of the coating in terms of homogeneity, meaning that variations of coating particle size/thickness are comparably small. These are ideal conditions for the post-mortem analysis on composite cathodes shown later since no significant dependence on the analysis area is to be expected.

To characterize the coating composition, we performed XPS and ToF-SIMS analyses. XPS is used for basic statements on the material composition, which is complemented by ToF-SIMS for characterizing the locally resolved material distribution. Figure 2A shows a comparison of the XP detail spectra of the coated CAM with two reference samples. For the coated CAM (Figure 2A, top), the energetic signal position of contributions in the Nb 3d and the O 1s spectra agree well with literature values for $LiNbO_3$.[37,38] In addition, contributions, which can be assigned to Li_2CO_3, are visible in the C 1s and O 1s spectra.[39] ATR-IR measurements (see the Supporting Information, Figure S2) and a comparison of the energetic XP signal positions with a Li_2CO_3-coated NCM622 reference further verify the presence of Li_2CO_3.[26] Apart from both the $LiNbO_3$ and Li_2CO_3, contributions from aliphatic carbon can be observed in the C 1s signal and an additional signal caused by NCM622 is visible in the O 1s spectrum for the coated particles.[40,41] The latter is not very surprising for the coated CAM considering the particulate nature of the coating.

To get more information about the microstructure of the coating, we prepared a model sample by coating a silicon wafer (see Experimental Section) followed by ToF-SIMS analysis. The flat geometry of the silicon wafer allows a reliable characterization of the microstructure using ToF-SIMS. Depth profiling in fast imaging mode was performed to enable a 3D reconstruction of the coating particles with a high spatial resolution and simultaneously chemical information. The suitability of the selected signals for the 3D reconstruction was verified by measurements performed in spectrometry mode (bunched mode), offering a higher mass resolution. Figure 2B shows the obtained 3D reconstructions. It can be seen that large particles were grown on the silicon substrate. The particle dimensions are much larger compared to the coating of the NCM622 particles, which is most likely related to the greater amount of material used and the substrate itself. Besides the changed surface composition, the reduced surface roughness in case of the silicon wafer can also have an influence on the nucleation and the subsequent material growth process. However, the XPS results (Figure 2A, middle) show similar chemical components, demonstrating the suitability of the model sample. Taking these considerations into account, several conclusions can be drawn from the model sample:

The inner region of the coating particles shows fragments, which can be related to $LiNbO_3$ (green). The $LiNbO_3$ is most probably present in an amorphous phase since the heating temperature was only 300 °C. For comparison, Glass *et al.* reported an initial crystallization temperature of 460 °C for $LiNbO_3$, whereas Özer and Lampert observed crystallization not before 550 °C for a synthesis route similar to this work.[42,43] Carbonate fragments originate from the surface of the particles (yellow), whereas C^- fragments are formed from regions between the particles (red). Based on the XPS results, we assume that the carbonate fragments are formed from Li_2CO_3. C^- is most probably related to ethoxide residues and related side products from the coating process. This could also explain the relative high signal intensity of corresponding contributions in the binding energy range of aliphatic carbon in the C 1s spectrum.

https://dx.doi.org/10.1021/acs.chemmater.0c04660
Chem. Mater. 2021, 33, 2110−2125

Overall, taking the FIB-SEM, XPS, and ToF-SIMS results into account, we propose the coating microstructure shown in Figure 2C, which can be described as follows: The coating is particulate with a mean particle size in the range of ~15 nm and consists of an amorphous $LiNbO_3$ core and a Li_2CO_3 containing shell. In between the particles, ethoxide residues and related side products from the synthesis process are conceivable.

In this context, it must be noted that small deviations from the postulated stoichiometry cannot be detected by XPS and ToF-SIMS. Calculations by Xiao *et al.* suggest that at the NCM (fully lithiated)/$LiNbO_3$ interface compounds such as Li_3NbO_4 can be formed.[44] We assume that it is almost impossible to distinguish such (partial) stoichiometric deviations due to small binding energy shifts in XP spectra and similar fragmentations in ToF-SIMS spectra. In addition, small concentrations are generally problematic taking the respective detection limit of the analytical methods into account. However, it should be noted that according to the aforementioned calculations, the reaction energy and thus the driving force for the reaction are very small. Calculations of Nolan *et al.* further support that the driving force for the reaction of $LiNbO_3$ with fully lithiated nickel-rich CAMs is low.[45] Therefore, based on our analytical results and the calculations mentioned, we will use the simplified term Li_2CO_3/$LiNbO_3$ coating in the following.

Electrochemical Cell Performance. To investigate the effect of the Li_2CO_3/$LiNbO_3$ coating on the ASSB long-term cycling performance, pelletized bulk-type cells were assembled and charged/discharged for 200 cycles. For comparison, similar cells comprising bare (uncoated) NCM622 were also tested. Initial specific charge and discharge capacities of 188 and 161 mAh·g^{-1} were achieved for the bare NCM622, corresponding to a Coulombic efficiency (CE) of 86% (Figure 3A, top). With subsequent cycling, fast capacity fading can be observed, reaching specific discharge capacities of 86 and 22 mAh·g^{-1} at the 50th and 200th cycle, respectively. For the Li_2CO_3/$LiNbO_3$-coated NCM622, initial specific charge and discharge capacities of 200 and 180 mAh·g^{-1} were achieved with a CE of 90% (Figure 3A, bottom). It can therefore be stated that the CAM coating leads to an improvement in the initial CE of 4%, together with an increased absolute charge/discharge capacity. With subsequent battery cycling, a steady but much less pronounced specific discharge capacity decay is apparent for the coated sample (Figure 3B), reaching 153 and 82 mAh·g^{-1} for the 50th and 200th cycle, respectively. Regarding the CE, both CAMs (coated and uncoated) approach 99.5% after around 38 cycles. However, the CEs for the bare NCM622 are roughly 0.5% lower than for the coated NCM622 in the following cycles (see the Supporting Information, Figure S3), indicating more pronounced interfacial side reactions.

Post-Mortem Analysis. In this chapter, we show the results of post-mortem analysis using XPS and ToF-SIMS for composite cathodes with bare and Li_2CO_3/$LiNbO_3$-coated NCM622. The aim was to obtain a comprehensive picture on the influence of the coating on the decomposition reactions in the composite cathode. In the following, the results are addressed separately in two parts according to the respective analytical method.

(I) X-Ray Photoelectron Spectroscopy

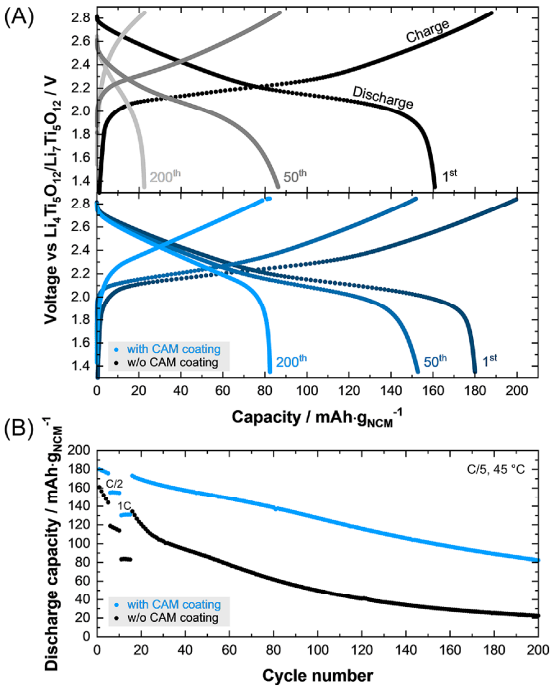

Figure 3. (A) Charge and discharge curves for bare (top) and Li_2CO_3/$LiNbO_3$-coated NCM622 (bottom) for the initial, 50th and 200th cycles. (B) Long-term cycling performance in terms of specific discharge capacities as a function of cycle number. The corresponding Coulombic efficiencies are shown in the Supporting Information. Application of the CAM coating leads to an enhanced ASSB performance, thus demonstrating its overall beneficial effect.

XPS depth profiling experiments were conducted to identify decomposition products and draw quantitative conclusions. Analogous to our previous work, the surface of the composite cathodes was initially cleaned by Ar^+ sputtering to reduce the detrimental effect of the current collector (see Experimental Section).[24] To characterize the influence of the CAM coating on the decomposition processes, we conducted analysis on composite cathodes with bare and coated NCM622 after 0 cycles (as-prepared) and 200 cycles. The S 2p and P 2p spectra will be used hereafter to discuss basic decomposition processes indicated by XPS (Figure 4A). Then, we address the signal changes in the Nb 3d spectrum as a function of different cycling stages (Figure 4B). The Cl 2p, O 1s, Li 1s, and C 1s detail spectra are shown in the Supporting Information (Figure S4).

Figure 4A shows a direct comparison of the S 2p and P 2p detail spectra before and after battery cycling for Li_2CO_3/$LiNbO_3$-coated and bare NCM622. Reference spectra for the Li_6PS_5Cl solid electrolyte are shown at the bottom of Figure 4A.

The S 2p and P 2p contributions of the Li_6PS_5Cl reference can mainly be related to the argyrodite structure. In the S 2p signal, three contributions can be distinguished. The main component at 161.6 eV corresponds to the PS_4^{3-} units, whereas the doublet at 160.2 eV can be attributed to the free S^{2-} species of the argyrodite structure.[33,46,47] In the latter binding energy range, also, Li_2S residues from the material

https://dx.doi.org/10.1021/acs.chemmater.0c04660
Chem. Mater. 2021, 33, 2110−2125

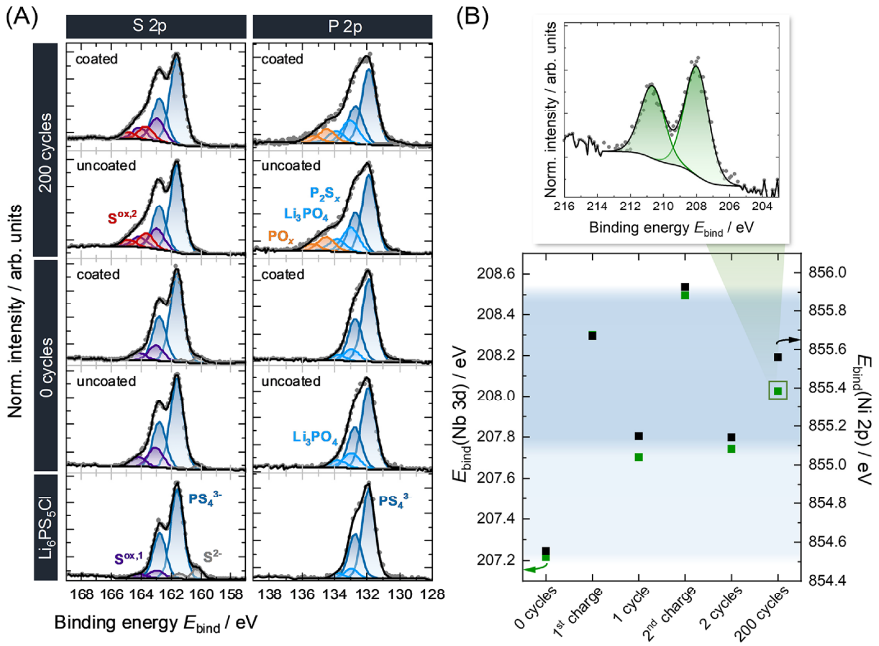

Figure 4. (A) S 2p and P 2p XP detail spectra of composite cathodes with and without $Li_2CO_3/LiNbO_3$ coating after 0 and 200 cycles. Li_6PS_5Cl reference spectra are shown at the bottom. The surface was initially cleaned by sputtering with Ar^+ ions. All detail spectra were measured with a pass energy of 23.50 eV. A Shirley background and GL(30) line shapes were used for signal fitting. The XP spectra were normalized in relation to the respective signal maximum for better comparison of the signal contributions. (B) Bottom: the mean energetic signal position of the Nb 3d (green) and Ni 2p signals (black) after surface cleaning is shown at different stages of cycling. The Nb 3d signals were measured using a pass energy of 23.50 eV, whereas the pass energy for the Ni 2p ranged from 29.35 to 46.95 eV. The graph reveals distinct signal shifts during the first charging step for both signals (light blue area), followed by a partially reversible shift in the subsequent cycles (dark blue area). Top: the Nb 3d signal after 200 cycles is shown as an example. It can be seen that a single doublet is already sufficient to represent the experimental data. Consequently, the Nb 3d signal shape has not changed significantly during battery cycling.

synthesis process are conceivable.[46] For higher binding energies, a signal shoulder is visible, which can be represented in the fitting model by using a single doublet at 163.0 eV. The origin of signals in this binding energy range has often been reported and discussed for thiophosphates in literature and is mostly related to polysulfides or various anionic frameworks that Li-P-S phases can pass through during redox reactions such as $P_2S_7^{4-}$ and $P_2S_6^{2-}$ toward the formation of P_2S_5.[24,33,46−53] Because the differences in the binding energy of such compounds are very small, an unambiguous assignment without additional proof is not possible. Therefore, we labeled the doublet with the general term $S^{ox,1}$. In the P 2p signal, fitting with two doublets is already sufficient to represent the experimental data. The main component at 131.9 eV can be assigned to the PS_4^{3-} units of the argyrodite structure.[33,46,47] A further doublet can be seen at 133.0 eV. This signal is often correlated with the same compounds already mentioned for the $S^{ox,1}$ signal. In addition, Li_3PO_4 can be detected in this binding energy range, which is particularly relevant for the composite cathodes.[54,55] Accordingly, both uncycled composite cathodes (with and without CAM coating) show a slight increase in this signal contribution. Since the signal contribution is slightly decreased for the composite cathode with CAM coating, the coating seems to somewhat suppress the formation of such species. As shown in our previous experimental study, the mere NCM622/SE contact can already lead to the formation of phosphates, most probably Li_3PO_4.[24,33] This is in agreement with calculations by Xiao *et al.*, who have shown that the contact between NCM(fully lithiated)/Li_6PS_5Cl can trigger the formation of Li_3PO_4.[44] Interestingly, according to their work, also the $LiNbO_3$/Li_6PS_5Cl contact can lead to the formation of Li_3PO_4. Taking our experimental data into account, we assume that the driving force for the Li_3PO_4 formation is lower for the $LiNbO_3$/Li_6PS_5Cl interface. However, it must be considered that other compounds such as polysulfides (e.g., P_2S_x) can also be found in this binding energy range, which makes it difficult to clearly assign this signal with XPS alone.[46,47]

For the S 2p signals of the uncycled composite cathodes, similar effects were observed. Accordingly, $S^{ox,1}$ is increased for both composite cathodes compared to the solid electrolyte reference, while the doublet is slightly lower when using the CAM coating. Therefore, also here, our data indicate that the coating suppresses the solid electrolyte decomposition reactions caused by the mere contact of the individual materials.

In contrast, the S 2p and P 2p detail spectra of the cycled composite cathodes largely match. In both cases, battery cycling leads to an increase in the S 2p signal shoulder at higher binding energies. A single doublet at 163.7 eV is already sufficient to represent the experimental data (termed $S^{ox,2}$ in the following). The origin of signals in this binding energy range has often been discussed, analogous to $S^{ox,1}$. Based on reports on the redox-behavior of thiophosphates and recent

https://dx.doi.org/10.1021/acs.chemmater.0c04660
Chem. Mater. 2021, 33, 2110−2125

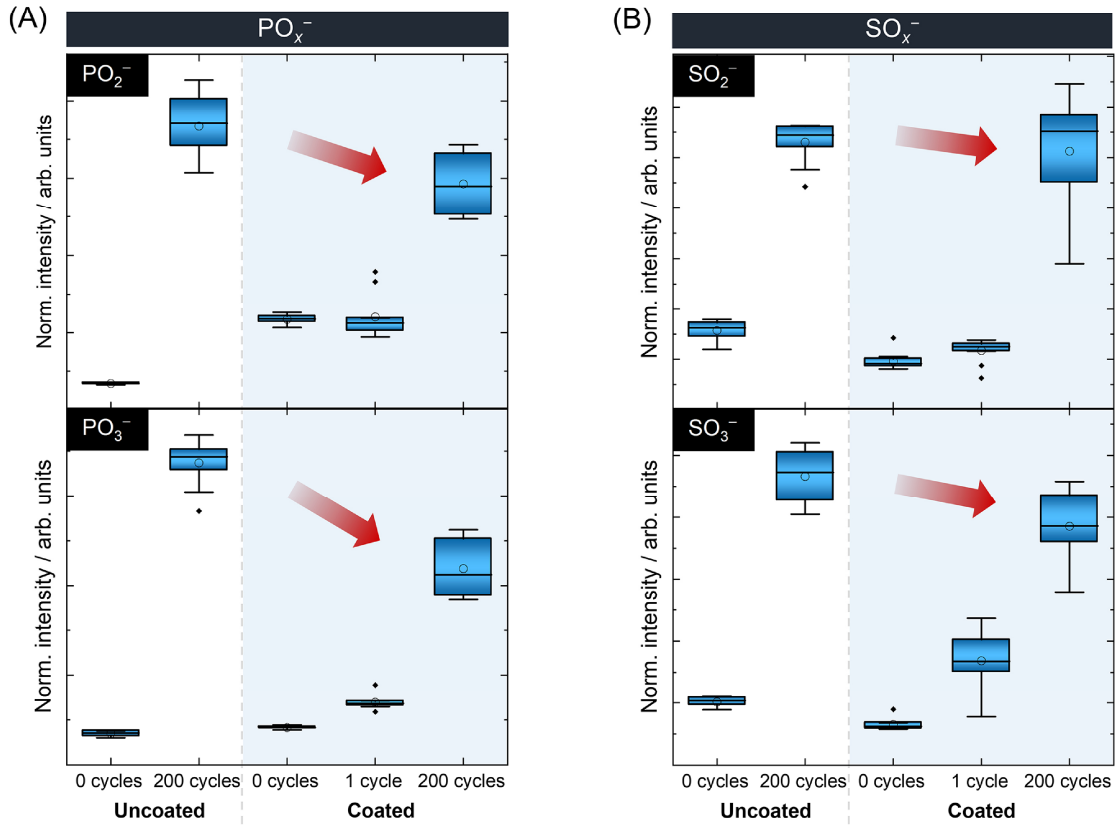

Figure 5. Results from ToF-SIMS surface analyses. Shown are boxplots of the normalized intensity of POx^- and SOx^- fragments (with $2 \leq x \leq 3$). The primary ion gun was operated in spectrometry mode (bunched mode) using Bi_3^+(25 keV) as primary ion species. Ten mass spectra were measured for each sample to minimize effects of the analysis area dependence. Electrochemical cycling leads in both cases (coated and uncoated) to significant increases in PO_x^- and SO_x^- fragments. The $Li_2CO_3/LiNbO_3$ coating is capable of somewhat suppressing the formation of phosphates and sulfates/sulfites.

studies on decomposition processes in NCM and thiophosphate-based composite cathodes, we hypothesize that polysulfide formation occurs during battery cycling, which is probably accompanied by dynamic anionic framework transitions that Li-P-S phases may undergo.[24,47−50,52] Because the S 2p decomposition signals $S^{ox,1}$ and $S^{ox,2}$ are comparable in both cases, the coating seems not to significantly suppress these reactions, as can be seen from the XPS data.

In addition, both P 2p spectra show similar signal broadening. In particular, the increase of the signal shoulder at higher binding energies matches to a great extent. The binding energy range of the signal shoulder indicates the formation of phosphates such as Li_3PO_4, $Ni_3(PO_4)_2$, $Mn_3(PO_4)_2$, and/or metaphosphates of these species.[36,54−56] At the same time, signal interferences with polysulfide species such as P_2S_x can be expected.[47] Overall, the P 2p spectra suggest the formation of oxygenated phosphorous species such as phosphates and metaphosphates (Li_3PO_4 and transition-metal phosphates seem reasonable) and can also support the conclusions drawn from the S 2p spectra regarding the formation of polysulfides such as P_2S_x and different anionic frameworks. Analogous to the S 2p spectra, also here, the XPS results indicate that the coating does not lead to a significant decrease in decomposition product concentrations. However, it must be noted that the detection limit of XPS is comparably high. Considering the microstructure of the composite cathodes and the underlying dimensions, it becomes obvious that the small quantities of decomposition products can lead to detection limit problems. Furthermore, the deconvolution of the individual decomposition processes (current collector/solid electrolyte, carbon additive/solid electrolyte, CAM/solid electrolyte) is highly challenging due to signal interferences of decomposition products, e.g., Li_3PO_4 and P_2S_x. For this reason, we conducted ToF-SIMS measurements to reveal concentration changes below the XPS detection limit (see next section).

Interestingly, analysis of the Nb 3d signal before and after battery cycling revealed a shift in the energetic signal position. To investigate this effect in more detail, we analyzed the Nb 3d spectrum at different cycling stages (green data points in Figure 4B). It can be seen that the Nb 3d signal shifts strongly toward higher binding energies during the initial charging step and shifts more or less reversibly to lower and higher binding energies in subsequent cycles. Because the Ni 2p signal (black data points in Figure 4B) shows a similar trend and all spectra were calibrated in relation to solid electrolyte signals, we assume that the signal shift represents the state of charge of the CAM and is not mainly caused by a change in the chemical

https://dx.doi.org/10.1021/acs.chemmater.0c04660
Chem. Mater. 2021, 33, 2110−2125

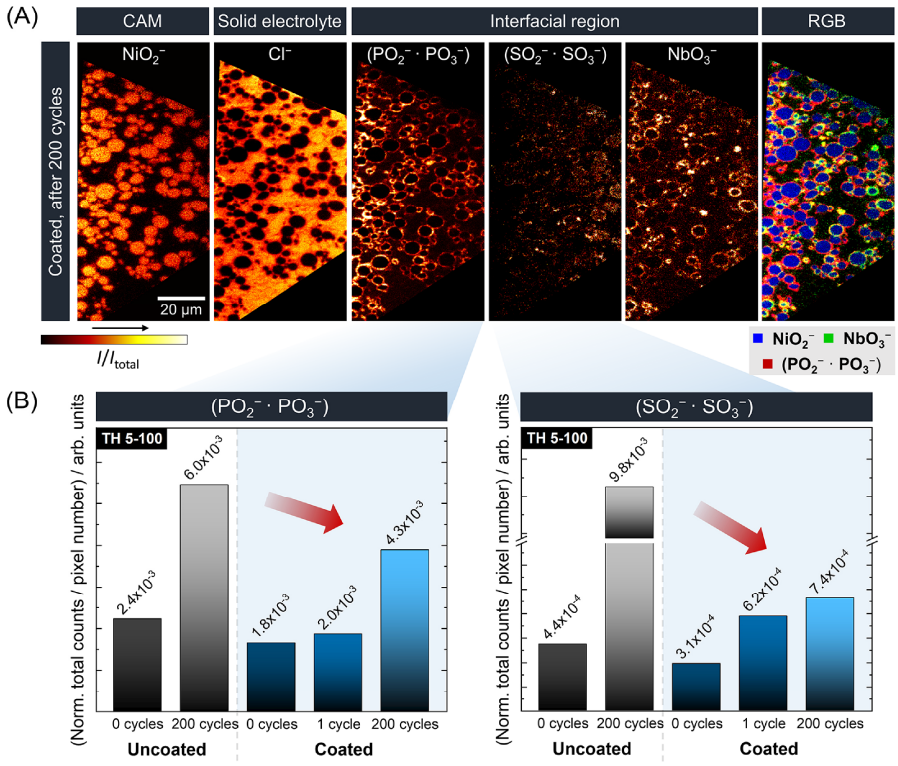

Figure 6. (A) ToF-SIMS measurement on a 45° crater sidewall of the cycled composite cathode with Li_2CO_3/$LiNbO_3$-coated NCM622. Shown are exemplary secondary ion images of negatively charged fragments and a RGB overlay. The cathode active material (NiO_2^-), the coating (NbO_3^-), the solid electrolyte (Cl^-), and the degradation layer ($(PO_2^- \cdot PO_3^-)$ and $(SO_2^- \cdot SO_3^-)$) can be clearly distinguished from each other. (B) Results of the ROI analysis for the multiplied $(PO_2^- \cdot PO_3^-)$ and $(SO_2^- \cdot SO_3^-)$ secondary ion images. Battery cycling leads to an increase in phosphate and sulfate/sulfite fragments. The Li_2CO_3/$LiNbO_3$ coating suppresses the reaction at the CAM/solid electrolyte interface.

environment or a reaction of the coating material (a detailed discussion is given in the Supporting Information). This is supported by the fact that the potential range of the ASSB is much higher than reported values for the redox activity of $LiNbO_3$ and material-related oxides such as $LiNbO_2$ and Nb_2O_5, and the Nb 3d signal shape does not change upon cycling (see Nb 3d signal in Figure 4B).[43,57−62] It has already been shown in the literature that these effects can be exploited in XPS experiments on model systems to obtain information on electronic and ionic contributions to the electrode potential and determine energy band diagrams experimentally.[63−66] However, since signal shifts in XP spectra can be caused by manifold (convoluted) effects, we cannot completely exclude (electro)chemical reactions of the coating material, even though there is no direct evidence for them.

(II) Time-of-Flight Secondary Ion Mass Spectrometry

ToF-SIMS analyses were performed to further characterize the decomposition processes in the composite cathodes below the detection limit of XPS (semiquantitative analysis). As described in previous studies, ToF-SIMS can reveal chemical processes that are not detected by XPS due to its higher sensitivity, e.g., formation of small quantities of sulfates/sulfites as demonstrated in the following.[24,33] This makes the method particularly attractive for studies on interfacial decomposition processes in ASSBs.

Surface analyses were performed to identify decomposition products and to reveal the influence of the CAM coating. In addition, ToF-SIMS analyses on FIB crater sidewalls were performed to verify the results of the surface analysis for the bulk material and reveal the local fragment distribution, to ensure that the observations can be correlated to the decomposition reactions at the CAM/solid electrolyte interface.

We analyzed composite cathodes with Li_2CO_3/$LiNbO_3$-coated NCM622 at different cycling stages (0, 1, and 200 cycles) and compared the results with data obtained for composite cathode without CAM coating (0 and 200 cycles).

For surface analysis, the overlap of the three different decomposition processes (current collector/solid electrolyte, carbon additive/solid electrolyte, CAM/solid electrolyte) must be taken into account, as we have described in more detail in a previous study.[24] However, despite the detrimental influence of the current collector/solid electrolyte interface, it is still possible to obtain reasonable data from ToF-SIMS surface analysis due to the higher sensitivity compared to XPS. Based on experience, XPS investigations inevitably require surface cleaning/sputtering since results of surface measurements differ significantly from depth profiling results. This makes it often almost impossible to obtain reliable data. In contrast, ToF-SIMS surface spectra often show comparable results to depth profiling as shown earlier.[24,33] However, to minimize the

https://dx.doi.org/10.1021/acs.chemmater.0c04660
Chem. Mater. 2021, 33, 2110−2125

effect of analysis area dependence, it is necessary to increase the statistics. Therefore, 10 measurements per sample were performed (the scattering of the data is indicated by the boxplots in Figure 5A and B).

According to previous work with ToF-SIMS, phosphate (PO_x^-) and sulfate/sulfite (SO_x^-) fragments are of particular interest in the context of the decomposition of thiophosphate-based composite cathodes.[24,33,67] Figure 5 illustrates the results of the surface analysis related to phosphate and sulfate/sulfite fragments in boxplots.

From the surface analysis, it is evident that battery cycling leads in both cases (uncoated and coated CAM) to significant increases in phosphate and sulfate/sulfite fragments. The results for the composite cathodes containing the Li_2CO_3/$LiNbO_3$-coated CAM indicate that the formation of decomposition products occurs successively and is not completed after the first cycle. This is in accordance with our XPS results (see the Supporting Information, Figure S6). After 200 cycles, the composite cathode with coated CAM shows decreased intensities for PO_x^- and SO_x^- fragments compared to the uncoated reference. This indicates that the Li_2CO_3/$LiNbO_3$ coating suppresses the formation of phosphates and sulfates/sulfites.

For the uncycled composite cathodes, the sulfate/sulfite formation due to the mere NCM/solid electrolyte contact seems largely reduced. This indicates, analogous to the XPS results, a suppression of the interfacial reaction due to the mere NCM/SE contact. This is also in accordance with calculations by Xiao *et al.*, who have shown that Li_2SO_4 is a favorable reaction product for NCM/Li_6PS_5Cl interfaces, whereas this is not the case for the $LiNbO_3$/Li_6PS_5Cl interface.[44]

In contrast, the suppression of the interfacial reaction is not as obvious for the phosphate fragments, which at first glance seems to contradict the XPS results. However, it should be noted that PO_2^- and PO_3^- show different trends (compare 0 cycles with 1 cycle for the coated case), which could be due to mass interferences. In addition, we cannot neglect the decomposition process overlap with the current collector/solid electrolyte interface in surface analyses. Indeed, we will show later that ToF-SIMS analyses on FIB crater sidewalls confirm the XPS results. Since the current collector/solid electrolyte interface influence can be excluded in these measurements, we assume a detrimental influence by the current collector here.[24]

In the next step, we analyzed FIB crater sidewalls to verify the surface analysis results for the bulk material and reveal the local fragment distribution with high lateral resolution. The latter is particularly important, to confirm that the results obtained can be correlated to the decomposition reactions at the CAM/solid electrolyte interface. It should be noted here that the maximum lateral resolution theoretically achieved is 122 nm (see Experimental Section). However, due to the topographic effects and inclined nature of the crater, this value should be interpreted as the maximum resolution under ideal conditions.

Figure 6A shows exemplary secondary ion images of the crater sidewall for the composite cathode with coated CAM after 200 cycles. The different components of the composite can be easily distinguished from each other using specific fragments. Accordingly, the NCM622 particles (NiO_2^- fragment), the Li_6PS_5Cl solid electrolyte (Cl^-), the CAM coating (NbO_3^-), and the decomposition layer (PO_x^- and SO_x^-) can be represented very well with high lateral resolution. The local distribution of phosphate and sulfate/sulfite fragments was studied by multiplication of secondary ion images to eliminate mass interferences analogously to our previous work.[33]

For the uncycled composite cathodes, the secondary ion images revealed that phosphate and sulfate/sulfite formation already takes place due to the mere material contact at the CAM/solid electrolyte interface. Battery cycling leads to a further increase in phosphate and sulfate/sulfite signals regardless of the CAM coating.[24,33]

For the composite cathode with coated CAM, even after 200 cycles, the coating fragment NbO_3^- can still be detected around the NCM622 secondary particles (Figure 6A). Therefore, a significant consumption/dissolution of the coating due to diffusion and (electro)chemical reactions does not seem to take place. Nevertheless, from the secondary ion images, it is apparent that phosphate (PO_x^-) and sulfate/sulfite (SO_x^-) formation occurs at the NCM/solid electrolyte interface, despite CAM coating.

In this context, the question arises whether there are differences in the detected decomposition product concentrations. To draw semiquantitative conclusions, a ROI analysis was performed analogous to previous studies.[24,33,68] The procedure of such an analysis is described in more detail in the Supporting Information. The results of the ROI analysis are shown in Figure 6B.

For the uncycled composite cathodes, comparable trends to the XPS analysis can be observed. Accordingly, the composite cathode containing the coated CAM shows a suppressed interfacial reaction due to the mere CAM/solid electrolyte contact, indicated by the lower amount of phosphate and sulfate/sulfite fragments. From the data for the composite cathodes containing coated CAM, it can be seen that the formation of such species is not completed after the first cycle but rather gradually increases during battery cycling, which is in accordance with our XPS results (see the Supporting Information, Figure S6).

After 200 cycles, the intensity of PO_x^- and SO_x^- fragments is significantly increased in both cases, but the protective nature of the CAM coating is clearly evident, as the signal intensities are lower in this case.

Overall, the SIMS results indicate a suppression of the interfacial reaction at the CAM/solid electrolyte interface and highlight the suitability of the method for such investigations. The XPS results related to the interfacial reaction by mere contact could be confirmed. In addition, the high sensitivity of the method allowed the detection of concentration differences for phosphates and sulfates/sulfites in the CAM/solid electrolyte interface region that could not be resolved with XPS.

■ DISCUSSION

In the following, we summarize the main findings of the results section and discuss them in the context of published work. First, we address the coating microstructure, especially its morphology and chemical composition. Based on this knowledge, we then discuss the influence of the CAM coating on the battery performance and the decomposition processes in the composite cathodes.

Coating Microstructure. The coating approach in this work led to a particulate coating with a mean layer thickness of ~15 nm. According to our XPS and ToF-SIMS data, the coating particles consist of a $LiNbO_3$ core, a Li_2CO_3 shell, and

https://dx.doi.org/10.1021/acs.chemmater.0c04660
Chem. Mater. 2021, 33, 2110−2125

small quantities of carbon-containing residues from the coating procedure. It can be assumed that the $LiNbO_3$ core is in an amorphous state since the heating temperature was only 300 °C and the crystallization temperature is usually ≥460 °C.[42,43] It has already been demonstrated that the amorphous phase exhibits a much higher lithium-ion conductivity compared to single-crystalline $LiNbO_3$, whereas the transport properties are reported to be strongly dependent on the grain boundary microstructure.[42,69] It should be noted that small deviations from the here postulated stoichiometry are virtually impossible to detect. The microstructure and spherical geometry of CAMs are not ideal for most analytical methods, and the small dimensions and concentration of the coating material are often in the range of the detection limit. Even the common combination of TEM, EDX, and EELS is, according to Kim et al., limited to basic statements about the local layer thickness and element distribution for a $Li_2CO_3/LiNbO_3$ hybrid coating and does not provide further insights into the coating microstructure.[26]

Calculations by Xiao *et al.* suggest that NCM (fully lithiated) can react with $LiNbO_3$ to form compounds such as Li_3NbO_4, $LiMnCoO_4$, and NiO.[44] However, the reaction energy and thus the driving force for the reaction of $LiNbO_3$ with fully lithiated NCM are comparably small. This is further supported by calculations of Nolan *et al.*[45] In addition, the half-lithiated Ni-rich cathode/$LiNbO_3$ interface should be stable.[44,45] Therefore, we do not assume a strong effect and expect only very low product concentrations in the interfacial region. Indeed, experimental identification of such compounds was not possible in this work. In addition to detection limitations of the analytical instruments, considering the chemical similarity of possible products, small binding energy differences in XP spectra and similar fragmentations in ToF-SIMS spectra further complicate analyses in this direction. For this reason, we cannot provide further insights into the reaction of the coating and CAM here.

Influence of the Coating on the ASSB Performance and the CAM/Solid Electrolyte Interfacial Decomposition. In general, the $Li_2CO_3/LiNbO_3$ coating leads to a significant improvement in long-term cycling performance. Accordingly, the absolute capacities are enhanced and the capacity fading during cycling is reduced. However, considering that a less-pronounced but steady capacity fading is clearly visible, detrimental interfacial reactions are still occurring in the composite cathode. In this context, it must be taken into account that interfacial reactions can generally occur at three different interfaces in composite cathodes as follows: (i) current collector/solid electrolyte, (ii) carbon additive/solid electrolyte, and (iii) CAM/solid electrolyte.[24] Since we only applied a protective coating to the CAM, we still expect unaffected detrimental interfacial reactions at the interfaces (i) and (ii).

The detrimental effect of carbon additives on the ASSB performance has already been investigated in the past.[24,32,70,71] Reports on the interfacial reaction of carbon with thiophosphates indicate decomposition products such as polysulfides and/or various anionic frameworks that Li-P-S phases can pass through during redox reactions.[24,50] Because the decomposition products from the interfaces (ii) and (iii) overlap in the S 2p spectra, it is almost impossible to separate the individual contributions. Hence, the pronounced formation of the signal shoulder at higher binding energies in the S 2p signal during battery cycling (Figure 4A) can partially be explained by reactions at the carbon additive/solid electrolyte interface. A further hint in this direction is that the formation of this signal shoulder is already almost completed after the initial cycles (Figure S6). In contrast, species that can be more clearly associated with interface reactions at the CAM/solid electrolyte interface such as phosphates and sulfates/sulfites (which require an oxygen source) tend to form successively. This is indicated by the P 2p signal (Figure S6) and ToF-SIMS investigations (Figures 5 and 6). Strategies to overcome the interfacial reaction at the carbon additive/solid electrolyte interface have already been demonstrated and shown to improve the performance of ASSBs.[72,73] Analogous to the CAM, this often comprises coating approaches.

Despite the decomposition overlap, our post-mortem analysis clearly revealed reactions that can unambiguously be attributed to the CAM/solid electrolyte interface. For the uncoated CAM, the XPS and ToF-SIMS data indicate distinct formation of oxygenated phosphorous and sulfur species such as phosphates and sulfates/sulfites. This is consistent with previous experimental and computational studies in the context of thiophosphate-based composite cathodes.[24,33,44,67,74,75] We have already proposed a scheme for the NCM622/β-Li_3PS_4 interfacial reaction in a previous study.[24] Since we find comparable results for NCM622/Li_6PS_5Cl, similar reactions are likely to occur. Considering recent calculations, we assume that thermodynamically preferred reaction paths involve the formation of transition metal sulfides as intermediate products, which ultimately transform into phosphates and sulfates in a metathesis-type reaction.[24,44,74,75] In this context, it should be noted that, in contrast to other experimental work, there is no clear evidence of transition-metal sulfide formation in our XPS and ToF-SIMS data.[27,76,77] In a previous work, we have already discussed the possibility of a misleading energy calibration of XP spectra and thus a misleading detection of transition-metal sulfides.[24] Apart from the possibility of a metathesis-type reaction, the formation of oxygenated phosphorous and sulfur compounds can also be partially ascribed to the chemical reaction of released O_2 (partially present as highly reactive singlet $^1O_2$) during battery cycling, either from the NCM lattice at high states of charge or from the electrochemical decomposition of Li_2CO_3 as reported in literature.[26,78−83]

Overall, the interfacial reactions at the CAM/solid electrolyte interface leads to the formation of oxygenated phosphorus and sulfur species, which can be accompanied by a formation of a rock-salt-like CAM phase.[24] In addition, we assume that oxidized, but not oxygenated, sulfur species such as polysulfides form near the interfaces due to electrochemical decomposition of the solid electrolyte (analogous to the current collector/solid electrolyte and carbon additive/solid electrolyte interfaces). Products such as Li_3PO_4, Li_2SO_4, and polysulfides tend to reduce the partial ionic conductivity locally in the interface region compared to the pristine CAM and solid electrolyte, resulting in an increase in resistance and thus a decrease in ASSB performance.[48,84−88] However, the actual properties of the interface layer formed depend largely on the compounds present, their precise stoichiometry and microstructure. Even for a single material in the interface region such as $LiNbO_3$, the material properties can vary significantly due to the crystallinity, defects, and the microstructure of the material (e.g., bulk vs grain boundary properties).[42,69] The complexity is further increased when interactions with other compounds in the interface region are considered. In model-type

https://dx.doi.org/10.1021/acs.chemmater.0c04660
Chem. Mater. 2021, 33, 2110−2125

experiments, pseudo-binary and pseudo-ternary phases and phase mixtures containing Li_3PO_4, Li_2SO_4, and Li_2CO_3, which are all reasonable compounds of interface layers, the influence of composition on electronic and ionic partial conductivities has already been systematically studied and was found to be strong.[85,89−91] Considering the low product fractions and small dimension of the degradation layer (nm range), the unequivocal experimental identification of specific compounds and their stoichiometries remain an enormous analytical challenge.

The $Li_2CO_3/LiNbO_3$ coating reduces but does not completely suppress the aforementioned interfacial reactions at the CAM/solid electrolyte interface, which is particular evident from the ToF-SIMS results (Figures 5 and 6). These findings are in accordance with a study by Visbal *et al.*, who observed similar trends by near-surface ToF-SIMS analyses for a diamond-like carbon coating on $LiNi_{0.8}Co_{0.15}Al_{0.05}O_2$ (NCA) in an amorphous Li_2S-P_2S_5 (75:25 mol %)-based composite cathode.[67] This suggests that the effects described seem somehow universal for thiophosphate-based ASSBs.

However, since the interfacial reaction cannot be completely prevented by the $Li_2CO_3/LiNbO_3$ coating, the question for the reason of this imperfect function arises. The remaining interfacial degradation can be related to the microstructure of the coating, namely, the coating morphology and coating composition.

The coating morphology is particulate. This implies the presence of uncoated/less-coated areas, where the interfacial reaction can occur almost unhindered. A homogenous layer is therefore preferable as a protective coating but often difficult to achieve experimentally. In addition, partial mechanical abrasion of the coating during cell assembly is conceivable, and chemomechanical volume changes during cell cycling can lead to exposure of uncoated areas.[92] Besides the morphology, also, the coating composition seems not ideal under consideration of the calculated stability against thiophosphate-based solid electrolytes.[44,93] According to Xiao *et al.*, the material combination $LiNbO_3/Li_6PS_5Cl$ has a nonnegligible negative reaction energy, which can lead to the formation of Li_3PO_4 among other products.[44] Consequently, phosphate fragments can partially also be related to the $LiNbO_3/Li_6PS_5Cl$ interface. However, the reaction energy is smaller compared to the bare NCM/Li_6PS_5Cl material combination, thus leading to a reduced driving force for the interfacial reaction. This is in accordance with our analytical results before and after battery cycling, showing a suppressed formation of decomposition products with the $Li_2CO_3/LiNbO_3$ coating.

The role of the Li_2CO_3 content in the coating is yet not completely clear. Kim et al. demonstrated that Li_2CO_3 alone may already have a beneficial effect on the ASSB performance compared to uncoated CAM.[26] However, according to a recent study by Strauss et al., the Li_2CO_3 content in the coating must be specifically tailored to the coating used.[83] The positive effect of Li_2CO_3 in many coatings can have various reasons: Taking the typical solid-state synthesis of lithium transition-metal oxides such as $LiNbO_3$ from Li_2CO_3 and Nb_2O_5 into account, a stabilizing effect of Li_2CO_3 on $LiNbO_3$ could be conceivable.[94] Considering the particulate nature of the coating, it is also possible that the positive influence of Li_2CO_3 is due to the fact that Li_2CO_3 prevents direct contact of the CAM with the solid electrolyte in less coated/uncoated areas between the coating particles. Accordingly, the Li_2CO_3 would compensate for the deficiencies of the coating microstructure and the optimum content of Li_2CO_3 would depend on the coating material and its overall microstructure. Therefore, we do not assume the Li_2CO_3 to be generally detrimental here. Nevertheless, as indicated by calculations, $LiNbO_3$ and probably also Li_2CO_3 do not seem to be the best choice and other coating materials should be more beneficial to suppress the interface reaction at the CAM/solid electrolyte interface.[44,45,93] In addition to the interface stability of the materials, it must be noted that material properties such as ionic and electrical partial conductivity play an important role in the choice of coating materials.[95] Since Li_2CO_3 has a relatively low ionic conductivity, it is certainly not an ideal coating material, although it seems to be able to partially stabilize the CAM/solid electrolyte interface compared to the uncoated interface.[96] Consequently, further optimization of the coating composition and the coating microstructure remains an important step toward long-term stable ASSBs.

Overall, the working principle of the $Li_2CO_3/LiNbO_3$ coating in this work can be related to the suppression of the interfacial reaction at the CAM/solid electrolyte interface. This leads to a reduced formation of phosphates (likely Li_3PO_4 and transition-metal phosphates) and sulfates/sulfites (likely Li_2SO_4 and transition-metal sulfates). Because the ionization probability of negatively charged phosphate and sulfate/sulfite fragments is basically high, ToF-SIMS is an excellent analytical method for investigating the protective effect of coatings in thiophosphate-based composite cathodes. In principle, it should be possible in this way to semiquantitatively benchmark the efficiency of protective coatings in suppressing interfacial reactions by using ToF-SIMS.

■ CONCLUSIONS

We investigated the influence of a $Li_2CO_3/LiNbO_3$ coating on $LiNi_{0.6}Co_{0.2}Mn_{0.2}O_2$ on the battery performance and the decomposition processes on the positive electrode side of a $Li_4Ti_5O_{12}/Li_6PS_5Cl$/Super C65|$Li_6PS_5Cl$|NCM622/$Li_6PS_5Cl$/Super C65 ASSB cell.

The coating microstructure is characterized in terms of morphology and chemical composition. A combination of FIB-SEM, XPS, and ToF-SIMS reveals a particulate coating with a mean layer thickness of ∼15 nm. The coating particles consist of an amorphous $LiNbO_3$ core, a Li_2CO_3 shell, and small quantities of carbon-containing residues form the coating procedure.

Electrochemical investigations reveal the positive effect of the protective coating on the ASSB performance. Accordingly, the capacity fading during cycling is decreased, and thus, the long-term cycling performance is significantly enhanced. Because the particulate character of the coating allows for unprotected areas and the coating composition is not ideal in terms of stability against the solid electrolyte, a less pronounced but steady capacity fading occurs.

Comprehensive post-mortem analyses of composite cathodes by using a combination of XPS and ToF-SIMS show that the CAM coating successfully suppresses the interfacial reaction at the CAM/solid electrolyte interface in terms of reduced formation of oxygenated phosphorous and sulfur compounds such as phosphates and sulfates/sulfites. In addition, we show that the formation of decomposition products in the interfacial region is successive and not fully completed after the initial cycles.

Overall, this work extends the knowledge of the working principle of protective coatings. This will help to better

https://dx.doi.org/10.1021/acs.chemmater.0c04660
Chem. Mater. 2021, 33, 2110−2125

understand the protective nature of coatings and design tailored CAM coatings and interfaces in the future. We also highlighted the suitability of ToF-SIMS for investigations on decomposition processes occurring in thiophosphate-based ASSBs. In principle, this allows for semiquantitatively benchmarking the influence of protective coatings on the decomposition processes in thiophosphate-based composite cathodes.

■ ASSOCIATED CONTENT

Supporting Information

The Supporting Information is available free of charge at https://pubs.acs.org/doi/10.1021/acs.chemmater.0c04660.

SEM images of the coated NCM622 secondary particles, ATR-IR spectra of the uncoated and Li_2CO_3/$LiNbO_3$-coated NCM622, Coulombic efficiency as a function of the cycle number, XP spectra of the Cl 2p, O 1s, Li 1s, and C 1s signals of a Li_6PS_5Cl reference and the (un)cycled composite cathodes, discussion on the Nb 3d shift in XP spectra, S 2p and P 2p detail spectra of composite cathodes with Li_2CO_3/$LiNbO_3$-coated NCM622 at different cycling stages, ROI analysis procedure scheme, and results of ROI analysis for different signal thresholds (PDF)

■ AUTHOR INFORMATION

Corresponding Author

Jürgen Janek − *Institute of Physical Chemistry, Justus Liebig University Giessen, Giessen D-35392, Germany; Center for Materials Research (LaMa), Justus Liebig University Giessen, Giessen D-35392, Germany; Battery and Electrochemistry Laboratory, Institute of Nanotechnology, Karlsruhe Institute of Technology (KIT), Eggenstein-Leopoldshafen D-76344, Germany;* orcid.org/0000-0002-9221-4756; Email: juergen.janek@phys.chemie.uni-giessen.de

Authors

Felix Walther − *Institute of Physical Chemistry, Justus Liebig University Giessen, Giessen D-35392, Germany; Center for Materials Research (LaMa), Justus Liebig University Giessen, Giessen D-35392, Germany*

Florian Strauss − *Battery and Electrochemistry Laboratory, Institute of Nanotechnology, Karlsruhe Institute of Technology (KIT), Eggenstein-Leopoldshafen D-76344, Germany;* orcid.org/0000-0001-5817-6349

Xiaohan Wu − *BASF SE, Ludwigshafen am Rhein D-67056, Germany*

Boris Mogwitz − *Institute of Physical Chemistry, Justus Liebig University Giessen, Giessen D-35392, Germany; Center for Materials Research (LaMa), Justus Liebig University Giessen, Giessen D-35392, Germany*

Jonas Hertle − *Institute of Physical Chemistry, Justus Liebig University Giessen, Giessen D-35392, Germany; Center for Materials Research (LaMa), Justus Liebig University Giessen, Giessen D-35392, Germany*

Joachim Sann − *Institute of Physical Chemistry, Justus Liebig University Giessen, Giessen D-35392, Germany; Center for Materials Research (LaMa), Justus Liebig University Giessen, Giessen D-35392, Germany*

Marcus Rohnke − *Institute of Physical Chemistry, Justus Liebig University Giessen, Giessen D-35392, Germany; Center for Materials Research (LaMa), Justus Liebig University Giessen, Giessen D-35392, Germany;* orcid.org/0000-0002-8867-950X

Torsten Brezesinski − *Battery and Electrochemistry Laboratory, Institute of Nanotechnology, Karlsruhe Institute of Technology (KIT), Eggenstein-Leopoldshafen D-76344, Germany;* orcid.org/0000-0002-4336-263X

Complete contact information is available at: https://pubs.acs.org/10.1021/acs.chemmater.0c04660

Notes

The authors declare no competing financial interest.

■ ACKNOWLEDGMENTS

The authors acknowledge financial support by BASF SE. F.S. is grateful to Fonds der Chemischen Industrie (FCI) for financial support through a Liebig fellowship. We thank J. Kulisch (BASF SE) for fruitful discussions.

■ REFERENCES

(1) Seino, Y.; Ota, T.; Takada, K.; Hayashi, A.; Tatsumisago, M. A Sulphide Lithium Super Ion Conductor Is Superior to Liquid Ion Conductors for Use in Rechargeable Batteries. *Energy Environ. Sci.* **2014**, *7*, 627−631.

(2) Janek, J.; Zeier, W. G. A Solid Future for Battery Development. *Nat. Energy* **2016**, *1*, 16141.

(3) Xu, W.; Wang, J.; Ding, F.; Chen, X.; Nasybulin, E.; Zhang, Y.; Zhang, J.-G. Lithium Metal Anodes for Rechargeable Batteries. *Energy Environ. Sci.* **2014**, *7*, 513−537.

(4) Ulvestad, A. *A Brief Review of Current Lithium Ion Battery Technology and Potential Solid State Battery Technologies*. 2018, arXiv:1803.04317. arXiv.org e-Print archive. https://arxiv.org/abs/1803.04317 (accessed November 5, 2020).

(5) Lee, Y.-G.; Fujiki, S.; Jung, C.; Suzuki, N.; Yashiro, N.; Omoda, R.; Ko, D.-S.; Shiratsuchi, T.; Sugimoto, T.; Ryu, S.; Ku, J. H.; Watanabe, T.; Park, Y.; Aihara, Y.; Im, D.; Han, I. T. High-Energy Long-Cycling All-Solid-State Lithium Metal Batteries Enabled by Silver−Carbon Composite Anodes. *Nat. Energy* **2020**, *5*, 299−308.

(6) Randau, S.; Weber, D. A.; Kötz, O.; Koerver, R.; Braun, P.; Weber, A.; Ivers-Tiffée, E.; Adermann, T.; Kulisch, J.; Zeier, W. G.; et al. Benchmarking the Performance of All-Solid-State Lithium Batteries. *Nat. Energy* **2020**, *5*, 259−270.

(7) Schnell, J.; Günther, T.; Knoche, T.; Vieider, C.; Köhler, L.; Just, A.; Keller, M.; Passerini, S.; Reinhart, G. All-Solid-State Lithium-Ion and Lithium Metal Batteries − Paving the Way to Large-Scale Production. *J. Power Sources* **2018**, *382*, 160−175.

(8) Goodenough, J. B.; Kim, Y. Challenges for Rechargeable Li Batteries. *Chem. Mater.* **2010**, *22*, 587−603.

(9) Ding, Y.; Cano, Z. P.; Yu, A.; Lu, J.; Chen, Z. Automotive Li-Ion Batteries: Current Status and Future Perspectives. *Electrochem. Energy Rev.* **2019**, *2*, 1−28.

(10) Chen, R.; Li, Q.; Yu, X.; Chen, L.; Li, H. Approaching Practically Accessible Solid-State Batteries: Stability Issues Related to Solid Electrolytes and Interfaces. *Chem. Rev.* **2020**, *120*, 6820−6877.

(11) Lee, H.; Oh, P.; Kim, J.; Cha, H.; Chae, S.; Lee, S.; Cho, J. Advances and Prospects of Sulfide All-Solid-State Lithium Batteries via One-to-One Comparison with Conventional Liquid Lithium Ion Batteries. *Adv. Mater.* **2019**, *31*, 1−26.

(12) Famprikis, T.; Canepa, P.; Dawson, J. A.; Islam, M. S.; Masquelier, C. Fundamentals of Inorganic Solid-State Electrolytes for Batteries. *Nat. Mater.* **2019**, *18*, 1278−1291.

(13) Wang, S.; Fang, R.; Li, Y.; Liu, Y.; Xin, C.; Richter, F. H.; Nan, C.-W. Interfacial Challenges for All-Solid-State Batteries Based on Sulfide Solid Electrolytes. *J. Mater.* **2021**, *7*, 209−218.

(14) Bielefeld, A.; Weber, D. A.; Janek, J. Microstructural Modeling of Composite Cathodes for All-Solid-State Batteries. *J. Phys. Chem. C* **2019**, *123*, 1626−1634.

(15) Shi, T.; Tu, Q.; Tian, Y.; Xiao, Y.; Miara, L. J.; Kononova, O.; Ceder, G. High Active Material Loading in All-Solid-State Battery Electrode via Particle Size Optimization. *Adv. Energy Mater.* **2019**, *10*, 1902881.
(16) Bielefeld, A.; Weber, D. A.; Janek, J. Modeling Effective Ionic Conductivity and Binder Influence in Composite Cathodes for All-Solid-State Batteries. *ACS Appl. Mater. Interfaces* **2020**, *12*, 12821−12833.
(17) Neumann, A.; Randau, S.; Becker-Steinberger, K.; Danner, T.; Hein, S.; Ning, Z.; Marrow, J.; Richter, F. H.; Janek, J.; Latz, A. Analysis of Interfacial Effects in All-Solid-State Batteries with Thiophosphate Solid Electrolytes. *ACS Appl. Mater. Interfaces* **2020**, *12*, 9277−9291.
(18) Park, J.; Kim, K. T.; Oh, D. Y.; Jin, D.; Kim, D.; Jung, Y. S.; Lee, Y. M. Digital Twin-Driven All-Solid-State Battery: Unraveling the Physical and Electrochemical Behaviors. *Adv. Energy Mater.* **2020**, *10*, 2001563.
(19) Park, K.-H.; Kaup, K.; Assoud, A.; Zhang, Q.; Wu, X.; Nazar, L. F. High-Voltage Superionic Halide Solid Electrolytes for All-Solid-State Li-Ion Batteries. *ACS Energy Lett.* **2020**, *5*, 533−539.
(20) Gent, W. E.; Abate, I. I.; Yang, W.; Nazar, L. F.; Chueh, W. C. Design Rules for High-Valent Redox in Intercalation Electrodes. *Joule* **2020**, *4*, 1369−1397.
(21) Culver, S. P.; Koerver, R.; Zeier, W. G.; Janek, J. On the Functionality of Coatings for Cathode Active Materials in Thiophosphate-Based All-Solid-State Batteries. *Adv. Energy Mater.* **2019**, *9*, 1900626.
(22) Gurung, A.; Pokharel, J.; Baniya, A.; Pathak, R.; Chen, K.; Lamsal, B. S.; Ghimire, N.; Zhang, W.-H.; Zhou, Y.; Qiao, Q. A Review on Strategies Addressing Interface Incompatibilities in Inorganic All-Solid-State Lithium Batteries. *Sustain. Energy Fuels* **2019**, *3*, 3279−3309.
(23) Zhang, X.-D.; Yue, F.-S.; Liang, J.-Y.; Shi, J.-L.; Li, H.; Guo, Y.-G. Structure Design of Cathode Electrodes for Solid-State Batteries: Challenges and Progress. *Small Struct.* **2020**, *1*, 2000042.
(24) Walther, F.; Randau, S.; Schneider, Y.; Sann, J.; Rohnke, M.; Richter, F. H.; Zeier, W. G.; Janek, J. Influence of Carbon Additives on the Decomposition Pathways in Cathodes of Lithium Thiophosphate-Based All-Solid-State Batteries. *Chem. Mater.* **2020**, *32*, 6123−6136.
(25) Ohta, N.; Takada, K.; Sakaguchi, I.; Zhang, L.; Ma, R.; Fukuda, K.; Osada, M.; Sasaki, T. $LiNbO_3$-Coated $LiCoO_2$ as Cathode Material for All Solid-State Lithium Secondary Batteries. *Electrochem. Commun.* **2007**, *9*, 1486−1490.
(26) Kim, A.-Y.; Strauss, F.; Bartsch, T.; Teo, J. H.; Hatsukade, T.; Mazilkin, A.; Janek, J.; Hartmann, P.; Brezesinski, T. Stabilizing Effect of a Hybrid Surface Coating on a Ni-Rich NCM Cathode Material in All-Solid-State Batteries. *Chem. Mater.* **2019**, *31*, 9664−9672.
(27) Jung, S.-K.; Gwon, H.; Lee, S.-S.; Kim, H.; Lee, J. C.; Chung, J. G.; Park, S. Y.; Aihara, Y.; Im, D. Understanding the Effects of Chemical Reactions at the Cathode−Electrolyte Interface in Sulfide Based All-Solid-State Batteries. *J. Mater. Chem. A* **2019**, *7*, 22967−22976.
(28) Jung, S. H.; Oh, K.; Nam, Y. J.; Oh, D. Y.; Brüner, P.; Kang, K.; Jung, Y. S. Li_3BO_3−Li_2CO_3: Rationally Designed Buffering Phase for Sulfide All-Solid-State Li-Ion Batteries. *Chem. Mater.* **2018**, *30*, 8190−8200.
(29) Xiong, X.; Wang, Z.; Yue, P.; Guo, H.; Wu, F.; Wang, J.; Li, X. Washing Effects on Electrochemical Performance and Storage Characteristics of $LiNi_{0.8}Co_{0.1}Mn_{0.1}O_2$ as Cathode Material for Lithium-Ion Batteries. *J. Power Sources* **2013**, *222*, 318−325.
(30) Nam, Y. J.; Park, K. H.; Oh, D. Y.; An, W. H.; Jung, Y. S. Diagnosis of Failure Modes for All-Solid-State Li-Ion Batteries Enabled by Three-Electrode Cells. *J. Mater. Chem. A* **2018**, *6*, 14867−14875.
(31) Strauss, F.; Bartsch, T.; de Biasi, L.; Kim, A.-Y.; Janek, J.; Hartmann, P.; Brezesinski, T. Impact of Cathode Material Particle Size on the Capacity of Bulk-Type All-Solid-State Batteries. *ACS Energy Lett.* **2018**, *3*, 992−996.
(32) Strauss, F.; Stepien, D.; Maibach, J.; Pfaffmann, L.; Indris, S.; Hartmann, P.; Brezesinski, T. Influence of Electronically Conductive Additives on the Cycling Performance of Argyrodite-Based All-Solid-State Batteries. *RSC Adv.* **2020**, *10*, 1114−1119.
(33) Walther, F.; Koerver, R.; Fuchs, T.; Ohno, S.; Sann, J.; Rohnke, M.; Zeier, W. G.; Janek, J. Visualization of the Interfacial Decomposition of Composite Cathodes in Argyrodite-Based All-Solid-State Batteries Using Time-of-Flight Secondary-Ion Mass Spectrometry. *Chem. Mater.* **2019**, *31*, 3745−3755.
(34) Maibach, J.; Lindgren, F.; Eriksson, H.; Edström, K.; Hahlin, M. Electric Potential Gradient at the Buried Interface between Lithium-Ion Battery Electrodes and the SEI Observed Using Photoelectron Spectroscopy. *J. Phys. Chem. Lett.* **2016**, *7*, 1775−1780.
(35) Lindgren, F.; Rehnlund, D.; Källquist, I.; Nyholm, L.; Edström, K.; Hahlin, M.; Maibach, J. Breaking Down a Complex System: Interpreting PES Peak Positions for Cycled Li-Ion Battery Electrodes. *J. Phys. Chem. C* **2017**, *121*, 27303−27312.
(36) Moulder, J. F.; Stickle, W. F.; Sobol, P. E.; Bomben, K. D. *Handbook of X-Ray Photoelectron Spectroscopy; A Reference Book of Standard Spectra for Identification and Interpretation of XPS Data*; Chastain, J., King, Jr., R. C., Eds.; Physical Electronics: Eden Prairie, US-MN, 1995.
(37) Iwanowski, R. J.; Heinonen, M.; Pracka, I.; Raczyńska, J.; Fronc, K.; Sobczak, J. W. Application of in Situ Surface Scraping for Extracting Bulk Component of XPS Signal − Example of $LiNbO_3$ and GaSb. *J. Alloys Compd.* **1999**, *286*, 162−166.
(38) Skryleva, E. A.; Kubasov, I. V.; Kiryukhantsev-Korneev, P. V.; Senatulin, B. R.; Zhukov, R. N.; Zakutailov, K. V.; Malinkovich, M. D.; Parkhomenko, Y. N. XPS Study of Li/Nb Ratio in $LiNbO_3$ Crystals. Effect of Polarity and Mechanical Processing on $LiNbO_3$ Surface Chemical Composition. *Appl. Surf. Sci.* **2016**, *389*, 387−394.
(39) Kanamura, K.; Tamura, H.; Shiraishi, S.; Takehara, Z. XPS Analysis of Lithium Surfaces Following Immersion in Various Solvents Containing $LiBF_4$. *J. Electrochem. Soc.* **1995**, *142*, 340−347.
(40) Bodenes, L.; Dedryvère, R.; Martinez, H.; Fischer, F.; Tessier, C.; Pérès, J.-P. Lithium-Ion Batteries Working at 85°C: Aging Phenomena and Electrode/Electrolyte Interfaces Studied by XPS. *J. Electrochem. Soc.* **2012**, *159*, A1739−A1746.
(41) Kosova, N. V.; Devyatkina, E. T.; Kaichev, V. V. Optimization of Ni^{2+}/Ni^{3+} Ratio in Layered $Li(Ni,Mn,Co)O_2$ Cathodes for Better Electrochemistry. *J. Power Sources* **2007**, *174*, 965−969.
(42) Glass, A. M.; Nassau, K.; Negran, T. J. Ionic Conductivity of Quenched Alkali Niobate and Tantalate Glasses. *J. Appl. Phys.* **1978**, *49*, 4808−4811.
(43) Özer, N.; Lampert, C. M. Electrochemical Lithium Insertion in Sol-Gel Deposited $LiNbO_3$ Films. *Sol. Energy Mater. Sol. Cells* **1995**, *39*, 367−375.
(44) Xiao, Y.; Miara, L. J.; Wang, Y.; Ceder, G. Computational Screening of Cathode Coatings for Solid-State Batteries. *Joule* **2019**, *3*, 1252−1275.
(45) Nolan, A. M.; Liu, Y.; Mo, Y. Solid-State Chemistries Stable with High-Energy Cathodes for Lithium-Ion Batteries. *ACS Energy Lett.* **2019**, *4*, 2444−2451.
(46) Auvergniot, J.; Cassel, A.; Foix, D.; Viallet, V.; Seznec, V.; Dedryvère, R. Redox Activity of Argyrodite Li_6PS_5Cl Electrolyte in All-Solid-State Li-Ion Battery: An XPS Study. *Solid State Ionics* **2017**, *300*, 78−85.
(47) Auvergniot, J.; Cassel, A.; Ledeuil, J. B.; Viallet, V.; Seznec, V.; Dedryvère, R. Interface Stability of Argyrodite Li_6PS_5Cl toward $LiCoO_2$, $LiNi_{1/3}Co_{1/3}Mn_{1/3}O_2$, and $LiMn_2O_4$ in Bulk All-Solid-State Batteries. *Chem. Mater.* **2017**, *29*, 3883−3890.
(48) Koerver, R.; Walther, F.; Aygün, I.; Sann, J.; Dietrich, C.; Zeier, W. G.; Janek, J. Redox-Active Cathode Interphases in Solid-State Batteries. *J. Mater. Chem. A* **2017**, *5*, 22750−22760.
(49) Koerver, R.; Aygün, I.; Leichtweiß, T.; Dietrich, C.; Zhang, W.; Binder, J. O.; Hartmann, P.; Zeier, W. G.; Janek, J. Capacity Fade in Solid-State Batteries: Interphase Formation and Chemomechanical Processes in Nickel-Rich Layered Oxide Cathodes and Lithium

https://dx.doi.org/10.1021/acs.chemmater.0c04660
Chem. Mater. 2021, 33, 2110−2125

Thiophosphate Solid Electrolytes. *Chem. Mater.* **2017**, *29*, 5574−5582.
(50) Erika, N.; Arthur, T. S.; Bonnick, P.; Suto, K.; John, M. The Discharge Mechanism for Solid-State Lithium-Sulfur Batteries. *MRS Adv.* **2019**, *4*, 2627−2634.
(51) Wang, Y.; Matsuyama, T.; Deguchi, M.; Hayashi, A.; Nakao, A.; Tatsumisago, M. X-Ray Photoelectron Spectroscopy for Sulfide Glass Electrolytes in the Systems $Li_2S-P_2S_5$ and $Li_2S-P_2S_5$−LiBr. *J. Ceram. Soc. Japan* **2016**, *124*, 597−601.
(52) Dietrich, C.; Koerver, R.; Gaultois, M. W.; Kieslich, G.; Cibin, G.; Janek, J.; Zeier, W. G. Spectroscopic Characterization of Lithium Thiophosphates by XPS and XAS − a Model to Help Monitor Interfacial Reactions in All-Solid-State Batteries. *Phys. Chem. Chem. Phys.* **2018**, *20*, 20088−20095.
(53) Tan, D. H. S.; Wu, E. A.; Nguyen, H.; Chen, Z.; Marple, M. A. T.; Doux, J.-M.; Wang, X.; Yang, H.; Banerjee, A.; Meng, Y. S. Elucidating Reversible Electrochemical Redox of Li_6PS_5Cl Solid Electrolyte. *ACS Energy Lett.* **2019**, *4*, 2418−2427.
(54) Appapillai, A. T.; Mansour, A. N.; Cho, J.; Shao-Horn, Y. Microstructure of $LiCoO_2$ with and without "$AlPO_4$" Nanoparticle Coating: Combined STEM and XPS Studies. *Chem. Mater.* **2007**, *19*, 5748−5757.
(55) Wang, B.; Liu, J.; Sun, Q.; Li, R.; Sham, T.-K.; Sun, X. Atomic Layer Deposition of Lithium Phosphates as Solid-State Electrolytes for All-Solid-State Microbatteries. *Nanotechnology* **2014**, *25*, 504007.
(56) Franke, R.; Chassé, T.; Streubel, P.; Meisel, A. Data Bank - Auger Parameters and Relaxation Energies of Phosphorus in Solid Compounds. *J. Electron Spectros. Relat. Phenom.* **1991**, *56*, 381−388.
(57) Pralong, V.; Reddy, M. A.; Caignaert, V.; Malo, S.; Lebedev, O. I.; Varadaraju, U. V.; Raveau, B. A New Form of $LiNbO_3$ with a Lamellar Structure Showing Reversible Lithium Intercalation. *Chem. Mater.* **2011**, *23*, 1915−1922.
(58) Lee, D.-C.; Shank, J. C.; Tellekamp, M. B.; Doolittle, W. A.; Alamgir, F. M. Thin-Film Lithium Niobites and Their Chemical Properties for Lithium-Ion Storage and Diffusion. *ChemElectroChem* **2019**, *6*, 5109−5115.
(59) Li, W.; Hu, C.; Zhou, M.; Wang, K.; Li, H.; Cheng, S.; Jiang, K. The Electrochemical Synthesis of $LiNbO_2$ in Molten Salts and Its Application for Lithium Ion Batteries with High Rate Capability. *Electrochim. Acta* **2016**, *189*, 231−236.
(60) Le Viet, A.; Reddy, M. V.; Jose, R.; Chowdari, B. V. R.; Ramakrishna, S. Nanostructured Nb_2O_5 Polymorphs by Electrospinning for Rechargeable Lithium Batteries. *J. Phys. Chem. C* **2010**, *114*, 664−671.
(61) Wei, M.; Wei, K.; Ichihara, M.; Zhou, H. Nb_2O_5 Nanobelts: A Lithium Intercalation Host with Large Capacity and High Rate Capability. *Electrochem. Commun.* **2008**, *10*, 980−983.
(62) Kumagai, N.; Koishikawa, Y.; Komaba, S.; Koshiba, N. Thermodynamics and Kinetics of Lithium Intercalation into Nb_2O_5 Electrodes for a 2 V Rechargeable Lithium Battery. *J. Electrochem. Soc.* **1999**, *146*, 3203−3210.
(63) Tonti, D.; Pettenkofer, C.; Jaegermann, W. Origin of the Electrochemical Potential in Intercalation Electrodes: Experimental Estimation of the Electronic and Ionic Contributions for Na Intercalated into TiS_2. *J. Phys. Chem. B* **2004**, *108*, 16093−16099.
(64) Hausbrand, R.; Becker, D.; Jaegermann, W. A Surface Science Approach to Cathode/Electrolyte Interfaces in Li-Ion Batteries: Contact Properties, Charge Transfer and Reactions. *Prog. Solid State Chem.* **2014**, *42*, 175−183.
(65) Schwöbel, A.; Jaegermann, W.; Hausbrand, R. Interfacial Energy Level Alignment and Energy Level Diagrams for All-Solid Li-Ion Cells: Impact of Li-Ion Transfer and Double Layer Formation. *Solid State Ionics* **2016**, *288*, 224−228.
(66) Cherkashinin, G.; Hausbrand, R.; Jaegermann, W. Performance of Li-Ion Batteries: Contribution of Electronic Factors to the Battery Voltage. *J. Electrochem. Soc.* **2019**, *166*, A5308−A5312.
(67) Visbal, H.; Aihara, Y.; Ito, S.; Watanabe, T.; Park, Y.; Doo, S. The Effect of Diamond-like Carbon Coating on $LiNi_{0.8}Co_{0.15}Al_{0.05}O_2$ Particles for All Solid-State Lithium-Ion Batteries Based on $Li_2SeP_2S_5$ Glass-Ceramics. *J. Power Sources* **2016**, *314*, 85−92.
(68) Ahmed, S.; Pokle, A.; Schweidler, S.; Beyer, A.; Bianchini, M.; Walther, F.; Mazilkin, A.; Hartmann, P.; Brezesinski, T.; Janek, J.; Volz, K. The Role of Intragranular Nanopores in Capacity Fade of Nickel-Rich Layered $Li(Ni_{1-x-y}Co_xMn_y)O_2$ Cathode Materials. *ACS Nano* **2019**, *13*, 10694−10704.
(69) Heitjans, P.; Masoud, M.; Feldhoff, A.; Wilkening, M. NMR and Impedance Studies of Nanocrystalline and Amorphous Ion Conductors: Lithium Niobate as a Model System. *Faraday Discuss.* **2007**, *134*, 67−82.
(70) Zhang, W.; Leichtweiß, T.; Culver, S. P.; Koerver, R.; Das, D.; Weber, D. A.; Zeier, W. G.; Janek, J. The Detrimental Effects of Carbon Additives in $Li_{10}GeP_2S_{12}$-Based Solid-State Batteries. *ACS Appl. Mater. Interfaces* **2017**, *9*, 35888−35896.
(71) Yoon, K.; Kim, J.-J.; Seong, W. M.; Lee, M. H.; Kang, K. Investigation on the Interface between $Li_{10}GeP_2S_{12}$ Electrolyte and Carbon Conductive Agents in All-Solid-State Lithium Battery. *Sci. Rep.* **2018**, *8*, 1−7.
(72) Deng, S.; Sun, Y.; Li, X.; Ren, Z.; Liang, J.; Doyle-Davis, K.; Liang, J.; Li, W.; Norouzi Banis, M.; Sun, Q.; et al. Eliminating the Detrimental Effects of Conductive Agents in Sulfide-Based Solid-State Batteries. *ACS Energy Lett.* **2020**, 1243−1251.
(73) Randau, S.; Walther, F.; Neumann, A.; Schneider, Y.; Negi, R. S.; Mogwitz, B.; Sann, J.; Becker-Steinberger, K.; Danner, T.; Hein, S.; Latz, A.; Richter, F. H.; Janek, J. On the Additive Microstructure in Composite Cathodes and Alumina-Coated Carbon Microwires for Improved All-Solid-State Batteries. *Chem. Mater.* **2021**, *4*, 1380−1393.
(74) Richards, W. D.; Miara, L. J.; Wang, Y.; Kim, J. C.; Ceder, G. Interface Stability in Solid-State Batteries. *Chem. Mater.* **2016**, *28*, 266−273.
(75) Nolan, A. M.; Zhu, Y.; He, X.; Bai, Q.; Mo, Y. Computation-Accelerated Design of Materials and Interfaces for All-Solid-State Lithium-Ion Batteries. *Joule* **2018**, *2*, 2016−2046.
(76) Lim, C. B.; Park, Y. J. Precursor-based Surface Modification of Cathodes Using Ta and W for Sulfide-based All-solid-state Batteries. *Sci. Rep.* **2020**, *10*, 10501.
(77) Zhang, Y.-Q.; Tian, Y.; Xiao, Y.; Miara, L. J.; Aihara, Y.; Tsujimura, T.; Shi, T.; Scott, M. C.; Ceder, G. Direct Visualization of the Interfacial Degradation of Cathode Coatings in Solid State Batteries: A Combined Experimental and Computational Study. *Adv. Energy Mater.* **2020**, *10*, 1903778.
(78) Bartsch, T.; Strauss, F.; Hatsukade, T.; Schiele, A.; Kim, A.-Y.; Hartmann, P.; Janek, J.; Brezesinski, T. Gas Evolution in All-Solid-State Battery Cells. *ACS Energy Lett.* **2018**, *3*, 2539−2543.
(79) Strauss, F.; Teo, J. H.; Schiele, A.; Bartsch, T.; Hatsukade, T.; Hartmann, P.; Janek, J.; Brezesinski, T. Gas Evolution in Lithium-Ion Batteries: Solid versus Liquid Electrolyte. *ACS Appl. Mater. Interfaces* **2020**, *12*, 20462−20468.
(80) Mahne, N.; Renfrew, S. E.; McCloskey, B. D.; Freunberger, S. A. Electrochemical Oxidation of Lithium Carbonate Generates Singlet Oxygen. *Angew. Chem., Int. Ed.* **2018**, *57*, 5529−5533.
(81) Hatsukade, T.; Schiele, A.; Hartmann, P.; Brezesinski, T.; Janek, J. Origin of Carbon Dioxide Evolved during Cycling of Nickel-Rich Layered NCM Cathodes. *ACS Appl. Mater. Interfaces* **2018**, *10*, 38892−38899.
(82) Wandt, J.; Freiberg, A. T. S.; Ogrodnik, A.; Gasteiger, H. A. Singlet Oxygen Evolution from Layered Transition Metal Oxide Cathode Materials and Its Implications for Lithium-Ion Batteries. *Mater. Today* **2018**, *21*, 825−833.
(83) Strauss, F.; Teo, J. H.; Maibach, J.; Kim, A.-Y.; Mazilkin, A.; Janek, J.; Brezesinski, T. Li_2ZrO_3-Coated NCM622 for Application in Inorganic Solid-State Batteries: Role of Surface Carbonates in the Cycling Performance. *ACS Appl. Mater. Interfaces* **2020**, *12*, 57146−57154.
(84) Kuwata, N.; Iwagami, N.; Matsuda, Y.; Tanji, Y.; Kawamura, J. Thin Film Batteries with Li_3PO_4 Solid Electrolyte Fabricated by Pulsed Laser Deposition. *ECS Trans.* **2019**, *16*, 53−60.

https://dx.doi.org/10.1021/acs.chemmater.0c04660
Chem. Mater. 2021, 33, 2110−2125

(85) Touboul, M.; Sephar, N.; Quarton, M. Electrical Conductivity and Phase Diagram of the System Li_2SO_4-Li_3PO_4. *Solid State Ionics* **1990**, *38*, 225−229.
(86) Wang, S.; Yan, M.; Li, Y.; Vinado, C.; Yang, J. Separating Electronic and Ionic Conductivity in Mix-Conducting Layered Lithium Transition-Metal Oxides. *J. Power Sources* **2018**, *393*, 75−82.
(87) Zahnow, J.; Bernges, T.; Wagner, A.; Bohn, N.; Binder, J. R.; Zeier, W. G.; Elm, M. T.; Janek, J. Impedance Analysis of NCM Cathode Materials: Electronic and Ionic Partial Conductivities and the Influence of Microstructure. *ACS Appl. Energy Mater.* **2021**, *4*, 1335−1345.
(88) Hakari, T.; Deguchi, M.; Mitsuhara, K.; Ohta, T.; Saito, K.; Orikasa, Y.; Uchimoto, Y.; Kowada, Y.; Hayashi, A.; Tatsumisago, M. Structural and Electronic-State Changes of a Sulfide Solid Electrolyte during the Li Deinsertion-Insertion Processes. *Chem. Mater.* **2017**, *29*, 4768−4774.
(89) Dissanayake, M. A. K. L.; Mellander, B.-E. Phase Diagram and Electrical Conductivity of the Li_2SO_4-Li_2CO_3 System. *Solid State Ionics* **1986**, *21*, 279−285.
(90) Homma, K.; Liu, Y.; Sumita, M.; Tamura, R.; Fushimi, N.; Iwata, J.; Tsuda, K.; Kaneta, C. Optimization of a Heterogeneous Ternary Li_3PO_4−Li_3BO_3−Li_2SO_4 Mixture for Li-Ion Conductivity by Machine Learning. *J. Phys. Chem. C* **2020**, *124*, 12865−12870.
(91) Nagao, K.; Nose, M.; Kato, A.; Sakuda, A.; Hayashi, A.; Tatsumisago, M. Preparation and Characterization of Glass Solid Electrolytes in the Pseudoternary System Li_3BO_3-Li_2SO_4-Li_2CO_3. *Solid State Ionics* **2017**, *308*, 68−76.
(92) Koerver, R.; Zhang, W.; de Biasi, L.; Schweidler, S.; Kondrakov, A. O.; Kolling, S.; Brezesinski, T.; Hartmann, P.; Zeier, W. G.; Janek, J. Chemo-Mechanical Expansion of Lithium Electrode Materials − on the Route to Mechanically Optimized All-Solid-State Batteries. *Energy Environ. Sci.* **2018**, *11*, 2142−2158.
(93) Zhu, Y.; He, X.; Mo, Y. First Principles Study on Electrochemical and Chemical Stability of Solid Electrolyte−Electrode Interfaces in All-Solid-State Li-Ion Batteries. *J. Mater. Chem. A* **2016**, *4*, 3253−3266.
(94) Shimada, S.; Kodaira, K.; Matsushita, T. A Study of the Formation of $LiNbO_3$ in the System Li_2CO_3-Nb_2O_5. *Thermochim. Acta* **1978**, *23*, 135−144.
(95) Nakamura, T.; Amezawa, K.; Kulisch, J.; Zeier, W. G.; Janek, J. Guidelines for All-Solid-State Battery Design and Electrode Buffer Layers Based on Chemical Potential Profile Calculation. *ACS Appl. Mater. Interfaces* **2019**, *11*, 19968−19976.
(96) Shi, S.; Qi, Y.; Li, H.; Hector, L. G., Jr. Defect Thermodynamics and Diffusion Mechanisms in Li_2CO_3 and Implications for the Solid Electrolyte Interphase in Li-Ion Batteries. *J. Phys. Chem. C* **2013**, *117*, 8579−8593.

https://dx.doi.org/10.1021/acs.chemmater.0c04660
Chem. Mater. 2021, 33, 2110−2125

4 Conclusions

In this doctoral thesis, interfacial degradation phenomena in NCM- and thiophosphate-based composite cathodes were studied in-depth. Detailed insights into the interfacial processes were provided and protective concepts to suppress interfacial degradation were developed and subsequently investigated.

As part of this thesis, the measuring capabilities of ToF-SIMS were fully exploited and routines for investigations related to degradation reactions in composite cathodes were developed and established. The combination of XPS and ToF-SIMS was found to be particularly useful to compensate for most of their individual method-related disadvantages, which include limitations in terms of lateral resolution, detection limits and the nature of information. In this way, it was possible to derive detailed compositional information related to interfacial degradation phenomena in composite cathodes.

Within this doctoral thesis, three independent reaction zones were identified within composite cathodes. This includes the interfaces of the thiophosphate-based SE towards (i) the current collector, (ii) the CAM and, if used, (iii) the conductive carbon additive.

The degradation reactions at the interfaces (i) and (iii) are mostly dominated by electrochemical decomposition reactions of the SE due to its narrow thermodynamic stability window. Although thiophosphate-based SEs are found to show redox behavior and the decomposition reactions are (partially) reversible, the typical lower cut-off potential of ASSBs is too high to allow for reduction reactions. Thus, oxidative reaction products are mostly irreversibly formed at these interfaces. A wide variety of decomposition products upon SE oxidation have been reported in the literature. Based on the results of this doctoral thesis and very recent studies, the decomposition reactions of thiophosphates are mainly driven by two reaction paths: First, anionic framework transformations of the SE towards the formation of the thermodynamically favored P_2S_5. Second, the formation of S^0-like species. For the latter, the results of this doctoral thesis indicate the formation of polysulfides (-S_x- species). Overall, the decomposition products degrade the properties of the SE (e.g., the ionic partial conductivity) and are therefore detrimental for the overall performance of the composite cathode and thus the ASSB. For this reason, the application of carbon additives, which is typically used to enhance the CAM utilization and to increase the electronic partial conductivity in common LIBs, is mostly accompanied by increased capacity fading. Thus, the application of carbon additives is often hindered in thiophosphate-based ASSBs and the beneficial effects cannot be maintained for higher cycle numbers.

Based on these results, a protective concept for conductive carbon additives was developed, which corresponds to an electronically insulation coating. The aim was to shield the potential from the SE and to prevent or at least suppress the electron transfer between SE and carbon and thus prevent decomposition reactions. In fact, the beneficial effect of the protective concept was demonstrated in a collaborative work related to this doctoral thesis and led finally to a patent application together with BASF SE.

Degradation reactions at the interface of the SE towards the CAM (interface (ii)) due to cell cycling were found to be manifold. Part of the degradation processes can be attributed to the electrochemical decomposition of the SE, analogous to interfaces (i) and (iii). In addition, it was shown in this doctoral thesis that capacity fading of NCM- and thiophosphate-based composite cathodes is accompanied by the formation of oxygenated phosphorous and sulfur species in

the NCM/SE interfacial region. Local compositional information derived by ToF-SIMS allowed to visualize the CEI formation at the NCM/SE interface with high spatial resolution corresponding to a uniform shell around NCM secondary particles. The formation of oxygenated phosphorus and sulfur species is most likely due to chemical reactions between NCM and SE, but may also be partly due to the chemical reaction of released O_2 (suggested to be partially present as singlet $^1O_2$). The latter can either originate from the NCM lattice at high SOC or from the electrochemical decomposition of Li_2CO_3, which is a typical surface contamination on Ni-rich NCM materials. Additionally, these interfacial processes can be accompanied by a rock-salt-like phase formation at the surface of the NCM particles. In contrast, no clear evidence for the formation of transition metal sulfides and transition metal phosphides was observed after cell cycling in this doctoral thesis. This suggests that the formation of transition metal sulfides, as predicted in the computational studies, is more likely to be intermediate.

Based on the results of this thesis, a reaction scheme for the interfacial reaction between NCM-based materials and β-Li_3PS_4 was proposed. It was assumed that the thermodynamically preferred reaction path involves the formation of transition metal sulfides as intermediate products which can further react to oxygenated phosphorous and sulfur compounds, for example, in a metathesis-type reaction.

In the last part of this doctoral thesis, the analytical approach developed and the knowledge gained on interfacial processes was used to study the beneficial effect of a protective Li_2CO_3/$LiNbO_3$ CAM coating on the ASSB performance in-depth. By combining FIB-SEM, XPS, and ToF-SIMS, the coating microstructure was comprehensively characterized in terms of morphology and chemical composition. The results revealed a particulate coating (mean layer thickness of ~15 nm) containing an amorphous $LiNbO_3$ core, a Li_2CO_3 shell, and a small fraction of carbon-containing residues form the coating process.

The reduced capacity fading during cell cycling could be attributed to a suppressed interfacial reaction at the CAM/SE interface, in particular, a reduced formation of oxygenated phosphorous and sulfur compounds. Thus, the protective coating seems mainly to suppress the chemical reaction of NCM and SE. Since the coating is particulate - allows for unprotected areas - and the coating composition is not ideal in terms of its stability against SE, a less pronounced, but steady capacity fading can be observed.

Overall, this doctoral thesis extends the knowledge on interfacial degradation and protective concepts in NCM- and thiophosphate-based composite cathodes considerably. This knowledge is essential to design targeted solutions for related interfacial issues, which are a key challenge on the way to long-term stability in ASSBs. In addition, this thesis provides advanced analytical approaches and measuring protocols for investigations on interfacial processes in composite cathodes. These can be easily transferred to other systems and allow, for example, to benchmark the effectiveness of protective coatings in suppressing individual degradation reactions.

5 Outlook

Several tasks and follow-up studies can be derived from this doctoral thesis, which could be considered in future work. Accordingly, three tasks related to interfacial degradation phenomena in composite cathodes are briefly presented, which are crucial for improving ASSB performance.

(i) Benchmarking CAM coatings.

Currently, it is very difficult to understand and compare the protective effects of CAM coatings, which makes it difficult to determine the most suitable CAM coatings for thiophosphate-based ASSBs. Often, an insufficient pre-characterization of the coating microstructure (morphology and composition) and an insufficient separation of the individual degradation processes in the composite cathode after cell cycling (see chapters 2.4 and 2.5) prevent a fundamental understanding of the mechanistic effects behind the improvement in ASSB performance and the often observed remaining capacity fading. In particular, for the latter, it often remains unclear whether an improper thermodynamic stability, morphological deficiencies (e.g., a too thin/too thick/inhomogeneous coating), or a non-ideal composition (e.g., impurities, stoichiometric deviations) cause such detrimental effects. A direct (quantitative) comparison of the effects of CAM coatings is therefore often not possible and fundamental conclusions on protective coatings cannot be drawn. However, benchmarking of CAM coatings is crucial to better understand the nature of the protective effect and to find the most suitable CAM coatings for thiophosphate-based ASSBs.

Essentially, a benchmarking approach for CAM coatings should comprise a comprehensive pre-characterization of the coating microstructure and electrochemical factors such as impedance, rate-performance, and long-term capacity fading, but should also include information on the interfacial processes during cell cycling to characterize the effectiveness of CAM coatings in suppressing degradation reactions. In this way, it should be possible to directly compare and understand the effects of the CAM coatings on the ASSB performance. Publication III already provides analytical approaches and measuring protocols to pre-characterize the coating microstructure and to analyze the influence of the CAM coating on the degradation processes within the composite cathode. In general, surface analysis is desirable for the latter task due to low experimental complexity, short measuring time and thus high throughput, but suffers from the detrimental influence of the current collector (see chapter 2.2). Surface cleaning routines such as sputtering with ion beams can, in principle, reduce the detrimental influence, but result in additional experimental effort and are time-consuming. Alternatively, to overcome these issues, a modified current collector was recently developed together with Jonas Hertle. This corresponds to a conventional steel stamp, which contains a small circular region (a few mm in diameter) of electrical insulator in the center of its contact area. In this area, the decomposition of the SE is suppressed and surface analyses without the related detrimental influence are possible. The suitability of this concept needs to be investigated in-depth in future studies.

(ii) Rational design of CAM coatings based on degradation products.

The results of this doctoral thesis emphasize the strong tendency of the formation of oxygenated phosphorous and sulfur species in the interfacial region of NCM and the SE. This implies that coatings based on similar chemistries could be superior to stabilize the CAM/SE interface, because the reaction between CAM and SE should be inhibited due to the pre-formation of similar products in the interfacial region. It could be advantageous here that the

composition of such an *artificial CEI* can be specifically optimized with regard to its transport properties. (Pseudo-)binary and -ternary systems containing, for example, Li_3PO_4 and Li_2SO_4 show phases with high ionic partial conductivities, which should be targeted for this approach.[127–130] Two main strategies are conceivable to prepare the coating. Accordingly, the coating could either be deposited (by various methods) on the CAM particle surface prior to cell assembly, or the coating could be achieved by a reactive-coating approach. The latter exploits the strong intrinsic tendency to form oxygenated phosphorous and sulfur species by the chemical reaction of the oxide-based CAM and the thiophosphate-based SE. In principle, utilizing local additives on the CAM particle surface opens up the possibility to specifically tune the local composition and thus the properties of the CEI formed. For this purpose, the CEI can be formed either by thermal treatments of CAM/SE/additive mixtures or intrinsically during cell operation. However, further studies are needed to verify these considerations.

(iii) CAM single crystals.

At present, polycrystalline CAMs are still predominantly used. In recently published studies it has been shown that single crystals can have significant advantages in terms of ASSB performance.[123–125] For example, by using single crystals, morphological/structural degradation effects, such as particle cracking, can be reduced, which are particularly disadvantageous for ASSBs due to the immobile SE that cannot penetrate the cracks formed during cell cycling.

From an analytical point of view, single crystals could have the advantage that the otherwise rough particle surface is smoother and thus, for example, the interface to CAM coating is more easily accessible for analytical methods. Additionally, although the lower roughness decreases the fraction of interfacial surface, which seems to be a drawback in terms of the detection limit, the single crystals are usually smaller than the polycrystalline material, which in turn increases the surface-to-volume fraction (see chapter 2.2). Overall, single crystals appear to be very promising and investigations in this direction should be undertaken in the future.

6 Literature

(1) Yoshino, A. The Birth of the Lithium-Ion Battery. *Angew. Chemie Int. Ed.* **2012**, *51* (24), 5798–5800. https://doi.org/10.1002/anie.201105006.

(2) Placke, T.; Kloepsch, R.; Dühnen, S.; Winter, M. Lithium Ion, Lithium Metal, and Alternative Rechargeable Battery Technologies: The Odyssey for High Energy Density. *J. Solid State Electrochem.* **2017**, *21* (7), 1939–1964. https://doi.org/10.1007/s10008-017-3610-7.

(3) Service, R. F. Lithium-Ion Battery Development Takes Nobel. *Science* **2019**, *366* (6463), 292–292. https://doi.org/10.1126/science.366.6463.292.

(4) Janek, J.; Adelhelm, P. Zukunftstechnologien. In *Handbuch Lithium-Ionen-Batterien*; Korthauer, R., Ed.; Springer Berlin Heidelberg: Berlin, Heidelberg, 2013; pp 199–217. https://doi.org/10.1007/978-3-642-30653-2_16.

(5) Janek, J.; Zeier, W. G. A Solid Future for Battery Development. *Nat. Energy* **2016**, *1* (9), 1–4. https://doi.org/10.1038/nenergy.2016.141.

(6) Creutzig, F.; Jochem, P.; Edelenbosch, O. Y.; Mattauch, L.; Vuuren, D. P. Van; McCollum, D.; Minx, J. Transport: A Roadblock to Climate Change Mitigation? *Science* **2015**, *350* (6263), 911–912. https://doi.org/10.1126/science.aac8033.

(7) Goodenough, J. B.; Kim, Y. Challenges for Rechargeable Li Batteries. *Chem. Mater.* **2010**, *22* (3), 587–603. https://doi.org/10.1021/cm901452z.

(8) Ding, Y.; Cano, Z. P.; Yu, A.; Lu, J.; Chen, Z. Automotive Li-Ion Batteries: Current Status and Future Perspectives. *Electrochem. Energy Rev.* **2019**, *2* (1), 1–28. https://doi.org/10.1007/s41918-018-0022-z.

(9) Xu, W.; Wang, J.; Ding, F.; Chen, X.; Nasybulin, E.; Zhang, Y.; Zhang, J.-G. Lithium Metal Anodes for Rechargeable Batteries. *Energy Environ. Sci.* **2014**, *7* (2), 513–537. https://doi.org/10.1039/C3EE40795K.

(10) Lin, D.; Liu, Y.; Cui, Y. Reviving the Lithium Metal Anode for High-Energy Batteries. *Nat. Nanotechnol.* **2017**, *12* (3), 194–206. https://doi.org/10.1038/nnano.2017.16.

(11) Albertus, P.; Babinec, S.; Litzelman, S.; Newman, A. Status and Challenges in Enabling the Lithium Metal Electrode for High-Energy and Low-Cost Rechargeable Batteries. *Nat. Energy* **2018**, *3* (1), 16–21. https://doi.org/10.1038/s41560-017-0047-2.

(12) Liu, J.; Bao, Z.; Cui, Y.; Dufek, E. J.; Goodenough, J. B.; Khalifah, P.; Li, Q.; Liaw, B. Y.; Liu, P.; Manthiram, A.; et al. Pathways for Practical High-Energy Long-Cycling Lithium Metal Batteries. *Nat. Energy* **2019**, *4* (3), 180–186. https://doi.org/10.1038/s41560-019-0338-x.

(13) Cheng, X.-B.; Zhang, R.; Zhao, C.-Z.; Zhang, Q. Toward Safe Lithium Metal Anode in Rechargeable Batteries: A Review. *Chem. Rev.* **2017**, *117* (15), 10403–10473. https://doi.org/10.1021/acs.chemrev.7b00115.

(14) Wu, F.; Maier, J.; Yu, Y. Guidelines and Trends for Next-Generation Rechargeable Lithium and Lithium-Ion Batteries. *Chem. Soc. Rev.* **2020**, *49* (5), 1569–1614. https://doi.org/10.1039/C7CS00863E.

(15) Seino, Y.; Ota, T.; Takada, K.; Hayashi, A.; Tatsumisago, M. A Sulphide Lithium Super Ion Conductor Is Superior to Liquid Ion Conductors for Use in Rechargeable Batteries. *Energy Environ. Sci.* **2014**, *7* (2), 627–631. https://doi.org/10.1039/C3EE41655K.

(16) Randau, S.; Weber, D. A.; Kötz, O.; Koerver, R.; Braun, P.; Weber, A.; Ivers-Tiffée, E.; Adermann, T.; Kulisch, J.; Zeier, W. G.; et al. Benchmarking the Performance of All-Solid-State Lithium Batteries. *Nat. Energy* **2020**, *5* (3), 259–270. https://doi.org/10.1038/s41560-020-0565-1.

(17) Lee, Y.; Fujiki, S.; Jung, C.; Suzuki, N.; Yashiro, N.; Omoda, R.; Ko, D.; Shiratsuchi, T.; Sugimoto, T.; Ryu, S.; et al. High-Energy Long-Cycling All-Solid-State Lithium Metal Batteries Enabled by Silver–Carbon Composite Anodes. *Nat. Energy* **2020**, *5* (4), 299–308. https://doi.org/10.1038/s41560-020-0575-z.

(18) Schnell, J.; Günther, T.; Knoche, T.; Vieider, C.; Köhler, L.; Just, A.; Keller, M.; Passerini, S.; Reinhart, G. All-Solid-State Lithium-Ion and Lithium Metal Batteries – Paving the Way to Large-Scale Production. *J. Power Sources* **2018**, *382*, 160–175. https://doi.org/10.1016/j.jpowsour.2018.02.062.

(19) Chen, R.; Li, Q.; Yu, X.; Chen, L.; Li, H. Approaching Practically Accessible Solid-State Batteries: Stability Issues Related to Solid Electrolytes and Interfaces. *Chem. Rev.* **2020**, *120* (14), 6820–6877. https://doi.org/10.1021/acs.chemrev.9b00268.

(20) Gao, Z.; Sun, H.; Fu, L.; Ye, F.; Zhang, Y.; Luo, W.; Huang, Y. Promises, Challenges, and Recent Progress of Inorganic Solid-State Electrolytes for All-Solid-State Lithium Batteries. *Adv. Mater.* **2018**, *30* (17), 1705702. https://doi.org/10.1002/adma.201705702.

(21) Chen, S.; Xie, D.; Liu, G.; Mwizerwa, J. P.; Zhang, Q.; Zhao, Y.; Xu, X.; Yao, X. Sulfide Solid Electrolytes for All-Solid-State Lithium Batteries: Structure, Conductivity, Stability and Application. *Energy Storage Mater.* **2018**, *14*, 58–74. https://doi.org/10.1016/j.ensm.2018.02.020.

(22) Reddy, M. V.; Julien, C. M.; Mauger, A.; Zaghib, K. Sulfide and Oxide Inorganic Solid Electrolytes for All-Solid-State Li Batteries: A Review. *Nanomaterials* **2020**, *10* (8), 1606. https://doi.org/10.3390/nano10081606.

(23) Sakuda, A.; Hayashi, A.; Tatsumisago, M. Sulfide Solid Electrolyte with Favorable Mechanical Property for All-Solid-State Lithium Battery. *Sci. Rep.* **2013**, *3* (1), 1–5. https://doi.org/10.1038/srep02261.

(24) Yamamoto, M.; Takahashi, M.; Terauchi, Y.; Kobayashi, Y.; Ikeda, S.; Sakuda, A. Fabrication of Composite Positive Electrode Sheet with High Active Material Content and Effect of Fabrication Pressure for All-Solid-State Battery. *J. Ceram. Soc. Japan* **2017**, *125* (5), 391–395. https://doi.org/10.2109/jcersj2.16321.

(25) Kato, A.; Yamamoto, M.; Sakuda, A.; Hayashi, A.; Tatsumisago, M. Mechanical Properties of Li_2S–P_2S_5 Glasses with Lithium Halides and Application in All-Solid-State Batteries. *ACS Appl. Energy Mater.* **2018**, *1* (3), 1002–1007. https://doi.org/10.1021/acsaem.7b00140.

(26) Lee, H.; Oh, P.; Kim, J.; Cha, H.; Chae, S.; Lee, S.; Cho, J. Advances and Prospects of Sulfide All-Solid-State Lithium Batteries via One-to-One Comparison with Conventional Liquid Lithium Ion Batteries. *Adv. Mater.* **2019**, *31* (29), 1900376. https://doi.org/10.1002/adma.201900376.

(27) Lau, J.; DeBlock, R. H.; Butts, D. M.; Ashby, D. S.; Choi, C. S.; Dunn, B. S. Sulfide Solid Electrolytes for Lithium Battery Applications. *Adv. Energy Mater.* **2018**, *8* (27), 1800933. https://doi.org/10.1002/aenm.201800933.

(28) Zhu, Y.; He, X.; Mo, Y. Origin of Outstanding Stability in the Lithium Solid Electrolyte Materials: Insights from Thermodynamic Analyses Based on First-Principles Calculations.

ACS Appl. Mater. Interfaces **2015**, *7* (42), 23685–23693. https://doi.org/10.1021/acsami.5b07517.

(29) Richards, W. D.; Miara, L. J.; Wang, Y.; Kim, J. C.; Ceder, G. Interface Stability in Solid-State Batteries. *Chem. Mater.* **2016**, *28* (1), 266–273. https://doi.org/10.1021/acs.chemmater.5b04082.

(30) Zhu, Y.; He, X.; Mo, Y. First Principles Study on Electrochemical and Chemical Stability of Solid Electrolyte–Electrode Interfaces in All-Solid-State Li-Ion Batteries. *J. Mater. Chem. A* **2016**, *4* (9), 3253–3266. https://doi.org/10.1039/C5TA08574H.

(31) Nolan, A. M.; Zhu, Y.; He, X.; Bai, Q.; Mo, Y. Computation-Accelerated Design of Materials and Interfaces for All-Solid-State Lithium-Ion Batteries. *Joule* **2018**, *2* (10), 2016–2046. https://doi.org/10.1016/j.joule.2018.08.017.

(32) Xiao, Y.; Miara, L. J.; Wang, Y.; Ceder, G. Computational Screening of Cathode Coatings for Solid-State Batteries. *Joule* **2019**, *3* (5), 1252–1275. https://doi.org/10.1016/j.joule.2019.02.006.

(33) Hakari, T.; Deguchi, M.; Mitsuhara, K.; Ohta, T.; Saito, K.; Orikasa, Y.; Uchimoto, Y.; Kowada, Y.; Hayashi, A.; Tatsumisago, M. Structural and Electronic-State Changes of a Sulfide Solid Electrolyte during the Li Deinsertion–Insertion Processes. *Chem. Mater.* **2017**, *29* (11), 4768–4774. https://doi.org/10.1021/acs.chemmater.7b00551.

(34) Auvergniot, J.; Cassel, A.; Foix, D.; Viallet, V.; Seznec, V.; Dedryvère, R. Redox Activity of Argyrodite Li_6PS_5Cl Electrolyte in All-Solid-State Li-Ion Battery: An XPS Study. *Solid State Ionics* **2017**, *300*, 78–85. https://doi.org/10.1016/j.ssi.2016.11.029.

(35) Auvergniot, J.; Cassel, A.; Ledeuil, J. B.; Viallet, V.; Seznec, V.; Dedryvère, R. Interface Stability of Argyrodite Li_6PS_5Cl toward $LiCoO_2$, $LiNi_{1/3}Co_{1/3}Mn_{1/3}O_2$, and $LiMn_2O_4$ in Bulk All-Solid-State Batteries. *Chem. Mater.* **2017**, *29* (9), 3883–3890. https://doi.org/10.1021/acs.chemmater.6b04990.

(36) Koerver, R.; Walther, F.; Aygün, I.; Sann, J.; Dietrich, C.; Zeier, W. G.; Janek, J. Redox-Active Cathode Interphases in Solid-State Batteries. *J. Mater. Chem. A* **2017**, *5* (43), 22750–22760. https://doi.org/10.1039/C7TA07641J.

(37) Walther, F.; Koerver, R.; Fuchs, T.; Ohno, S.; Sann, J.; Rohnke, M.; Zeier, W. G.; Janek, J. Visualization of the Interfacial Decomposition of Composite Cathodes in Argyrodite-Based All-Solid-State Batteries Using Time-of-Flight Secondary-Ion Mass Spectrometry. *Chem. Mater.* **2019**, *31* (10), 3745–3755. https://doi.org/10.1021/acs.chemmater.9b00770.

(38) Walther, F.; Randau, S.; Schneider, Y.; Sann, J.; Rohnke, M.; Richter, F. H.; Zeier, W. G.; Janek, J. Influence of Carbon Additives on the Decomposition Pathways in Cathodes of Lithium Thiophosphate-Based All-Solid-State Batteries. *Chem. Mater.* **2020**, *32* (14), 6123–6136. https://doi.org/10.1021/acs.chemmater.0c01825.

(39) Randau, S.; Walther, F.; Neumann, A.; Schneider, Y.; Negi, R. S.; Mogwitz, B.; Sann, J.; Becker-Steinberger, K.; Danner, T.; Hein, S.; et al. On the Additive Microstructure in Composite Cathodes and Alumina-Coated Carbon Microwires for Improved All-Solid-State Batteries. *Chem. Mater.* **2021**, *33* (4), 1380–1393. https://doi.org/10.1021/acs.chemmater.0c04454.

(40) Walther, F.; Strauss, F.; Wu, X.; Mogwitz, B.; Hertle, J.; Sann, J.; Rohnke, M.; Brezesinski, T.; Janek, J. The Working Principle of a Li_2CO_3/$LiNbO_3$ Coating on NCM for Thiophosphate-Based All-Solid-State Batteries. *Chem. Mater.* **2021**, *33* (6), 2110–2125.

https://doi.org/10.1021/acs.chemmater.0c04660.

(41) Culver, S. P.; Koerver, R.; Zeier, W. G.; Janek, J. On the Functionality of Coatings for Cathode Active Materials in Thiophosphate-Based All-Solid-State Batteries. *Adv. Energy Mater.* **2019**, *9* (24), 1900626. https://doi.org/10.1002/aenm.201900626.

(42) Gerischer, H.; Decker, F.; Scrosati, B. The Electronic and the Ionic Contribution to the Free Energy of Alkali Metals in Intercalation Compounds. *J. Electrochem. Soc.* **1994**, *141* (9), 2297–2300. https://doi.org/10.1149/1.2055115.

(43) Tonti, D.; Pettenkofer, C.; Jaegermann, W. Origin of the Electrochemical Potential in Intercalation Electrodes: Experimental Estimation of the Electronic and Ionic Contributions for Na Intercalated into TiS_2. *J. Phys. Chem. B* **2004**, *108* (41), 16093–16099. https://doi.org/10.1021/jp047450o.

(44) Hausbrand, R.; Becker, D.; Jaegermann, W. A Surface Science Approach to Cathode/Electrolyte Interfaces in Li-Ion Batteries: Contact Properties, Charge Transfer and Reactions. *Prog. Solid State Chem.* **2014**, *42* (4), 175–183. https://doi.org/10.1016/j.progsolidstchem.2014.04.010.

(45) Schwöbel, A.; Jaegermann, W.; Hausbrand, R. Interfacial Energy Level Alignment and Energy Level Diagrams for All-Solid Li-Ion Cells: Impact of Li-Ion Transfer and Double Layer Formation. *Solid State Ionics* **2016**, *288*, 224–228. https://doi.org/10.1016/j.ssi.2015.12.029.

(46) Cherkashinin, G.; Hausbrand, R.; Jaegermann, W. Performance of Li-Ion Batteries: Contribution of Electronic Factors to the Battery Voltage. *J. Electrochem. Soc.* **2019**, *166* (3), A5308–A5312. https://doi.org/10.1149/2.0441903jes.

(47) Chakraborty, A.; Kunnikuruvan, S.; Kumar, S.; Markovsky, B.; Aurbach, D.; Dixit, M.; Major, D. T. Layered Cathode Materials for Lithium-Ion Batteries: Review of Computational Studies on $LiNi_{1-x-y}Co_xMn_yO_2$ and $LiNi_{1-x-y}Co_xAl_yO_2$. *Chem. Mater.* **2020**, *32* (3), 915–952. https://doi.org/10.1021/acs.chemmater.9b04066.

(48) Molenda, J.; Baster, D.; Milewska, A.; Świerczek, K.; Bora, D. K.; Braun, A.; Tobola, J. Electronic Origin of Difference in Discharge Curve between Li_xCoO_2 and Na_xCoO_2 Cathodes. *Solid State Ionics* **2015**, *271*, 15–27. https://doi.org/10.1016/j.ssi.2014.09.032.

(49) Zhang, W.; Weber, D. A.; Weigand, H.; Arlt, T.; Manke, I.; Schröder, D.; Koerver, R.; Leichtweiss, T.; Hartmann, P.; Zeier, W. G.; et al. Interfacial Processes and Influence of Composite Cathode Microstructure Controlling the Performance of All-Solid-State Lithium Batteries. *ACS Appl. Mater. Interfaces* **2017**, *9* (21), 17835–17845. https://doi.org/10.1021/acsami.7b01137.

(50) Neudeck, S.; Walther, F.; Bergfeldt, T.; Suchomski, C.; Rohnke, M.; Hartmann, P.; Janek, J.; Brezesinski, T. Molecular Surface Modification of NCM622 Cathode Material Using Organophosphates for Improved Li-Ion Battery Full-Cells. *ACS Appl. Mater. Interfaces* **2018**, *10* (24), 20487–20498. https://doi.org/10.1021/acsami.8b04405.

(51) Ahmed, S.; Pokle, A.; Schweidler, S.; Beyer, A.; Bianchini, M.; Walther, F.; Mazilkin, A.; Hartmann, P.; Brezesinski, T.; Janek, J.; et al. The Role of Intragranular Nanopores in Capacity Fade of Nickel-Rich Layered $Li(Ni_{1-x-y}Co_xMn_y)O_2$ Cathode Materials. *ACS Nano* **2019**, *13* (9), 10694–10704. https://doi.org/10.1021/acsnano.9b05047.

(52) Muramatsu, H.; Hayashi, A.; Ohtomo, T.; Hama, S.; Tatsumisago, M. Structural Change of Li_2S–P_2S_5 Sulfide Solid Electrolytes in the Atmosphere. *Solid State Ionics* **2011**, *182* (1), 116–119. https://doi.org/10.1016/j.ssi.2010.10.013.

(53) Xiong, X.; Wang, Z.; Yue, P.; Guo, H.; Wu, F.; Wang, J.; Li, X. Washing Effects on Electrochemical Performance and Storage Characteristics of $LiNi_{0.8}Co_{0.1}Mn_{0.1}O_2$ as Cathode Material for Lithium-Ion Batteries. *J. Power Sources* **2013**, *222*, 318–325. https://doi.org/10.1016/j.jpowsour.2012.08.029.

(54) Liu, W.; Oh, P.; Liu, X.; Lee, M.-J.; Cho, W.; Chae, S.; Kim, Y.; Cho, J. Nickel-Rich Layered Lithium Transition-Metal Oxide for High-Energy Lithium-Ion Batteries. *Angew. Chemie Int. Ed.* **2015**, *54* (15), 4440–4457. https://doi.org/10.1002/anie.201409262.

(55) Jung, R.; Morasch, R.; Karayaylali, P.; Phillips, K.; Maglia, F.; Stinner, C.; Shao-Horn, Y.; Gasteiger, H. A. Effect of Ambient Storage on the Degradation of Ni-Rich Positive Electrode Materials (NMC811) for Li-Ion Batteries. *J. Electrochem. Soc.* **2018**, *165* (2), A132–A141. https://doi.org/10.1149/2.0401802jes.

(56) Sångeland, C.; Mindemark, J.; Younesi, R.; Brandell, D. Probing the Interfacial Chemistry of Solid-State Lithium Batteries. *Solid State Ionics* **2019**, *343*, 115068. https://doi.org/10.1016/j.ssi.2019.115068.

(57) Lou, S.; Yu, Z.; Liu, Q.; Wang, H.; Chen, M.; Wang, J. Multi-Scale Imaging of Solid-State Battery Interfaces: From Atomic Scale to Macroscopic Scale. *Chem* **2020**, *6* (9), 2199–2218. https://doi.org/10.1016/j.chempr.2020.06.030.

(58) Chen, C.; Jiang, M.; Zhou, T.; Raijmakers, L.; Vezhlev, E.; Wu, B.; Schülli, T. U.; Danilov, D. L.; Wei, Y.; Eichel, R.; et al. Interface Aspects in All-Solid-State Li-Based Batteries Reviewed. *Adv. Energy Mater.* **2021**, *11* (13), 2003939. https://doi.org/10.1002/aenm.202003939.

(59) Strauss, F.; Kitsche, D.; Ma, Y.; Teo, J. H.; Goonetilleke, D.; Janek, J.; Bianchini, M.; Brezesinski, T. Operando Characterization Techniques for All-Solid-State Lithium-Ion Batteries. *Adv. Energy Sustain. Res.* **2021**, 2100004. https://doi.org/10.1002/aesr.202100004.

(60) Vickerman, J. C.; Gilmore, I. S. *Surface Analysis – The Principal Techniques*, 2nd ed.; John Wiley & Sons, Ltd: Chichester, UK, 2009. https://doi.org/10.1002/9780470721582.

(61) van der Heide, P. *X-Ray Photoelectron Spectroscopy: An Introduction to Principles and Practices*; John Wiley & Sons, Inc.: Hoboken, NJ, USA, 2011. https://doi.org/10.1002/9781118162897.

(62) Mahoney, C. M. *Cluster Secondary Ion Mass Spectrometry: Principles and Applications*; John Wiley & Sons, Inc.: Hoboken, NJ, USA, 2013. https://doi.org/10.1002/9781118589335.

(63) van der Heide, P. *Secondary Ion Mass Spectrometry: An Introduction to Principles and Practices*; John Wiley & Sons, Inc.: Hoboken, NJ, USA, 2014. https://doi.org/10.1002/9781118916780.

(64) Ajay, A.; Schörmann, J.; Jiménez-Rodriguez, M.; Lim, C. B.; Walther, F.; Rohnke, M.; Mouton, I.; Amichi, L.; Bougerol, C.; Den Hertog, M. I.; et al. Ge Doping of GaN beyond the Mott Transition. *J. Phys. D. Appl. Phys.* **2016**, *49* (44), 445301. https://doi.org/10.1088/0022-3727/49/44/445301.

(65) Strauss, F.; de Biasi, L.; Kim, A.-Y.; Hertle, J.; Schweidler, S.; Janek, J.; Hartmann, P.; Brezesinski, T. Rational Design of Quasi-Zero-Strain NCM Cathode Materials for Minimizing Volume Change Effects in All-Solid-State Batteries. *ACS Mater. Lett.* **2020**, *2* (1), 84–88. https://doi.org/10.1021/acsmaterialslett.9b00441.

(66) Koerver, R.; Zhang, W.; de Biasi, L.; Schweidler, S.; Kondrakov, A. O.; Kolling, S.; Brezesinski, T.; Hartmann, P.; Zeier, W. G.; Janek, J. Chemo-Mechanical Expansion of Lithium Electrode Materials – on the Route to Mechanically Optimized All-Solid-State Batteries. *Energy Environ. Sci.* **2018**, *11* (8), 2142–2158. https://doi.org/10.1039/C8EE00907D.

(67) Kondrakov, A. O.; Schmidt, A.; Xu, J.; Geßwein, H.; Mönig, R.; Hartmann, P.; Sommer, H.; Brezesinski, T.; Janek, J. Anisotropic Lattice Strain and Mechanical Degradation of High- and Low-Nickel NCM Cathode Materials for Li-Ion Batteries. *J. Phys. Chem. C* **2017**, *121* (6), 3286–3294. https://doi.org/10.1021/acs.jpcc.6b12885.

(68) Shi, T.; Zhang, Y.-Q.; Tu, Q.; Wang, Y.; Scott, M. C.; Ceder, G. Characterization of Mechanical Degradation in an All-Solid-State Battery Cathode. *J. Mater. Chem. A* **2020**, *8* (34), 17399–17404. https://doi.org/10.1039/D0TA06985J.

(69) Doux, J.-M.; Yang, Y.; Tan, D. H. S.; Nguyen, H.; Wu, E. A.; Wang, X.; Banerjee, A.; Meng, Y. S. Pressure Effects on Sulfide Electrolytes for All Solid-State Batteries. *J. Mater. Chem. A* **2020**, *8* (10), 5049–5055. https://doi.org/10.1039/C9TA12889A.

(70) Jung, S. H.; Kim, U.; Kim, J.; Jun, S.; Yoon, C. S.; Jung, Y. S.; Sun, Y. Ni-Rich Layered Cathode Materials with Electrochemo-Mechanically Compliant Microstructures for All-Solid-State Li Batteries. *Adv. Energy Mater.* **2020**, *10* (6), 1903360. https://doi.org/10.1002/aenm.201903360.

(71) Schweidler, S.; de Biasi, L.; Garcia, G.; Mazilkin, A.; Hartmann, P.; Brezesinski, T.; Janek, J. Investigation into Mechanical Degradation and Fatigue of High-Ni NCM Cathode Material: A Long-Term Cycling Study of Full Cells. *ACS Appl. Energy Mater.* **2019**, *2* (10), 7375–7384. https://doi.org/10.1021/acsaem.9b01354.

(72) Dewald, G. F.; Ohno, S.; Kraft, M. A.; Koerver, R.; Till, P.; Vargas-Barbosa, N. M.; Janek, J.; Zeier, W. G. Experimental Assessment of the Practical Oxidative Stability of Lithium Thiophosphate Solid Electrolytes. *Chem. Mater.* **2019**, *31* (20), 8328–8337. https://doi.org/10.1021/acs.chemmater.9b01550.

(73) Koerver, R.; Aygün, I.; Leichtweiß, T.; Dietrich, C.; Zhang, W.; Binder, J. O.; Hartmann, P.; Zeier, W. G.; Janek, J. Capacity Fade in Solid-State Batteries: Interphase Formation and Chemomechanical Processes in Nickel-Rich Layered Oxide Cathodes and Lithium Thiophosphate Solid Electrolytes. *Chem. Mater.* **2017**, *29* (13), 5574–5582. https://doi.org/10.1021/acs.chemmater.7b00931.

(74) Erika, N.; Arthur, T. S.; Bonnick, P.; Suto, K.; John, M. The Discharge Mechanism for Solid-State Lithium-Sulfur Batteries. *MRS Adv.* **2019**, *4* (49), 2627–2634. https://doi.org/10.1557/adv.2019.255.

(75) Wang, Y.; Matsuyama, T.; Deguchi, M.; Hayashi, A.; Nakao, A.; Tatsumisago, M. X-Ray Photoelectron Spectroscopy for Sulfide Glass Electrolytes in the Systems Li_2S–P_2S_5 and Li_2S–P_2S_5–LiBr. *J. Ceram. Soc. Japan* **2016**, *124* (5), 597–601. https://doi.org/10.2109/jcersj2.16006.

(76) Dietrich, C.; Koerver, R.; Gaultois, M. W.; Kieslich, G.; Cibin, G.; Janek, J.; Zeier, W. G. Spectroscopic Characterization of Lithium Thiophosphates by XPS and XAS – a Model to Help Monitor Interfacial Reactions in All-Solid-State Batteries. *Phys. Chem. Chem. Phys.* **2018**, *20* (30), 20088–20095. https://doi.org/10.1039/C8CP01968A.

(77) Tan, D. H. S.; Wu, E. A.; Nguyen, H.; Chen, Z.; Marple, M. A. T.; Doux, J.; Wang, X.; Yang, H.; Banerjee, A.; Meng, Y. S. Elucidating Reversible Electrochemical Redox of Li_6PS_5Cl Solid Electrolyte. *ACS Energy Lett.* **2019**, *4* (10), 2418–2427.

https://doi.org/10.1021/acsenergylett.9b01693.

(78) Swamy, T.; Chen, X.; Chiang, Y.-M. Electrochemical Redox Behavior of Li Ion Conducting Sulfide Solid Electrolytes. *Chem. Mater.* **2019**, *31* (3), 707–713. https://doi.org/10.1021/acs.chemmater.8b03420.

(79) Schwietert, T. K.; Arszelewska, V. A.; Wang, C.; Yu, C.; Vasileiadis, A.; de Klerk, N. J. J.; Hageman, J.; Hupfer, T.; Kerkamm, I.; Xu, Y.; et al. Clarifying the Relationship between Redox Activity and Electrochemical Stability in Solid Electrolytes. *Nat. Mater.* **2020**, *19* (4), 428–435. https://doi.org/10.1038/s41563-019-0576-0.

(80) Wang, S.; Tang, M.; Zhang, Q.; Li, B.; Ohno, S.; Walther, F.; Pan, R.; Xu, X.; Xin, C.; Zhang, W.; et al. Lithium Argyrodite as Solid Electrolyte and Cathode Precursor for Solid-State Batteries with Long Cycle Life. **2021**, *submitted.*

(81) Park, S. W.; Oh, G.; Park, J.; Ha, Y.; Lee, S.; Yoon, S. Y.; Kim, B. G. Graphitic Hollow Nanocarbon as a Promising Conducting Agent for Solid-State Lithium Batteries. *Small* **2019**, *15* (18), 1900235. https://doi.org/10.1002/smll.201900235.

(82) Tang, H.; Deng, Z.; Lin, Z.; Wang, Z.; Chu, I.-H.; Chen, C.; Zhu, Z.; Zheng, C.; Ong, S. P. Probing Solid–Solid Interfacial Reactions in All-Solid-State Sodium-Ion Batteries with First-Principles Calculations. *Chem. Mater.* **2018**, *30* (1), 163–173. https://doi.org/10.1021/acs.chemmater.7b04096.

(83) Haruyama, J.; Sodeyama, K.; Tateyama, Y. Cation Mixing Properties toward Co Diffusion at the $LiCoO_2$ Cathode/Sulfide Electrolyte Interface in a Solid-State Battery. *ACS Appl. Mater. Interfaces* **2017**, *9* (1), 286–292. https://doi.org/10.1021/acsami.6b08435.

(84) Sakuda, A.; Hayashi, A.; Tatsumisago, M. Interfacial Observation between $LiCoO_2$ Electrode and Li_2S–P_2S_5 Solid Electrolytes of All-Solid-State Lithium Secondary Batteries Using Transmission Electron Microscopy. *Chem. Mater.* **2010**, *22* (3), 949–956. https://doi.org/10.1021/cm901819c.

(85) Visbal, H.; Aihara, Y.; Ito, S.; Watanabe, T.; Park, Y.; Doo, S. The Effect of Diamond-like Carbon Coating on $LiNi_{0.8}Co_{0.15}Al_{0.05}O_2$ Particles for All Solid-State Lithium-Ion Batteries Based on Li_2S–P_2S_5 Glass-Ceramics. *J. Power Sources* **2016**, *314*, 85–92. https://doi.org/10.1016/j.jpowsour.2016.02.088.

(86) Tsukasaki, H.; Uchiyama, T.; Yamamoto, K.; Mori, S.; Uchimoto, Y.; Kowada, H.; Hayashi, A.; Tatsumisago, M. Exothermal Mechanisms in the Charged $LiNi_{1/3}Mn_{1/3}Co_{1/3}O_2$ Electrode Layers for Sulfide-Based All-Solid-State Lithium Batteries. *J. Power Sources* **2019**, *434*, 226714. https://doi.org/10.1016/j.jpowsour.2019.226714.

(87) Zhang, Y.; Tian, Y.; Xiao, Y.; Miara, L. J.; Aihara, Y.; Tsujimura, T.; Shi, T.; Scott, M. C.; Ceder, G. Direct Visualization of the Interfacial Degradation of Cathode Coatings in Solid State Batteries: A Combined Experimental and Computational Study. *Adv. Energy Mater.* **2020**, *10* (27), 1903778. https://doi.org/10.1002/aenm.201903778.

(88) Jung, S.-K.; Gwon, H.; Lee, S.-S.; Kim, H.; Lee, J. C.; Chung, J. G.; Park, S. Y.; Aihara, Y.; Im, D. Understanding the Effects of Chemical Reactions at the Cathode–Electrolyte Interface in Sulfide Based All-Solid-State Batteries. *J. Mater. Chem. A* **2019**, *7* (40), 22967–22976. https://doi.org/10.1039/C9TA08517C.

(89) Lim, C. B.; Park, Y. J. Precursor-Based Surface Modification of Cathodes Using Ta and W for Sulfide-Based All-Solid-State Batteries. *Sci. Rep.* **2020**, *10* (1), 10501. https://doi.org/10.1038/s41598-020-67493-6.

(90) Jung, S. H.; Oh, K.; Nam, Y. J.; Oh, D. Y.; Brüner, P.; Kang, K.; Jung, Y. S. Li_3BO_3–Li_2CO_3: Rationally Designed Buffering Phase for Sulfide All-Solid-State Li-Ion Batteries. *Chem. Mater.* **2018**, *30* (22), 8190–8200. https://doi.org/10.1021/acs.chemmater.8b03321.

(91) Banerjee, A.; Tang, H.; Wang, X.; Cheng, J.-H.; Nguyen, H.; Zhang, M.; Tan, D. H. S.; Wynn, T. A.; Wu, E. A.; Doux, J.-M.; et al. Revealing Nanoscale Solid–Solid Interfacial Phenomena for Long-Life and High-Energy All-Solid-State Batteries. *ACS Appl. Mater. Interfaces* **2019**, *11* (46), 43138–43145. https://doi.org/10.1021/acsami.9b13955.

(92) Maibach, J.; Lindgren, F.; Eriksson, H.; Edström, K.; Hahlin, M. Electric Potential Gradient at the Buried Interface between Lithium-Ion Battery Electrodes and the SEI Observed Using Photoelectron Spectroscopy. *J. Phys. Chem. Lett.* **2016**, *7* (10), 1775–1780. https://doi.org/10.1021/acs.jpclett.6b00391.

(93) Lindgren, F.; Rehnlund, D.; Källquist, I.; Nyholm, L.; Edström, K.; Hahlin, M.; Maibach, J. Breaking Down a Complex System: Interpreting PES Peak Positions for Cycled Li-Ion Battery Electrodes. *J. Phys. Chem. C* **2017**, *121* (49), 27303–27312. https://doi.org/10.1021/acs.jpcc.7b08923.

(94) Yamagishi, Y.; Morita, H.; Nomura, Y.; Igaki, E. Visualizing Lithium Distribution and Degradation of Composite Electrodes in Sulfide-Based All-Solid-State Batteries Using Operando Time-of-Flight Secondary Ion Mass Spectrometry. *ACS Appl. Mater. Interfaces* **2021**, *13* (1), 580–586. https://doi.org/10.1021/acsami.0c18505.

(95) Zuo, T.; Rueß, R.; Pan, R.; Walther, F.; Rohnke, M.; Schröder, D.; Janek, J. Diffusion-Controlled Interfacial Degradation of the NCM/LGPS Composite Cathode in Solid-State Batteries. **2021**, *submitted.*

(96) Bartsch, T.; Strauss, F.; Hatsukade, T.; Schiele, A.; Kim, A.-Y.; Hartmann, P.; Janek, J.; Brezesinski, T. Gas Evolution in All-Solid-State Battery Cells. *ACS Energy Lett.* **2018**, *3* (10), 2539–2543. https://doi.org/10.1021/acsenergylett.8b01457.

(97) Strauss, F.; Teo, J. H.; Schiele, A.; Bartsch, T.; Hatsukade, T.; Hartmann, P.; Janek, J.; Brezesinski, T. Gas Evolution in Lithium-Ion Batteries: Solid versus Liquid Electrolyte. *ACS Appl. Mater. Interfaces* **2020**, *12* (18), 20462–20468. https://doi.org/10.1021/acsami.0c02872.

(98) Kim, A.-Y.; Strauss, F.; Bartsch, T.; Teo, J. H.; Hatsukade, T.; Mazilkin, A.; Janek, J.; Hartmann, P.; Brezesinski, T. Stabilizing Effect of a Hybrid Surface Coating on a Ni-Rich NCM Cathode Material in All-Solid-State Batteries. *Chem. Mater.* **2019**, *31* (23), 9664–9672. https://doi.org/10.1021/acs.chemmater.9b02947.

(99) Strauss, F.; Teo, J. H.; Maibach, J.; Kim, A.-Y.; Mazilkin, A.; Janek, J.; Brezesinski, T. Li_2ZrO_3-Coated NCM622 for Application in Inorganic Solid-State Batteries: Role of Surface Carbonates in the Cycling Performance. *ACS Appl. Mater. Interfaces* **2020**, *12* (51), 57146–57154. https://doi.org/10.1021/acsami.0c18590.

(100) Hatsukade, T.; Schiele, A.; Hartmann, P.; Brezesinski, T.; Janek, J. Origin of Carbon Dioxide Evolved during Cycling of Nickel-Rich Layered NCM Cathodes. *ACS Appl. Mater. Interfaces* **2018**, *10* (45), 38892–38899. https://doi.org/10.1021/acsami.8b13158.

(101) Wang, R.; Yu, X.; Bai, J.; Li, H.; Huang, X.; Chen, L.; Yang, X. Electrochemical Decomposition of Li_2CO_3 in NiO–Li_2CO_3 Nanocomposite Thin Film and Powder Electrodes. *J. Power Sources* **2012**, *218*, 113–118. https://doi.org/10.1016/j.jpowsour.2012.06.082.

(102) Shi, S.; Qi, Y.; Li, H.; Hector, L. G. Defect Thermodynamics and Diffusion Mechanisms in Li_2CO_3 and Implications for the Solid Electrolyte Interphase in Li-Ion Batteries. *J. Phys. Chem. C* **2013**, *117* (17), 8579–8593. https://doi.org/10.1021/jp310591u.

(103) Ling, C.; Zhang, R.; Takechi, K.; Mizuno, F. Intrinsic Barrier to Electrochemically Decompose Li_2CO_3 and LiOH. *J. Phys. Chem. C* **2014**, *118* (46), 26591–26598. https://doi.org/10.1021/jp5093306.

(104) Mahne, N.; Renfrew, S. E.; McCloskey, B. D.; Freunberger, S. A. Electrochemical Oxidation of Lithium Carbonate Generates Singlet Oxygen. *Angew. Chemie Int. Ed.* **2018**, *57* (19), 5529–5533. https://doi.org/10.1002/anie.201802277.

(105) Wandt, J.; Freiberg, A. T. S.; Ogrodnik, A.; Gasteiger, H. A. Singlet Oxygen Evolution from Layered Transition Metal Oxide Cathode Materials and Its Implications for Lithium-Ion Batteries. *Mater. Today* **2018**, *21* (8), 825–833. https://doi.org/10.1016/j.mattod.2018.03.037.

(106) Gurung, A.; Pokharel, J.; Baniya, A.; Pathak, R.; Chen, K.; Lamsal, B. S.; Ghimire, N.; Zhang, W.-H.; Zhou, Y.; Qiao, Q. A Review on Strategies Addressing Interface Incompatibilities in Inorganic All-Solid-State Lithium Batteries. *Sustain. Energy Fuels* **2019**, *3* (12), 3279–3309. https://doi.org/10.1039/C9SE00549H.

(107) Zhang, X.-D.; Yue, F.-S.; Liang, J.-Y.; Shi, J.-L.; Li, H.; Guo, Y.-G. Structure Design of Cathode Electrodes for Solid-State Batteries: Challenges and Progress. *Small Struct.* **2020**, *1* (3), 2000042. https://doi.org/10.1002/sstr.202000042.

(108) Deng, S.; Sun, Y.; Li, X.; Ren, Z.; Liang, J.; Doyle-Davis, K.; Liang, J.; Li, W.; Norouzi Banis, M.; Sun, Q.; et al. Eliminating the Detrimental Effects of Conductive Agents in Sulfide-Based Solid-State Batteries. *ACS Energy Lett.* **2020**, *5* (4), 1243–1251. https://doi.org/10.1021/acsenergylett.0c00256.

(109) Takada, K. Progress and Prospective of Solid-State Lithium Batteries. *Acta Mater.* **2013**, *61* (3), 759–770. https://doi.org/10.1016/j.actamat.2012.10.034.

(110) Haruyama, J.; Sodeyama, K.; Han, L.; Takada, K.; Tateyama, Y. Space–Charge Layer Effect at Interface between Oxide Cathode and Sulfide Electrolyte in All-Solid-State Lithium-Ion Battery. *Chem. Mater.* **2014**, *26* (14), 4248–4255. https://doi.org/10.1021/cm5016959.

(111) de Klerk, N. J. J.; Wagemaker, M. Space-Charge Layers in All-Solid-State Batteries; Important or Negligible? *ACS Appl. Energy Mater.* **2018**, *1* (10), 5609–5618. https://doi.org/10.1021/acsaem.8b01141.

(112) Nomura, Y.; Yamamoto, K.; Hirayama, T.; Ouchi, S.; Igaki, E.; Saitoh, K. Direct Observation of a Li-Ionic Space-Charge Layer Formed at an Electrode/Solid-Electrolyte Interface. *Angew. Chemie* **2019**, *131* (16), 5346–5350. https://doi.org/10.1002/ange.201814669.

(113) Cheng, Z.; Liu, M.; Ganapathy, S.; Li, C.; Li, Z.; Zhang, X.; He, P.; Zhou, H.; Wagemaker, M. Revealing the Impact of Space-Charge Layers on the Li-Ion Transport in All-Solid-State Batteries. *Joule* **2020**, *4* (6), 1311–1323. https://doi.org/10.1016/j.joule.2020.04.002.

(114) Nakamura, T.; Amezawa, K.; Kulisch, J.; Zeier, W. G.; Janek, J. Guidelines for All-Solid-State Battery Design and Electrode Buffer Layers Based on Chemical Potential Profile Calculation. *ACS Appl. Mater. Interfaces* **2019**, *11* (22), 19968–19976. https://doi.org/10.1021/acsami.9b03053.

(115) Nolan, A. M.; Liu, Y.; Mo, Y. Solid-State Chemistries Stable with High-Energy Cathodes for Lithium-Ion Batteries. *ACS Energy Lett.* **2019**, *4* (10), 2444–2451. https://doi.org/10.1021/acsenergylett.9b01703.

(116) Xiao, Y.; Wang, Y.; Bo, S.-H.; Kim, J. C.; Miara, L. J.; Ceder, G. Understanding Interface Stability in Solid-State Batteries. *Nat. Rev. Mater.* **2020**, *5* (2), 105–126. https://doi.org/10.1038/s41578-019-0157-5.

(117) Ito, Y.; Sakurai, Y.; Yubuchi, S.; Sakuda, A.; Hayashi, A.; Tatsumisago, M. Application of $LiCoO_2$ Particles Coated with Lithium Ortho-Oxosalt Thin Films to Sulfide-Type All-Solid-State Lithium Batteries. *J. Electrochem. Soc.* **2015**, *162* (8), A1610–A1616. https://doi.org/10.1149/2.0771508jes.

(118) Yubuchi, S.; Ito, Y.; Matsuyama, T.; Hayashi, A.; Tatsumisago, M. 5 V Class $LiNi_{0.5}Mn_{1.5}O_4$ Positive Electrode Coated with Li_3PO_4 Thin Film for All-Solid-State Batteries Using Sulfide Solid Electrolyte. *Solid State Ionics* **2016**, *285*, 79–82. https://doi.org/10.1016/j.ssi.2015.08.001.

(119) Ohta, N.; Takada, K.; Zhang, L.; Ma, R.; Osada, M.; Sasaki, T. Enhancement of the High-Rate Capability of Solid-State Lithium Batteries by Nanoscale Interfacial Modification. *Adv. Mater.* **2006**, *18* (17), 2226–2229. https://doi.org/10.1002/adma.200502604.

(120) Thierfelder, C.; Sanna, S.; Schindlmayr, A.; Schmidt, W. G. Do We Know the Band Gap of Lithium Niobate? *Phys. status solidi* **2010**, *7* (2), 362–365. https://doi.org/10.1002/pssc.200982473.

(121) Lee, S.-H.; Jin, B.-S.; Kim, H.-S. Superior Performances of B-Doped $LiNi_{0.84}Co_{0.10}Mn_{0.06}O_2$ Cathode for Advanced LIBs. *Sci. Rep.* **2019**, *9* (1), 17541. https://doi.org/10.1038/s41598-019-54115-z.

(122) Sun, H. H.; Ryu, H.-H.; Kim, U.-H.; Weeks, J. A.; Heller, A.; Sun, Y.-K.; Mullins, C. B. Beyond Doping and Coating: Prospective Strategies for Stable High-Capacity Layered Ni-Rich Cathodes. *ACS Energy Lett.* **2020**, *5* (4), 1136–1146. https://doi.org/10.1021/acsenergylett.0c00191.

(123) Liu, X.; Zheng, B.; Zhao, J.; Zhao, W.; Liang, Z.; Su, Y.; Xie, C.; Zhou, K.; Xiang, Y.; Zhu, J.; et al. Electrochemo-Mechanical Effects on Structural Integrity of Ni-Rich Cathodes with Different Microstructures in All Solid-State Batteries. *Adv. Energy Mater.* **2021**, *11* (8), 2003583. https://doi.org/10.1002/aenm.202003583.

(124) Li, X.; Peng, W.; Tian, R.; Song, D.; Wang, Z.; Zhang, H.; Zhu, L.; Zhang, L. Excellent Performance Single-Crystal NCM Cathode under High Mass Loading for All-Solid-State Lithium Batteries. *Electrochim. Acta* **2020**, *363*, 137185. https://doi.org/10.1016/j.electacta.2020.137185.

(125) Fantin, R.; Trevisanello, E.; Ruess, R.; Pokle, A.; Conforto, G.; Richter, F. H.; Volz, K.; Janek, J. Synthesis and Postprocessing of Single-Crystalline $LiNi_{0.8}Co_{0.15}Al_{0.05}O_2$ for Solid-State Lithium-Ion Batteries with High Capacity and Long Cycling Stability. *Chem. Mater.* **2021**, *33* (7), 2624–2634. https://doi.org/10.1021/acs.chemmater.1c00471.

(126) Trevisanello, E.; Ruess, R.; Conforto, G.; Richter, F. H.; Janek, J. Polycrystalline and Single Crystalline NCM Cathode Materials—Quantifying Particle Cracking, Active Surface Area, and Lithium Diffusion. *Adv. Energy Mater.* **2021**, *11* (18), 2003400. https://doi.org/10.1002/aenm.202003400.

(127) Touboul, M.; Sephar, N.; Quarton, M. Electrical Conductivity and Phase Diagram of the System Li_2SO_4-Li_3PO_4. *Solid State Ionics* **1990**, *38* (3–4), 225–229.

https://doi.org/10.1016/0167-2738(90)90425-Q.

(128) Dissanayake, M. A. K. L.; Mellander, B.-E. Phase Diagram and Electrical Conductivity of the Li_2SO_4-Li_2CO_3 System. *Solid State Ionics* **1986**, *21* (4), 279–285. https://doi.org/10.1016/0167-2738(86)90190-6.

(129) Nagao, K.; Nose, M.; Kato, A.; Sakuda, A.; Hayashi, A.; Tatsumisago, M. Preparation and Characterization of Glass Solid Electrolytes in the Pseudoternary System Li_3BO_3-Li_2SO_4-Li_2CO_3. *Solid State Ionics* **2017**, *308*, 68–76. https://doi.org/10.1016/j.ssi.2017.05.009.

(130) Homma, K.; Liu, Y.; Sumita, M.; Tamura, R.; Fushimi, N.; Iwata, J.; Tsuda, K.; Kaneta, C. Optimization of a Heterogeneous Ternary Li_3PO_4–Li_3BO_3–Li_2SO_4 Mixture for Li-Ion Conductivity by Machine Learning. *J. Phys. Chem. C* **2020**, *124* (24), 12865–12870. https://doi.org/10.1021/acs.jpcc.9b11654.

7 Appendix

7.1 Supporting Information

7.1.1 Publication I

Supporting Information

Visualization of the Interfacial Decomposition of Composite Cathodes in Argyrodite-Based All-Solid-State Batteries Using Time-of-Flight Secondary-Ion Mass Spectrometry

Felix Walther [a,b], Raimund Koerver [a,b], Till Fuchs [a,b], Saneyuki Ohno [a,b], Joachim Sann [a,b], Marcus Rohnke [a,b], Wolfgang G. Zeier [a,b] and Jürgen Janek [a,b,*]

[a] *Institute of Physical Chemistry, Justus-Liebig-University Giessen, Heinrich-Buff-Ring 17, D-35392 Giessen, Germany.*

[b] *Center for Materials Research (LaMa), Justus-Liebig-University Giessen, Heinrich-Buff-Ring 16, D-35392 Giessen, Germany.*

X-ray Diffraction (XRD)

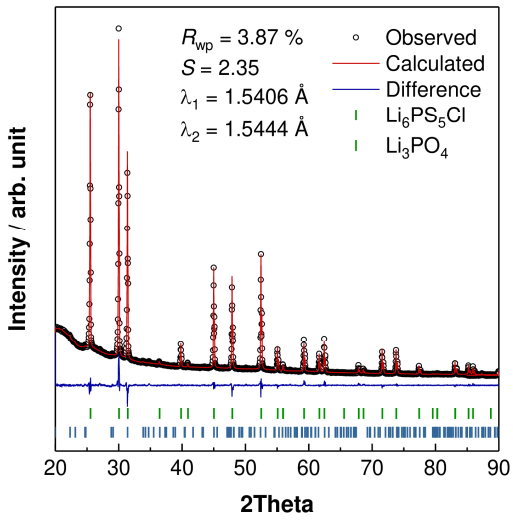

Figure S1 - Shown is the X-ray diffraction pattern of the synthesized Li_6PS_5Cl. A PANalytical Empyrean powder diffractometer in Bragg-Brentano geometry equipped with a Cu Kα radiation source was used. The step size during the measurement was 0.026°. A silicon zero background holder with a polyimide foil (Kapton) was used to avoid air- and moisture-induced decomposition during the measurements. Rietveld refinements were performed with the software package TOPAS-Academic V6 (Bruker Corporation). Thompson-Cox-Hastings pseudo-Voigt functions were used for the profiles. The XRD pattern reveals a highly pure material. Only 2 wt% of Li_3PO_4 was found.

Scanning Electron Microscopy (SEM)

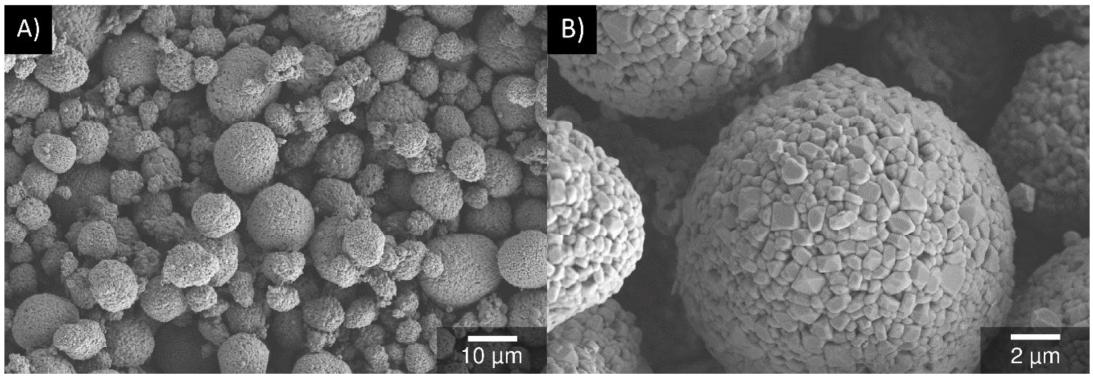

Figure S2 - Scanning electron micrographs showing the morphology and microstructure of the pristine NCM622 particles: A) Overview image, B) Secondary particle surface.

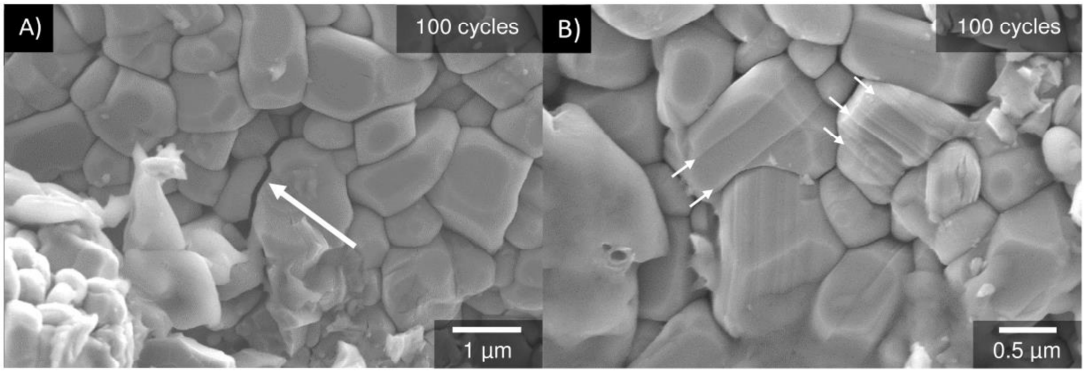

Figure S3 - Scanning electron micrographs of the secondary particle surface of the composite cathode after 100 cycles. Microstructure images were obtained from disassembled cells. The NCM622 particles show signs of chemo-mechanical degradation after battery cycling: A) Particle cracks and fragmentation, B) Stacking sequence changes of the NCM622.

X-ray Photoelectron Spectroscopy (XPS)

Detail spectra of Li 1s and Ni 2p

Figure S4 shows the detail spectra of the Li 1s and the Ni 2p signal of the Li_6PS_5Cl reference, the cycled and the uncycled composite cathode after surface cleaning (see below). The spectra were measured with a pass energy of 46.95 eV and calibrated in relation to the signal of adventitious carbon at 284.8 eV. Both signals do not show a significant influence by battery cycling. In the case of the Ni 2p signal, a slightly oxidized signal shoulder seems to occur after battery cycling. Actually, this shoulder depends on the sputter depth and changes without any trend. Thus, the slightly oxidized shoulder cannot be unambiguously assigned to battery cycling. The binding energies of the Li 1s and the Ni 2p signal fit to reported values for the Li_6PS_5Cl argyrodite and NCM materials, respectively.[1–3] The formation of LiCl, which was reported for example for the composite cathode of a $Li_4Ti_5O_{12}/Li_6PS_5Cl/LiCoO_2$ full cell, is not observed as clearly here and thus seems to play a minor role in our cell set-up.

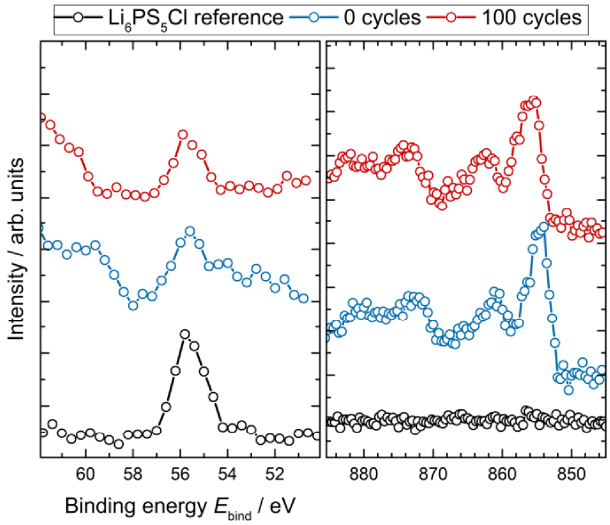

Figure S4 - XP spectra of the Li 1s and the Ni 2p signal of the Li_6PS_5Cl reference, the uncycled and the cycled composite cathode. All spectra were calibrated in relation to the signal of adventitious carbon at 284.8 eV.

Influence of surface cleaning on the S 2p signal

Since surface impurities such as adsorbates significantly decrease the signal intensity and have an influence on the detected signal features, the surface was cleaned by gentle sputtering with Ar^+ ions. The acceleration voltage was 0.5 kV and the rasterized area was (6 × 6) mm^2 to enable a low impact on the sample surface. Depth profiling was performed in order to monitor signal changes and to be able to identify possible disturbing effects caused by sputtering. Figure S5 shows the S 2p signal as a function of the sputtering time. Weak sulfite and sulfate signals can be detected on the surface and disappear as a result of sputtering. At the same time, the overall signal intensity increases significantly and reaches a maximum. It can be seen that the signal contributions of the main signal are maintained and are not modified by further sputtering, indicating a gentle sputter process with minor influence on the signal features. The disappearance of SO_x signals due to sputtering can have various causes. One possibility is a surface contamination. As shown in the manuscript, due to the high reactivity of the argyrodite small amounts of water and oxygen (even in the ppm range) can lead to the formation of sulfates such as Li_2SO_4. Accordingly, the surface contamination is removed by sputtering until the concentration is below the detection limit of XPS. However, the ToF-SIMS analysis also revealed SO_x^- fragments in the bulk.

The other possibility is based on the orientation of the analyzed surface to the current collector in the ASSB. Koerver *et al.* have shown that the concentration of degradation products in ASSBs based on thiophosphates is increased towards the current collector[4]. Bielefeld *et al.* showed that this can partially be attributed to the lower contact probability of the NCM particles away from the current collector[5].

Our analysis takes place on the surface that was oriented towards the current collector. Therefore, it seems reasonable that the concentration of degradation products is higher on the surface and decreases due to sputtering. Below a certain concentration, the degradation products are no longer detectable with XPS, but still with ToF-SIMS.

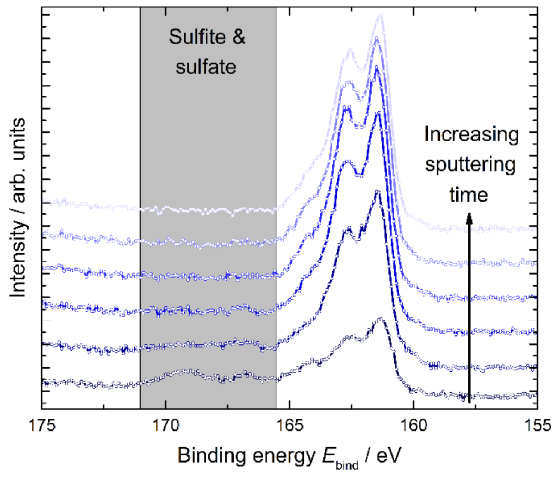

Figure S5 - XP spectra of the S 2p signal of the cycled composite cathode depending on the sputtering time. All spectra were calibrated in relation to the signal of adventitious carbon at 284.8 eV. The initial signals in the binding energy range of sulfite and sulfates disappear by sputtering. Further sputtering does not modify the main signal.

Time-of-Flight Secondary Ion Mass Spectrometry (ToF-SIMS)

Surface measurements – $LiCl^-$ and exemplary transition metal containing fragments

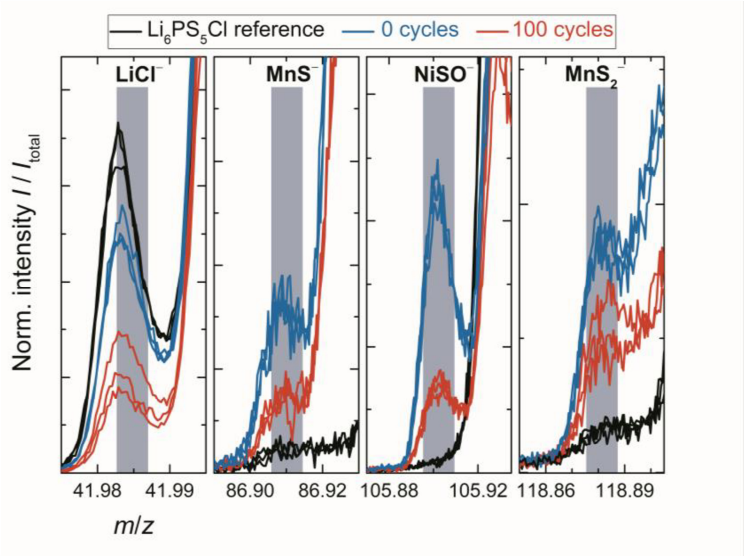

Figure S6 - Negatively charged fragments from surface spectra measured with ToF-SIMS operated in spectrometry mode using 25 keV Bi_3^+ primary ions. For each sample, mass spectra were measured in three different surface positions to ensure reproducibility of the results. The intensities are normalized to the total ion signal. Battery cycling leads to a decrease in signal intensity of fragments which can be attributed to $LiCl^-$, MnS^-, $NiSO^-$ and MnS_2^-, indicating the formation of the phosphate and sulfate containing SEI at the NCM622/SE-interface.

Surface measurements - SO_x^- fragment intensities (with $0 \leq x \leq 3$)

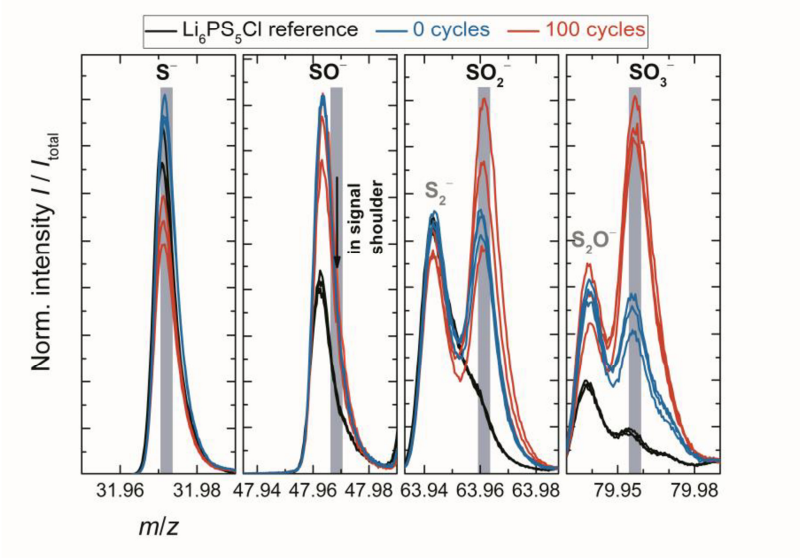

Figure S7 - SO_x^- fragments (with $0 \leq x \leq 3$) from surface spectra measured with ToF-SIMS operated in spectrometry mode using 25 keV Bi_3^+ primary ions. For each sample, mass spectra were measured in three different surface positions to ensure reproducibility of the results. The intensities are normalized to the total ion signal. Battery cycling leads to an increase in signal intensity of SO_x^- fragments with higher oxygen content x, analogous to PO_x^- fragments.

Depth profiling in the near-surface region – PO_x^- and SO_x^- fragment intensities (with $0 \leq x \leq 3$)

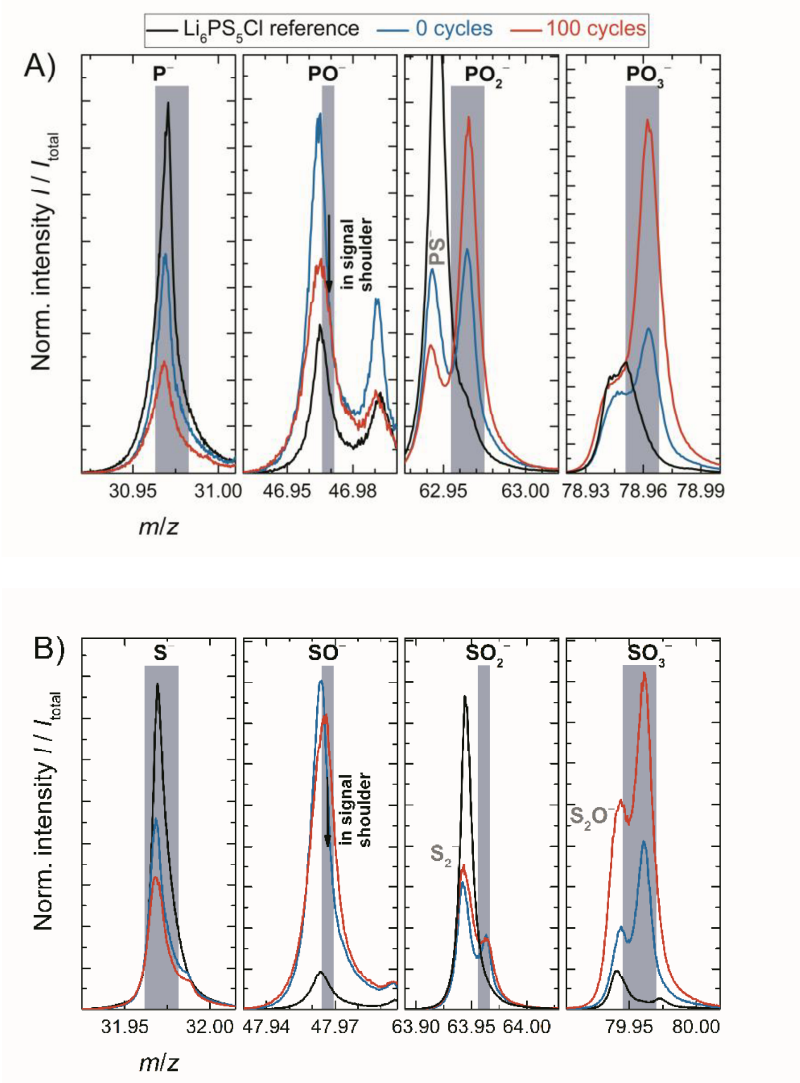

Figure S8 - PO_x^- (A) and SO_x^- (B) fragments (with $0 \leq x \leq 3$) from depth profiling experiments in the near-surface region measured with ToF-SIMS operated in fast imaging mode with delayed extraction using 25 keV Bi_3^+ primary ions. The intensities are normalized to the total ion signal. Battery cycling leads to an increase in signal intensity of PO_x^- and SO_x^- fragments with higher oxygen content x. The results show the same trends as the surface spectra. In order to exclude a surface effect, the depth profiles were also reconstructed without the first scan. This did not lead to a change in the observed trends.

Depth profiling in the near-surface region – local fragment distribution of SO_x^- fragments

Figure S9 shows the local distribution of SO_x^- fragments. The SI images of SO_x^- fragments with $1 \leq x \leq 3$ show significant mass interferences. In particular, the SO_2^- signal can be found in the entire analysis area. However, in order to be able to draw conclusions about the local distribution of SO_x^- fragments, the SI images were multiplied with each other. It was assumed that in areas where SO_3^- is found, SO_2^-, SO^- and S^- fragments must also be detectable. By multiplication, matching areas are retained, while non-matching ones are eliminated by multiplication with zero. A prerequisite for this is that the interferences have different origins and are not present in all four SI images. This simple approach is suitable to eliminate mass interferences due to low mass resolution. Figure S9 shows that the resulting multiplied SI image shows local signal enrichments at the NCM622/SE-interface, analogous to PO_x^- fragments.

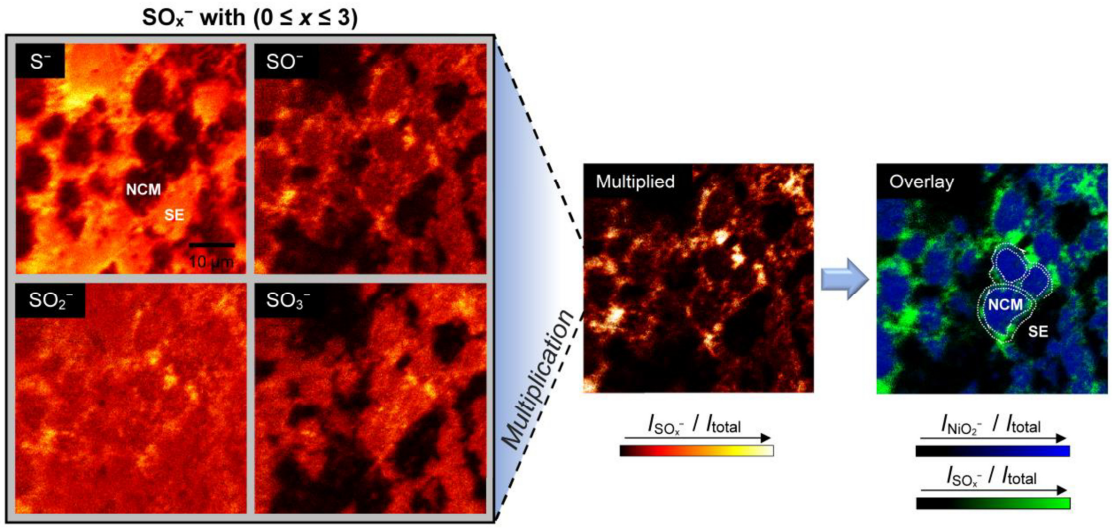

Figure S9 - Local distribution of SO_x^- fragments (with $0 \leq x \leq 3$) from depth profiling experiments in the surface-near region measured with ToF-SIMS operated in fast imaging mode with delayed extraction using 25 keV Bi_3^+ primary ions. The SI images are normalized to the total ion image. The multiplied SI image shows local SO_x^- fragment enrichments at the NCM622/SE-interface, which is analogous to the results of the PO_x^- fragments.

Focused ion beam secondary ion mass spectrometry (FIB-SIMS) – local distribution of SO_x^- fragments

The approach from Figure S9 was used to determine the local distribution of SO_x^- fragments in the SI images of the FIB crater sidewalls. Figure S10 shows secondary electron (SE) and corresponding secondary ion (SI) images of the crater sidewalls depending on the sputtering time. The SI image overlays contain the multiplied SO_x^- fragments (red, representing the SEI), the Cl^- fragment (green, representing the SE) and the NiO_2^- fragment (blue, representing the NCM622 particles). It can be seen that battery cycling leads to an increase of SO_x^- fragments at the NCM622/SE-interface, analogous to PO_x^- fragments.

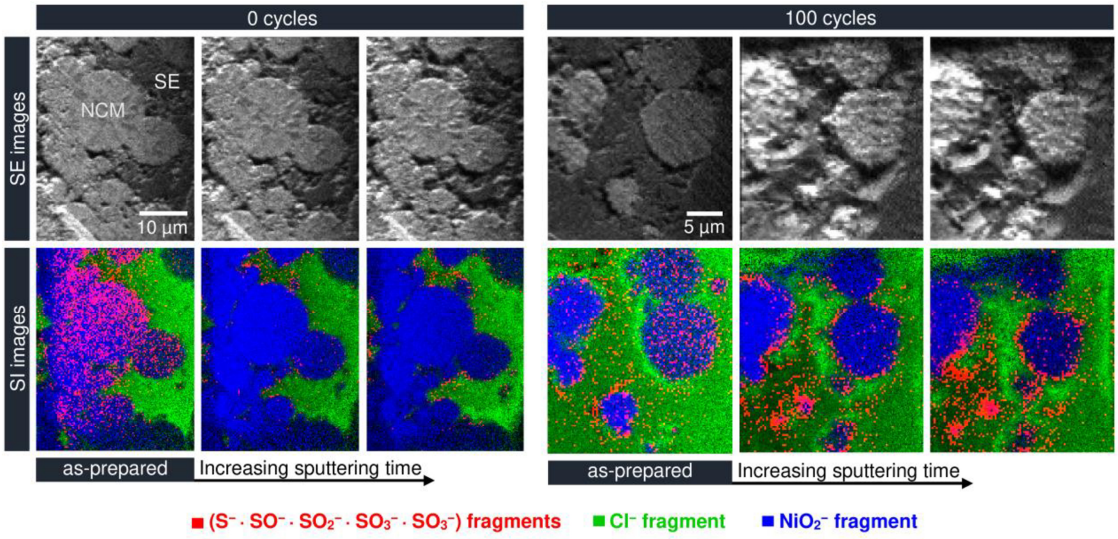

Figure S10 - ToF-SIMS imaging on crater sidewalls for the uncycled and the cycled composite cathode. Shown are secondary electron (SE) and corresponding secondary ion (SI) images of the crater sidewall depending on the sputtering time (surface cleaning). The cleaning step was realized by rasterizing the analysis beam over the analysis area in DC mode and is necessary to remove the defect layer caused by the focused ion beam. In order to determine the local distribution of SO_x^- fragments, the SI images of S^-, SO^-, SO_2^- and SO_3^- were multiplied analogously to the approach shown in Figure S9. The SI image overlays show an increase of SO_x^- fragments at the NCM622/SE-interface after battery cycling.

FIB-SIMS – single-pixel normalization approach

Region-of-interest (ROI) analysis was performed in order to determine the influence of battery cycling on the signal intensity of PO_x^- fragments. A direct comparison of the signal intensities is not suitable since the analysis area is small and contain a different number of particles with different interface sizes. The interface size in turn depends on the NCM622 particle sizes and the plane in which the particles are cut. For the analysis, a threshold of the combined (PO_2^- + PO_3^-) signal between 1% and 100% was defined for the SI images shown in the Manuscript Figure 5 and the number of the pixels within this threshold were determined. Afterwards, the total counts (non-normalized and normalized to the total ion signal) of the (PO_2^- + PO_3^-) signal were divided by the number of pixels eliminating the disturbing effects and allowing a better comparison of signal intensities. The results show that battery cycling leads to an increase in the local signal intensity of PO_x^- fragments (factor 1.4 - 1.7).

For SO_x^- fragments, this normalization approach is not suitable, since the original data show mass interference and the multiplication approach modifies the signals too much in terms of signal intensity. Nevertheless, the overall results of our investigations indicate that similar results can be expected for SO_x^- fragments.

Table 1 - Region-of-interest (ROI) analysis results of the SI images of the FIB crater sidewalls. The combined (PO_2^- + PO_3^-) signal was used and a signal threshold was defined between 1% and 100%. The number of pixels, the maximum counts (MC) and the total counts (TC) within this threshold were determined for the normalized and the non-normalized intensity. In both cases, the results show that the signal intensity of the combined (PO_2^- + PO_3^-) signal increases after battery cycling.

	non-normalized		*normalized to the total ion signal*	
	0 cycles	100 cycles	0 cycles	100 cycles
Pixels	40102	32454	40102	32454
MC (PO_2^- + PO_3^-)	32	39	1	1
TC (PO_2^- + PO_3^-)	109900	152000	2251	2603
TC / pixel	2.7405	4.6836	0.05613	0.08021
	→ factor 1.71		→ factor 1.43	

Supplementary References

(1) Chen, Z.; Wang, J.; Chao, D.; Baikie, T.; Bai, L.; Chen, S.; Zhao, Y.; Sum, T. C.; Lin, J.; Shen, Z. Hierarchical Porous LiNi1/3$Co_{1/3}Mn_{1/3}O_2$ Nano-/Micro Spherical Cathode Material: Minimized Cation Mixing and Improved Li+ Mobility for Enhanced Electrochemical Performance. *Sci. Rep.* **2016**, *6*, 25771.

(2) Kosova, N. V.; Devyatkina, E. T.; Kaichev, V. V. Optimization of Ni^{2+}/Ni^{3+} Ratio in Layered Li(Ni,Mn,Co)O_2 Cathodes for Better Electrochemistry. *J. Power Sources* **2007**, *174* (2), 965–969.

(3) Auvergniot, J.; Cassel, A.; Foix, D.; Viallet, V.; Seznec, V.; Dedryvère, R. Redox Activity of Argyrodite Li_6PS_5Cl Electrolyte in All-Solid-State Li-Ion Battery: An XPS Study. *Solid State Ionics* **2017**, *300*, 78–85.

(4) Koerver, R.; Walther, F.; Aygün, I.; Sann, J.; Dietrich, C.; Zeier, W. G.; Janek, J. Redox-Active Cathode Interphases in Solid-State Batteries. *J. Mater. Chem. A* **2017**, *5* (43), 22750–22760.

(5) Bielefeld, A.; Weber, D. A.; Janek, J. Microstructural Modeling of Composite Cathodes for All-Solid-State Batteries. *J. Phys. Chem. C* **2019**, *123* (3), 1626−1634.

7.1.2 Publication II

Supporting Information

Influence of Carbon Additives on the Decomposition Pathways in Cathodes of Lithium Thiophosphate-Based All-Solid-State Batteries

Felix Walther [a,b], Simon Randau [a,b], Yannik Schneider [a,b], Joachim Sann [a,b], Marcus Rohnke [a,b], Felix H. Richter [a,b], Wolfgang G. Zeier [a,b] and Jürgen Janek[a,b,*]

[a]*Institute of Physical Chemistry, Justus-Liebig-University Giessen, Heinrich-Buff-Ring 17, D-35392 Giessen, Germany.*

[b]*Center for Materials Research (LaMa), Justus-Liebig-University Giessen, Heinrich-Buff-Ring 16, D-35392 Giessen, Germany.*

Table of Contents

Scanning Electron Microscopy (SEM)

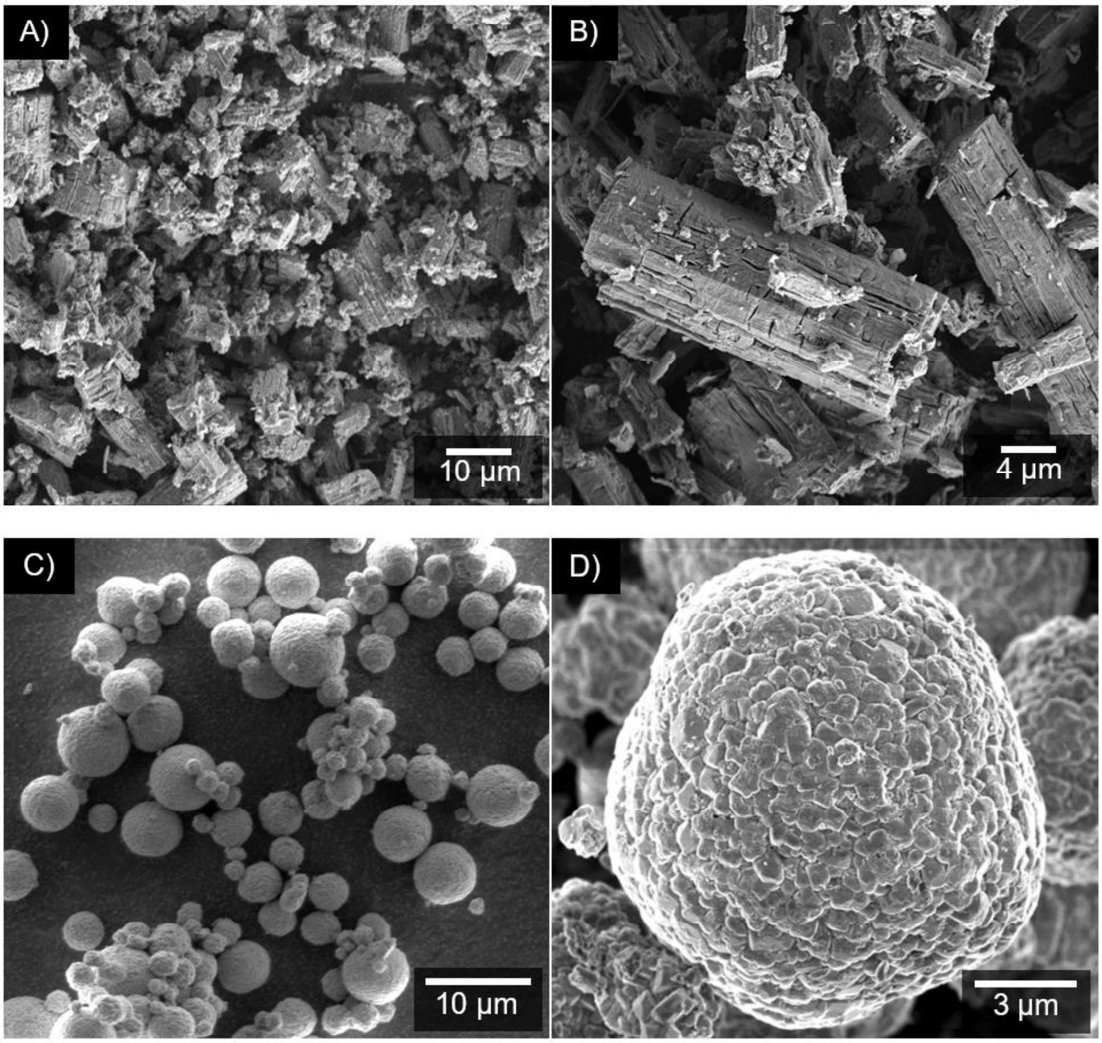

Figure S1. Scanning electron micrographs showing the microstructure and the morphology of the solid electrolyte β-Li_3PS_4 and the active material NCM622. A) Overview image of the solid electrolyte, B) Large-magnification image of the solid electrolyte, C) Overview image showing the particle size distribution, D) Large-magnification image of single NCM622 secondary particles formed by several primary particles.

Electrochemical Cell Performance

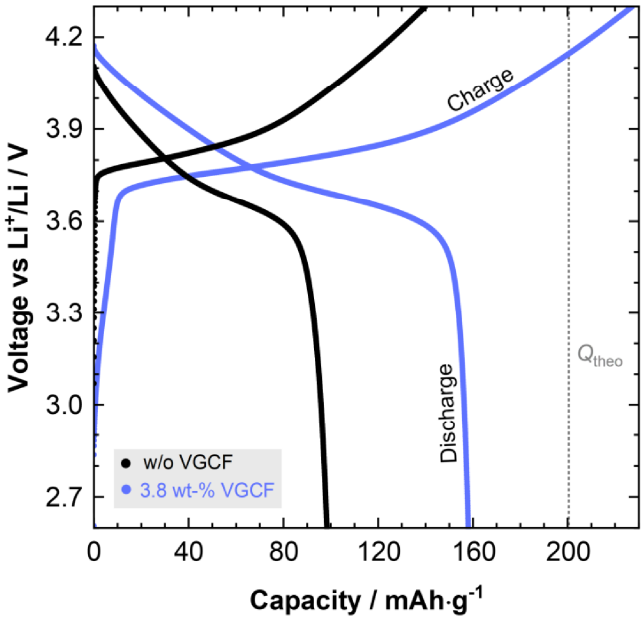

Figure S2. Charge and discharge curve for the first cycle of a Li | β-Li_3PS_4 | $LiNi_{0.6}Co_{0.2}Mn_{0.2}$/β-$Li_3PS_4$ ASSB cell with 3.8 wt % VGCF in the composite cathode. The slope at the beginning of the first charge curve is smaller compared to the reference without VGCF, indicating an increase in side reactions. Additionally, the charge and discharge capacity are further increased compared to the sample with 3 wt % VGCF, supporting the hypothesis of further capacity contributions due to decomposition reactions.

X-ray Photoelectron Spectroscopy (XPS)

(Un)cycled Composite Cathodes and β-Li_3PS_4 Reference

Figure S3 shows the XP detail spectra of the O 1s, Li 1s and C 1s signals of the (un)cycled composite cathodes and the β-Li_3PS_4 reference. The O 1s and the C 1s signal were measured using a pass energy of 23.50 eV, the Li 1s signal with a pass energy of 29.35 eV. The energy calibration procedure is described in the manuscript and further discussed below in the context of the C 1s signal.

The oxygen species of the β-Li_3PS_4 reference can probably be attributed to minor impurities of Li_3PO_4 and Li_2SO_4 (cannot be seen in the S 2p signal due to low concentrations and the XPS detection limit), which can be formed in contact with water. Oxygen-containing adsorbates on the surface (e.g., C=O-type bonds) can also be found in this binding energy range, making a clear assignment often challenging. However, all experiments were done under inert gas atmosphere (Ar) and vacuum conditions. Therefore, we assume Li_3PO_4 and Li_2SO_4 to be more reasonable. The P 2p detail spectra support this assumption, since a component can be found in the binding energy range of Li_3PO_4.[1,2] For the β-Li_3PS_4 reference, the signal ratio of the components we assign to Li_3PO_4 is 1.0:4.2 (P:O) showing a high degree of conformity to the theoretical ratio for Li_3PO_4. The origin of water traces can have various reasons. Conceivable are water residues in the glovebox atmosphere (even if in the ppm-range), water residues from the chamber walls in the transfer vessel and in the XPS instrument, degassing of the adhesive tape for sample holder and sample fixation. However, the total amount is rather low (6.1 at % of oxygen in the sample). Both species slightly increase for both uncycled composite cathodes, indicating that the mere NCM622/SE contact leads to the formation of phosphates and sulfates such as Li_3PO_4 and Li_2SO_4, respectively. Again, reactions with oxygen-containing adsorbates and water residues on the NCM622 secondary particle surface (despite drying) are reasonable explanations. Secondary ion images derived from ToF-SIMS analysis on FIB crater sidewalls show local phosphate fragment enrichments in the NCM622/SE interfacial region, further supporting this assumption. However, the surface species on the NCM surface (and those on the VGCF surface) can also contribute to these signals themselves. Besides oxygen-containing adsorbates on the surface (e.g. indicate by C=O-type bonds as described above), Li_2CO_3 is also conceivable for NCM materials, which can be found in this binding energy range.[3] In case of Li_2SO_4, the concentration seems to be near the XPS detection limit in the S 2p signal, making a further verification and quantification impossible. Nevertheless, semiquantitative analysis by using ToF-SIMS is possible (see manuscript). In the case of the composite cathodes, a further O 1s component can be seen at 529.4 eV, which we attribute to NCM622 lattice oxygen.[4,5]

Battery cycling leads to an increase of signals in the binding energy range of phosphates such as Li_3PO_4 and transition-metal phosphates and sulfates, supporting the conclusions drawn from the P 2p detail spectra and ToF-SIMS measurements (see manuscript). Parallel to this, the NCM622 lattice oxygen signal almost disappears. This indicates the formation of a degradation layer in the NCM622/SE interfacial region, covering the secondary particles.[6] Due to the surface sensitivity of XPS, the lattice oxygen signal cannot be detected above a certain degradation layer thickness (roughly ~ 10 nm), which explains the weakening of the signal. Interestingly, the lattice oxygen signal is weaker in the case of the cycled composite cathode with VGCF compared to the cycled composite cathode without VGCF. We assume, that this is due to the higher utilization of active material by using VGCF. Accordingly, the probability to find non-connected (non-active) NCM622 secondary particles within the analysis area is reduced, which in turns leads to a higher probability of seeing degradation layer formation on every NCM622 secondary particle.

The Li 1s signals do not show a significant influence of battery cycling. The binding energy of the main component fits well to the β-Li_3PS_4 reference. A small signal shoulder at lower binding energies can be attributed to the NCM material.[7] Due to the relatively low signal-to-noise ratio, a further detailed analysis is not recommended.

The C 1s detail spectra show binding energy shifts, which can be attributed to detrimental surface effects.[8,9] As Maibach *et al.* pointed out, surface layers can cause potential gradients which can lead to relative signal shifts of surface and bulk signals.[8] Since the binding energies of the main components of the bulk material (in the S 2p, the P 2p and the Li 1s signal) should not change systematically, we assume that the deviations in the binding energy of the C 1s signal are due to such a surface layer. An energy calibration in relation to the signal of adventitious carbon would have led to a systematic shift of the bulk signals. This can easily lead to misinterpretations and must therefore be carefully considered, as Maibach *et al.* revealed.[8] Therefore, a further analysis of the C 1s detail spectra is not possible, since the relative binging energy shift due to detrimental surface layer species cannot be easily determined and corrected. Consequently, a further analysis would lead to misleading conclusions.

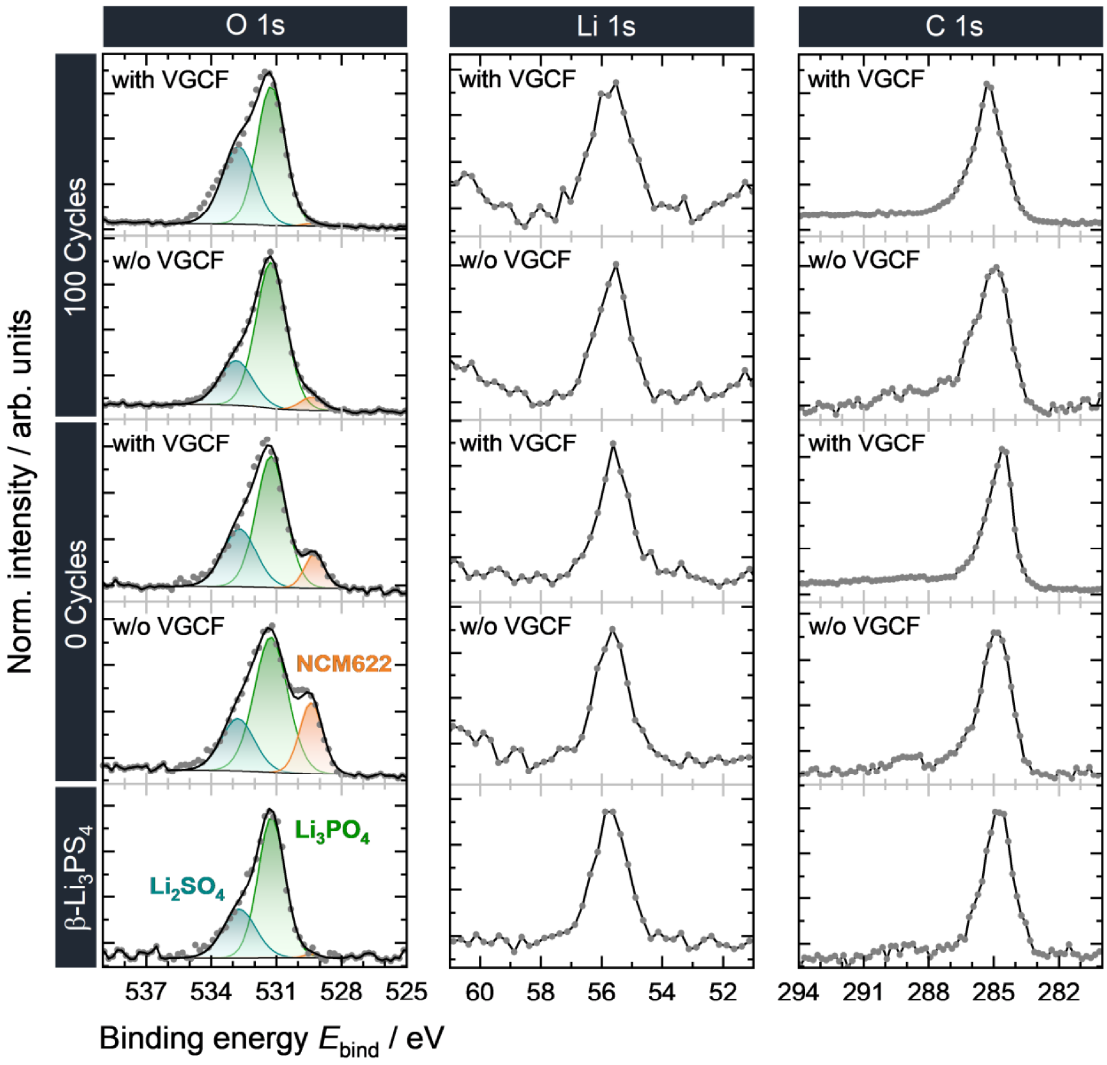

Figure S3. XP spectra of the O 1s, Li 1s and C 1s signals of a β-Li_3PS_4 reference and the (un)cycled composite cathodes. The pass energies ranged between 23.50 eV (O 1s, C 1s) and 29.35 eV (Li 1s). Signal fitting was performed using a Shirley background and GL(30) line-shapes.

Cyclic Voltammetry Experiment

To investigate possible degradation reactions in the conductive additive/SE interfacial region, a cyclic voltammetry (CV) experiment was performed with a VGCF/SE composite. The aim of the experiment was to test whether an applied potential leads to decomposition reactions at the VGCF/SE interface. The decomposition products were then investigated using XPS.

VGCF/β-Li_3PS_4 Composite and Cell Assembly

β-Li_3PS_4 and VGCF (dried in a Büchi furnace at 200 °C over night) were mixed in the same mass ratio as in the composite cathode, corresponding to a VGCF/β-Li_3PS_4 composite with 9.1 mass-% VGCF. The composite was mixed with an agate mortar for 15 min. For cell assembly (cell set up is described in the manuscript), 30 mg of the β-Li_3PS_4 was placed at the bottom of the inner PEEK cylinder first and then manually compressed with both steel stamps. 30 mg of the VGCF/SE composite was added as working electrode. Afterward, the pellet was compressed uniaxially at 30 kN (approx. 380 MPa) for three minutes. An indium foil (chemPUR) with a diameter of 8 mm was used as counter electrode (CE), to exclude decomposition reactions at the CE/SE interface. A pressure of approximately 50 MPa was applied using an external frame around the cell casing.

Cyclic Voltammetry

Cyclic voltammetry (CV) experiments were carried out using VMP-300 and SP-150 Biologic potentiostats. Starting from the OCV, the first sweep (oxidative sweep) was carried out to 5.5 V versus In/InLi. Due to the 2-point cell set-up, the anode also acts as reference electrode. The reverse sweep was carried out from 5.5 V to 0 V (versus the reference potential) followed by an OCV step. The scan speed was 1 $mV \cdot s^{-1}$. Figure S4 shows the cyclic voltammogram. The currents measured during CV indicate decomposition/degradation reactions. The decomposition products are further characterized by using XPS.

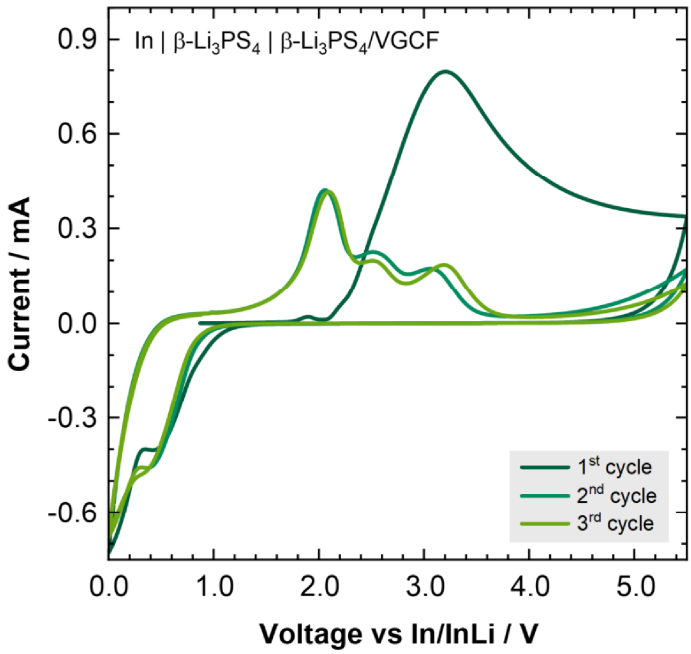

Figure S4. Cyclic voltammogram for a In | β-Li_3PS_4 | VGCF/β-Li_3PS_4 cell.

XP Spectra of the VGCF/SE Composite Before and After the CV Experiment

Figure S5 shows the XP spectra of the S 2p, the P 2p and the O 1s signal of a VGCF/SE composite before and after the CV experiment (described in the manuscript). It is evident that sulfur and phosphorous signals appear at higher binding energies during the CV experiment. Before the CV experiment, all detail spectra show a high degree of similarity compared to the signals of the uncycled composite cathodes (see Figure 2 in the manuscript). Only the NCM signal is missing in the O 1s spectrum since the VGCF/SE composite does not contain NCM. Accordingly, a slight increase in oxidized species can be seen in the S 2p and P 2p detail spectra compared to the β-Li_3PS_4 reference. We assume that oxygen-containing surface groups or water residuals on the VGCF surface can lead to the formation of phosphates such as Li_3PO_4. This is supported by a study by Park *et al.* which reveals that functional groups on carbon additives can lead to side reactions with thiophosphate-based SEs.[10] Although the data indicate the formation of species in the binding energy range of polysulfides, we cannot prove this here.

After the CV experiment, the signals intensities of oxidized species are increased. The S 2p signal shows a high degree of similarity compared to the S 2p signal of the cycled composite cathode without VGCF, indicating polysulfide formation (see Figure 2 in the manuscript). In contrast, the P 2p signal shows only a slight increase in oxidized species, which is not as high

as in the case of the cycled composite cathodes. Basically, P_2S_n and phosphates such as Li_3PO_4 can be found in this binding energy range.[1,2,11] The latter compound can be formed by the reaction of SE with oxygen-containing surface species on the VGCF surface. We assume that such reactions were not fully completed by the mere VGCF/SE contact. The CV experiment enforces the reaction with the remaining surface species until almost no further oxygen source is present. At the same time, the anion lattice can be damaged leading to the formation of P_2S_n species. In the case of the composite cathode, the NCM622 particles continue to serve as an oxygen source, allowing the formation of additional phosphate species in the higher binding energy range. In contrast to the cycled composite cathodes, no species were observed for the VGCF/SE composite at binding energies of ~134.0 eV. Since transition metal phosphates are found in this binding energy range, it seems plausible that these species are observed in the case of the composite cathodes (containing NCM622) but not in the case of the VGCF/SE composite (no transition metal species present). This supports our hypothesis of formation of transition metal phosphates in the NCM/SE interfacial region.

Overall, the data shows that decomposition reactions occur at the VGCF/SE interface, which seems to be mainly dominated by the formation of polysulfides.

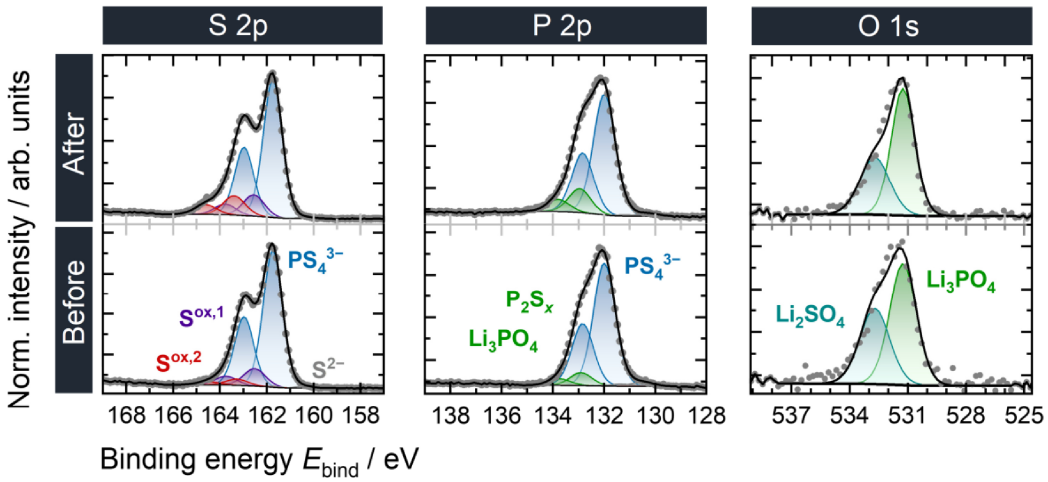

Figure S5. XP spectra of the S 2p, P 2p and O 1s signals of the VGCF/SE composite before and after the CV experiment. The pass energy was 23.50 eV in all cases. A Shirley background and GL(30) line shapes were used for signal fitting. The XP spectra were normalized by the respective signal maximum in order to be able to compare the contributions of the signal components more easily.

Time-of-Flight Secondary Ion Mass Spectrometry (ToF-SIMS)

Depth Profiling – Exemplary Negatively Charged Fragments

Figure S6 shows exemplary negatively charged fragments for phosphates, sulfates/sulfites and polysulfides derived from depth profiling experiments. Phosphate fragments (PO_2^-, PO_3^-) increase along with battery cycling, supporting the conclusions drawn from XPS depth profiling experiments and ToF-SIMS surface analysis. At the same time, the PS^- fragments decrease, indicating damage of the SE anion lattice. It seems that both effects (PO_x^- signal increase and PS^- signal decrease) are more pronounced in electrodes with VGCF. On the one hand, this is due to the higher utilization of the active material by using VGCF. Accordingly, the degradation layer forms on almost every NCM622 secondary particle surface, leading to the detection of more decomposition products. On the other hand, a further contribution (also to the phosphate formation, see Figure S5) comes from the VGCF/SE composite itself. Next to phosphate fragments, battery cycling leads (with and without VGCF) by trend to an increase in long-chain polysulfide fragments such as S_2^-, S_2O^- and S_3O^-. In contrast to ToF-SIMS surface analysis, polysulfide fragments with longer S-chains such as S_6^- and S_8^- (see Figure S7) could not be detected anymore due to the enhanced fragmentation induced by the sputter species (Cs^+, 2 keV). Nevertheless, the trend can be clearly identified, supporting the XPS and the ToF-SIMS surface analysis data. Interestingly, sulfate/sulfite fragments (SO_2^-, SO_3^-) increase only in the case of the cycled composite cathode without VGCF significantly. These observations are consistent with the surface analysis. These results indicate that sulfate/sulfite formation is not preferred in the case with VGCF, whereas polysulfide formation seems dominant.

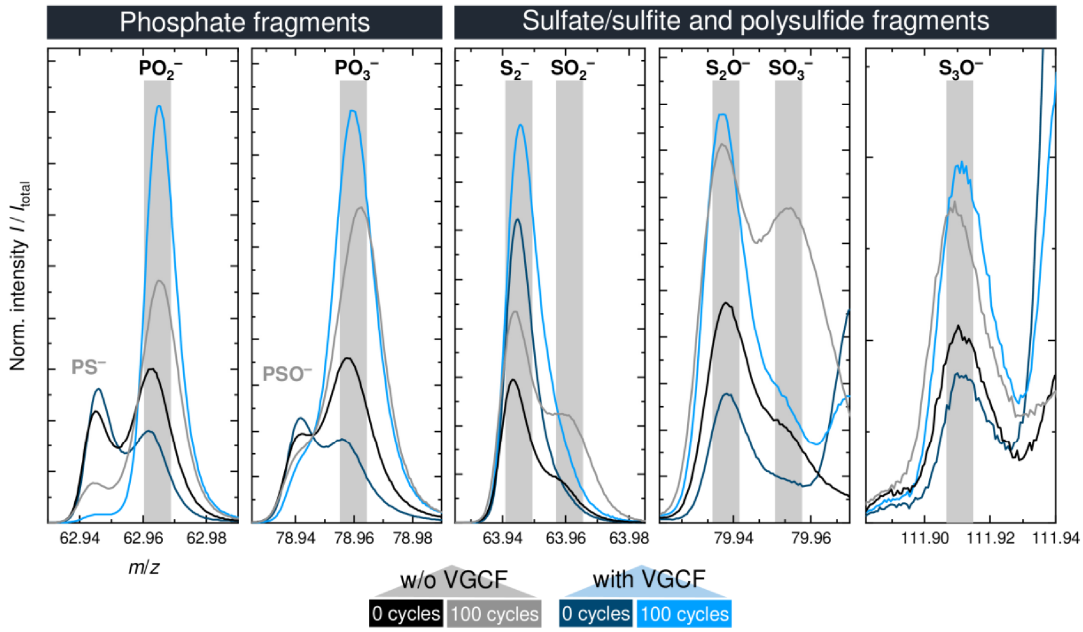

Figure S6. Negatively charged fragments from depth profiles measured with the primary ion gun operated in spectrometry mode (25 keV Bi_3^+) and Cs^+ (2 keV) as sputter species. The intensities are normalized to the total ion signal.

Surface Measurements - Li^- and S_x^- Fragments

Figure S7 shows exemplary negatively charged fragments for lithium species and polysulfides. The mass spectra were obtained from surface measurements. The Li^- fragment reveals that the cycled composite cathodes were measured in the delithiated state, since the Li^- signal is weaker in both cases compared to the uncycled references. Interestingly, with VGCF, the signal intensity is much lower compared to the cycled sample without VGCF. Also, the dependence on the analysis spot position appears smaller (recognized by the average signal deviations). Both indicate a higher utilization of the active material with VGCF, which causes more mobile lithium species and leads to a decrease of the Li^- signal. In addition to the fragments for polysulfides in the manuscript, Figure S7 shows the long-chain S_x^- fragments S_6^- and S_8^-. Taking the fragments in the manuscript (Figure 4) and in Figure S7 into account, we concluded that by using VGCF the amount of polysulfides and also the mean chain-length of the -$[S]_n$- units increases. These observations are consistent with the conclusions drawn from XPS analysis (see Figure 2).

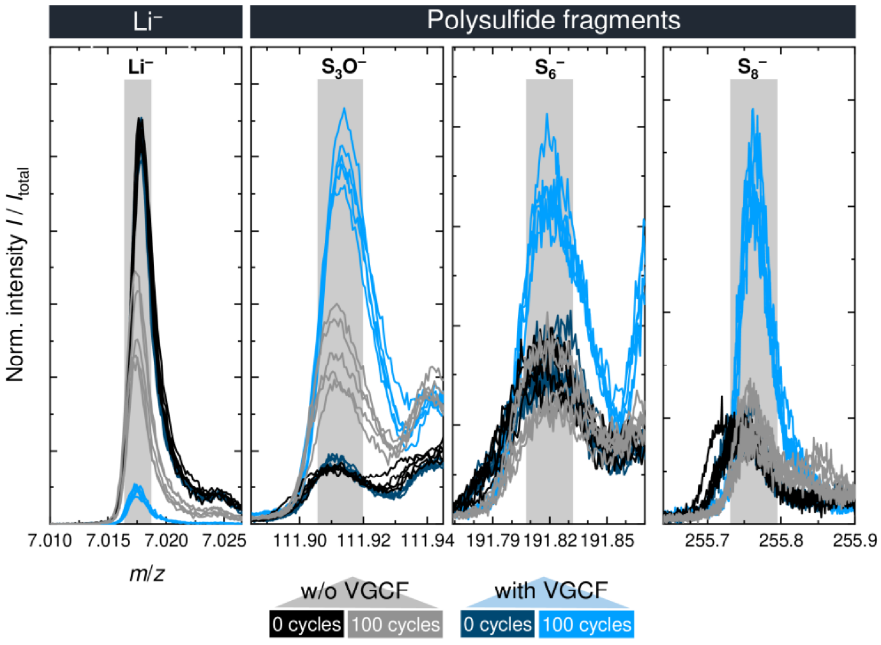

Figure S7. Li^-, S_3O^-, S_6^- and S_8^- fragments from surface spectra measured with the primary ion gun operated in spectrometry mode using 25 keV Bi_3^+ primary ions. For each sample, five mass spectra were measured at different surface positions to ensure reproducibility of the results. The intensities are normalized to the total ion signal.

ToF-SIMS Analysis on FIB Crater Sidewalls – Single-Pixel Normalization Approach

Region-of-interest (ROI) analysis was performed in order to determine the influence of the carbon additive VGCF and battery cycling. A direct comparison of the secondary ion images and the corresponding signal intensities is not possible since the FIB cut planes reveal scattering of features such as different number of NCM622 particles and different NCM622/SE area ratios within the analysis area. For this reason, we performed a ROI analysis. A scheme of the procedure is shown in Figure S8. A ROI is defined using a signal threshold (5% - 100% in this case). Afterward, the number of the pixels within this threshold and the signal intensities of signals of interest are extracted. By normalizing the signal intensities to the number of pixels, deviations such as different NCM622/SE ratios within the analysis area are minimized. For the ROI analysis, we used secondary ion images, which were normalized to the total secondary ion image to compensate topographic effects of the FIB crater. The signal intensity of all signals (and thus the total ion signal) decrease with increasing distance from the sample surface / the focus height (down the crater). Under the assumption that the signal decrease is approximately the same for all secondary ions, normalizing the secondary ion images to the total secondary ion image compensates topographic effects due to the FIB crater to some extent.

In order to analyze phosphate formation within the bulk, we used the multiplied ($PO_2^- \cdot PO_3^-$) secondary ion image. Multiplying both secondary ion images minimizes the influence of mass interference and helps to achieve more reliable results.[6]

To study polysulfide formation in more detail, we used the S_3^- and the S_4^- signals due to relatively small mass interference with neighboring signals compared to other S_x^- signals. In addition, S_x^- signals with $x > 4$ could not unambiguously identified due to the FIB damage (high fragmentation of long-chain polysulfides).

Regarding SO_x^- fragments, this approach was not suitable, since the original data showed too weak signals and strong mass interferences (multiplication approach could not be satisfactorily used). This indicates only small amounts of sulfates/sulfites, since ToF-SIMS typically has high sensitivities for such compounds. Therefore, it was not possible to get further insights about the location of sulfate/sulfite formation with ToF-SIMS measurements on FIB crater sidewalls in this study.

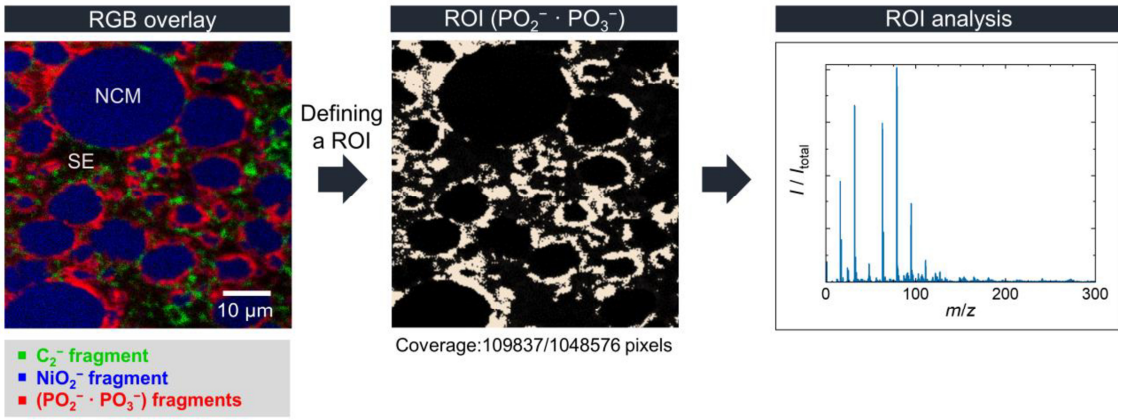

Figure S8. Scheme of the region-of-interest (ROI) analysis procedure for the multiplied (PO_2^- · PO_3^-) signal. After defining a threshold in the (PO_2^-·PO_3^-) secondary ion image (middle picture), the number of pixels within this threshold and the signal intensities of interest were determined and semiquantitative analysis was performed afterward.

Table 1. ROI analysis results for the FIB crater sidewalls. The multiplied (PO_2^-·PO_3^-) secondary ion image normalized to the total ion secondary ion image was used with a signal threshold of 5% - 100%. The number of pixels and the total counts (TC) within this threshold were determined. The results show that the signal intensity of phosphate fragments increases due to battery cycling with and without VGCF confirming the XPS results and the ToF-SIMS surface analysis and depth profiling results.

	normalized to the total ion signal SI			
	w/o VGCF		with VGCF	
	0 Cycles	100 Cycles	0 Cycles	100 Cycles
TC (PO_2^- · PO_3^-)	129.6	3114	268.4	2490
Pixels	35856	187140	71078	175676
TC / pixel	0.004	0.017	0.004	0.014
	→ factor 4.6		→ factor 3.8	

Table 2. ROI analysis results for the FIB crater sidewalls. The S_3^- (A) and the multiplied ($S_3^- \cdot S_4^-$) (B) secondary ion image normalized to the total ion secondary ion image was used with a signal threshold of 5% - 100%. The number of pixels and the total counts (TC) within this threshold were determined. The results show the tendency of an increase in polysulfide fragments due to battery cycling. Due to the FIB damage, the increase is not very strong (factor 1.1 – 1.7). Nevertheless, the data suggest that polysulfide formation is more pronounced with VGCF further supporting the XPS and ToF-SIMS results.

(A)

	normalized to the total ion signal SI			
	w/o VGCF		with VGCF	
	0 Cycles	100 Cycles	0 Cycles	100 Cycles
TC (S_3^-)	987.1	1837	1712	2763
Pixels	74560	130711	125517	120004
TC / pixel	1.3E-02	1.4E-02	1.4E-02	2.3E-02
	→ factor 1.1		→ factor 1.7	

(B)

	normalized to the total ion signal SI			
	w/o VGCF		with VGCF	
	0 Cycles	100 Cycles	0 Cycles	100 Cycles
TC ($S_3^- \cdot S_4^-$)	0.5474	2.545	1.692	3.11
Pixels	4824	18970	12074	14113
TC / pixel	1.1E-04	1.3E-04	1.4E-04	2.2E-04
	→ factor 1.2		→ factor 1.6	

Reaction Scheme with Formation of a Rock-Salt Like NiO Phase

Figure S9 shows a reaction scheme for the NCM/SE interfacial reaction during charging with formation of a rock-salt like NiO phase. These equations must be seen as a simplified degradation scheme that can describe our experimental results. We assume that the thermodynamically preferred reaction path involves the formation of transition metal sulfides as intermediate products, as suggested by calculations.[12–14] However, it is also possible to describe the experimental results with a direct formation of a rock-salt like NiO phase. For simplification, we choose $M_3(PO_4)_2$ for transition metal phosphates and MSO_4 for transition metal sulfates, although other stoichiometries and oxidation states are conceivable as well. In addition, we consider the reaction products Li_3PO_4 and Li_2SO_4 in our reaction scheme, which are also suggested by calculations.[12–14] We hypothesize equations with different polysulfide species, since we cannot distinguish experimentally between the polysulfides P_2S_n, Li_2S_n and $(Li_3PS_4)_2S_n$. Combinations of the equations can lead to an increase in polysulfide chain length, which corresponds to our experimental observation.

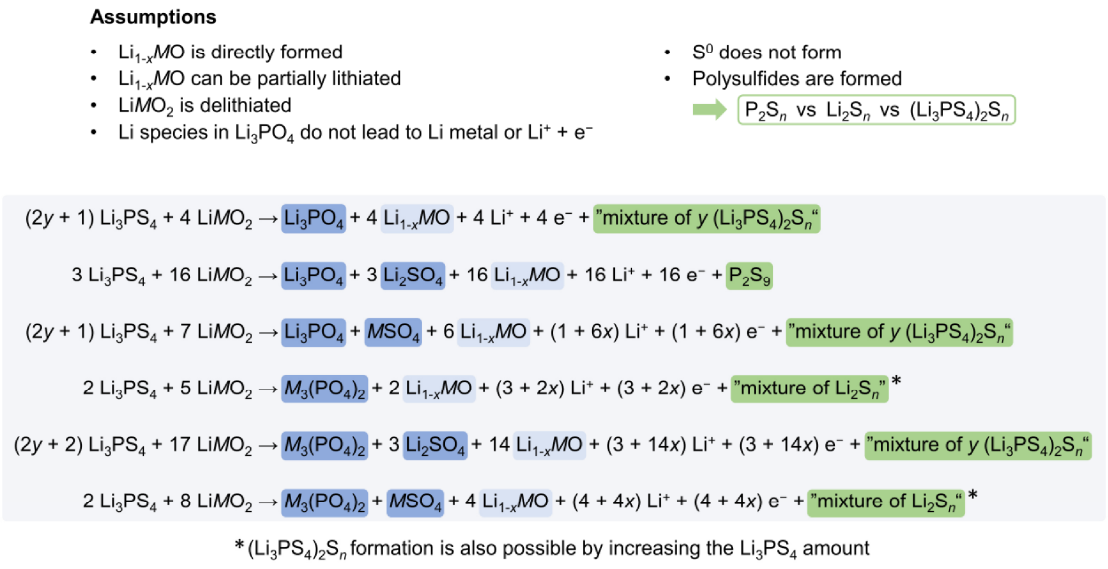

Figure S9. Reaction scheme for the electrochemically driven NCM/SE interfacial reaction during battery charging under the formation of a rock-salt like NiO phase. Basic assumptions for the reaction equations are given on the top. Reactions of the SE with the NCM material can lead to the formation of different phosphates, sulfates as well as polysulfides. For the polysulfides (marked in green), various combinations with different sulfur chain length S_n are often possible to meet the stoichiometry. If this is the case, these species are labeled with the term "mixture of".

Supplementary References

(1) Wang, B.; Liu, J.; Sun, Q.; Li, R.; Sham, T.-K.; Sun, X. Atomic Layer Deposition of Lithium Phosphates as Solid-State Electrolytes for All-Solid-State Microbatteries. *Nanotechnology* **2014**, *25* (50), 504007. https://doi.org/10.1088/0957-4484/25/50/504007.

(2) Appapillai, A. T.; Mansour, A. N.; Cho, J.; Shao-Horn, Y. Microstructure of $LiCoO_2$ with and without "$AlPO_4$" Nanoparticle Coating: Combined STEM and XPS Studies. *Chem. Mater.* **2007**, *19* (23), 5748–5757. https://doi.org/10.1021/cm0715390.

(3) An, S. J.; Li, J.; Sheng, Y.; Daniel, C.; Wood, D. L. Long-Term Lithium-Ion Battery Performance Improvement via Ultraviolet Light Treatment of the Graphite Anode. *J. Electrochem. Soc.* **2016**, *163* (14), A2866–A2875. https://doi.org/10.1149/2.0171614jes.

(4) Bodenes, L.; Dedryvère, R.; Martinez, H.; Fischer, F.; Tessier, C.; Pérès, J.-P. Lithium-Ion Batteries Working at 85°C: Aging Phenomena and Electrode/Electrolyte Interfaces Studied by XPS. *J. Electrochem. Soc.* **2012**, *159* (10), A1739–A1746. https://doi.org/10.1149/2.061210jes.

(5) Kosova, N. V.; Devyatkina, E. T.; Kaichev, V. V. Optimization of Ni^{2+}/Ni^{3+} Ratio in Layered $Li(Ni,Mn,Co)O_2$ Cathodes for Better Electrochemistry. *J. Power Sources* **2007**, *174* (2), 965–969. https://doi.org/10.1016/j.jpowsour.2007.06.051.

(6) Walther, F.; Koerver, R.; Fuchs, T.; Ohno, S.; Sann, J.; Rohnke, M.; Zeier, W. G.; Janek, J. Visualization of the Interfacial Decomposition of Composite Cathodes in Argyrodite-Based All-Solid-State Batteries Using Time-of-Flight Secondary-Ion Mass Spectrometry. *Chem. Mater.* **2019**, *31* (10), 3745–3755. https://doi.org/10.1021/acs.chemmater.9b00770.

(7) Andreu, N.; Flahaut, D.; Dedryvère, R.; Minvielle, M.; Martinez, H.; Gonbeau, D. XPS Investigation of Surface Reactivity of Electrode Materials: Effect of the Transition Metal. *ACS Appl. Mater. Interfaces* **2015**, *7* (12), 6629–6636. https://doi.org/10.1021/am5089764.

(8) Maibach, J.; Lindgren, F.; Eriksson, H.; Edström, K.; Hahlin, M. Electric Potential Gradient at the Buried Interface between Lithium-Ion Battery Electrodes and the SEI Observed Using Photoelectron Spectroscopy. *J. Phys. Chem. Lett.* **2016**, *7* (10), 1775–1780. https://doi.org/10.1021/acs.jpclett.6b00391.

(9) Lindgren, F.; Rehnlund, D.; Källquist, I.; Nyholm, L.; Edström, K.; Hahlin, M.; Maibach, J. Breaking Down a Complex System: Interpreting PES Peak Positions for Cycled Li-Ion Battery Electrodes. *J. Phys. Chem. C* **2017**, *121* (49), 27303–27312. https://doi.org/10.1021/acs.jpcc.7b08923.

(10) Park, S. W.; Oh, G.; Park, J.; Ha, Y.; Lee, S.; Yoon, S. Y.; Kim, B. G. Graphitic Hollow Nanocarbon as a Promising Conducting Agent for Solid□State Lithium Batteries. *Small* **2019**, *15* (18), 1900235. https://doi.org/10.1002/smll.201900235.

(11) Auvergniot, J.; Cassel, A.; Ledeuil, J. B.; Viallet, V.; Seznec, V.; Dedryvère, R. Interface Stability of Argyrodite Li_6PS_5Cl toward $LiCoO_2$, $LiNi_{1/3}Co_{1/3}Mn_{1/3}O_2$, and $LiMn_2O_4$ in Bulk All-Solid-State Batteries. *Chem. Mater.* **2017**, *29* (9), 3883–3890. https://doi.org/10.1021/acs.chemmater.6b04990.

(12) Richards, W. D.; Miara, L. J.; Wang, Y.; Kim, J. C.; Ceder, G. Interface Stability in Solid-State Batteries. *Chem. Mater.* **2016**, *28* (1), 266–273. https://doi.org/10.1021/acs.chemmater.5b04082.

(13) Nolan, A. M.; Zhu, Y.; He, X.; Bai, Q.; Mo, Y. Computation-Accelerated Design of Materials and Interfaces for All-Solid-State Lithium-Ion Batteries. *Joule* **2018**, *2* (10), 2016–2046. https://doi.org/10.1016/j.joule.2018.08.017.

(14) Xiao, Y.; Miara, L. J.; Wang, Y.; Ceder, G. Computational Screening of Cathode Coatings for Solid-State Batteries. *Joule* **2019**, *3* (5), 1252–1275. https://doi.org/10.1016/j.joule.2019.02.006.

7.1.3 Publication III

Supporting Information

The Working Principle of a Li_2CO_3/$LiNbO_3$ Coating on NCM for Thiophosphate-Based All-Solid-State Batteries

Felix Walther [a,b], Florian Strauss [c], Xiaohan Wu [d], Boris Mogwitz [a,b], Jonas Hertle [a,b], Joachim Sann [a,b], Marcus Rohnke [a,b], Torsten Brezesinski [c] and Jürgen Janek [a,b,c,*]

[a]*Institute of Physical Chemistry, Justus Liebig University Giessen, Heinrich-Buff-Ring 17, D-35392 Giessen, Germany.*

[b]*Center for Materials Research (LaMa), Justus Liebig University Giessen, Heinrich-Buff-Ring 16, D-35392 Giessen, Germany.*

[c]*Battery and Electrochemistry Laboratory, Institute of Nanotechnology, Karlsruhe Institute of Technology (KIT), Hermann-von-Helmholtz-Platz 1, D-76344 Eggenstein-Leopoldshafen, Germany.*

[d]*BASF SE, Carl-Bosch-Str. 38, D-67056 Ludwigshafen am Rhein, Germany.*

**E-mail: juergen.janek@phys.chemie.uni-giessen.de*

Table of Contents

Scanning Electron Microscopy (SEM)

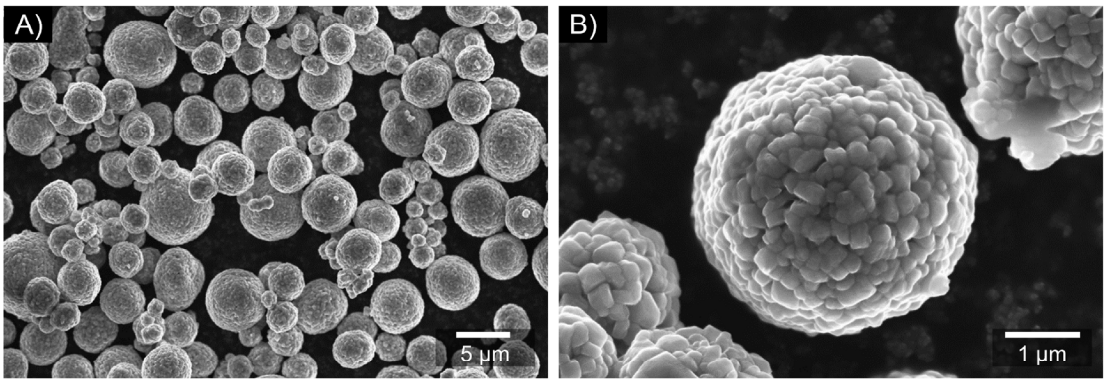

Figure S1. Scanning electron micrographs showing the microstructure and the morphology of the cathode active material NCM622. Shown are images of the Li_2CO_3/$LiNbO_3$ coated NCM622 material. A) Overview image depicting the particle size distribution, B) Large-magnification image of single NCM622 secondary particles which are formed by several primary crystallites.

Attenuated Total Reflection-Infrared Spectroscopy (ATR-IR)

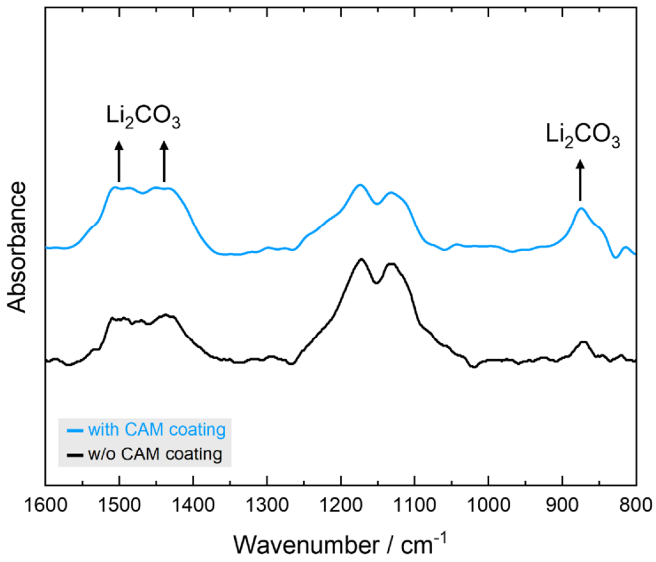

Figure S2. ATR-IR spectra of the uncoated and the Li_2CO_3/$LiNbO_3$ coated cathode active material (NCM622). Bands in the wavenumber range between 1425 cm^{-1} – 1510 cm^{-1} can be attributed to stretching vibrations and the band around 870 cm^{-1} corresponds to the deformation vibration of Li_2CO_3.[1] It can be seen that both cathode active materials contain Li_2CO_3, which is further increased in the case of the coated NCM622. The bands in the wavenumber range from 1130 cm^{-1} to 1175 cm^{-1} were already described and stem from the cathode active material itself.[2]

Electrochemical Cell Performance

Coulombic Efficiency as a Function of the Cycle Number

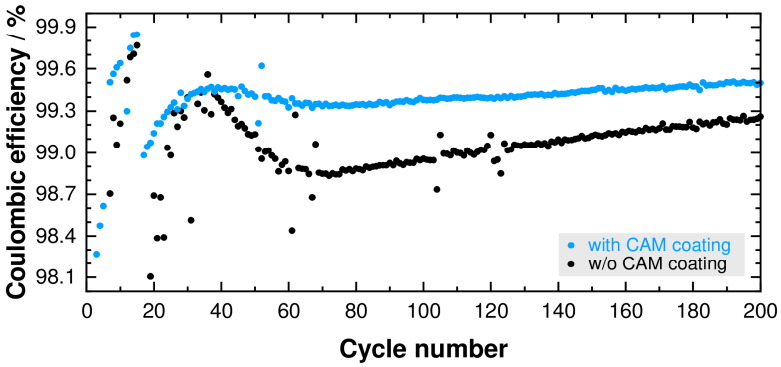

Figure S3. Coulombic efficiency (CE) as a function of the cycle number. The CAM coating leads to an increase in CE and thus to an enhanced ASSB performance. The battery performance data indicate a reduced interfacial reaction within the composite cathode due to the CAM coating.

X-ray Photoelectron Spectroscopy (XPS)

Post-Mortem Analyses - Cl 2p, O 1s, Li 1s and C 1s Detail Spectra

Figure S4 shows the XP detail spectra of Cl 2p, O 1s, Li 1s and C 1s of a Li_6PS_5Cl reference and the (un)cycled composite cathodes containing (un)coated NCM622.

The Cl 2p signal does not show a significant change. A single doublet is sufficient to represent the experimental data in all cases. The energetic signal position at 198.7 eV does not change, which is in accordance to recent reports.[3,4] Consequently, the formation of decomposition products containing Cl cannot be resolved by using XPS. It is conceivable, that the binding energy difference between the decomposition products and the solid electrolyte is not sufficient and/or the detection limit of XPS is too high to resolve the low decomposition product fractions.

The O 1s spectrum contains several contributions from oxides, phosphates and sulfates/sulfites. Since the binding energies of these species are very close to each other and we expect interdependent contributions, signal fitting would require many assumptions and fitting constrains. The suitability of the fit model would be questionable. We therefore describe the O 1s spectrum in the following mostly qualitatively.
The overall oxygen content in the Li_6PS_5Cl reference is rather low (8.3 at.-%) and can be attributed to minor impurities and oxygen-containing adsorbates on the surface. The binding energies of the contribution at 531.2 eV indicate Li_3PO_4, which has a signal interference with oxygen-containing adsorbates (e.g., C=O-type bonds).[4–6] The ratio of the elements we can attribute to Li_3PO_4 in the P 2p and O 1s spectrum is 1.00:4.98 (P:O). This indicates that Li_3PO_4 mainly dominates the signal with a small contribution by oxygen-containing adsorbates. Thiophosphates are known to be highly reactive and moisture sensitive. A reaction with water might explain the formation of species such as Li_3PO_4. However, since all experiments and transfer steps were done under dry argon atmosphere and vacuum conditions, we assume a minor influence here. Nevertheless, water residues in the glovebox atmosphere (ppm-range), water residues from the chamber walls in the transfer systems and in the XPS system, degassing of the adhesive tape for sample fixation cannot be completely excluded.
The second main contribution at 533.4 eV is unknown. Since Li_6PS_5Cl by NEI Corporation was used, we cannot further comment on potential impurities due to the synthesis process here and cannot unambiguously clarify the origin of this species. Since this contribution cannot be seen for the other samples, this signal seems specific for the NEI Corporation solid electrolyte and does not play a role for the other samples.

For the uncycled composite cathodes, a further contribution can be seen at 529.3 eV, which we attribute to NCM622 lattice oxygen.[7–9] Contributions by $LiNbO_3$ (~530.3 eV) and Li_2CO_3 (~531.5 eV) can explain the signal broadening for the Li_2CO_3/$LiNbO_3$ coated sample compared to the uncoated sample.
For both cycled composite cathodes, the signal of the NCM622 lattice oxygen vanished due to the formation of a decomposition layer at the NCM622/solid electrolyte interface. The O 1s spectrum is mainly dominated by signals which can be attributed to phosphates and sulfates such as Li_3PO_4 (~531.2 eV) and Li_2SO_4 (~532.0 eV), respectively.[4–6,10] For the uncoated sample, the signal shoulder at higher binding energies seems more pronounced compared to the uncoated sample. However, quantitative statements are not recommended here due to interdependent contributions which makes a reliable fit model almost impossible.

The Li 1s signal shapes do not indicate significant differences. Since the binding energy of the main component for all samples is in first approximation in accordance with the Li_6PS_5Cl reference, we assume that the Li 1s signal is dominated by the contribution of the solid electrolyte. For the uncycled samples, the small shoulder at lower binding energies can be attributed to the NCM material.[11] This contribution vanishes due to the decomposition layer formation at the NCM622/solid electrolyte interface, which suppresses the NCM material signals. The contributions by $LiNbO_3$ (~55.0 eV) and Li_2CO_3 (~55.1 eV) are hard to separate, since the binding energies are very close to each other and the signals are convoluted by the contribution of solid electrolyte.[12–14] The same is true for decomposition products such as Li_3PO_4 (~55.4 eV referenced to C 1s at 284.8 eV), making a further analysis rather speculative.[14,15]
In the context of battery materials, the C 1s signal has already been reported to be difficult to analyze. Accordingly, Maibach et al. have already described the detrimental effects of potential gradients caused by surface layers on battery materials.[16,17] In a previous work, we reported analogous observations for thiophosphate-based composite cathodes.[9] Consequently, an energy calibration in relation to the signal of adventitious carbon can easily lead to a systematic shift of the bulk signals and thus to wrong conclusions. A cross-check with bulk signals is mandatory. Also here, signal broadening effects and slight binding energy shifts can be seen, which makes a further analysis of the C 1s detail spectra impossible.

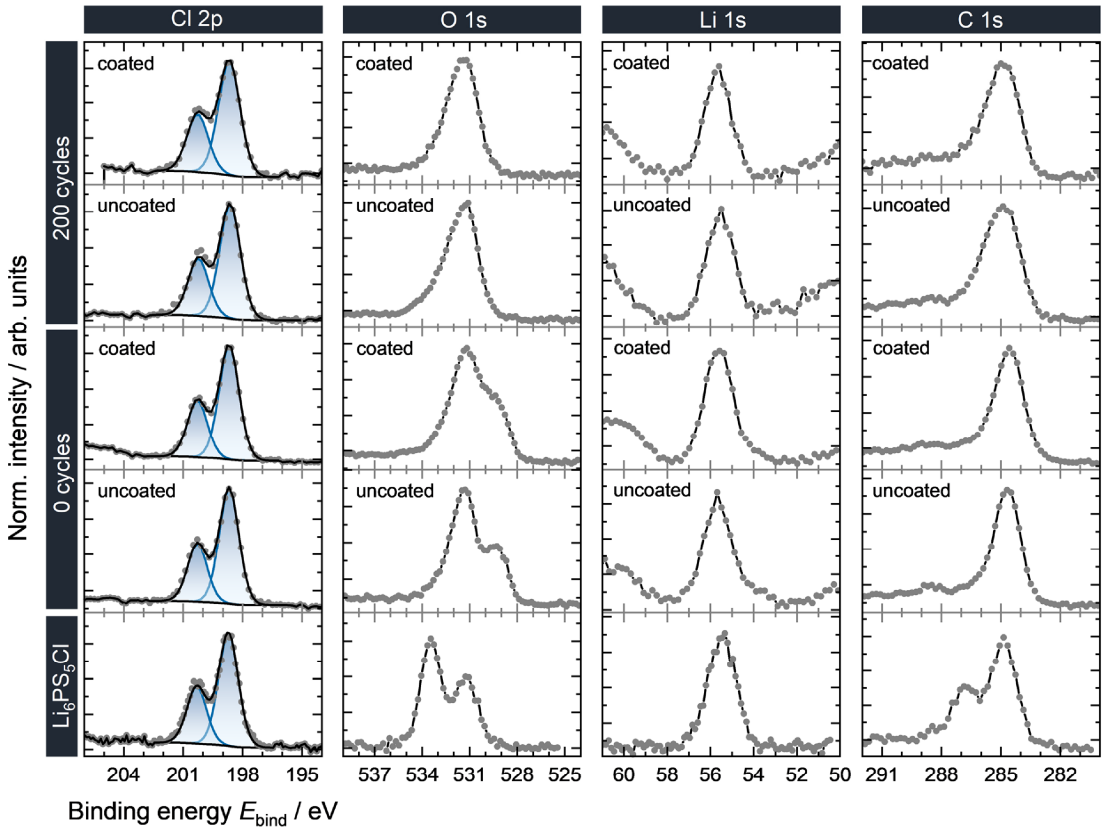

Figure S4. XP spectra of the Cl 2p, O 1s, Li 1s and C 1s signals of a Li_6PS_5Cl reference and the (un)cycled composite cathodes. The pass energy ranged between 23.50 eV (O 1s, C 1s, Cl 2p, Li 1s) and 29.35 eV (Li 1s of the solid electrolyte reference). Signal fitting was performed using a Shirley background, GL(30) line-shapes and common fitting restrictions.[14]

Post-Mortem Analyses - Nb 3d Signal Shift

The post-mortem analyses of the composite cathodes with coated CAM revealed a shift in the energetic signal position of the Nb 3d signal in the XP spectrum after battery cycling. In order to investigate this effect in more detail, we analyzed the Nb 3d spectrum at different cycling stages (see green data points in Figure 4B). For a better interpretation of the experimental data, it must be noted here that all spectra were calibrated in relation to the S 2p signal for the PS_4^{3-} unit of the solid electrolyte, and a flood gun was used to compensate charging effects.
Figure 4B shows that the Nb 3d signal massively shifts toward higher binding energies during the initial charging step. In the subsequent charge/discharge steps, the Nb 3d signal shifts more or less reversibly to lower binding energies during discharging and to higher binding energies during charging. A signal shift to higher binding energies in XP spectra is often directly associated with a change in the chemical environment and/or a change of the oxidation state (chemical shift). Following this approach, the higher binding energy would indicate a transition to a higher oxidation state. Since Nb is already in the formal 5+ oxidation state in $LiNbO_3$, a transition to oxidation state 6+ can be excluded. Even if the initial shift during charging is caused by another effect such as differential charging, the subsequent reversible shift in the subsequent cycles cannot be explained by redox behavior (e.g. a Nb^{5+}/Nb^{4+} transition). Although redox behavior has been reported for $LiNbO_3$ and various similar material-related oxides such as $LiNbO_2$ and Nb_2O_5, typical potentials for these reactions are significantly below the lower cut-off voltage of the ASSB.[18–24] In addition, the Nb 3d signal shape remains unchanged which would be highly unusual for a redox step and would indicate a 100% transition between the two oxidation states (see Figure 4B). Therefore, we exclude redox effects to cause the signal shifts here. A second approach to describe the signal shifts is based on a change in the electronic states, i.e. the electronic band structure of the compounds.[25–28] A closer look at the Ni 2p signal reveals signal shifts comparable to those of the Nb 3d signal (see black data points in Figure 4B), even though the Ni 2p signal shift is convoluted by the transition of the Ni oxidation state during battery charging. However, the observed signal shifts seem therefore to be correlated to the entire coated CAM. Consequently, a relation to the state of charge of the CAM seems obvious.
Battery charging is associated with a removal of Li^+ and e^- from the CAM. We assume that the release of e^- would in turn lead to a lowering of the Fermi level E_F as previously described for $LiCoO_2$.[29] Since the binding energy E_{bind} in XP spectra corresponds to the difference between E_F and the core levels, one could expect a decrease in the E_{bind}, which seems to contradict the experimental observation. However, since the energy calibration of the XP spectra were related to the solid electrolyte, the relative signal shift of CAM and solid electrolyte must be discussed and therefore the band structure of the solid electrolyte must be taken into account. In the

following, we use the simplified scheme of the band structure in Figure S5 to provide a possible explanation for the observed effects.

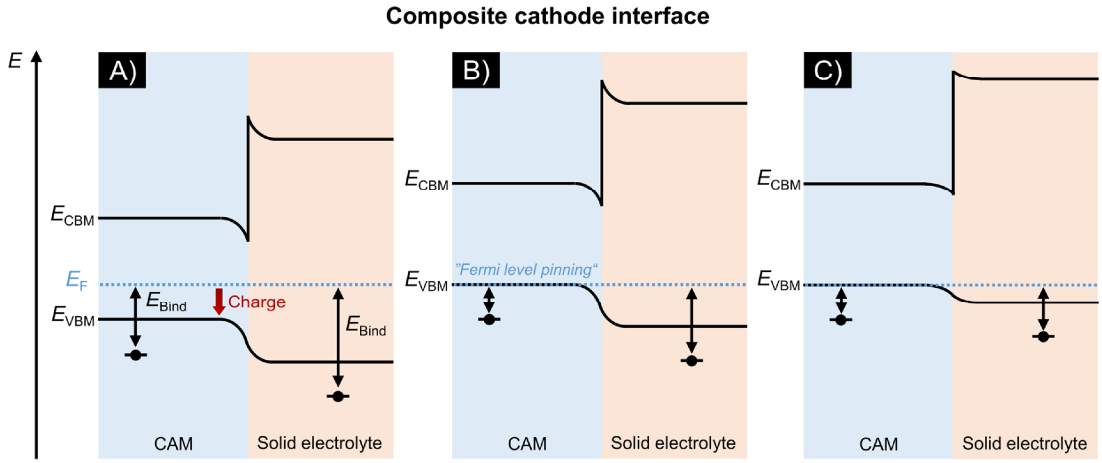

Figure S5. Scheme on the electronic energy band diagram at the CAM/solid electrolyte interface during ASSB charging. E_{VBM} and E_{CBM} denote the valence band maximum and the conduction band minimum, respectively. It is assumed here that the Fermi levels E_F of the CAM and the solid electrolyte align under equilibrium conditions. The binding energy E_{bind} in XP spectra corresponds to the difference between E_F and the core levels. The band bending at the interface is exemplary and cannot be directly related to the materials used in this work. A) State before the first charge step; the red arrow indicates the lowering of the Fermi level E_F during charge. B) State during battery charging, which can be described as a simultaneous decrease in the Fermi level E_F in both materials near the interface. Since we define the Fermi level E_F as reference energy, E_{VBM} and E_{CBM} rise relative to the Fermi level. C) The decrease in E_F is reduced at E_{VBM} of the CAM ("Fermi level pinning"), whereas the decrease in the solid electrolyte continues.

The CAM is a small-band gap semiconductor, whereas the solid electrolyte is an electronic insulator, i.e. wide-band gap semiconductor (Figure S5).[30] The coating material $LiNbO_3$ can also be treated as a semiconductor.[31] For the sake of simplicity, we neglect the coating material in the scheme and describe the basic considerations without taking its influence into account. If both materials (CAM and solid electrolyte) are in direct contact to each other, it can be assumed that their Fermi levels E_F will align under equilibrium conditions near the interface (Figure S5A). Under the assumption that the difference between the core levels and E_F does not change by this alignment, the binding energy E_{bind} in XP spectra will not be influenced. It must be noted that the band bending in Figure S5 is exemplary and cannot be directly related to the materials used.

If the battery cell is charged, Li^+ and e^- are released from the CAM, which leads to a lowering of the Fermi level E_F in the CAM as previously described for $LiCoO_2$ (Figure S5B).[29] Under equilibrium conditions, the Fermi levels of both the CAM and the solid electrolyte will align again near the interface, which can be described as a simultaneous lowering of the Fermi level in both materials. For the sake of simplicity, we defined the Fermi levels as a reference point in Figure S5, so that in consequence the valence and conduction band edges appear to rise in the scheme.

However, the lowering of the Fermi level does not lead to a relative signal shift between solid electrolyte and CAM signals until the valence band edge is reached, since the change in the Fermi energy is the same for both materials. Assuming that the valence band edge of the CAM is energetically higher than of the solid electrolyte, the Fermi level decrease will be reduced down at the valence band edge of the CAM ("Fermi level pinning"), whereas a decrease in the solid electrolyte continues (here represented by an increase of the valence and conduction band edge). As a consequence, the energetic difference between the Fermi level and the core states (the binding energy) is faster decreased in the solid electrolyte than in the CAM. From this point on, an energy calibration in relation to the solid electrolyte would lead to an apparent signal shift of CAM signals toward higher binding energies in XP spectra.

During discharging, an opposite effect would occur. The filling of the empty states of the solid electrolyte leads to a fast rise in the Fermi level, whereas the rise is comparably slow in the CAM. Analogously to the situation described before, this would lead to an apparent signal shift of CAM signals toward lower binding energies in XP spectra. After a certain threshold, the Fermi level rise continues more or less simultaneously in both materials with no further consequence for the XP spectra. Since the initial signal shift during charging is irreversible, we assume pronounced material changes during the initial cycle which influence the electronic states/the electronic band structure. In subsequent cycles, the shift seems partially reversible, which indicates only minor changes after the initial cycle.

At this point it must be noted, that this is a simplified picture. The described effects are highly dependent on the electronic states and their energetic position.[29] Accordingly, the basic assumption of "Fermi pinning effects" here is highly dependent on donor and acceptor states, intrinsic defects and structural changes which in turn influence the band structure, to name a few. In addition, we neglect the influence of the ionic contribution which can influence the electronic states. In general, signal shifts in XP spectra can also be caused by differential charging, surface/interface dipoles and related effects such as potential gradients.[16,17,32–34] Since all these effects overlap in composite cathodes, it is highly challenging to deconvolute the individual contributions. Consequently, binding energy calibration is not trivial, as already highlighted in literature.[34,35]

Post-Mortem Analyses - Influence of Battery Cycling

Figure S6 shows the S 2p and P 2p detail spectra of composite cathodes with Li_2CO_3/$LiNbO_3$ coated NCM622 at different cycling stages (0 cycles, 0.5 cycles (1st charge), 1 cycle, 1.5 cycles (2nd charge), 2 cycles and 200 cycles) in order to monitor the decomposition product concentration evolution. In the following, we will describe the observations for the S 2p signal first and discuss the origin for the signal changes. After that, we will describe the P 2p signal changes in more detail.

The S 2p spectra show an increase in the signal shoulder at higher binding energies due to battery cycling. The origin of the formed species ($S^{ox,1}$, $S^{ox,2}$) is addressed in more detail in the manuscript and can basically be related to the formation of polysulfides and/or various possible anionic frameworks that Li-P-S phases can pass through during redox reactions. It can be seen that the formation of such species takes mainly place during the initial charge step and does not significantly change in the following charge/discharge steps. Nevertheless, it can be seen that the signal shoulder at higher binding energies is slightly increased after the charging steps (1st charge, 2nd charge) compared to the full cycles (1 cycle, 2 cycles). The opposite behavior can be observed for the S^{2-} species (more species after discharging). This observation is in accordance with recent reports on the redox behavior of thiophosphates and their decomposition products. Accordingly, the formation of polysulfides and/or various anionic frameworks is (partially) reversible. Typically, the potential window of ASSBs does not allow a complete reduction of these species. For this reason, we can see a strong increase in $S^{ox,1}$ and $S^{ox,2}$ during the initial charging step but no strong change in the following cycle steps. The lower cut-off potential during discharging seems to allow only a minor partial reversibility of the reactions occurring.
In this context it must be taken into account that the formation of $S^{ox,1}$ and $S^{ox,2}$ is not necessarily related to the cathode active material/solid electrolyte interface. As already reported in previous studies, reactions at the carbon additive/solid electrolyte interface can also lead to the formation of such species. Since (uncoated) C65 was used as conductive additive in this study, the rise in the signals $S^{ox,1}$ and $S^{ox,2}$ is at least partially due to the carbon additive/solid electrolyte interface. Consequently, direct conclusions on the reactions at the cathode active material/solid electrolyte interface are not possible here.

The P 2p spectra show an increase in the signal shoulder at higher binding energies due to battery cycling. Next to the compounds mentioned in the context of the S 2p signal, phosphates such as Li_3PO_4 and transition metal phosphates can be found in this binding energy range and

seem reasonable for decomposition products. Analogous to the S 2p spectra, the signal shoulder at higher binding energies is slightly increased after the charging steps (1st charge, 2nd charge) compared to the full cycles (1 cycle, 2 cycles). This indicates again a partial reversibility of the reactions occurring. In contrast to the S 2p spectra, the formation of the P 2p signal shoulder at high binding energies is not distinctly pronounced after the initial cycles. If one compares the detail spectra after 2 cycles and 200 cycles (both discharged), it gets obvious that the formation of the decomposition products is rather successive with increasing cycle number. Since the formation of phosphates such as Li_3PO_4 and transition metal phosphates requires an oxygen source (NCM), we can neglect the influence of the carbon additive and can relate these observations mainly to the cathode active material/solid electrolyte interface. Overall, these results indicate that the interfacial reaction at the cathode active material/solid electrolyte interface is successive and not completed after the initial cycles. This is in accordance with the ToF-SIMS results shown in the manuscript.

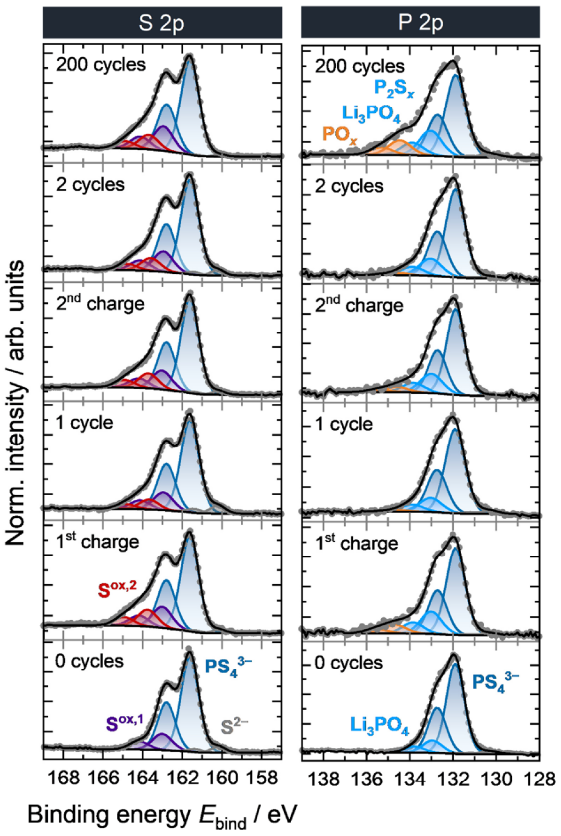

Figure S6. S 2p and P 2p detail spectra of composite cathodes with Li_2CO_3/$LiNbO_3$ coated NCM622 at different cycling stages (0 cycles, 0.5 cycles (1st charge), 1 cycle, 1.5 cycles (2nd charge), 2 cycles and 200 cycles). The pass energy was 23.50 eV in all cases. Signal fitting includes a Shirley background, GL(30) line-shapes and common fitting restrictions.[14]

Time-of-Flight Secondary Ion Mass Spectrometry (ToF-SIMS)

Region-of-Interest (ROI) Analysis

A direct comparison of secondary ion images and corresponding signals obtained from FIB craters is not possible since the FIB cut planes have different features, e.g. a different number of cathode active material particles and different NCM622/SE area ratios within the analysis area. Consequently, a ROI analysis is indispensable.

A scheme of the procedure is shown in Figure S7. First, the secondary ion images are normalized to the total secondary ion image to compensate topographic effects of the FIB crater. Afterward, a ROI is defined using a signal threshold. The number of the pixels within this threshold is extracted to normalize the signal intensities within the ROI. In this way, deviations in the FIB cut planes such as different NCM622/SE area ratios within the analysis area are minimized.

To analyze the phosphate and the sulfate/sulfite formation, we used the multiplied ($PO_2^- \cdot PO_3^-$) and ($SO_2^- \cdot SO_3^-$) secondary ion images. By multiplying secondary ion images, effects of mass interference can be minimized as already described in our previous work.[4] In this way, more reliable results are obtained.

Figure S8 shows the results of the ROI analysis for different signal thresholds (TH). Basically, increasing the lower limit reduces interferences due to signal noise. The trends for TH = 5-100 and TH = 10-100 match each other very well.

Battery cycling leads to an increase in the counts of phosphate and sulfate/sulfite fragments (PO_x^-, SO_x^-). The $Li_2CO_3/LiNbO_3$ coating seems to suppress the formation of both decomposition products. According to the results for the composite cathodes with $LiNbO_3/Li_2CO_3$ coated NCM622, the formation of decomposition products is rather successive and not completed after the initial cycle which supports the XPS results (see above).

For the uncycled composite cathodes, the $Li_2CO_3/LiNbO_3$ coating seems also to suppress the initial decomposition reactions due to the mere contact of the composite cathode materials. A more detailed discussion on the influence of the cathode active material coating is given in the manuscript.

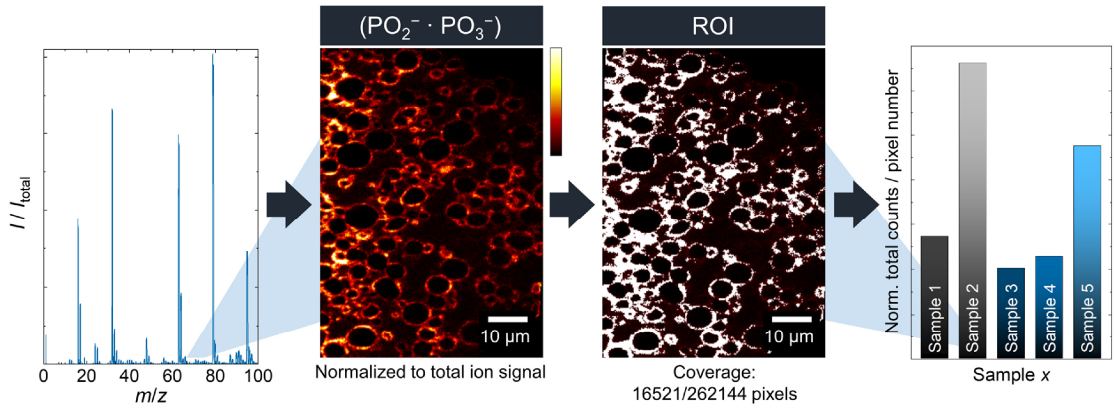

Figure S7. Region-of-interest (ROI) analysis procedure using the multiplied ($PO_2^- \cdot PO_3^-$) signal as an example. A signal threshold is defined in the ($PO_2^- \cdot PO_3^-$) secondary ion image. The number of pixels within this signal threshold is extracted and the signal intensities are normalized. In this way, deviations in FIB cut planes such as different NCM622/SE area ratios within the analysis area can be minimized and a semiquantitative analysis can be performed.

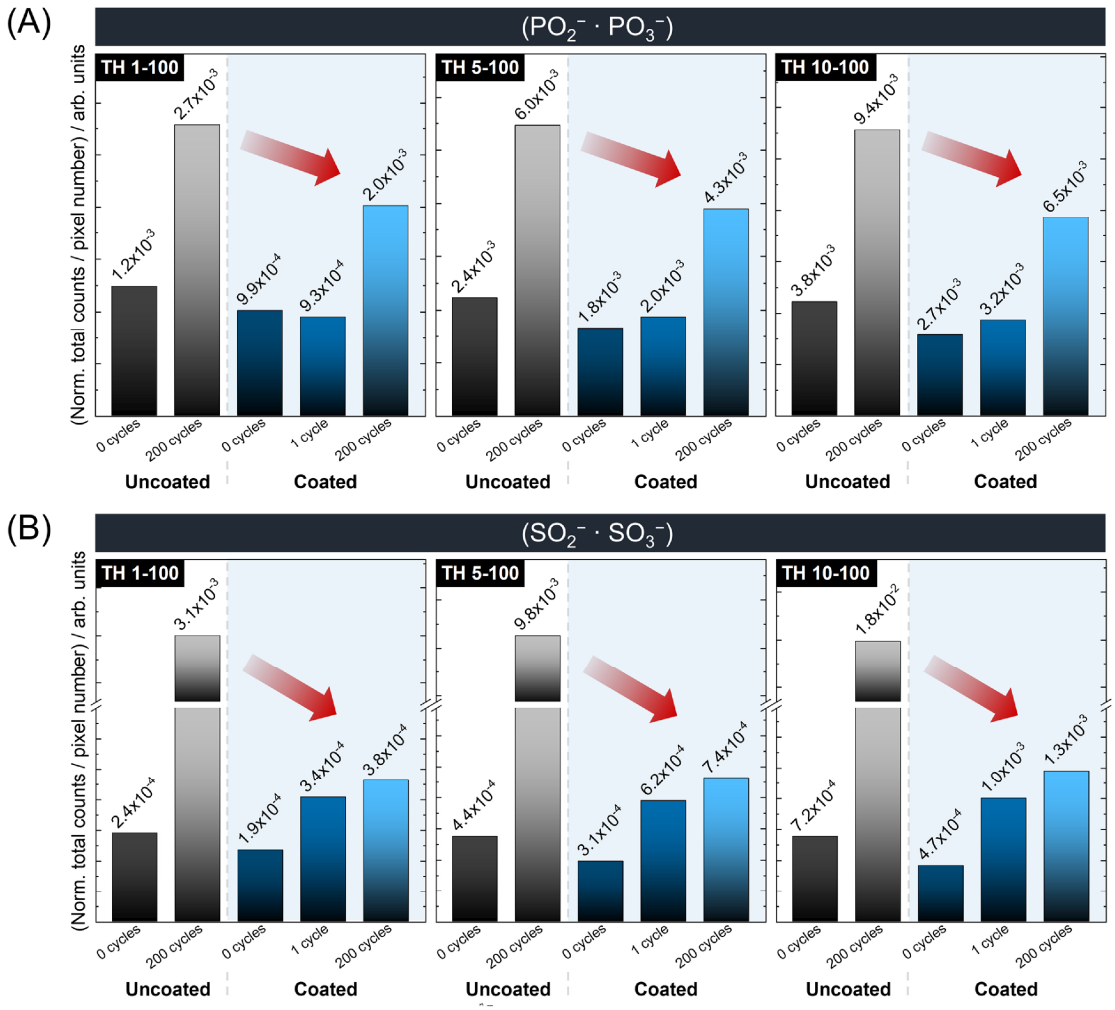

Figure S8. Results of the ROI analysis for different signal thresholds (TH). Battery cycling leads to an increase in phosphate and sulfate/sulfite fragments (PO_x^-, SO_x^-). The $LiNbO_3$/Li_2CO_3 coating suppresses the formation of both decomposition products.

Supplementary References

(1) Busca, G.; Lorenzelli, V. Infrared Spectroscopic Identification of Species Arising from Reactive Adsorption of Carbon Oxides on Metal Oxide Surfaces. *Mater. Chem.* **1982**, *7* (1), 89–126. https://doi.org/10.1016/0390-6035(82)90059-1.

(2) Kim, A.-Y.; Strauss, F.; Bartsch, T.; Teo, J. H.; Hatsukade, T.; Mazilkin, A.; Janek, J.; Hartmann, P.; Brezesinski, T. Stabilizing Effect of a Hybrid Surface Coating on a Ni-Rich NCM Cathode Material in All-Solid-State Batteries. *Chem. Mater.* **2019**, *31* (23), 9664–9672. https://doi.org/10.1021/acs.chemmater.9b02947.

(3) Auvergniot, J.; Cassel, A.; Foix, D.; Viallet, V.; Seznec, V.; Dedryvère, R. Redox Activity of Argyrodite Li_6PS_5Cl Electrolyte in All-Solid-State Li-Ion Battery: An XPS Study. *Solid State Ionics* **2017**, *300*, 78–85. https://doi.org/10.1016/j.ssi.2016.11.029.

(4) Walther, F.; Koerver, R.; Fuchs, T.; Ohno, S.; Sann, J.; Rohnke, M.; Zeier, W. G.; Janek, J. Visualization of the Interfacial Decomposition of Composite Cathodes in Argyrodite-Based All-Solid-State Batteries Using Time-of-Flight Secondary-Ion Mass Spectrometry. *Chem. Mater.* **2019**, *31* (10), 3745–3755. https://doi.org/10.1021/acs.chemmater.9b00770.

(5) Appapillai, A. T.; Mansour, A. N.; Cho, J.; Shao-Horn, Y. Microstructure of $LiCoO_2$ with and without "$AlPO_4$" Nanoparticle Coating: Combined STEM and XPS Studies. *Chem. Mater.* **2007**, *19* (23), 5748–5757. https://doi.org/10.1021/cm0715390.

(6) Wang, B.; Liu, J.; Sun, Q.; Li, R.; Sham, T.-K.; Sun, X. Atomic Layer Deposition of Lithium Phosphates as Solid-State Electrolytes for All-Solid-State Microbatteries. *Nanotechnology* **2014**, *25* (50), 504007. https://doi.org/10.1088/0957-4484/25/50/504007.

(7) Bodenes, L.; Dedryvère, R.; Martinez, H.; Fischer, F.; Tessier, C.; Pérès, J.-P. Lithium-Ion Batteries Working at 85°C: Aging Phenomena and Electrode/Electrolyte Interfaces Studied by XPS. *J. Electrochem. Soc.* **2012**, *159* (10), A1739–A1746. https://doi.org/10.1149/2.061210jes.

(8) Kosova, N. V.; Devyatkina, E. T.; Kaichev, V. V. Optimization of Ni^{2+}/Ni^{3+} Ratio in Layered $Li(Ni,Mn,Co)O_2$ Cathodes for Better Electrochemistry. *J. Power Sources* **2007**, *174* (2), 965–969. https://doi.org/10.1016/j.jpowsour.2007.06.051.

(9) Walther, F.; Randau, S.; Schneider, Y.; Sann, J.; Rohnke, M.; Richter, F. H.; Zeier, W. G.; Janek, J. Influence of Carbon Additives on the Decomposition Pathways in Cathodes of Lithium Thiophosphate-Based All-Solid-State Batteries. *Chem. Mater.* **2020**, *32* (14),

6123–6136. https://doi.org/10.1021/acs.chemmater.0c01825.

(10) Nagao, K.; Hayashi, A.; Deguchi, M.; Tsukasaki, H.; Mori, S.; Tatsumisago, M. Amorphous $LiCoO_2$-Li_2SO_4 Active Materials: Potential Positive Electrodes for Bulk-Type All-Oxide Solid-State Lithium Batteries with High Energy Density. *J. Power Sources* **2017**, *348*, 1–8. https://doi.org/10.1016/j.jpowsour.2017.02.038.

(11) Andreu, N.; Flahaut, D.; Dedryvère, R.; Minvielle, M.; Martinez, H.; Gonbeau, D. XPS Investigation of Surface Reactivity of Electrode Materials: Effect of the Transition Metal. *ACS Appl. Mater. Interfaces* **2015**, *7* (12), 6629–6636. https://doi.org/10.1021/am5089764.

(12) Iwanowski, R. J.; Heinonen, M.; Pracka, I.; Raczyńska, J.; Fronc, K.; Sobczak, J. W. Application of in Situ Surface Scraping for Extracting Bulk Component of XPS Signal – Example of $LiNbO_3$ and GaSb. *J. Alloys Compd.* **1999**, *286* (1–2), 162–166. https://doi.org/10.1016/S0925-8388(98)01000-7.

(13) Skryleva, E. A.; Kubasov, I. V.; Kiryukhantsev-Korneev, P. V.; Senatulin, B. R.; Zhukov, R. N.; Zakutailov, K. V.; Malinkovich, M. D.; Parkhomenko, Y. N. XPS Study of Li/Nb Ratio in $LiNbO_3$ Crystals. Effect of Polarity and Mechanical Processing on $LiNbO_3$ Surface Chemical Composition. *Appl. Surf. Sci.* **2016**, *389*, 387–394. https://doi.org/10.1016/j.apsusc.2016.07.108.

(14) Moulder, J. F.; Stickle, W. F.; Sobol, P. E.; Bomben, K. D. *Handbook of X-Ray Photoelectron Spectroscopy; A Reference Book of Standard Spectra for Identification and Interpretation of XPS Data*; Chastain, J., King Jr., R. C., Eds.; Physical Electronics: Eden Prairie, US-MN, 1995.

(15) Morgan, W. E.; Van Wazer, J. R.; Stec, W. J. Inner-Orbital Photoelectron Spectroscopy of the Alkali Metal Halides, Perchlorates, Phosphates, and Pyrophosphates. *J. Am. Chem. Soc.* **1973**, *95* (3), 751–755. https://doi.org/10.1021/ja00784a018.

(16) Maibach, J.; Lindgren, F.; Eriksson, H.; Edström, K.; Hahlin, M. Electric Potential Gradient at the Buried Interface between Lithium-Ion Battery Electrodes and the SEI Observed Using Photoelectron Spectroscopy. *J. Phys. Chem. Lett.* **2016**, *7* (10), 1775–1780. https://doi.org/10.1021/acs.jpclett.6b00391.

(17) Lindgren, F.; Rehnlund, D.; Källquist, I.; Nyholm, L.; Edström, K.; Hahlin, M.; Maibach, J. Breaking Down a Complex System: Interpreting PES Peak Positions for Cycled Li-Ion Battery Electrodes. *J. Phys. Chem. C* **2017**, *121* (49), 27303–27312. https://doi.org/10.1021/acs.jpcc.7b08923.

(18) Özer, N.; Lampert, C. M. Electrochemical Lithium Insertion in Sol-Gel Deposited $LiNbO_3$ Films. *Sol. Energy Mater. Sol. Cells* **1995**, *39* (2–4), 367–375. https://doi.org/10.1016/0927-0248(96)80002-X.

(19) Pralong, V.; Reddy, M. A.; Caignaert, V.; Malo, S.; Lebedev, O. I.; Varadaraju, U. V.; Raveau, B. A New Form of $LiNbO_3$ with a Lamellar Structure Showing Reversible Lithium Intercalation. *Chem. Mater.* **2011**, *23* (7), 1915–1922. https://doi.org/10.1021/cm1036524.

(20) Lee, D.; Shank, J. C.; Tellekamp, M. B.; Doolittle, W. A.; Alamgir, F. M. Thin-Film Lithium Niobites and Their Chemical Properties for Lithium-Ion Storage and Diffusion. *ChemElectroChem* **2019**, *6* (19), 5109–5115. https://doi.org/10.1002/celc.201901347.

(21) Li, W.; Hu, C.; Zhou, M.; Wang, K.; Li, H.; Cheng, S.; Jiang, K. The Electrochemical Synthesis of $LiNbO_2$ in Molten Salts and Its Application for Lithium Ion Batteries with High Rate Capability. *Electrochim. Acta* **2016**, *189*, 231–236. https://doi.org/10.1016/j.electacta.2015.12.085.

(22) Viet, A. Le; Reddy, M. V.; Jose, R.; Chowdari, B. V. R.; Ramakrishna, S. Nanostructured Nb_2O_5 Polymorphs by Electrospinning for Rechargeable Lithium Batteries. *J. Phys. Chem. C* **2010**, *114* (1), 664–671. https://doi.org/10.1021/jp9088589.

(23) Wei, M.; Wei, K.; Ichihara, M.; Zhou, H. Nb_2O_5 Nanobelts: A Lithium Intercalation Host with Large Capacity and High Rate Capability. *Electrochem. commun.* **2008**, *10* (7), 980–983. https://doi.org/10.1016/j.elecom.2008.04.031.

(24) Kumagai, N.; Koishikawa, Y.; Komaba, S.; Koshiba, N. Thermodynamics and Kinetics of Lithium Intercalation into Nb_2O_5 Electrodes for a 2 V Rechargeable Lithium Battery. *J. Electrochem. Soc.* **1999**, *146* (9), 3203–3210. https://doi.org/10.1149/1.1392455.

(25) Tonti, D.; Pettenkofer, C.; Jaegermann, W. Origin of the Electrochemical Potential in Intercalation Electrodes: Experimental Estimation of the Electronic and Ionic Contributions for Na Intercalated into TiS_2. *J. Phys. Chem. B* **2004**, *108* (41), 16093–16099. https://doi.org/10.1021/jp047450o.

(26) Hausbrand, R.; Becker, D.; Jaegermann, W. A Surface Science Approach to Cathode/Electrolyte Interfaces in Li-Ion Batteries: Contact Properties, Charge Transfer and Reactions. *Prog. Solid State Chem.* **2014**, *42* (4), 175–183. https://doi.org/10.1016/j.progsolidstchem.2014.04.010.

(27) Schwöbel, A.; Jaegermann, W.; Hausbrand, R. Interfacial Energy Level Alignment and Energy Level Diagrams for All-Solid Li-Ion Cells: Impact of Li-Ion Transfer and Double

Layer Formation. *Solid State Ionics* **2016**, *288*, 224–228. https://doi.org/10.1016/j.ssi.2015.12.029.

(28) Cherkashinin, G.; Hausbrand, R.; Jaegermann, W. Performance of Li-Ion Batteries: Contribution of Electronic Factors to the Battery Voltage. *J. Electrochem. Soc.* **2019**, *166* (3), A5308–A5312. https://doi.org/10.1149/2.0441903jes.

(29) Molenda, J.; Baster, D.; Milewska, A.; Świerczek, K.; Bora, D. K.; Braun, A.; Tobola, J. Electronic Origin of Difference in Discharge Curve between Li_xCoO_2 and Na_xCoO_2 Cathodes. *Solid State Ionics* **2015**, *271*, 15–27. https://doi.org/10.1016/j.ssi.2014.09.032.

(30) Chakraborty, A.; Kunnikuruvan, S.; Kumar, S.; Markovsky, B.; Aurbach, D.; Dixit, M.; Major, D. T. Layered Cathode Materials for Lithium-Ion Batteries: Review of Computational Studies on $LiNi_{1-x-y}Co_x Mn_yO_2$ and $LiNi_{1-x-y}Co_xAl_y$. *Chem. Mater.* **2020**, *32* (3), 915–952. https://doi.org/10.1021/acs.chemmater.9b04066.

(31) Thierfelder, C.; Sanna, S.; Schindlmayr, A.; Schmidt, W. G. Do We Know the Band Gap of Lithium Niobate? *Phys. status solidi* **2010**, *7* (2), 362–365. https://doi.org/10.1002/pssc.200982473.

(32) Yu, X.-R.; Hantsche, H. Vertical Differential Charging in Monochromatized Small Spot X-Ray Photoelectron Spectroscopy. *Surf. Interface Anal.* **1993**, *20* (7), 555–558. https://doi.org/10.1002/sia.740200702.

(33) Pertsin, A. J.; Pashunin, Y. M. Differential Charging in XPS Studies of Polymer/Metal Interfaces. *Appl. Surf. Sci.* **1990**, *44* (3), 171–178. https://doi.org/10.1016/0169-4332(90)90047-4.

(34) Oswald, S.; Thoss, F.; Zier, M.; Hoffmann, M.; Jaumann, T.; Herklotz, M.; Nikolowski, K.; Scheiba, F.; Kohl, M.; Giebeler, L.; et al. Binding Energy Referencing for XPS in Alkali Metal-Based Battery Materials Research (II): Application to Complex Composite Electrodes. *Batteries* **2018**, *4* (3), 36. https://doi.org/10.3390/batteries4030036.

(35) Greczynski, G.; Hultman, L. X-Ray Photoelectron Spectroscopy: Towards Reliable Binding Energy Referencing. *Prog. Mater. Sci.* **2020**, *107*, 100591. https://doi.org/10.1016/j.pmatsci.2019.100591.

7.2 Scientific Contributions

7.2.1 List of Publications

2021 Wang, S.; Zhang, W.; Chen, X.; Das, D.; Ruess, R.; Gautam, A.; Walther, F.; Ohno, S.; Koerver, R.; Zhang, Q.; et al. Influence of Crystallinity of Lithium Thiophosphate Solid Electrolytes on the Performance of Solid-State Batteries. *Adv. Energy Mater.* **2021**, 2100654. https://doi.org/10.1002/aenm.202100654.

Walther, F.; Strauss, F.; Wu, X.; Mogwitz, B.; Hertle, J.; Sann, J.; Rohnke, M.; Brezesinski, T.; Janek, J. The Working Principle of a Li_2CO_3/$LiNbO_3$ Coating on NCM for Thiophosphate-Based All-Solid-State Batteries. *Chem. Mater.* **2021**, 33 (6), 2110–2125. https://doi.org/10.1021/acs.chemmater.0c04660.

Randau, S.; Walther, F.; Neumann, A.; Schneider, Y.; Negi, R. S.; Mogwitz, B.; Sann, J.; Becker-Steinberger, K.; Danner, T.; Hein, S.; et al. On the Additive Microstructure in Composite Cathodes and Alumina-Coated Carbon Microwires for Improved All-Solid-State Batteries. *Chem. Mater.* **2021**, 33 (4), 1380–1393. https://doi.org/10.1021/acs.chemmater.0c04454.

2020 Walther, F.; Randau, S.; Schneider, Y.; Sann, J.; Rohnke, M.; Richter, F. H.; Zeier, W. G.; Janek, J. Influence of Carbon Additives on the Decomposition Pathways in Cathodes of Lithium Thiophosphate-Based All-Solid-State Batteries. *Chem. Mater.* **2020**, 32 (14), 6123–6136. https://doi.org/10.1021/acs.chemmater.0c01825.

2019 Hofmann, P.; Walther, F.; Rohnke, M.; Sann, J.; Zeier, W. G.; Janek, J. LATP and $LiCoPO_4$ Thin Film Preparation – Illustrating Interfacial Issues on the Way to All-Phosphate SSBs. *Solid State Ionics* **2019**, 342, 115054. https://doi.org/10.1016/j.ssi.2019.115054.

Ahmed, S.; Pokle, A.; Schweidler, S.; Beyer, A.; Bianchini, M.; Walther, F.; Mazilkin, A.; Hartmann, P.; Brezesinski, T.; Janek, J.; et al. The Role of Intragranular Nanopores in Capacity Fade of Nickel-Rich Layered $Li(Ni_{1-x-y}Co_xMn_y)O_2$ Cathode Materials. *ACS Nano* **2019**, 13 (9), 10694–10704. https://doi.org/10.1021/acsnano.9b05047.

Walther, F.; Koerver, R.; Fuchs, T.; Ohno, S.; Sann, J.; Rohnke, M.; Zeier, W. G.; Janek, J. Visualization of the Interfacial Decomposition of Composite Cathodes in Argyrodite-Based All-Solid-State Batteries Using Time-of-Flight Secondary-Ion Mass Spectrometry. *Chem. Mater.* **2019**, 31 (10), 3745–3755. https://doi.org/10.1021/acs.chemmater.9b00770.

2018 Hille, P.; Walther, F.; Klement, P.; Müßener, J.; Schörmann, J.; Kaupe, J.; Mitić, S.; Rosemann, N. W.; Chatterjee, S.; Beyer, A.; et al. Influence of the Atom Source Operating Parameters on the Structural and Optical Properties of $In_xGa_{1-x}N$ Nanowires Grown by Plasma-Assisted Molecular Beam Epitaxy. *J. Appl. Phys.* **2018**, 124 (16), 165703. https://doi.org/10.1063/1.5050391.

Neudeck, S.; Walther, F.; Bergfeldt, T.; Suchomski, C.; Rohnke, M.; Hartmann, P.; Janek, J.; Brezesinski, T. Molecular Surface Modification of NCM622 Cathode Material Using Organophosphates for Improved Li-Ion Battery Full-Cells. *ACS*

Appl. Mater. Interfaces **2018**, 10 (24), 20487–20498. https://doi.org/10.1021/acsami.8b04405.

Stock, D.; Dongmo, S.; Walther, F.; Sann, J.; Janek, J.; Schröder, D. Homogeneous Coating with an Anion-Exchange Ionomer Improves the Cycling Stability of Secondary Batteries with Zinc Anodes. *ACS Appl. Mater. Interfaces* **2018**, 10 (10), 8640–8648. https://doi.org/10.1021/acsami.7b18623.

2017 Koerver, R.; Walther, F.; Aygün, I.; Sann, J.; Dietrich, C.; Zeier, W. G.; Janek, J. Redox-Active Cathode Interphases in Solid-State Batteries. *J. Mater. Chem. A* **2017**, 5 (43), 22750–22760. https://doi.org/10.1039/C7TA07641J.

2016 Ajay, A.; Schörmann, J.; Jiménez-Rodriguez, M.; Lim, C. B.; Walther, F.; Rohnke, M.; Mouton, I.; Amichi, L.; Bougerol, C.; Den Hertog, M. I.; et al. Ge Doping of GaN beyond the Mott Transition. *J. Phys. D. Appl. Phys.* **2016**, 49 (44), 445301. https://doi.org/10.1088/0022-3727/49/44/445301.

7.2.2 List of Patents

2021 Electron-conducting additive for cathodes, Walther, F.; Randau, S.; Richter, F. H.; Janek, J., European patent, application no. 20201700.0.

7.2.3 List of Conference Contributions

2020 "BASF International Scientific Network for Electrochemistry and Batteries - Meetings" (**2020**) – Online Presentation

2019 "SIMS22 - International Conference on Secondary Ion Mass Spectrometry" in Kyoto, Japan (**2019**) – Oral Presentation

"ECEE 2019 - Electrochemical Conference on Energy and the Environment: Bioelectrochemistry and Energy Storage" in Glasgow, Scotland (**2019**) - Oral Presentation

"BASF International Scientific Network for Electrochemistry and Batteries - Meetings" in Bad Dürkheim, Germany (**2019**) - Oral Presentation

"Bunsentagung 2019 - 118th General Assembly of the German Bunsen Society for Physical Chemistry" in Jena, Germany (**2019**) - Oral Presentation

2018 "SIMS Europe" in Münster, Germany (**2018**) - Oral Presentation

"BASF International Scientific Network for Electrochemistry and Batteries - Meetings" in Bad Dürkheim, Germany (**2018**) - Oral Presentation

2017 "SIMS21 - International Conference on Secondary Ion Mass Spectrometry" in Kraków, Poland (**2017**) – Poster Presentation

2016 "DPG-Frühjahrstagung der Sektion Kondensierte Materie" in Regensburg, Germany (**2016**) – Poster Presentation

8 Acknowledgement

(written in native language)

An dieser Stelle möchte ich mich herzlich bei all denjenigen bedanken, die mich während meiner Promotionszeit begleitet und unterstützt haben.

Zunächst möchte ich Prof. Dr. Jürgen Janek für den fachlichen Rahmen meiner Promotion danken. Spannende industrienahe Forschungsprojekte, hervorragende Forschungsbedingungen und die Möglichkeit, an (inter)nationalen Konferenzen teilnehmen zu können, haben ein fachliches Umfeld geschaffen, in dem ich mich wissenschaftlich voll entfalten konnte. Auf persönlicher Ebene möchte ich mich für die Betreuung, das stetige Interesse an meiner Arbeit und ganz besonders für die auch sehr wichtige nicht-wissenschaftliche Persönlichkeitsförderung bedanken.

PD Dr. Marcus Rohnke und Dr. Joachim Sann möchte ich dafür danken, dass sie mich in die Geheimnisse der Oberflächen- und Grenzflächenanalytik eingeweiht haben, jederzeit für Fragen und fachliche Diskussionen offen waren und mich stets unterstützt haben. Nicht zuletzt der hohe wissenschaftliche Standard, aber auch das entgegengebrachte Vertrauen ermöglichte mir die Weiterentwicklung meiner fachlichen Kompetenz. PD Dr. Marcus Rohnke und Prof. Dr. Michael Dürr möchte ich zudem herzlich für die Übernahme der Korreferate dieser Arbeit danken.

Ein großer Dank gilt den vielen Projekt- und Kooperationspartnern, mit denen ich gemeinsam in spannenden Forschungsprojekten arbeiten durfte. Besonders hervorzuheben sind Prof. Dr. Wolfgang G. Zeier und Dr. Raimund Koerver, die mich förderten und mein fachliches Selbstvertrauen gestärkt haben. Ich bedanke mich bei der BASF SE für die Finanzierung der Forschungsarbeiten im Rahmen des „International Network for Batteries and Electrochemistry" und den wertvollen wissenschaftlichen Austausch innerhalb des Netzwerkes. Insbesondere die Zusammenarbeit mit Dr. Xiaohan Wu und Jonas Hertle hat mir sehr viel Spaß gemacht und es war aufregend, den Fortschritt des Projektes zu sehen und mitzugestalten.

Mein besonderer Dank gilt meinen Kolleg:innen und Freund:innen, insbesondere Dr. Daniel Stock, Christine Kern, Dr. Peter Schmitz, Adrian Schürmann, Dr. Raimund Koerver, Dr. Kaija Schäpe, Svenja Otto, Yannik Moryson, Jonas Hertle, Dr. Tong-Tong Zuo und Dr. Sean Culver. Einerseits möchte ich mich für zahlreiche fachliche Unterhaltungen und das Korrekturlesen meiner wissenschaftlichen Arbeiten bedanken, anderseits für die vielen gemeinsamen nicht-wissenschaftlichen Gespräche, Besuche der Mensa, die eine oder andere Kaffeepause und die vielen schönen gemeinsamen Erlebnisse inner- und außerhalb der Universität.

An dieser Stelle möchte ich mich ebenfalls von ganzem Herzen für die Erfindung des Kaffees bedanken. Ohne den schwarzen Trunk der Glückseligkeit wäre diese Arbeit wohl nicht ansatzweise denkbar gewesen.

Abschließend möchte ich diejenigen hervorheben, die das Fundament im meinem Leben bilden - meine Familie und meine Freunde. Speziell meinen Eltern, meiner Schwester und meiner Freundin danke ich für ihr Verständnis, anhaltende Unterstützung und die vielen großen und kleinen Ablenkungen und Aufmunterungen während der Promotionszeit. Meine Familie trägt den wohl größten Anteil zu dieser Arbeit, denn sie sind das, was mich ausmacht.